Chaotic Mixing in Wavy-type Channels and Two-layer Shallow Flows

Wei-Koon Lee
St Catherine's College
University of Oxford

A thesis submitted for the degree of
Doctor of Philosophy

Michaelmas 2011

This thesis is dedicated to

my wife and my two lovely daughters,

for being there with me, for me,

along this journey of adventure with God.

Acknowledgements

I would like to express my heartiest gratitude to my two supervisors, Prof Alistair Borthwick and Prof Paul Taylor, who have given me immeasurable guidance in this academic pursuit. It is such an honour to work with them, to have the priviledge of access to their scholarly advice and insight. Their gentleness, patience and encouragement have always been a powerful lifting force that keeps me going in the time when the outlook seems bleak. Their assurance and confidence in me have helped me to build up my self-belief, an invaluable asset that shall propel me forward in my future undertaking. I am also indebted to them for the many opportunities opened up to me, in particular teaching, and academic interactions with the larger body of research communities around the world. Truly, they are the single most important success factor of the completion of my doctorate research.

I would like to express my appreciation to the staff members in the Department of Engineering Science Computing Support Group, as well as Oxford e-Research Centre, home of the Oxford Supercomputing Centre, for their technical support, which is pivotal in the nature of this work. My thanks also goes to the wider adminstrative support rendered by the departmental staff, and those in St. Catherine's College. I am most grateful to my college advisor, Dr Byron Byrne, for his encouragement, genuine concern and advice throughout my study.

It is such pleasure to work with the many outstanding people, current and former ones, in the Ocean Engineering Dynamics Group, as well as the visiting academics and students. Many thanks to Prof Rodney Eatock Taylor, Dr Ben Rogers, Dr QiuHua Liang, Dr Thomas Adcock, for their encouragement, probing questions and helpful advice, and for the many other graduate students within the group for their friendship and assistance in the time when it is needed.

I owe much to Dr Manuel Castro, whom through our correspondence electronically, and the brief meeting in person during a conference in the beautiful city of Santiago de Compostela, has obliged me with his full attention, and has willingly spent much time with me on the problems I raised.

The visible world is governed by the forces in the invisible realms. I strongly believe in the power of prayer and would like to thank my brothers and sisters in Cornerstone Church, Headington, for their love, fellowship and prayer on my behalf. I am most thankful to Pastor Philip Herklots for building and supporting me spiritually, providing me with a training ground in preparation for God's work in my life.

To my parents, there is no word to express my thankfulness to what they have done and invested in my life. Thanks to them, and my in-laws, for releasing me, my wife and my children to a faraway land to pursue my dream and aspiration. Not to forget my brother and sister, and their respective families, as well as my sisters-in-law and their respective families, to whom myself and my wife cast our cares especially that towards our parents. Special thanks to my colleague in Malaysia, Siong-Wee Lee for helping me out on she-knows-what in my absence.

Last but not least, my appreciation goes to the leadership and the administrators of Universiti Teknologi MARA, and the Ministry of Higher Education, Malaysia, for the funding and support without which this work will not be possible. Our country needs a better tomorrow; our people deserves a better future.

Abstract

This thesis examines chaotic mixing in wavy-type channels and two-layer shallow water flow.

For wavy-type channels, the equations of motion for vortices and fluid particles are derived assuming two-dimensional irrotational, incompressible flow. Instantaneous positions of the vortices and particles are determined using Lagrangian tracking, and are conformally mapped to the physical domain. Unsteady vortex motion is analysed, and vortex-induced chaotic mixing in the channels studied. The dynamics of mixing associated with the evolution of the separation bubble, and the invariant manifolds are examined. Mixing efficiencies of the different channel configurations are compared statistically. Fractal enhancement of productivity is identified in the study of auto-catalytic reaction in the wavy channel.

For the two-layer shallow water model, an entropy-correction free Roe-type two-layer shallow water solver is developed for a hyperbolic system with non-conservative products and source terms. The scheme is well-balanced and satisfies the C-property such that smooth steady solutions are second order accurate. Numerical treatment of the wet-dry front of both layers and the loss of hyperbolicity are incorporated. The solver is tested rigorously on a number of 1D and 2D benchmark test cases. For 2D implementation, a dynamically adaptive quadtree grid generation system is adopted, giving results which are in excellent agreement with those on regular grids at a much lower cost. It is also shown that algebraic

balancing cannot be applied directly to a two-layer shallow water flow due to the lack of simultaneous referencing for the still water position for both layers. The adaptive two-layer shallow water solver is applied successfully to flow in an idealised tidal channel and to tidal-driven flow in Tampa Bay, Florida. Finally, chaotic advection and particle mixing is studied for wind-induced recirculation in two-layer shallow water basins, as well as Tampa Bay, Florida.

Contents

List of Figures

Chapter 1

Introduction

1.1 Background

Mixing, whether occurring naturally or intentionally driven, is an important process which can span a huge range of spatial and time scales. It not only results in dispersion and advection of fluid particles leading to reduction of non-uniformities or gradients in composition, properties or temperature of the material in bulk, but is also an agency for the movement and transfer of materials to or from surfaces of particles or phases. This includes heat and mass transfer, leaching, gas absorption, solid suspension, etc. From explaining various natural processes such as atmospheric, oceanic and geophysical flows, to the design of fluid control devices, the importance of mixing in engineering science cannot be overemphasised.

The phenomenon of Lagrangian chaos has been a subject of great interest following the landmark demonstration by Aref (1984) of chaotic particle motion beyond that of the underlying fluid dynamics. Using what is now known as the blinking vortex model, Aref reported complex particle motion induced by the simple time-periodic agitation of a pair of point vortices in an idealised two-dimensional closed fluid system. The enhancement of mixing in relatively simple Eulerian unsteady flows has since been extensively documented. Chaotic motion, or chaos in general, is characterised by sensitivity to initial conditions, aperiodic motion with rapid divergence, and unpredictability despite being deterministic.

The study of chaos has in itself developed into a major subject in modern science. A system which demonstrates chaotic behaviour is better described as a dynamical system. Ottino (1989) and Tél & Gruiz (2006) give detailed accounts of mixing and chaos, and describe the many analytical tools developed in the field of nonlinear dynamics which advanced rapidly in the 1980s.

1.2 Chaotic mixing in environmental fluids

Aref (2002) in a review of the development of chaotic advection and its application in fluid mechanics, highlighted, amongst others, the shallow water regime. Shallow water bodies such as wide rivers, lakes, coastal lagoons and estuaries have been extensively researched owing to their importance regarding the sustainability of aquatic eco-systems. The shallow water domain is characterised by highly localised flow features depending on the local bathymetry and shoreline, and the complexity is compounded by tidal processes, wave-current interactions, turbulence, salinity gradients, etc. These physical processes provide the backdrop where active and passive particles are advected and dispersed whilst the corresponding chemical and biological processes occur. Figure 1.1 shows an example of a vast algal bloom in the sea. This has a filamental structure which may be attributed to chaotic mixing. Owing to the similar dynamics, dispersion of contaminants may typically follow a comparable pattern, though not necessarily observable by the naked eye. This phenomenon suggests that pollutants in water bodies subjected to chaotic mixing are not evenly distributed but demonstrate localised high and low concentrations which may vary considerably from those predicted by a simplified averaging model. Furthermore, the inherent filamental strucure provides a much larger surface of contact for active components to react with the background fluid. In this case, the potential and actual qualitative and quantitative evolutionary behaviour can be very different from the assumption that the tracers exist as a single patch of uniform concentration with simple boundary or

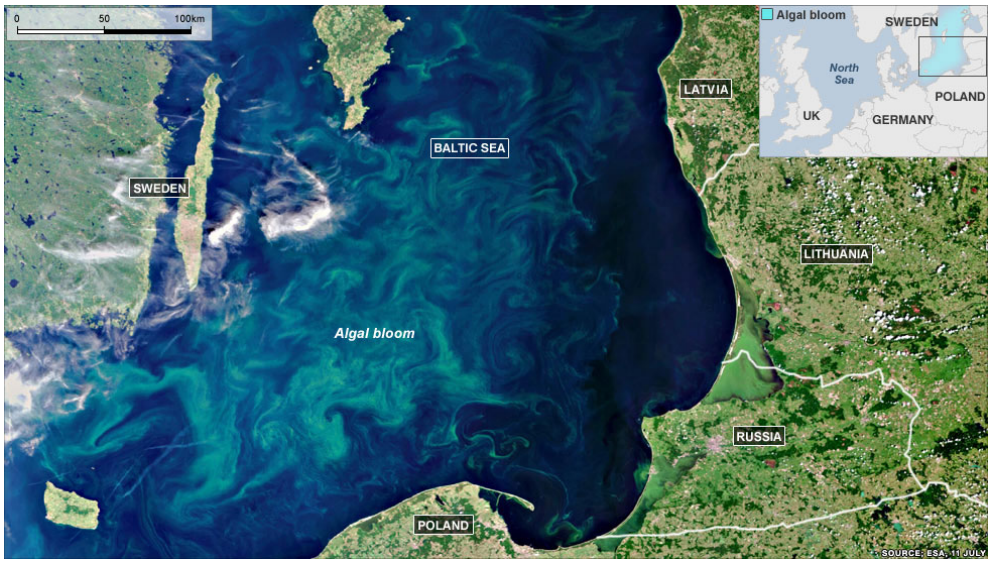

Figure 1.1: Satellite imagery of vast algal bloom in the Baltic Sea which exhibits filamental structure due to chaotic mixing (Image taken from BBC website, 26 Jul 2010: `http://www.bbc.co.uk/news/science-environment-10740097`).

propagating front. Hence, a good understanding of the dynamics of chaotic mixing is essential in order that the dispersion of contaminants and their ultimate fate can be better simulated to assess their impact on fragile aquatic and marine environments.

The simple point vortex model as proposed by Aref (1984) has been a popular tool in the study of chaotic mixing. Rom-Kedar *et al.* (1990) considered mixing and transport in a wavy channel governed by flow due to an oscillating vortex-pair. The model was later used by Waseda & Mitsudera (2002) to model the shallow coastal water of the Enshu-Nada Sea, Japan, and showed that chaotic advection could serve as an efficient transport mechanism for fish eggs and larvae spawning along the coast. Budyansky *et al.* (2004) studied a simple two-dimensional open flow composed of a fixed point vortex and a background periodic current, and showed that the tracer dynamics is typically chaotic in the mixing region. Budyansky *et al.* also found that the boundary of the vortex core acts as a dynamical trap for advected particles resulting in a fractal-like scattering function which depends on the trapping time. The model was later extended to a simple kinematic ocean model for the numerical

study of transport and chaotic mixing of Lagrangian coherent structures (Budyansky *et al.*, 2007*a*,*b*), and the simulations agreed well with published laboratory results.

Lagrangian structures in the open ocean are typically analysed using velocity data obtained or derived from various sources, including satellite-tracked buoys (e.g. Osborne *et al.*, 1986), surface drifters (e.g. Lacorata *et al.*, 2001), sequential satellite images of sea-surface temperature (e.g. Abraham & Bowen, 2002), very high frequency radar technology (e.g. Lekien *et al.*, 2005; Coulliette *et al.*, 2007), etc. Numerical simulations of Lagrangian chaos in coastal and estuarine waters are equally abundant. Amongst others, Ridderinkhof & Loder (1994) resolved the topographic variations responsible for spatial structures in the tidal and residual currents using a finite-element model that uses a harmonic method to solve the three-dimensional shallow water equations; Orre *et al.* (2006) considered surface mixing induced by one or more of the dominant tidal components in a well-mixed fjord, but ignored wind forcing and nonlinear effects; Novikov & Bagtzoglou (2006) studied the chaotic nature of the tidally-dominated Lower Hudson River estuarine system.

The results of modelling chaotic motion have proved useful to determine the optimum pollutant discharge point and time (Lekien *et al.*, 2005; Novikov & Bagtzoglou, 2006; Coulliette *et al.*, 2007), and to recommend appropriate coastal modifications to enhance mixing (Bagtzoglou & Novikov, 2007). Owing to escalating environmental concerns, the study of environmental fluid mechanics as a dynamical system is likely to play an increasingly important role.

1.3 Stratification

Density stratification is a ubiquitous phenomenon in open water bodies. The ocean, for example, has a distinct vertical structure with an upper layer of water heated by solar radiation on top of denser and colder deep water. Similar structures, known as epilimnion (the top layer), hypolimnion (the bottom layer) and metalimnion (the

thermocline in the middle) are also commonly found in stratified lakes. In estuaries, stratification typically occurs due to the presence of denser sea water and fresh water input from the river. Traditionally, estuarine flows may be classified on the basis of stratification, i.e. well-mixed, partially-stratified, and salt wedge. Unlike lakes and oceans, stratification in estuaries is dominated by the effect of salinity difference rather than temperature difference, and is highly dynamic under the combined action of cyclic tidal current flow and variable river runoff.

Studies of chaos in barotropic flows (e.g. Kozlov & Koshel, 1999, 2001; Kozlov *et al.*, 2005; Koshel & Prants, 2006) and baroclinic flows (e.g. Klein, 1990; Mundt & Hart, 1994; Mundt *et al.*, 1995; Read *et al.*, 1998; von Hardenberg *et al.*, 2000; Koshel & Prants, 2006) have been reported. For baroclinic flows, the primary focus has been on mixing in the vertical plane. The effect of density stratification on horizontal mixing in an estuary dominated by tidal forcing has not been much explored to date. Stirling (2000, 2003) studied the effect of chaotic advection and transport on the patchiness of pollutant clouds in partially stratified estuaries. Stirling used a stream function approach to model the flow in the vertical section, taking into consideration secondary circulation. The Poincaré map for the fundamental velocity field which dominates the large scale global dynamics of the estuarine flow revealed barriers (KAM tori) and partial barriers (cantori) in the vertical cross section of the estuary. Stirling showed that an optimal discharge region and time, or velocity, could be determined based on the lower bound of the vertical fluxes and the exit time of the pollutant clouds. The model represents the traverse circulations caused by the density difference between the fresh river water and the salty sea water using a ratio of the buoyancy-driven to the bend-driven circulation in the vertical cross section of the curved estuary. However, it does not account for strong vertical stratification or the formation of a salt-wedge. River inflow is represented using a ratio of its strength to that of the tide, applied to the longitudinal velocity component, which is further

decoupled from the lateral and vertical velocity such that each vertical cross section is essentially a replica of the others.

The above literature on chaotic mixing is by no means exhaustive. However, there is a lack of research related to chaotic mixing in stratified estuarine waters. Hence it is of great interest to investigate chaotic advection in a stratified shallow water domain representative of what would commonly be encountered in lakes and coastal waters.

1.4 Aims and objectives

The present research aims to examine the dynamics of chaotic mixing in a stratified shallow water regime. The objectives are as follows:

1. To investigate chaotic mixing in wavy channels and hence become familiar with the analytical tools of chaotic mixing;

2. To derive and solve numerically the governing equations for a two-layer shallow water flow;

3. To verify the two-layer shallow water solver in 1D and 2D using appropriate test cases;

4. To develop a two-layer shallow water solver based on an adaptive quadtree grid, and examine the efficiency of the scheme;

5. To simulate and analyse chaotic behaviour in a wind-induced stratified basin;

6. To simulate and analyse chaotic behaviour in a tidal-forced estuary.

1.5 Synopsis

Chapter 2 considers chaotic mixing in wavy channels. A literature review is first presented, followed by the derivation of the conformally mapped governing equations for inviscid, incompressible flow in 2D wavy channels. Simulation results are analysed using tools typically used for the study of dynamical systems. In Chapter 3, the system of equations governing a two-layer shallow water flow is derived. The numerical scheme is presented, including a discussion on an unsuccessful attempt to adopt algebraic balancing between the flux gradient and source terms. The quadtree grid generation system is briefly introduced. Chapter 4 presents results obtained for a number of 1D and 2D benchmark test cases. The efficiency of the adaptive grid system is also assessed and discussed. The model is shown to work successfully for an idealised tidal channel, as well as a real tidal-driven estuary. Chapter 5 describes the analysis of chaotic mixing in shallow water bodies including wind-induced circulation, and tidal-driven flow. Finally, conclusions and recommendations for future work are listed in Chapter 6.

1.6 Publications

The material presented in Chapter 2 has been published in *Journal of Fluid Mechanics* under the title of 'Vortex-induced chaotic mixing in wavy channels' (Lee *et al.*, 2010*b*); the work in Chapter 3 and part of the results in Chapter 4 has been published in *Journal of Computational Physics* under the title of 'A fast adaptive quadtree scheme for a two-layer shallow water model' (Lee *et al.*, 2011). Further publications are in progress based partly on the completed work presented in Chapter 5.

Chapter 2

Chaotic mixing in wavy channels

2.1 Introduction and literature review

The transport and mixing problem in a wavy channel can be characterised by a relatively simple flow field but intrinsically complex chaotic particle motions due to vortical stirring. Hence, unless the flow is fully turbulent, a point vortex model involving few degrees of freedom could be a particularly attractive way to give a simple and concise description of the flow field which is dominated by vortex-induced circulation.

Rom-Kedar *et al.* (1990) examined transport and mixing in a two-dimensional, inviscid, incompressible flow governed by an oscillating vortex-pair. They studied the global topology of chaotic particle motions for small perturbations of an external strain-rate field that caused the vortex-pair to oscillate about its equilibrium position. For the perturbed flow, the invariant stable and unstable manifolds, defined as the sets of all phase space points from which particles can reach the hyperbolic fixed point in forward and reversed time, respectively (Tél & Gruiz, 2006), are shown to intersect each other transversely, resulting in tangled flow structures which are responsible for fluid transport in the mixing region. The dynamics of the unsteady vortical flow reported by Rom-Kedar *et al.* (1990) approximates the study of flows in furrowed channels with wavy wall profiles and time-periodic volumetric flow rates considered by Sobey (1980). The flow field in the vicinity of the oscillating vortex-pair

corresponds to the instant when the vortex formed from flow separation is ejected into the main stream, with recirculating flow between the vortex and the wall. It is thus limited to the case when the oscillating vortex-pair is sufficiently distant from the wall. In this thesis, the effects when the vortices move in relatively large orbits such that they interact with the wall via image vortices is examined.

Flow over wavy boundaries is a generic problem in fluid mechanics. It is important in the generation and growth of waves on the open ocean, where the rapid growth of short steep waves is largely due to flow separation at their sharp crests (see e.g. Csanady, 2001). It is also of direct relevance in the modelling of 'singing pipes', where high speed gas or liquid flow in corrugated pipes can excite acoustic organ-pipe modes (e.g. Crawford, 1974; Silverman & Cushman, 1989; Cadwell, 1994; and the discussions by Walker, 2007, section 3.39). In each of these problems, a simple point vortex potential flow model could be useful for exploring some of the important physical processes.

Numerical simulation (Sobey, 1980) and experimental observations (Stephanoff *et al.*, 1980) of flows in furrowed channels have revealed that flow separation occurs in the hollows at Reynolds numbers above a threshold value. For unsteady flow, deceleration of fluid in the diverging part of the channel leads to the cyclic formation, growth, ejection and decay of vortices which enhance convective mixing. This behaviour has allowed the design of devices capable of efficient mixing and mass transfer in an open system in the absence of turbulence, such as membrane oxygenators. Sobey (1982) made similar observations for flows in wavy channels with asymmetric geometry. Sobey (1985) further studied the occurrence of Lagrangian convective dispersion caused by unsteady separation during oscillatory flow through a furrowed channel in the absence of Brownian diffusion, and demonstrated that the variance of fluid particles grows approximately linearly with time.

Using a similar numerical scheme to that of Sobey (1980), Ralph (1986) presented

results for viscous oscillatory flow in wavy-walled tubes with the aid of flow visualisation. At large Strouhal number, the flow structure is similar to that obtained by Sobey (1980) at low Reynolds number but high enough that separation occurs. Development of time-asymmetric flows in a limited region of the parameter space may be regarded as a bifurcation of the flow structure and is suggestive of transition to turbulence, analogous to a forced nonlinear oscillator from the viewpoint of a dynamical system (Roberts & Mackley, 1996). In a study of self-sustaining oscillatory flows in a converging-diverging channel, Guzmán & Amon (1994) postulated that the transition from laminar to chaotic flow occurs via a series of Hopf bifurcations as the Reynolds number is increased, consistent with the Ruelle–Takens–Newhouse scenario of the onset of chaos. Chaotic particle trajectories have been verified and analysed using measures such as fractal dimensions and Lyapunov exponents (Guzmán & Amon, 1996; Amon *et al.*, 1996).

2.2 Problem formulation

In this study, mixing is considered of an inviscid flow in furrowed open flow devices characterised by a wavy wall profile previously described by Taylor (1981). The flow field comprises a uniform mean flow and self-sustaining point vortices in the furrows. Strong mixing cases are considered where the circulations induced by the point vortices dominate over other processes such as boundary effects at the wall. Our primary interest is to investigate the particle advection. Using a simple approximation, both the vortices and the particles are assumed to take on the velocity of the resulting flow field and are tracked using a Lagrangian technique. Since the study involves only kinematical considerations, the model is independent of Reynolds number but should apply to a real laminar flow subjected to external stirring actions such as in blinking vortex experiments (Aref, 1984). Analysis of particle motion in such flows from a Lagrangian point of view is very similar to that of flow visualisation techniques. The

focus is on on mixing induced by unsteady vortex motion. It is shown that the present point vortex model reproduces some of the salient features of mixing in a wavy channel similar to that obtained from numerical solution of the Navier–Stokes equations (Sobey, 1980). In addition, several observations unique to the present model are presented and discussed.

The chapter is organised as follows: Section 2.3 presents the derivation of the equations of motion for the vortex and passive particles in three different configurations, namely: the wavy wall problem, the symmetrical channel and the skew-symmetrical channel. Section 2.4 describes briefly the numerical solver. Section 2.4.1 examines the vortex motion, analytically and numerically. It is shown that the vortices move in regular trajectories with negligible influence from neighbouring vortices. Section 2.4.2 looks at the presence of Lagrangian chaos in all three configurations under the stirring action of the vortices. Section 2.4.3 shows that chaotic mixing is primarily induced by the unsteady dynamics of the separation bubbles which move and evolve in size as the vortices evolve. An effective vortex core, free flow region and mixing region in the flow field are identified. In this study, the dynamics are shown to be related to an oscillatory unidirectional flow of a real fluid described by Sobey (1980). Structures are presented for the stable and unstable manifolds and their role in the mixing process discussed. Section 2.4.4 investigates the efficiencies of passive mixing in the three configurations. The effect of Brownian diffusion is found to increase lateral particle dispersion at the expense of longitudinal particle dispersion. Section 2.4.5 considers auto-catalytic reaction in the wavy channel and the fractal form of the unstable manifold. Conclusions are listed in Section 2.5.

2.3 Governing equations

Two-dimensional irrotational, incompressible fluid flow is considered. The stream function automatically satisfies the continuity equation, and the velocity potential exists everywhere in the fluid except at singularities.

2.3.1 Flow over a wavy wall

Consider a uniform flow field of velocity U in the x-direction over a flat wall located at $y = 0$. A point vortex which is rotating clockwise in the flow field has strength of $-\kappa$, and the actual circulation is $-2\pi\kappa$. Using the method of images (Milne-Thomson, 1968), the complex potential function is given by

$$w(z) = Uz + \mathrm{i}\kappa \log((z - \overline{z}_v)/(z - z_v)), \tag{2.1}$$

where z_v is the vortex position, and the overbar indicates the complex conjugate. The flow regime is bounded by the wall ($y \geq 0$) and the complex velocity is

$$\frac{\mathrm{d}w}{\mathrm{d}z} = U + \mathrm{i}\kappa \left[\frac{1}{z - \overline{z}_v} - \frac{1}{z - z_v} \right]. \tag{2.2}$$

A conformal transformation that maps the flat wall in the z-plane onto a wavy wall in the ζ-plane is given as

$$\zeta = f(z) = z + \mathrm{i}\epsilon \exp(\mathrm{i}Kz), \tag{2.3}$$

where the constants ϵ and K are the amplitude and the wavenumber of the wall, respectively (Taylor, 1981). To satisfy the smooth wall condition and ensure the existence of a conformal transformation for the fluid region, the constants are restricted such that $\epsilon K \leq 1$. The complex velocity at any point in the ζ-plane can be calculated using the chain rule,

$$\frac{\mathrm{d}W}{\mathrm{d}\zeta} = \frac{\mathrm{d}w}{\mathrm{d}z}\frac{\mathrm{d}z}{\mathrm{d}\zeta} = \frac{\mathrm{d}w}{\mathrm{d}z}\frac{1}{f'(z)} = u_\xi - \mathrm{i}v_\eta. \tag{2.4}$$

Equation (2.4) shows that the complex velocities are not mapped one to one, but are proportional depending on the mapping functions. Although the transformation function $\zeta = f(z)$ can be chosen to be a simple analytic function, solution of the inverse transformation $z = f^{-1}(\zeta)$ will require numerical iteration. To avoid this, the vortex position in the ζ-plane is expressed in the form of $\zeta(z) = \xi(x, y) + \mathrm{i}\eta(x, y)$. Taking the time derivative, followed by the complex conjugate, the motion of passive particles when tracked in the z-plane can thus be written as

$$\frac{\mathrm{d}\overline{z}}{\mathrm{d}t} = \frac{1}{|f'(z)|^2}\frac{\mathrm{d}w}{\mathrm{d}z}. \tag{2.5}$$

A direct transformation using (2.3) will then give the particle trajectories in the physical domain in the ζ-plane but followed in the z-plane.

For vortex tracking, Routh (1881) introduced a correction term to account for the fact that the transformation of the vortex path in one plane is not the path in the new plane. Thus, the vortex motion in terms of its position in the z-plane is

$$\frac{\mathrm{d}\overline{z}_v}{\mathrm{d}t} = \frac{1}{|f'(z_v)|^2}\left\{U + \mathrm{i}\kappa\left[\frac{1}{z_v - \overline{z}_v} + \frac{f''(z_v)}{2f'(z_v)}\right]\right\}. \tag{2.6}$$

Equation (2.2) can be extended to represent a row of $2N + 1$ vortices which are in-phase and of equal strength, with one vortex spaced every wavelength λ $(= 2\pi/K)$ along the wall, within the uniform flow field of velocity U (Figure 2.1), giving

$$w(z) = Uz + \mathrm{i}\kappa\sum_{n=-N}^{N}\log\left[\frac{(z - \overline{z}_v) + n\lambda}{(z - z_v) + n\lambda}\right], \tag{2.7}$$

where the coordinates of the vortex array in the z-plane are $(x_v \pm n\lambda, y_v)$, $n = 0, 1, \ldots, N$. The equations of motion for the passive particles and the vortex $(z = z_v)$ are thus

$$\frac{\mathrm{d}\overline{z}}{\mathrm{d}t} = \frac{1}{|f'(z)|^2}\left\{U + \mathrm{i}\kappa\sum_{n=-N}^{N}\left[\frac{1}{z - \overline{z}_v + n\lambda} - \frac{1}{z - z_v + n\lambda}\right]\right\}, \tag{2.8}$$

and

$$\frac{\mathrm{d}\overline{z}_v}{\mathrm{d}t} = \frac{1}{|f'(z_v)|^2}\left\{U + \mathrm{i}\kappa\left[\sum_{n=-N}^{N}\left(\frac{1}{z - \overline{z}_v + n\lambda}\right) + \frac{f''(z_v)}{2f'(z_v)}\right]\right\}, \tag{2.9}$$

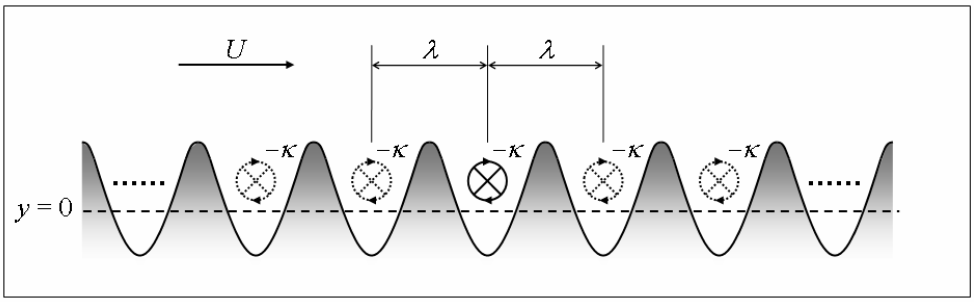

Figure 2.1: Wavy wall problem with an array of vortices.

respectively.

Considering a system with an infinite number of vortices such that $N = \infty$, the summation term in (2.8) and (2.9) can be written as

$$\sum_{-\infty}^{\infty} \frac{1}{z - \overline{z}_v + n\lambda} = \sum_{-\infty}^{\infty} \frac{z - \overline{z}_v}{(z - \overline{z}_v)^2 + n^2(\mathrm{i}\lambda)^2}.$$

Following Lamb (1953), we have

$$\frac{k}{2\pi} \sum_{-\infty}^{\infty} \frac{b}{b^2 + n^2 a^2} = \frac{k}{2a} \coth \frac{\pi b}{a}.$$

Equations (2.8) and (2.9) thus become

$$\frac{\mathrm{d}\overline{z}}{\mathrm{d}t} = \frac{1}{|f'(z)|^2} \left\{ U + \mathrm{i}\kappa \left[\frac{K}{2\mathrm{i}} \coth \frac{K(z - \overline{z}_v)}{2\mathrm{i}} - \frac{K}{2\mathrm{i}} \coth \frac{K(z - z_v)}{2\mathrm{i}} \right] \right\}, \tag{2.10}$$

and

$$\frac{\mathrm{d}\overline{z}_v}{\mathrm{d}t} = \frac{1}{|f'(z_v)|^2} \left\{ U + \mathrm{i}\kappa \left[\frac{K}{2\mathrm{i}} \coth y_v K + \frac{f''(z_v)}{2f'(z_v)} \right] \right\}, \tag{2.11}$$

respectively.

2.3.2 Flow in a symmetrical wavy channel

A channel of uniform width 2π where the walls are located at $y = \pm\mathrm{i}\pi$ in the z-plane is considered. The flow field comprises a uniform velocity of U and a pair of point vortices, one of strength κ located at $z = z_v$, and the other of strength $-\kappa$ located at $z = \overline{z}_v$. Using the method of images as before, the above problem becomes one of an

infinite number of vortex pairs in the y-direction. At an arbitrary point of interest z, the complex velocity can be expressed as

$$\frac{\mathrm{d}w}{\mathrm{d}z} = U + \mathrm{i}\kappa \sum_{n=-\infty}^{\infty} \left[\frac{1}{z - z_v + \mathrm{i}2n\pi} - \frac{1}{z - \overline{z}_v + \mathrm{i}2n\pi} \right]. \tag{2.12}$$

Rewriting the summation term as in the preceding section followed by integration, the complex potential function of the flow system is thus

$$w(z) = Uz + \mathrm{i}\kappa \log \frac{\sin \mathrm{i}(z - \overline{z}_v)/2}{\sin \mathrm{i}(z - z_v)/2} \tag{2.13}$$

as obtained previously by Cannell & Williams (1973).

The uniform width channel in the z-plane above is conformally mapped to a symmetrical wavy channel in the ζ-plane using the mapping function

$$\zeta = f(z) = z + \mathrm{i}\epsilon[\exp(\mathrm{i}Kz) - \exp(-\mathrm{i}Kz)], \tag{2.14}$$

where K again is the wavenumber. However, ϵ is no longer the amplitude of the wave on the wall but is simply proportional to it (Taylor, 1981).

Consider $2N + 1$ pairs of in-phase vortices of equal but opposite strength in the symmetrical wavy channel, with one vortex per wavelength of the wall, within the uniform flow field of velocity U (Figure 2.2), where the coordinates of the vortex array in the z-plane are $(x_v \pm n\lambda, \pm y_v)$, $n = 0, 1, \ldots, N$. Following the derivation presented in Section 2.3.1, the motion of the passive particles tracked in the z-plane is thus

$$\frac{\mathrm{d}\overline{z}}{\mathrm{d}t} = \frac{1}{|f'(z)|^2} \left\{ U + \frac{\kappa}{2} \sum_{n=-N}^{N} \left[\cot \frac{\mathrm{i}}{2}(z - z_v + n\lambda) - \cot \frac{\mathrm{i}}{2}(z - \overline{z}_v + n\lambda) \right] \right\}. \tag{2.15}$$

For vortex tracking, the correction term due to Routh (1881) is introduced as before, giving

$$\frac{\mathrm{d}\overline{z}_v}{\mathrm{d}t} = \frac{1}{|f'(z_v)|^2} \left\{ U + \mathrm{i}\kappa \sum_{n=-N}^{N} \left[-\frac{1}{2\mathrm{i}} \cot \frac{\mathrm{i}}{2}(z_v - \overline{z}_v + n\lambda) \right] + \frac{f''(z_v)}{2f'(z_v)} \right\}. \tag{2.16}$$

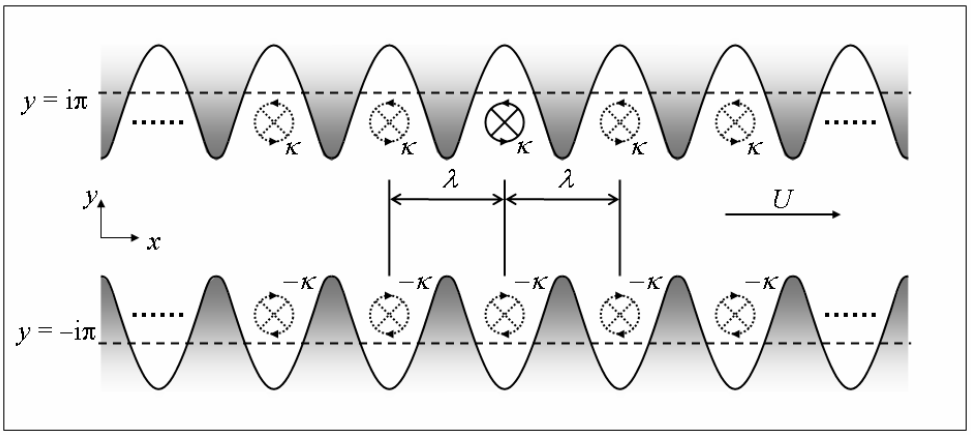

Figure 2.2: Symmetrical wavy channel with an array of vortices.

2.3.3 Flow in a skew-symmetrical wavy channel

Consider a channel of uniform width 2π where the walls are located at $y = 0$ and $y = \mathrm{i}2\pi$, respectively in the z-plane. The flow field comprises a uniform velocity U, a pair of point vortices, one with strength κ located at $z = z_v$ and another with strength -κ located at $z = c_v = (\overline{z}_v + \lambda/2) + \mathrm{i}2\pi$. Using the method of images (Figure 2.3), the infinite number of vortices in the y-direction is first considered. The complex velocity at a point of interest z can be written as

$$\frac{\mathrm{d}w}{\mathrm{d}z} = U + \mathrm{i}\kappa \sum_{n=-\infty}^{\infty} \left[\frac{1}{z - z_v + \mathrm{i}4n\pi} - \frac{1}{z - \overline{z}_v + \mathrm{i}4n\pi} + \frac{1}{z - \overline{c}_v + \mathrm{i}4n\pi} - \frac{1}{z - c_v + \mathrm{i}4n\pi} \right], \tag{2.17}$$

where the infinite summation term can be treated as in Section 2.3.1.

Next, $2N + 1$ ($-N$ to N) vortices along the upper wall is considered. This corresponds to $2N$ ($-N$ to $N - 1$) vortices along the lower wall such that symmetry is maintained in the longitudinal direction (Figure 2.4). Incorporating this into (2.17), we get

$$\frac{\mathrm{d}w}{\mathrm{d}z} = U + \mathrm{i}\kappa \sum_{n=-N}^{N} M, \tag{2.18}$$

where

$$M = \frac{1}{4\mathrm{i}} \left[\cot \frac{\mathrm{i}(z - Z_v)}{4} - \cot \frac{\mathrm{i}(z - \overline{Z}_v)}{4} + \cot \frac{\mathrm{i}(z - \overline{C}_v)}{4} - \cot \frac{\mathrm{i}(z - C_v)}{4} \right],$$

and $Z_v = z_v + n\lambda$, $C_v = [\overline{z}_v + \lambda(2n+1)/2] + \mathrm{i}2\pi$.

The motion of passive particles and vortices tracked in the z-plane can be described by

$$\frac{\mathrm{d}\overline{z}}{\mathrm{d}t} = \frac{1}{|f'(z)|^2}\left\{U + \mathrm{i}\kappa \sum_{n=-N}^{N} M\right\}, \tag{2.19}$$

and

$$\frac{\mathrm{d}\overline{z}_v}{\mathrm{d}t} = \frac{1}{|f'(z_v)|^2}\left\{U + \mathrm{i}\kappa\left[\sum_{n=-N}^{N}\left(-\frac{\cot \mathrm{i}(z_v - \overline{Z}_v)/4}{4\mathrm{i}} - \frac{\cot \mathrm{i}(z_v - C_v)/4}{4\mathrm{i}}\right) + \frac{f''(z_v)}{2f'(z_v)}\right]\right\}, \tag{2.20}$$

respectively, where the mapping function used to transform the uniform channel into a skew-symmetrical wavy channel is

$$\zeta = f(z) = z + \mathrm{i}\epsilon[\exp(\mathrm{i}K(z - \mathrm{i}\pi)) + \exp(-\mathrm{i}K(z - \mathrm{i}\pi))]. \tag{2.21}$$

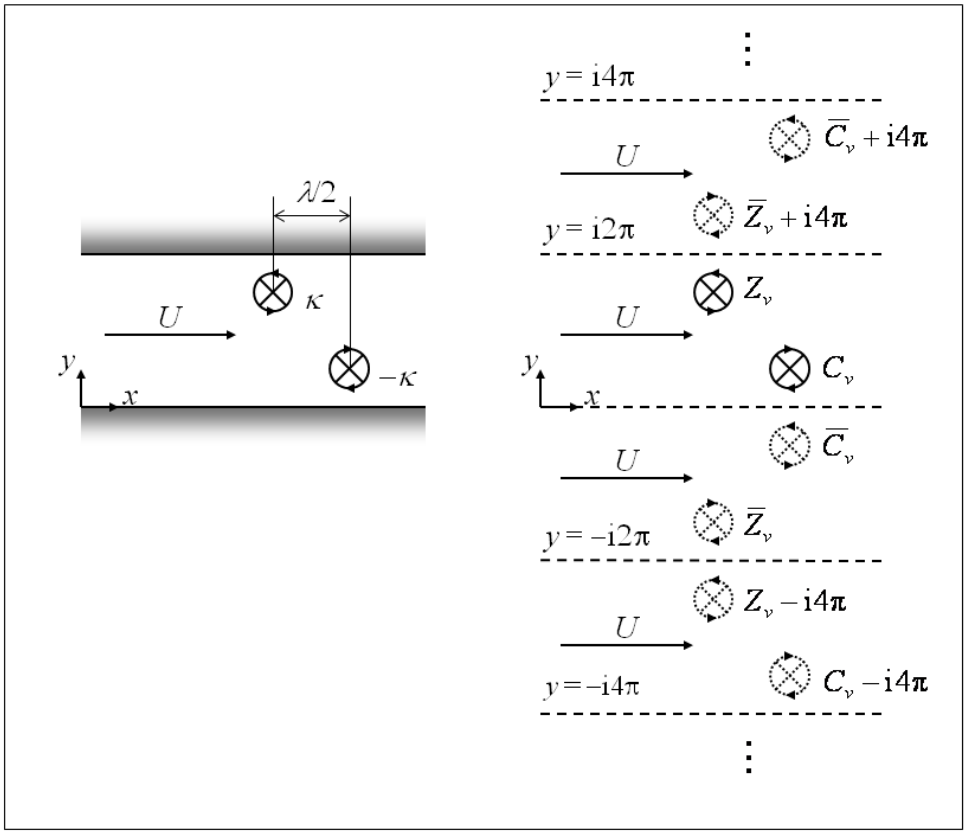

Figure 2.3: Method of images for skew-symmetrical wavy channel.

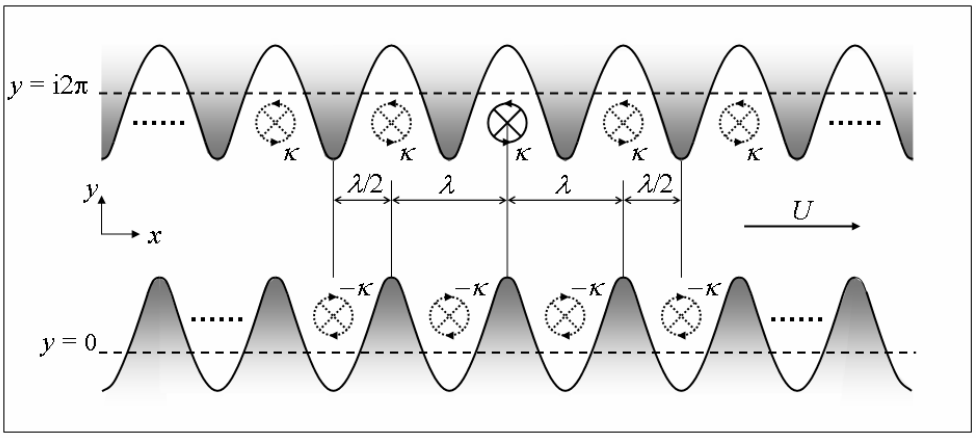

Figure 2.4: Skew-symmetrical wavy channel with an array of vortices.

2.4 Numerical results and discussions

The wall wavelength λ is chosen as the characteristic length L_0 to non-dimensionalise the length scales, giving $\tilde{x} = x/L_0$, $\tilde{y} = y/L_0$, $\tilde{\xi} = \xi/L_0$, and $\tilde{\eta} = \eta/L_0$. Letting the mean incoming velocity U_0 be the characteristic velocity, the dimensionless velocity, vortex strength, and time are thus given by $\tilde{U} = U/U_0$, $\tilde{\kappa} = \kappa/U_0L_0$, and $\tilde{t} = U_0t/L_0$, respectively. Two dimensionless parameters are defined herein, namely the dimensionless amplitude of vortex motion Λ $(= \Delta\xi/\lambda)$, and the Strouhal number Ω $(= \lambda/UT)$, where T is the period of the resonance. The classical fourth-order Runge–Kutta scheme (RK4) is adopted to solve the equations of motion in the z-plane. A time step Δt of 0.01 gives stable, converged solutions and is used throughout, unless otherwise stated. All figures are plotted using the dimensionless quantities and the tildes are dropped for convenience.

2.4.1 Vortex motion in the vicinity of the wavy wall

2.4.1.1 Perturbation analysis of vortex motion

For the wavy wall problem (Section 2.3.1), the equilibrium position of the vortex is taken to be in the middle of the wall corrugation such that $\xi_e = \pi$, and $\eta_e = 0$. Solving the mapping function (2.3) then yields the corresponding position in the

computational domain given by $x_e = \pi$, and an inverse function $y_e \exp(y_e) = \epsilon$. Defining the vortex position as $z_v = x_v + \mathrm{i}y_v = (x_e + X) + \mathrm{i}(y_e + Y)$, where X and Y are small perturbations from the equilibrium position in the z-plane, the case of a single vortex ($N = 0$) as described by (2.6) can then be written as

$$\frac{\mathrm{d}\overline{z}_v}{\mathrm{d}t} = \dot{X} - \mathrm{i}\dot{Y}, \tag{2.22}$$

where the dot indicates time derivative. For a stationary vortex, the equilibrium vortex strength can thus be expressed as

$$\kappa_e = \frac{-2U(\epsilon + \exp y_e)}{-\epsilon + \exp y_e \coth y_e + \epsilon \coth y_e}. \tag{2.23}$$

Setting the wavy wall parameters $\epsilon = 0.5$ and $K = 1$ after Taylor (1981), the above formulations give $y_e \approx 0.3517$ and $\kappa_e \approx -0.7743U$. Adopting unit uniform flow ($U = 1$) throughout and $\kappa = \kappa_e$, different degrees of mixing, characterised by the amplitude of vortex motion Λ can thus be selected by defining only the initial vortex position (x_{v0}, y_{v0}). For convenience, let $x_{v0} = x_e$ (i.e. $X = 0$) such that the initial vortex position is always in the middle of the trough and the sole parameter that remains to be specified is the perturbation term Y where $y_{v0} = y_e + Y$.

The equilibrium vortex strength reduces monotonically with decreasing value of ϵ, which represents the wall waviness for $K = 1$. In an experimental study of vortices in wavy profiles, Wierschem *et al.* (2003) reported increasing critical flow thickness for vortex formation at reduced wall waviness. In their experiment, the vortex formed is essentially stationary and symmetrical due to steady gravity-driven flow. Hence, except in the limit where ϵ vanishes, our analytical equilibrium vortex strength in the middle of the furrow is analogous to weak to strong vortical motion as wall waviness increases.

Writing the linear approximation of the single vortex motion in the form of $\dot{X} = a_1 Y$, and $\dot{Y} = a_2 X$, the coefficients a_1 and a_2 are readily determined. The angular frequency of the vortex motion, $\omega = 2\pi f = \sqrt{a_1 a_2}$ is thus a function of ϵ. Figure 2.5

shows the Strouhal number ω/UK $(= \lambda/UT)$ as a function of ϵK. The Strouhal number is only weakly dependent on ϵK, reducing from a maximum of 0.27 when $\epsilon K \approx 0.3$, to slightly below 0.24 when $\epsilon K \to 1$. The reversed and stronger variation for $\epsilon K < 0.3$ is of little interest as the small wall amplitude is unlikely to produce good mixing (Ottino, 1989). In particular for $\epsilon K = 0.5$, the fundamental Strouhal number of a vortex is given by $\omega = 0.2611$.

Writing the solution of the linear approximation in the form of an undamped sinusoidal wave as a function of time t, let $X = A \sin \omega t$, and $Y = -\alpha A \cos \omega t$, where α is a scaling factor which relates the amplitude of the vortex motion in the y-direction to that in the x-direction such that $0 < |\alpha| < 1$, and A is the dimensionless amplitude of motion in the x-direction. Substituting into the linear approximation and solving yields $\alpha = -0.1562$.

Solving (2.22) to a third-order approximation, two resonant terms of the fundamental Strouhal number arise due to the nonlinearity of the frequency of response (Nayfeh, 1985). A correction term of the order of A^2 is applied to the Strouhal number and the scaling factor, respectively, giving

$$\omega = \omega_0 + c_1 A^2, \quad \alpha = \alpha_0 + c_2 A^2, \tag{2.24a, b}$$

where $\omega_0 = 0.2611$ and $\alpha_0 = -0.1562$ as previously determined. Substituting ω and

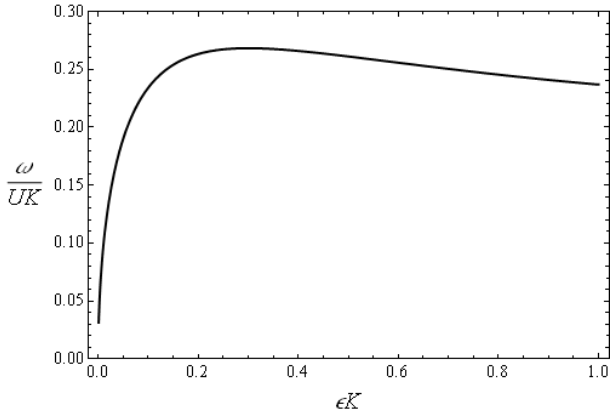

Figure 2.5: Strouhal number of vortex as a function of ϵK.

α into the modified linear approximation equations and solving, the coefficients, c_1 and c_2 are obtained as 0.0266 and -0.0095, respectively. The complete solution to third-order approximation of the vortex motion is thus given by

$$X = A\sin\omega t - 0.1107A^2\sin 2\omega t - 0.0035A^3\sin 3\omega t, \qquad (2.25a)$$

$$Y = 0.0320A^2 - \alpha A\cos\omega t - 0.0084A^2\cos 2\omega t - 0.0032A^3\cos 3\omega t. \qquad (2.25b)$$

Using the same approach, a perturbation analysis for the case where $N = \infty$ was performed and resulted in similar expressions for the Strouhal number and the scaling factor.

2.4.1.2 Vortex path in a wavy trough

Figure 2.6 shows the path taken by a single vortex when released from 5 different initial positions. If the vortex is too close to the wall, the coupling effect with its image has a dominant influence, causing the vortex to move upstream along the wall. On the other hand, if the vortex is too far away from the wall, the uniform flow effect sweeps the vortex downstream, tracing the wall topography. Generally, if both κ and U are positive, or negative, then the vortex will be swept downstream, or upstream, respectively, by the uniform flow regardless of initial position. If $U = 0$, the vortex will couple with its image to form a simple vortex pair which advances at a velocity of $\kappa/2d$ along the x-direction, where d is the distance of the vortices from the wall. Our interest lies mainly with vortices located in the vicinity of the wall trough where the opposing flow effect from their respective images and the uniform flow field causes the vortices to be trapped in hydrodynamic oscillations.

Figure 2.7 compares the analytical vortex paths ($N = 0$) derived in Section 2.4.1.1 to those obtained numerically from Lagrangian tracking. A small time step of $\Delta t = 0.001$ is adopted to simulate accurately the vortex motion. It can be seen that analytical results obtained from the perturbation analysis are in good agreement with the numerical predictions for small perturbation $|Y| \ll 0.09$ ($A \ll 0.2061$).

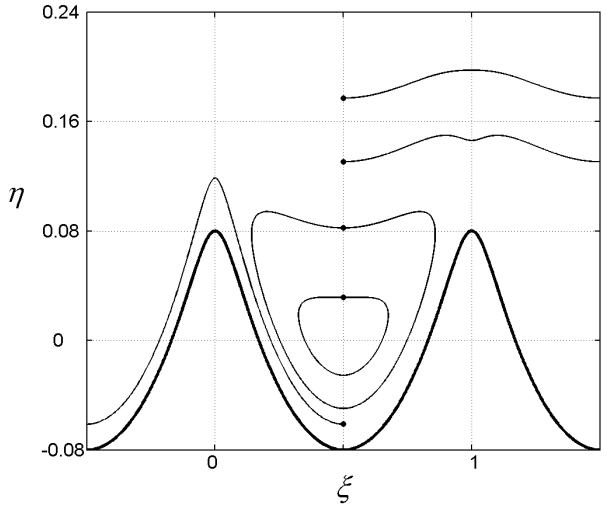

Figure 2.6: Single vortex motion along the wavy wall: •, initial position; ——, vortex trajectories.

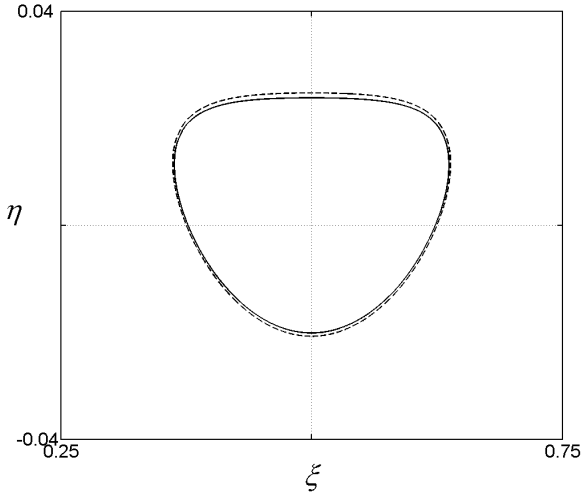

Figure 2.7: Comparison of vortex path derived from perturbation analysis (- - - - -) and numerical iteration (——): $N = 0$, $z_v = (\pi, 0.260)$, $Y = -0.09$.

2.4.1.3 Frequency-amplitude correlation

Figure 2.8 plots the Strouhal number Ω versus the dimensionless amplitude Λ for wavy wall cases with a single vortex ($N = 0$) and an infinite number of vortices ($N = \infty$). The solid curves give the frequency-amplitude correlation calculated numerically for different perturbations of initial vortex position, whereas the dashed curves plot the analytical frequency-amplitude correlation as described by $(2.24a)$ where the equiva-

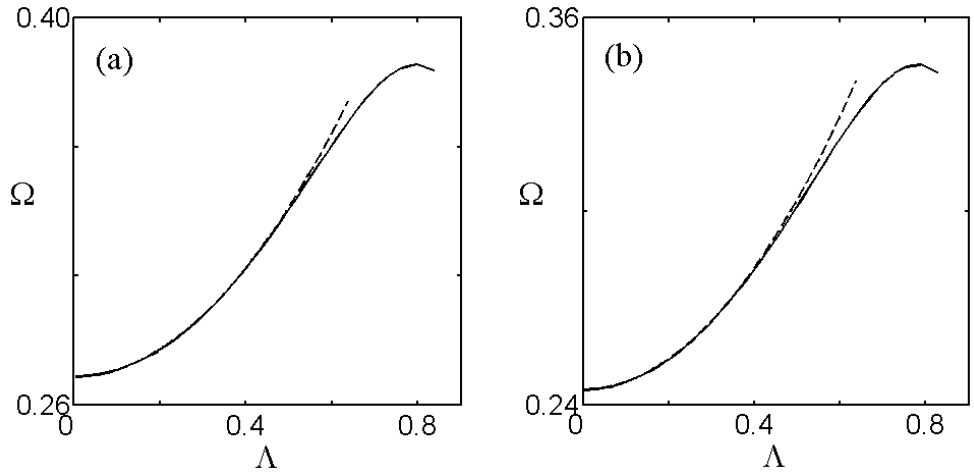

Figure 2.8: Comparison of frequency-amplitude correlation derived from perturbation analysis (- - - - -) and numerical iteration (——): (a) $N = 0$; (b) $N = \infty$.

lent dimensionless forms may be written as $\Omega = \omega/UK$ and $\Lambda = A = \Delta x/\lambda$. From the numerical solutions, we can see that Ω increases slowly with respect to Λ but shows an abrupt drop as Λ approaches the wavelength of the wall. This corresponds to lateral vortex motion beyond the wall crest level which approaches the point of escape from the influence of its image. The Strouhal number of the vortex array is slightly lower than the case of a single vortex. For linear perturbation away from the equilibrium position ($\Lambda = 0$), Ω equals 0.2611 and 0.2477 for the cases $N = 0$, and $N = \infty$, respectively, which agree well with the analytical results in Section 2.4.1.1. The third-order analytical approximation gives an excellent approximation of the frequency-amplitude correlation for perturbation up to $\Lambda \sim 0.5$ for both $N = 0$, and $N = \infty$.

2.4.1.4 Effect of neighbouring vortices

The effect of having more than one vortex along the wall on the vortex path is now examined. Neighbouring vortices, separated by the corrugations of the wall, are in-phase and thus move identically. Figure 2.9 shows, for the wavy wall problem, the paths traced by a single vortex ($N = 0$) in comparison with the path traced by the same vortex with three neighbours on both sides ($N = 3$), and when there is an

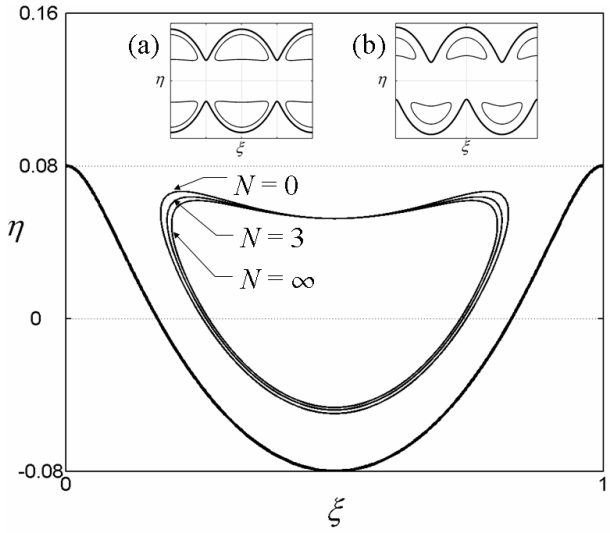

Figure 2.9: Effect of neighbouring vortices on vortex path in wavy wall problem. Inset showing similar plots for: (a) symmetrical wavy channel ($N = 0, 5, 10$); (b) skew-symmetrical wavy channel ($N = 1, 5, 10$).

infinite number of vortices along the wall ($N = \infty$). The results suggest that the vortex motion is only weakly affected by the presence of neighbouring vortices and thus increasing N has a diminishing effect on the individual vortex path. Essentially, the regular trajectories can be attributed to the lack of interactions between the isolated vortices. In the same figure, insets (a) and (b) present similar plots for the symmetrical wavy wall channel and skew-symmetrical wavy channel, respectively.

2.4.2 Lagrangian particle tracking

This section examines the trajectories of particles released into the flow field at different distances from the wall. The wall amplitude and wavenumber for the wavy wall problem is as previously set, whereas the channel parameters for both symmetrical and skew-symmetrical wavy channels are selected as $\epsilon = 0.35$ and $K = 0.45$, following Taylor (1981). For optimum mixing effect, vortex motion with maximum amplitude is desirable (Ottino, 1989). However, vortices which move beyond the crest level can only be kept from being swept away by the uniform flow by means of external stirring. Hence, the amplitude of motion is limited such that the vortex chosen has a

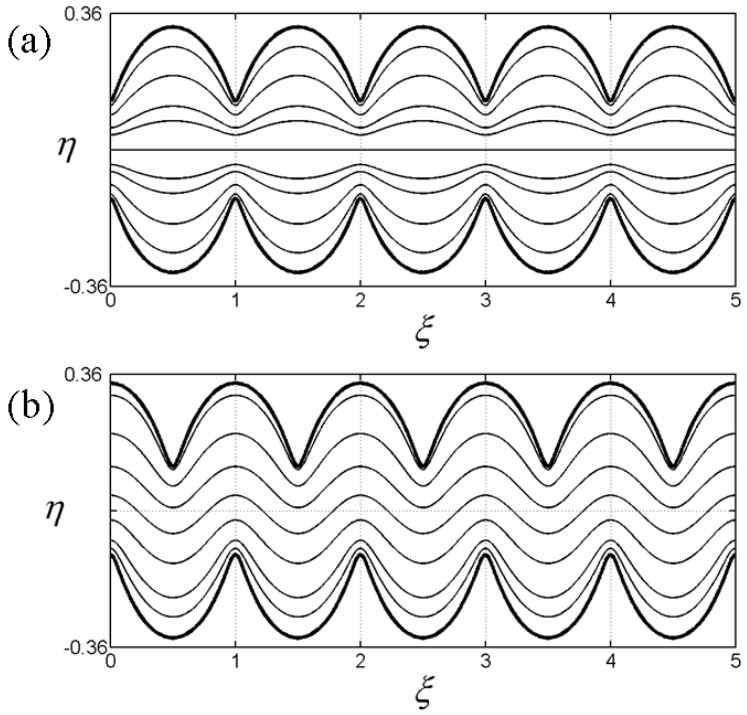

Figure 2.10: Particle trajectories under uniform flow field: (a) symmetrical wavy channel; (b) skew-symmetrical wavy channel.

trajectory which remains within the corrugations.

2.4.2.1 Lagrangian trajectories

In the absence of vortex stirring ($\kappa = 0$), particles are purely advected by the uniform flow and thus trace the streamlines which follow the shape of the wall (Figures 2.10a,b). In the symmetrical wavy channel (Figure 2.10a), the particle located at the middle of the channel follows a horizontal trajectory, separating the channel into two non-interacting zones. The presence of vortices in the flow field alters the particle trajectories significantly depending on particle initial positions. Figures 2.11a-c show diverse particle motions under the stirring action of an infinite number of vortices for all three wavy configurations, where particles which are entrained by a vortex can be easily recognised from the looping in their trajectories.

For the wavy wall problem (Figure 2.11a), all four particles are observed to pass over the third trough without being entrained. One of the particles is entrained twice

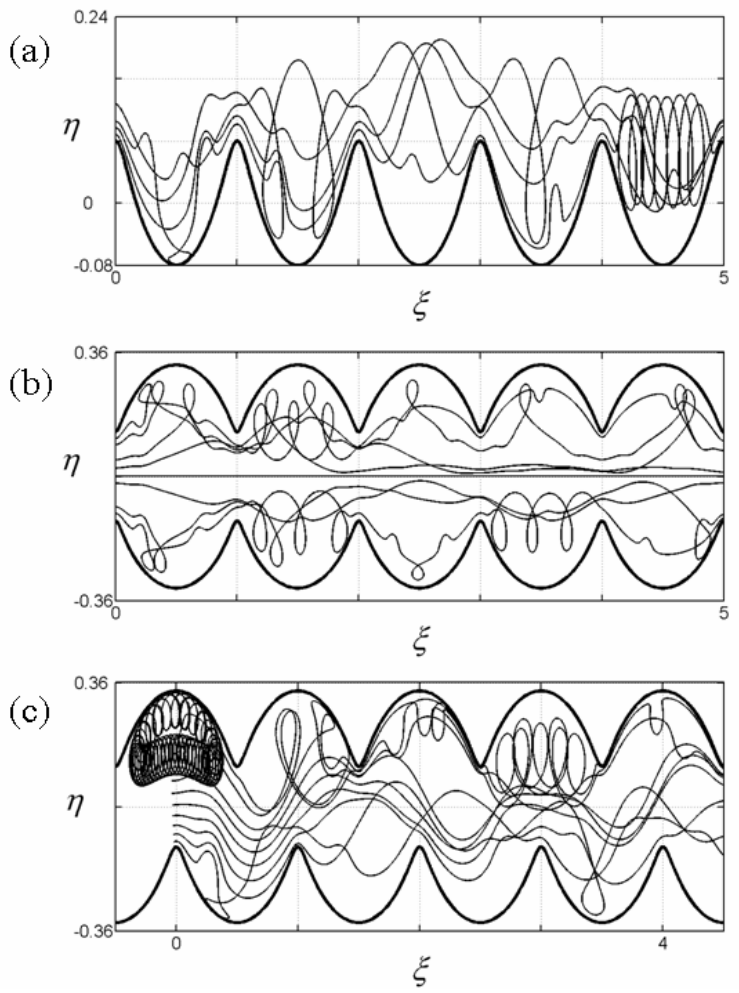

Figure 2.11: Particle trajectories for the case with infinite number of vortices in: (a) wavy wall; (b) symmetrical wavy channel; (c) skew-symmetrical wavy channel.

by the vortex in the second trough, and another trajectory is caught in resonance with the vortex in the fifth trough and only ejected after a considerable time. Particle distances from the wall are generally altered after each successive interaction with the vortices, regardless of whether the particles are entrained or else oscillate slightly as they pass over each trough.

For the symmetrical wavy channel (Figure 2.11b), the particle at the middle of the channel still traces a horizontal trajectory which forms an invariant centre line. Hence, the mixing efficiency of a symmetrical wavy channel is only comparable with that of a wavy wall bounded by a smooth wall on one side. In Figure 2.11c, 9 particles

are seeded into the skew-symmetrical wavy channel at $\xi = 0$, one of which is in close proximity to the vortex centre and is thus caught in extended resonance with the vortex motion. Here, an adaptive time step is adopted to resolve particle tracks in close proximity to the singular point at a vortex centre, and care is taken to avoid the singularity which is not of interest (or consequence) in the present study. For particle motions in the symmetrical and skew-symmetrical wavy channel, (2.15) and (2.19) are only evaluated for finite values of N due to the fact that a double infinite summation for vortices arising from the method of images combined with a second infinite summation for the array of vortices along the channel is not possible in analytic form. Hence, the case where $N = \infty$ in the channel is replicated by employing periodic end boundary conditions with prescribed upstream ($x = 0$) and downstream ($x = \lambda$) limits. The value of N is arbitrarily chosen to be 5 to approximate, at reasonable computational cost, the vortex path where there are infinite number of vortices along the channel, recalling that further increasing N has a diminishing effect on the vortex trajectory (Section 2.4.1.4). The number of times a particle exits and re-enters the computational domain is then tracked so that a continuous trajectory can be mapped to the physical domain. The periodic boundary condition serves to replicate a physical channel of infinite length with an infinite number of vortices in the flow direction, and should not be taken as producing a closed system.

In Figure 2.11, observation of chaotic particle trajectories in all three wavy configurations suggests that the systems are likely to be chaotic (Ottino, 1989; Rom-Kedar *et al.*, 1990). Since each vortex is trapped locally within a trough and does not interact significantly with its neighbours except with its own image, the observed chaotic particle motion is attributed entirely to the unsteady motion of a single vortex in its locality. If a finite number of vortices is employed along the wall or in the channel, then advected particles approach the vortex-populated furrows from the asymptotically simple region, and eventually escape to the asymptotic region again. In either

case, the systems exhibit the characteristics of transient chaos, i.e. chaotic scattering of the advected particles occurs over a finite time on interaction with the vortices.

The observation is in qualitative agreement with the laminar and transitional flow regimes for Reynolds numbers of 125 and 400 reported by Guzmán & Amon (1996) and Amon *et al.* (1996) for oscillatory flow in a sinusoidal channel. In both papers, the particle trajectories are determined by integrating the advection equation $\mathrm{d}\mathbf{x}/\mathrm{d}t = \mathbf{u}(\mathbf{x}, t)$, where $\mathbf{u}(\mathbf{x}, t)$ is the numerically simulated Eulerian velocity field, and exponential divergence of initially nearby particles is verified by positive finite-time Lagrangian Lyapunov exponents of selected test particles. Furthermore, the onset of Lagrangian chaos is associated with the first Hopf bifurcation. More recently, Biemond *et al.* (2008) showed, by means of a topological argument, that the onset of chaotic motion follows immediately the onset of periodic motion of the fluid, provided stagnation points are present in the flow. In Section 2.4.3, it is pointed out that this is indeed the case for the present problem.

2.4.2.2 Snapshots of particle positions

Figures 2.12a,b provide snapshots of a line of 301 equally-spaced particles advecting in the symmetrical wavy channel. Figure 2.12a shows the time evolution of the line of particles in the absence of any vortices. Unobstructed particles in the middle of the channel form a leading front which propagates downstream. As it traverses the converging and diverging sections of the channel, the flow undergoes alternate acceleration and deceleration, and thus narrows and widens correspondingly. The width of the leading front eventually reduces, and particles nearer the walls increasingly lag behind as they become held up in ever larger numbers of furrows. The line of particles is stretched in the diverging section of the channel and folded at the wall corrugations. Particles along the upper and lower wall are of course symmetric about the invariant centre-line.

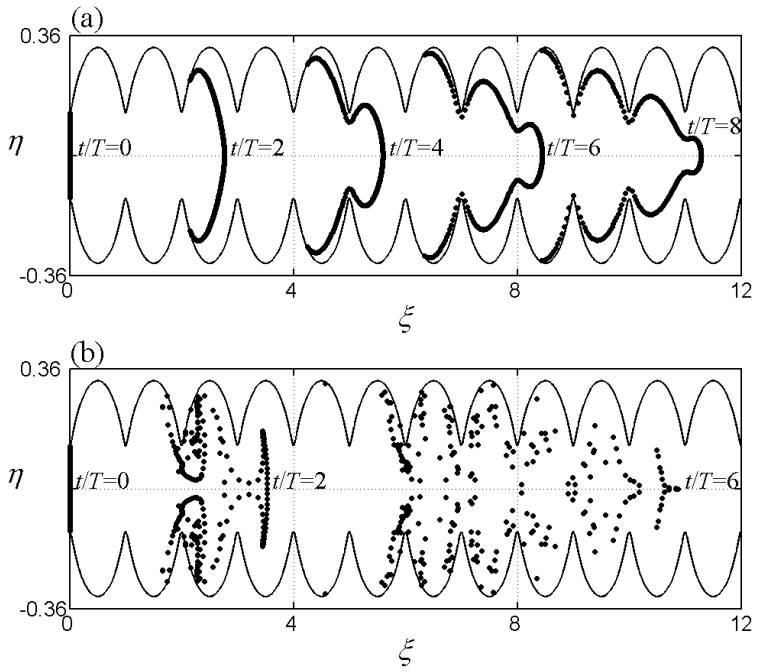

Figure 2.12: Snapshots of positions of a line of 301 particles (•) in the symmetrical wavy channel: (a) no vortices; (b) infinite number of vortices.

In Figure 2.12b, the same line of particles is subjected to vortex stirring. In addition to stretching and folding, the particles become dispersed. Particles near the walls soon break up from the leading front and become increasingly scattered. The non-entrained portion of the leading front is advected further ahead than in the previous case when there is no vortex in the flow field (see particle line for $t/T = 2$, and $t/T = 6$). This is due to the increased velocity induced by the counter-clockwise rotating vortices at the upper wall, and clockwise vortices at the lower wall. In contrast, entrained particles spend more time in the furrows. Consequently, these particles lag further behind the leading front than their counterparts in the case without vortices. Increased particle scatter is evident. Symmetry about the centre-line is nonetheless maintained.

Figures 2.13a,b show similar plots for the skew-symmetrical wavy channel. When there are no vortices (Figure 2.13a), the line of particles deforms unevenly due to the asymmetry, forming a leading front which is skewed in an oscillatory manner

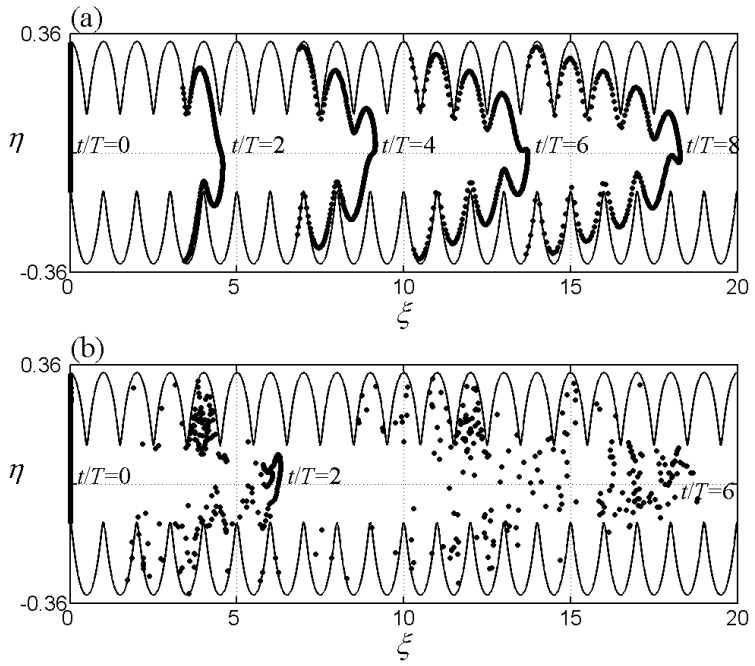

Figure 2.13: Snapshots of positions of a line of 301 particles (•) in the skew-symmetrical wavy channel: (a) no vortices; (b) infinite number of vortices.

where the profile is influenced by the nearest corrugation. For the symmetrical wavy channel, the line of particles occupies an increasing number of furrows with time and is stretched and folded. Particles sufficiently distant from the wall are advected primarily under the influence of the uniform flow field and tend to traverse furthest.

In Figure 2.13b, vortical stirring is observed to obliterate the line of particles in less than two cycles (by $t/T = 2$). Similar to the symmetrical wavy channel, the leading front moves further ahead while the entrained particles lag further behind. Certain particles initially located close to the vortex centre became trapped in the trough where they are released throughout the duration of the simulation. This agrees with the Lagrangian trajectories shown in Figure 2.11c and those presented by Guzmán & Amon (1996) and Amon *et al.* (1996). Contrary to the symmetrical wavy channel, there is no symmetry in the particle distribution, and hence mixing can potentially take place across the channel width, making the skew-symmetrical channel superior to its symmetrical counterpart with regard to mixing efficiency. In Section 2.4.4.2,

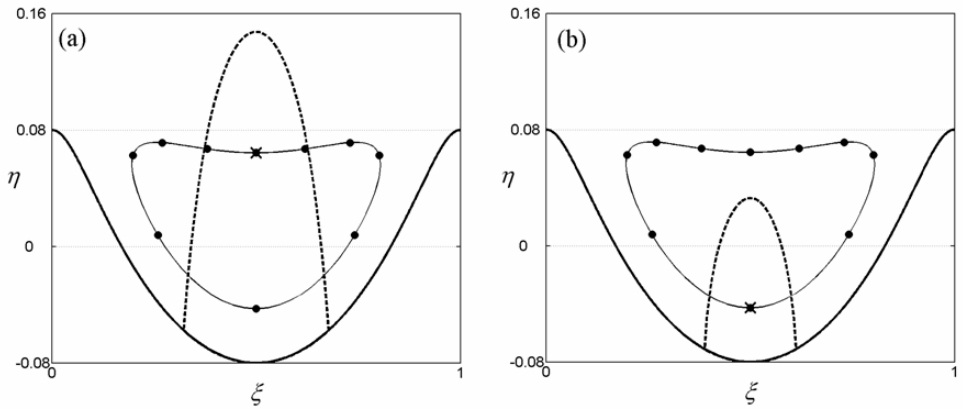

Figure 2.14: Vortex trajectory (——) and positions (•) at $T/10$ increment in a wavy trough. Also shown is the separation bubble (- - - - -) corresponding to the vortex position marked ×.

the above problem will be revisited to show that transport across the centre-line of the symmetrical wavy channel is possible if the effect of diffusion is included.

2.4.3 Dynamics of separation bubble

The mixing effect observed in Section 2.4.2 can be associated with the presence of a separation bubble in the vicinity of the vortex, whose area and shape evolve continuously as the vortex moves. To examine the dynamics of the separation bubble, consider a case involving a single furrow in the wavy wall, where $t/T = 0$ and $t/T = 0.5$ correspond to instants when the vortex is located at the highest and lowest positions, respectively, in the middle of the furrow (Figures 2.14a,b). The separation bubble is derived from the instantaneous streamlines separating an exterior region of positive stream function from an interior region of negative stream function. The separation bubble always joins the wall at two separation points, each of which constitutes an instantaneous stagnation point in the flow field. As pointed out in Section 2.4.2.1, with the presence of stagnation points in the flow, the onset of chaotic motion follows immediately the onset of periodic motion of the fluid (Biemond *et al.*, 2008).

2.4.3.1 Variation of the area of separation bubble and vortex motion

The area of the separation bubble A_b is derived from the physical domain, and is normalised by its largest value at $t/T = 0$. Figure 2.15 shows that A_b reduces over half the cycle as the vortex moves clockwise, and expands in the second half of the cycle. The time-dependent variation of A_b is closely related to that of the vortex vertical position y_v and the changes in distance between the two separation points (see inset in Figure 2.15), both of which reduce from $t/T = 0$ to 0.5. The slight increase in A_b at the lowest point in the trough ($t/T = 0.5$) can be solely attributed to the increase in wall curvature (Figure 2.14). The changes reverse during the second half of the cycle, as expected. Overall, the area of the separation bubble varies by a factor of 3.1 over the cycle, implying that significant mass exchange is likely to take place across the separation boundary, favouring mixing as anticipated from the large-amplitude motion of the vortex.

Figure 2.16 shows the relative motion of the separation points with respect to the vortex. As the vortex traverses from $t/T = 0$ to 0.3, the separation points move slower than the vortex. From $t/T = 0.3$ onwards, the vortex starts to move upstream along the wall (see instantaneous vortex position in Figure 2.14). The upstream separation point moves ahead at a slightly larger velocity whereas the downstream separation point trails behind (Figure 2.16). On approaching the lowest point in the trough, the vortex velocity continues to increase at a higher rate compared to that of the two separation points. The inset of Figure 2.17 shows the velocity U of the separation points with respect to their positions. When the vortex moves upstream close to the wall (lower half of the loop) U is twice that when the vortex moves downstream away from the wall (the plateau on the upper half of the loop). The factor of 2 is slightly less than that of the vortex motion where $U_{max}/|U_{min}| \approx 2.3$ (Figure 2.16). Figure 2.17 also displays the velocity components (U, V) of the vortex. At $t/T = 0$, the vortex velocity in the x- and y-directions are $U = U_{max}$ and $V = 0$, respectively (rightmost

point on plot). As the vortex rotates in the clockwise direction, V increases slightly, then changes to negative as the vortex moves downward into the trough. Meanwhile, U reduces. By $t/T = 0.5$, U reaches its negative maximum whereas V returns to zero (leftmost point on plot). Whereas the magnitude of U varies by a factor of 2.3, that of V on the other hand varies by a much larger factor of 15.3. Relating the velocity of the vortex to its instantaneous position (Figure 2.14), it is obvious that the sweeping motion along the wall (from $t/T = 0.3$ to 0.7) occurs rapidly compared to the downstream motion when the vortex is distant from the wall. This suggests that the vortex image has a dominant influence. In a complete cycle, the parametric $U - V$ plot thus resembles a highly distorted figure '8'.

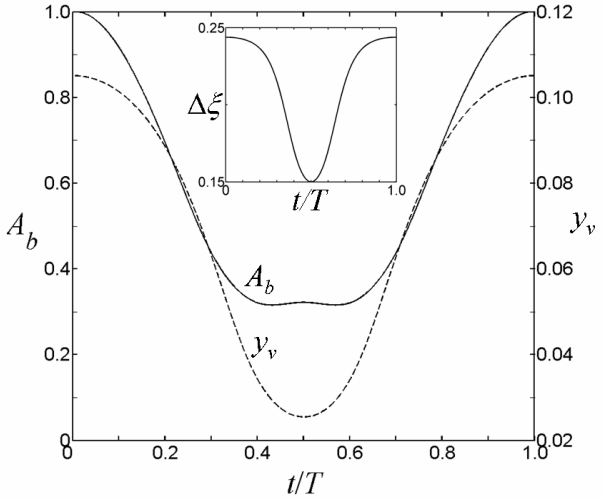

Figure 2.15: Temporal variation of the area of separation bubble A_b and vortex vertical distance y_v from the wall. Inset showing temporal variation of horizontal distance $\Delta\xi$ between the two separation points.

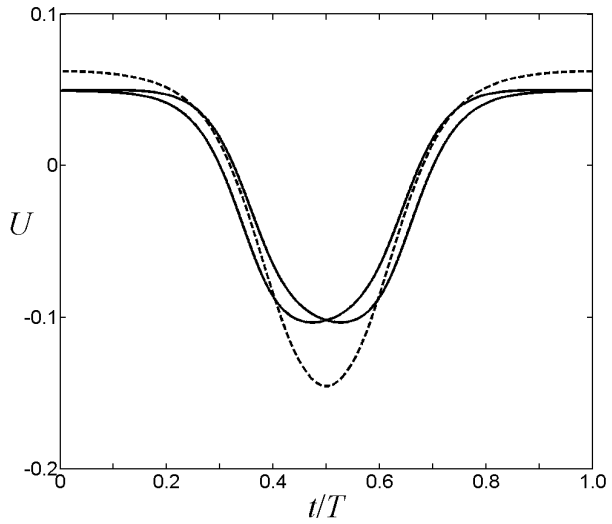

Figure 2.16: Temporal variation of channel longitudinal velocity U: ----- vortex; —— separation points.

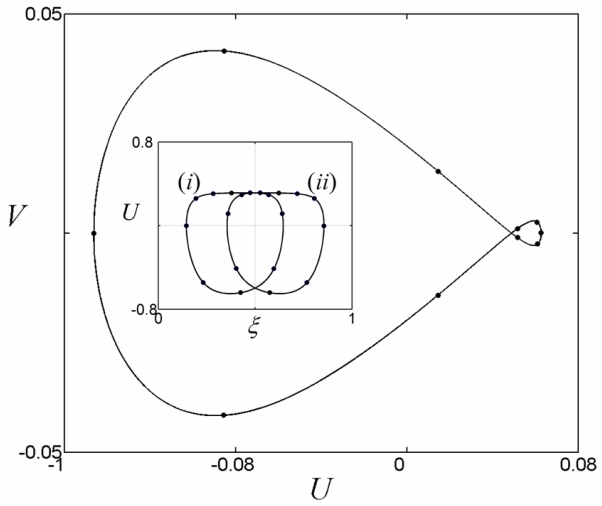

Figure 2.17: Velocity (U, V) of vortex tracked in the z-plane (• indicates $T/10$ increment). Inset showing velocity U of the two separation points with respect to their position ξ in the physical domain.

2.4.3.2 Particles escape from the separation bubble

This section examines the escape rate and particle trapping within the separation bubble. Particles are seeded into the separation bubble at equally spaced intervals over the computational domain. The corresponding particle distribution in the physical domain is slightly distorted due to the mapping functions; however, this does

not pose any issue for the present qualitative investigation. The number of particles used is in the order of 1000 for the case when the initial vortex positions are set at $t/T = 0.5$. Retaining the same intervals, the number of particles used when the initial vortex position is located at $t/T = 0$ is thus approximately a factor of 3 more, proportional to the increase in the bubble area. Adaptive time stepping is used to track accurately the particle trajectories in close proximity to the singular point at vortex centre. Particles located within a distance of less than $0.05/\lambda$ from the vortex centre are discarded. This constitutes less than 2% of the total number of particles seeded.

Figure 2.18 shows sequential snapshots of the particles escaping from within the separation bubble in the wavy trough, where the vortex initial position is set at $t/T = 0$. In Figure 2.18*ii*, it is observed that a large proportion of the seeded particles is ejected from the downstream surface of the bubble in the first one-tenth of the cycle as the separation bubble moves to the right. These particles form a series of arrow-like features pointing in the direction of their motion which tend to encircle the vortex. Particles to the left of the arrows have only moved minimally from their initial positions near the downstream surface of the bubble, and lag behind as the vortex traverses. Particles to the right of the arrows, which originate from the now white background in the separation bubble, have moved a considerable distance comparatively. The arrow-like feature is an artifact of the finite number of particles followed. A compact blob would result if more particles are tracked (see e.g. Figures 2.26 and 2.28). The white background essentially represents particles outside the separation bubble, herein referred to as the white particles. It can be observed that, during this same time period, the white particles sweep into the bubble rapidly from the upstream surface curling past the vortex centre, suggesting that particles to the east of the vortex possess relatively larger velocity compared to those to the west, which is confirmed by the instantaneous velocity field (not shown). The boundary be-

tween the white particles and the seeded particles is the original separation boundary which is now greatly stretched under the stirring action of the vortex. Its deformed shape is akin to the unstable manifold numerically computed by Rom-Kedar *et al.* (1990) using the Melnikov technique for small perturbation. Further discussions on the stable and unstable manifolds in the present model are given in the next section. In Figure 2.18*iii* ($t/T = 0.2$), it can be seen that the white particles have curled further reaching the south-east of the vortex, effectively completing a loop around the vortex. Note also that they have exited the separation bubble and the leading front is attempting to re-enter the bubble again. Meanwhile, the tail end of the train of particles still lingers in the vicinity of its earlier position. Figure 2.18*iii* also shows the formation of a tongue-like feature which stretches downstream, leading eventually to particles escaping from the trough (Figure 2.18*iv*). When the vortex starts to sweep along the wall, it is relatively close to the downstream wall, which hinders particles from winding further around the vortex. Consequently, both the seeded particles and the white particles drain away under the action of the uniform flow (Figure 2.18*v*). By $t/T = 0.5$ (Figure 2.18*vi*), the vortex centre is at its lowest position and surrounded by the remaining seeded particles which are held in close proximity to the vortex centre thereafter. A considerable proportion of the separation bubble is now filled with white particles in the outer band. Re-seeding the separation bubble at $t/T = 0.5$ (Figure 2.18*vii*), Figure 2.18*viii* shows that within one-tenth of a cycle, a large fraction of the particles is swept downstream from the bubble as the vortex moves upstream at relatively high velocity. The number of seeded particles which remains trapped around the vortex (Figure 2.18*ix*) is essentially the same regardless of whether or not re-seeding is performed at $t/T = 0.5$. This suggests that particles trapped are solely those initially in close proximity with the vortex centre, whereas re-seeded particles which fill the white band within the separation bubble in Figure 2.18*vi* are essentially all expelled. Hence, this confirms the presence of a

non-escape zone which may be referred to as the vortex 'core', a generic feature of point-vortex dynamics (e.g. Babiano *et al.*, 1994; Boffetta *et al.*, 1996; Amon *et al.*, 1996; Neufeld & Tél, 1997, 1998). The series of snapshots in Figure 2.18 also shows that the white particles, though freely entering and escaping the separation bubble, cannot penetrate the vortex core occupied by the seeded particles. This is due to the presence of irrational orbits known as KAM tori, which act as transport barriers between the stable region in the vortex core and the unstable region outside (e.g. Rom-Kedar *et al.*, 1990). Hence, the vortex singularity is essentially shielded by the surrounding regions of permanently trapped fluid, and plays no role in the unsteady mixing process. Indeed the same dynamics would result if the vortex core is replaced by a non-singular vortex patch of constant vorticity whilst preserving the same total circulation. The above observation is important for engineering applications, noting that in Lagrangian investigations of particle trajectories the precise fate of individual particles is not necessarily of major importance, instead it is key to reveal the possible presence of regions where pollutants cannot escape, and where treatment materials such as surfactants or dispersants for oil spills cannot enter. In Section 2.4.4.2, it is shown that if diffusion is considered, it is then likely that the particles within the vortex core will eventually escape (Chorin, 1973). For the active mixing problem (Section 2.4.5), the vortex core is exploited as a source of reacted catalytic particles with which approaching particles entering the separation bubble may react.

Figure 2.19 shows the fraction of particles trapped n as a function of non-dimensional time t/T in a fixed observation window which consists of a single trough. Particles seeded within the separation bubble escape primarily in the first cycle, after which there are only a few instances when a small number of particles are expelled as the vortex traverses past its lowest position at high velocities, leaving those particles which fail to wind around the vortex, to drift downstream. Figure 2.19 also shows that n is not sensitive to the total number of particles seeded. In a study of a contin-

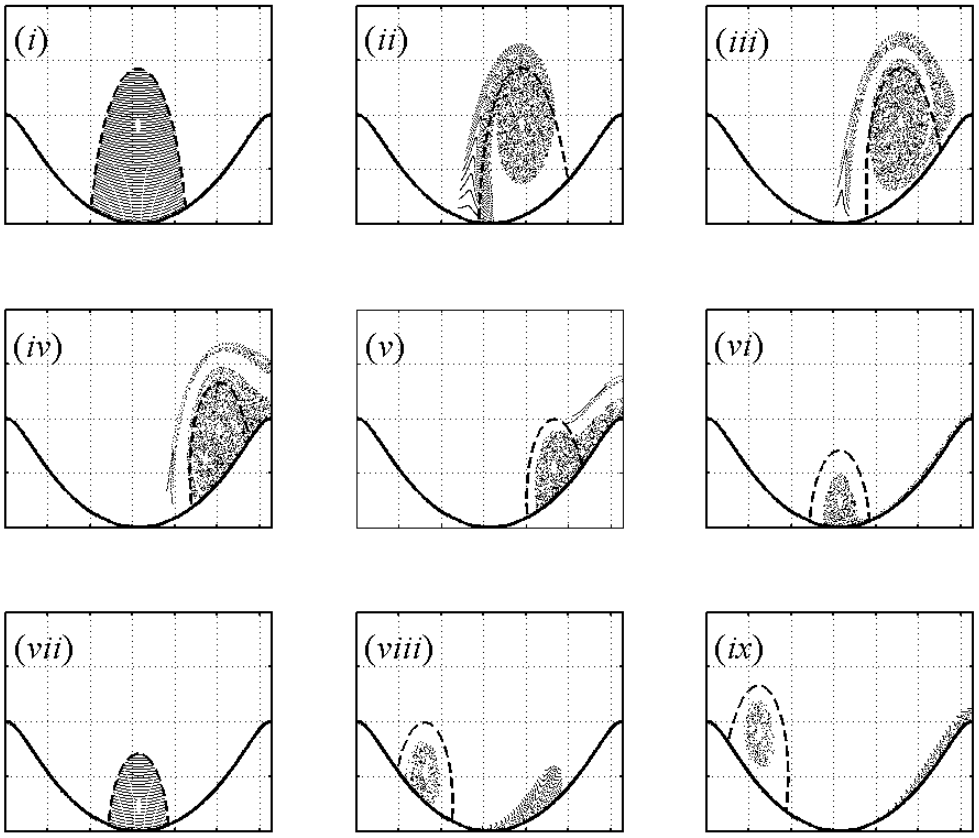

Figure 2.18: Sequential snapshots of particles escaping from within the separation bubble (-----) in the wavy wall problem (η vs ξ). Plots (*i-vi*) show fate of particles seeded into the separation bubble from $t/T = 0$ through $t/T = 0.5$ at $T/10$ increment; plots (*vii-ix*) show fate of particles seeded into the separation bubble from $t/T = 0.5$ through $t/T = 0.7$ at $T/10$ increment.

uously modulated free-surface flow, Wilson *et al.* (2006) reported equivalent temporal behaviour of the percentage of initial tracers remaining in seeded-eddy simulations in a study of mixing effects involving a separation bubble attached to a curved free surface. The drop in the tracer population is associated with the detrainment of fluid from the eddy region, whereas the flat plateau represents the entrainment phase, noting that the incoming fresh fluid are devoid of tracers. For large perturbation, as considered in the present study, a considerable proportion of the seeded tracers are ejected within the first cycle. The subsequent cascading reduction of tracer population obtained by Wilson *et al.* (2006) is however not obvious in the simulation owing to the large perturbation adopted to optimise mixing. Rom-Kedar *et al.* (1990) ob-

tained a similar finding from the simulated escape of particles from a lobe. Likewise, Wierschem & Aksel (2004) observed similar behaviour in an experimental study of the loss of fluorescent tracers from an eddy in a wavy corrugation.

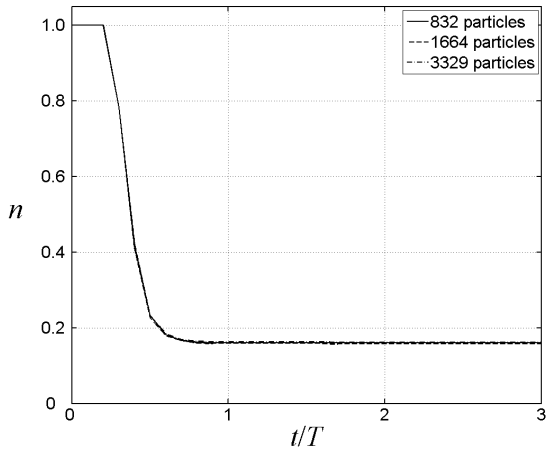

Figure 2.19: Fraction of particles trapped in the trough n as a function of nondimensional time and effect of number of particles.

Despite the foregoing discussion, note that the calculation of n is based on the number of particles which remain in the trough instead of in the separation bubble. This explains why n only reduces after a short lag, due to the finite time taken for any of the seeded particles to reach the downstream boundary of the observation window. Wilson *et al.* (2006) use this approach to calculate n because the end of the domain is easier to define. The same approach is used in order to address the boundary particles in the potential model. Should n be computed based on the fraction of particles that never leave the separation bubble, its value will not approach a constant but will alternate between two discrete values, the difference of which represents the small number of boundary particles which periodically enter and leave the separation bubble. Considering the case when vortex motion commences from the position $t/T = 0$, boundary particles located to the east of the separation bubble are swept downstream, whereas those inside the separation bubble are ejected upstream as the bubble moves in the opposite direction. This is because the wall is an invariant

manifold, unstable downstream but stable upstream of the downstream separation point in the perturbed system of the vortex motion (Rom-Kedar *et al.*, 1990). The opposing motion means the particles will inevitably become increasingly close to one another on the wall, forming a conglomerate point at plot resolution. For a wavy wall or channel that has an infinite number of vortices, a conglomerate point of boundary particles thus exists in each and every trough. These conglomerate points assume an oscillatory gliding motion along the wall upstream of the trough, entering and leaving the separation bubble periodically but unable to traverse the separation bubble.

2.4.3.3 Mixing region, free flow region and vortex core

In the preceding section, it was observed that particles are able to enter and leave the separation bubble as it swells and shrinks. Substantial mass exchange between the flow and the separation bubble is induced by the stirring action of the vortex. Consider a large ensemble of particles seeded over four consecutive troughs horizontally extending up to elevation $y = 0.24$ in the z-plane. A single vortex is introduced in the rightmost seeded trough such that there is a continuous stream of particles approaching the vortex over one complete cycle. The region within $0.05/\lambda$ of the vortex centre, defined as the vortex core, is herein excluded. The motion of the particles is observed using a reference frame moving with the single vortex, the initial position of which is set at $t/T = 0$.

As the vortex and particles are set in motion, particles entrained are greatly stretched and wind around the vortex at high velocities (Figure 2.20*i*), resembling the motion of the white particles in Figure 2.18*ii*. This results in a chaotic-sea-of-mixing region characterised by apparent particle scatter. The mixing region at this instant is significantly larger than the separation bubble, and comparable to the size of the wavy trough. The mixed particles are subsequently ejected when the vortex sweeps downstream along the wall. Particles which have undergone mixing appear 'scattered' in the plots (Figure 2.20*i*,*ii*) whereas the others maintain a regular

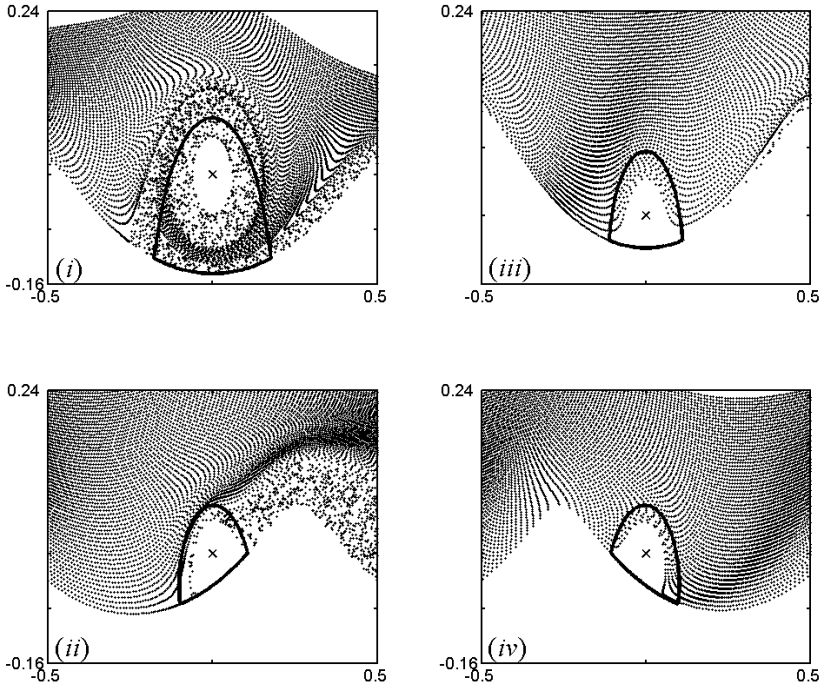

Figure 2.20: Instantaneous snapshots of particles motion (•) on a reference frame co-moving with the vortex (×): (*i*) $t/T = 0$ or $t/T = 1$; (*ii*-*iv*) correspond to $t/T = 0.4$, 0.5, and 0.6, respectively. Note that the vacated zone in the vicinity of the vortex represents the vortex core (——, separation bubble).

but distorted arrangement with the neighbouring particles. Since no further particle entrainment occurs after $t/T = 0.4$, the size of the mixing region shrinks. By $t/T = 0.5$ (Figure 2.20*iii*), the mixing region is virtually non-existent and it develops again shortly after $t/T = 0.6$ (Figure 2.20*iv*). Particles entering and leaving the separation bubble during these times do not wind around the vortex but stream past the vortex core. Indeed, the mixing region 'vanished' from the plot as a result of the finite number of particles deployed. Of most interest in this context, is the fact that the size of the mixing region varies greatly over half a cycle.

Whilst the snapshots of the ensemble of particles in Figure 2.20 provide a glimpse of the mixing and free flow region (and indirectly the vacated, non-penetrable vortex core), the transient nature of chaos means that each of these regions is defined in

terms of the respective sets of trajectories. It may thus be construed that the mixing region is made up of a set of trajectories which wind around the vortex a finite number of times. Trajectories which never wind around the vortex constitute the free flow region, and trajectories which wind around the vortex infinitely make up the vortex core (e.g. Rom-Kedar *et al.*, 1990; Amon *et al.*, 1996; Budyansky *et al.*, 2007*b*). Trajectories of the mixing region and the free flow region are responsible for mass exchange in and out of the separation bubble whereas the vortex core behaviour is essentially isolated from the flow field. The free flow region further out is not seeded and thus appears as a band of white particles in the upper part of the plots (see Figure 2.20*i*). Particles in this region do not enter into the vicinity of the vortex or the trough, and are advected mainly by the uniform flow with superimposed small oscillatory motion induced by the vortex. In the simulation shown above, all seeded particles pass the vortex after one-and-a-half cycles. No particle is trapped, and none penetrate into the vacated vortex core.

The present model of a unidirectional uniform flow field superposed with oscillatory vortex motion is analogous to aspects of oscillatory flow of a real fluid as studied by Sobey (1980) and Ralph (1986) using Navier–Stokes solvers. Sobey (1980) investigated the flow structure in wavy channels by considering different ratios of the oscillation amplitude to the mean flow amplitude. In the present study, the dimensionless amplitude for vortex motion is in the order of 0.6, 0.65 and 0.75 for the wavy wall, symmetrical channel and skew-symmetrical channel, respectively, under unit uniform flow. Hence, the cases considered herein approach the oscillatory unidirectional flows considered by Sobey (1980) where the ratio of the oscillatory component to the mean flow is taken to be in the order of $(1 - 0.55)/0.55 \approx 0.8$. Noting that the omni-present vortex core is a non-interacting region, the birth of the mixing region is analogous to flow separation in oscillatory flow of a real fluid, which leads to vortex formation. During the first half-cycle, the separated region in the real fluid grows

and the vortex bulges into the mainstream, eventually occupying most of the trough. The same behaviour is observed in the present model from $t/T = 0.5$ to 1.0. In the second half of the cycle, the real fluid flows into the upstream part of the furrow as the flow accelerates, thus displacing the vortex which is eventually eliminated as the bulk flow accelerates. Whereas the periodic shedding of vorticity is not relevant here, the process of vortex decay is replicated in the form of a vanishing mixing region that persists from $t/T = 0$ to 0.5. Essentially, the present model, which comprises a uniform flow with internally induced unsteady oscillation, produces the same dynamics in the periodic growth and elimination of the mixing zone as an externally induced unsteady oscillatory flow of a real fluid, noting that the qualitative flow behaviour is not sensitive to the wall profile (Sobey, 1980). The similarity between the present results and the solutions of the unsteady Navier–Stokes equations by Sobey (1980) and Ralph (1986) lend much merit to the point vortex model in the study of vortex-induced mixing.

2.4.3.4 The invariant manifolds

In this section, the unstable and stable manifolds are examined in greater detail. Figure 2.21 shows exemplar plots of the instantaneous unstable and stable manifolds, numerically constructed by releasing a particle at each time step at the instantaneous hyperbolic points (i.e. the stagnation points A and B in Figure 2.22) in the flow field in forward and backward times, respectively. Particles starting on these invariant manifolds in the continuous time flow emerge as an infinite set of discrete points on these curves in the Poincaré section. In snapshots of a flow, the unstable manifolds appear as smooth curves. The stable manifolds, however, are not readily observable. Due to the symmetry of the system in space, these invariant curves are essentially mirror images of one another about the vertical axis through the middle of each furrow, for instance at $t/T = 1.0$ (Figure 2.21a) and similarly at $t/T = 0.5$ (not shown). At other times, such as $t/T = 0.3$ (Figure 2.21b), the mirror image of the

curves about the vertical axis through the middle of the furrow gives the structure of the invariant curves at $t/T = 0.7$ due to the symmetry of the system with time over a cycle, noting that the stable and unstable manifolds are thus swapped in the mirror image construction (Figure 2.22*ii* and *iv*). Hence, the unstable manifold for a flow from left to right becomes the stable one for a flow from right to left, and *vice versa*.

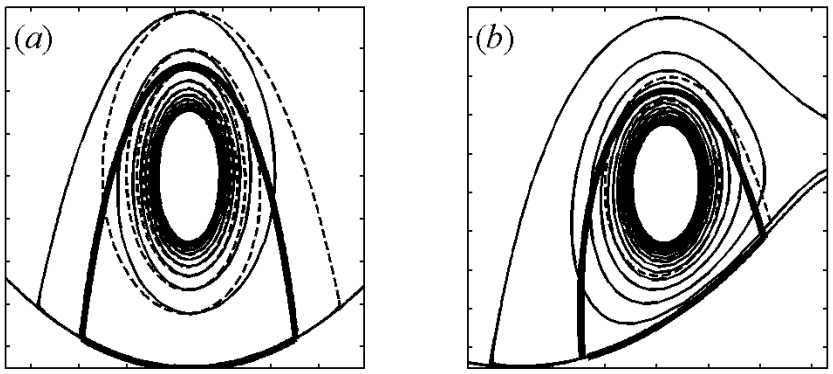

Figure 2.21: The stable (- - - - -) and unstable (——) manifolds at (a) $t/T = 1.0$, and (b) $t/T = 0.3$. Here, the separation bubble is shown in thick solid line.

In Section 2.4.3.2, it is highlighted that the wall is an invariant manifold. With reference to Figure 2.22, the unstable manifold to the east of point B, and the two branches of the stable manifold towards point A (arrows in figure indicate direction of particle motion along the invariant curves) lie exactly on the wall. In the unperturbed system, the unstable manifold of point A is also the stable manifold of point B, and its position coincides with the separation bubble, thus separating the exterior free flow region and the interior region. In this case, the manifold structure is topologically equivalent to one-half of the oscillating vortex-pair flow (e.g. Rom-Kedar *et al.*, 1990; Rom-Kedar & Wiggins, 1990; Wilson *et al.*, 2006). When the system is perturbed, the spiral nature of the invariant manifolds produces infinite self-similar crisscrossing tangles at all scales (Figures 2.21 and 2.22). In the discussions that follow, the role of the infinite set of intersections between the stable and unstable manifold in the

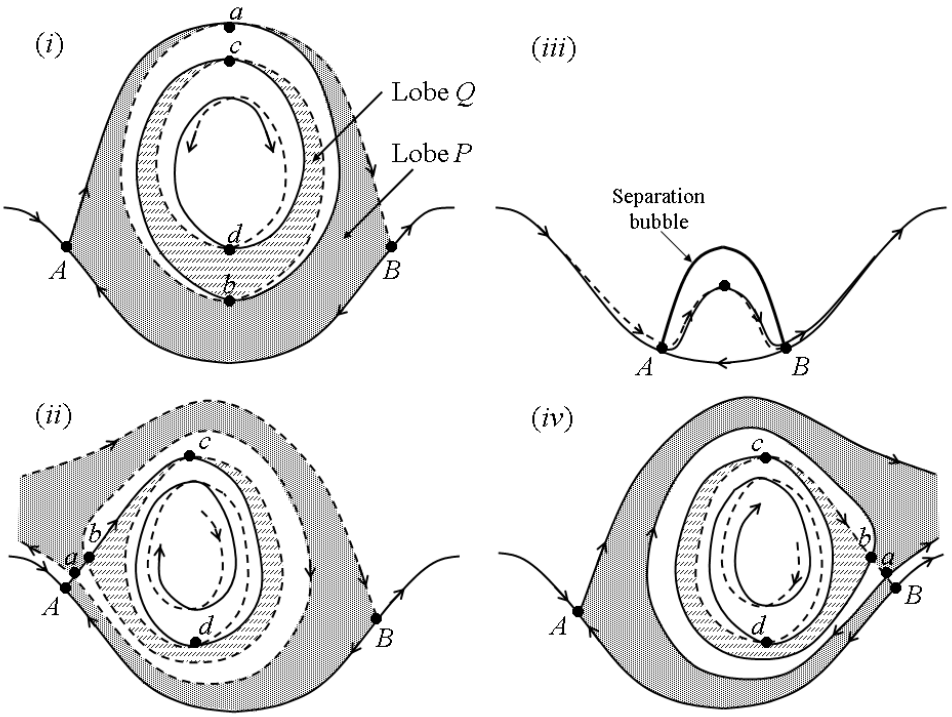

Figure 2.22: Schematic illustration of the stable (- - - - -) and unstable (——) manifolds at (i) $t/T = 1.0$, (ii) $t/T = 0.3$, (iii) $t/T = 0.5$, and , (iv) $t/T = 0.7$. The two shaded area bounded by segments of the unstable and stable manifolds defined by the intersection points a, b, c and d represent two different lobes which transport the fluid contained as the invariant curves traverse with the vortex motion. For clarity, only the separation bubble of (iii) is shown.

mechanism for mass transfer into and out of the mixing region is emphasised. In Section 2.4.5, we investigate the fractality of the invariant manifolds.

Since no flow is able to cross the invariant curves except solely by diffusion (considered separately in Section 2.4.4.2), the invariant curves divide the flow field into a free flow region in the exterior, and a recirculating zone in the interior (which consists of the mixing region and the vortex core). A parcel of fluid bounded by a segment of the unstable manifold and a segment of the stable manifold between two successive intersection points can be defined as a 'lobe' where the fluid which lies within it remains there for all time (e.g. Rom-Kedar *et al.*, 1990; Rom-Kedar & Wiggins, 1990; Wilson *et al.*, 2006). Figure 2.22 shows the evolution of two lobes as the invariant curves traverse with the vortex. Note that Figures 2.22i and iii match the time instants of

Figures 2.20*i* and *iii*, respectively. On the other hand, Figures 2.22*ii* and *iv* are at different times to those in Figures 2.20*ii* and *iv* in order to facilitate visualisation of the invariant curves. Figure 2.22*ii* shows that lobe P carries the fluid parcel from the upstream into the recirculating zone. Driven by the growing unstable manifold, the fluid in lobe P subsequently undergoes mass exchange in and out of the separation bubble but remains contained within the outermost invariant manifolds, that is, the invariant manifolds cover a region significantly larger than the separation bubble during these times (see Figure 2.20*i* and Figure 2.22*i*). When the lobe reaches the downstream end of the trough, the stable manifold starts to contract. Consequently, the lobe is ejected together with the bounding segments of the unstable manifold (Figure 2.22*iv*). Lobe Q undergoes the same processes as lobe P except that it grows earlier, shrinks later, and contains smaller quantity of fluid. Hence, particles closer to the vortex centre are entrained longer. Note also that the lobes enter and leave the separation bubble a finite number of times from their ingestion to their eventual ejection.

Just before the vortex reaches its lowest position (at approximately $t/T = 0.4$), the stable manifold contracts to its minimum and the last remaining lobe is stretched in the direction of the unstable manifold, draining the fluid it contains downstream. When the vortex starts to move upwards from its lowest position, a new lobe is entrained along the stable manifold of the hyperbolic point B. At this instant ($t/T = 0.5$), there is only a single intersection between the new stable manifold and the diminishing old unstable manifolds (Figure 2.22*iii*). A new unstable manifold grows immediately after the old one detaches from the hyperbolic point A (at approximately $t/T = 0.6$). During the transition, the region covered by the invariant curves is smaller than the separation bubble, which relates well to Figure 2.20*iii*.

Wilson *et al.* (2006) show that the entraining lobe and the detraining lobe can be overlapped. They observe that under large perturbation, self-intersecting turnstiles

are responsible for ejection of fluid ingested during the same cycle. The mechanism is similar to that shown in Figure 2.18. A close examination of the evolution of the lobes in Figure 2.22 suggests that the same lobe undergoes the entraining phase from $t/T = 0.5$ to $t/T = 1.0$ (or equivalently from $t/T = -0.5$ to $t/T = 0$), and the detraining phase from $t/T = 0$ to $t/T = 0.5$. In fact, due to the spiral structure of the invariant curves, the exterior and interior of the lobes cannot be distinguished. For the same reason, the 'turnstile' structure in the vicinity of the hyperbolic points is also different from that described by Rom-Kedar & Wiggins (1990) and Wilson *et al.* (2006). Here, the same lobe (e.g. lobe P) undergoes simultaneous contraction from both sides of the unstable manifold during the entraining phase (Figure 2.22*ii*), and later simultaneous stretching at both sides of the stable manifold during the detraining phase (Figure 2.22*iv*). Experimentally, Wierschem & Aksel (2004) show that the turnstile lobe mechanism is responsible for the breakup of the separatrix, thus permitting a spiraling inflow and outflow motion which governs the material exchange between the eddy in the furrow and the overlying steady flow.

2.4.4 Mixing efficiencies

2.4.4.1 Statistical dispersion of passive particles

This section compares the mixing efficiencies of three different configurations: the wavy wall, symmetrical wavy channel, and skew-symmetrical wavy channel. In each case, about 7000 particles, equally spaced in the z-plane, are seeded within one wavelength with a mean initial position of $\overline{x} = \lambda/2$ ($\overline{x} = 0$ for the case of skew-symmetrical channel), vacating the region within $0.05/\lambda$ from the vortex centre. An infinite number of vortices is used with maximum amplitude of motion contained within the trough. The particles seeded are tracked for 10 cycles, and the standard deviation σ of their positions along the axis of the channel calculated as a function of time. From Figure 2.23a, it can be seen that σ increases monotonically with time for all three cases

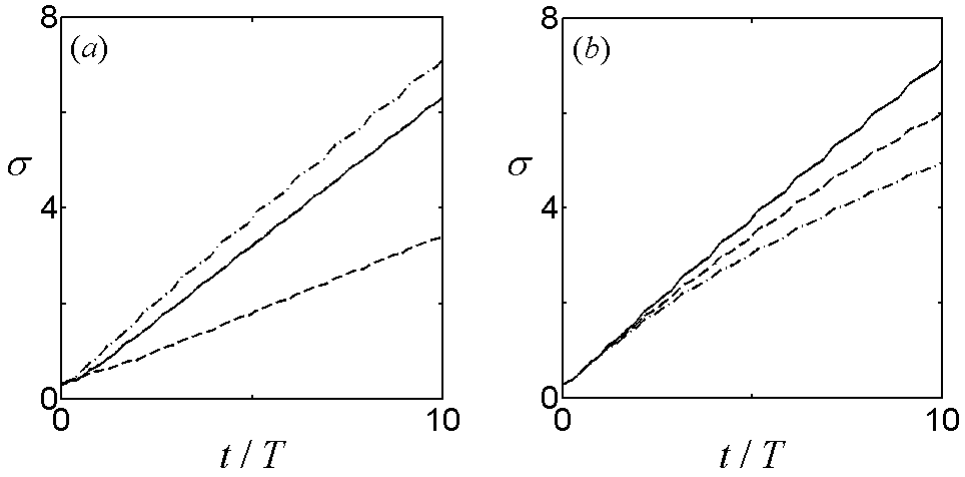

Figure 2.23: Mixing efficiencies measured in terms of standard deviation σ. (a) Comparing wavy wall (——), symmetrical wavy channel (- - - - -) and skew-symmetrical wavy channel (-·-·-·-); (b) effect of diffusion on passive mixing in skew-symmetrical wavy channel: $\nu = 0$ (——), $\nu = 0.001$ (- - - - -), $\nu = 0.005$ (-·-·-·-) .

(e.g. Sobey, 1985). In the wavy wall problem (particles seeded up to $y = 0.24$), particles steadily drift further away from the wall and thus have diminishing interactions with the vortices trapped in the wall corrugations. Therefore, the wavy wall configuration is not desirable for long-term or long-range mixing. The skew-symmetrical wavy channel outperforms the symmetrical wavy channel with significantly higher values of σ. In addition, the latter does not allow lateral mixing across the invariant centre-line as shown in Figure 2.24a, whereas the former permits cross centre-line mixing as illustrated in Figure 2.25a. In conclusion, the skew-symmetrical wavy channel is the most efficient in passive mixing (e.g. Nishimura & Matsune, 1996).

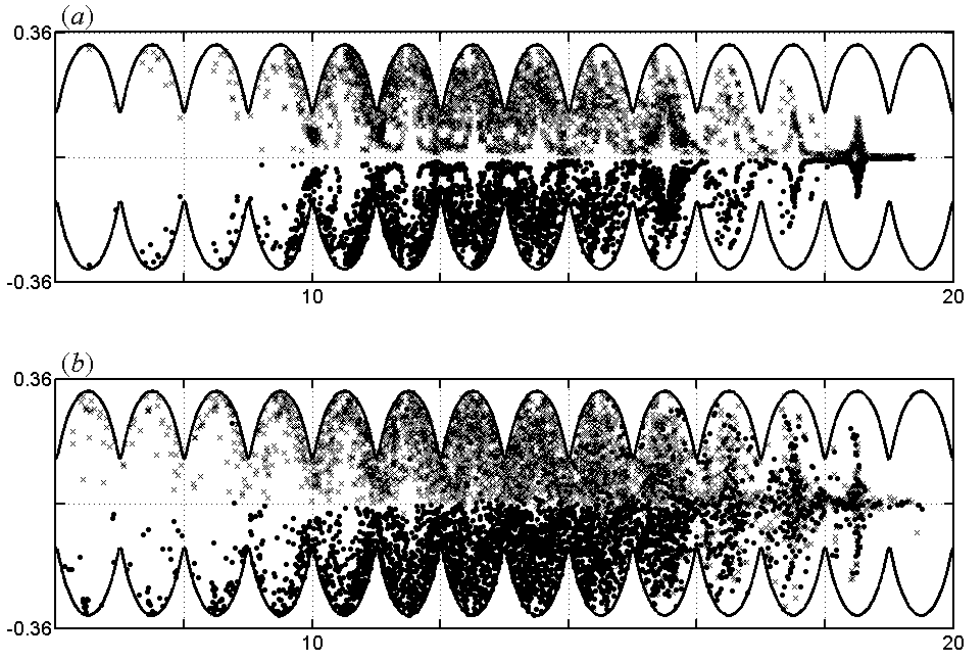

Figure 2.24: Particle positions at $t/T = 10$ for symmetrical wavy channel: (a) $\nu = 0$; (b) $\nu = 0.001$. (η vs ξ, initial particle positions are equally spaced in the z-plane within one wavelength with mean position $\overline{x} = \lambda/2$; $\times$ and $\bullet$ represents initial particle position above and below the centreline, respectively.)

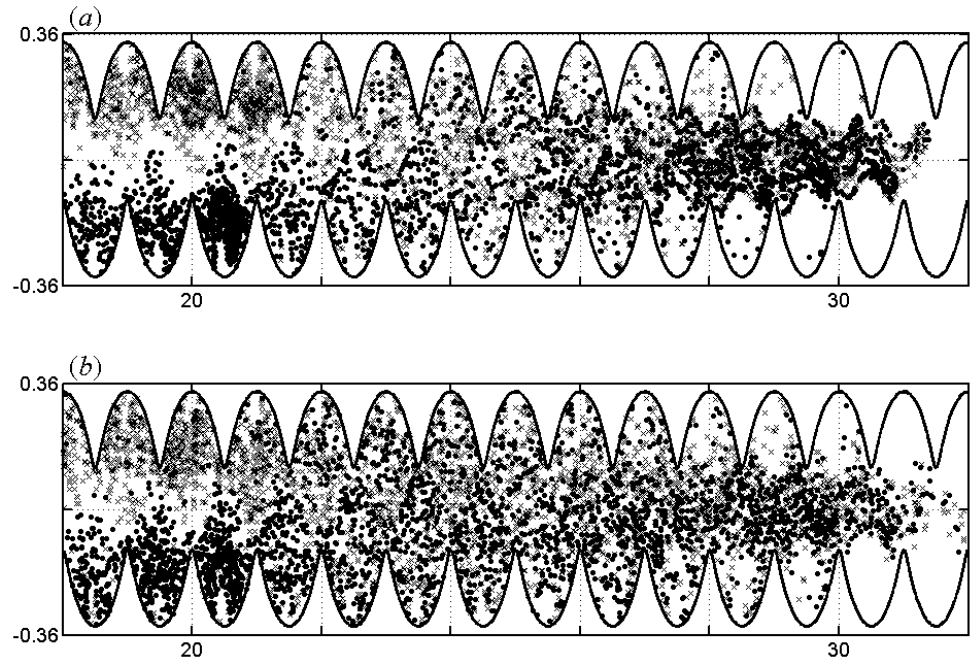

Figure 2.25: Particle positions at $t/T = 10$ for skew-symmetrical wavy channel: (a) $\nu = 0$; (b) $\nu = 0.001$. (η vs ξ, initial particle positions are equally spaced in the z-plane within one wavelength with mean position $\overline{x} = 0$; $\times$ and $\bullet$ represents initial particle position above and below the centreline, respectively).

2.4.4.2 Diffusion by random walk

The particle tracking scheme presented above models only the advection of passive tracers. Chorin (1973) proposed that advective and diffusive phenomena could be treated separately, where the latter may be simulated using a stochastic technique involving random particle displacements analogous to Brownian motion. It is assumed that at the end of every advective step, each particle undergoes a random walk in two orthogonal directions. The standard deviation of these random walks must be compatible with the analytical Gaussian solution of pure diffusion and therefore the fluctuating random velocity components of a particle are written as

$$u_r = r_1\sqrt{2\nu/\Delta t}, \quad v_r = r_2\sqrt{2\nu/\Delta t}, \tag{2.26a, b}$$

where the subscript r indicates random component, ν and Δt are the isotropic diffusion coefficient and time step, respectively, and r_1 and r_2 are independent normally distributed random numbers each with zero mean and unit standard deviation (e.g. Borthwick & Barber, 1992).

Owing to the fact that the distribution of the random number generated velocity components will inherently be distorted by the mapping functions, the random walks are performed based on length of displacements in the physical domain instead of the computational domain. Equations (2.26) are thus rewritten as

$$\Delta\xi_r = u_r\Delta t, \quad \Delta\eta_r = v_r\Delta t, \tag{2.27a, b}$$

where u_r and v_r are the random velocity components in the ζ-plane. It follows that the crux of the method lies in the inverse mapping of the particle position at the end of each random walk in order to proceed with the Lagrangian tracking. As there are no closed form solutions of the inverse mapping functions for all three cases, namely the wavy wall, symmetrical and skew-symmetrical wavy channel, the corresponding particle position in the z-plane is iteratively solved based on the orientation and

magnitude of displacement which are kept conformal by the mapping functions. In order to maintain the validity of the statistical distribution, all particles are solved using the same time step, which is chosen to be small ($\Delta t = 0.001$) in order to minimise the non-physical tendency of particles in the numerical solutions to cross the flow boundary or penetrate the vortex core. The few particles which do start to cross the boundary are halted at the boundary itself whereas particles which enter the vacated vortex core are returned to their initial positions and subjected to a fresh attempt.

Figures 2.24b and 2.25b show the particle positions at the end of the tenth cycle for the symmetrical and skew-symmetrical wavy channels for $\nu = 0.001$. Increasing scatter with the magnitude of diffusion coefficient is evident when $\nu = 0.005$ is used (not shown). For the symmetrical wavy wall problem, cross centre-line mixing is now possible, resulting in qualitative mixing which resembles the effect produced by the skew-symmetrical wavy channel with zero diffusivity (Figure 2.25a. Introduction of diffusion by random walks causes the skew-symmetrical wavy channel to produce even better particle scatter, notably in the lateral direction. Figure 2.23b shows the standard deviation as a function of time when different diffusion coefficients are used for the skew-symmetrical wavy channel. The same is observed for the symmetrical wavy channel. The decrease of σ with increasing diffusion is counter-intuitive but well founded. In Figures 2.12b and 2.13b, it is shown that under the influence of an infinite number of vortical stirrers, a line of particles spreads further longitudinally, with particles at the rear predominantly engaged in hydrodynamic resonance, and particles at the front mainly undisturbed. Due to diffusion, particles at the rear are now more likely to escape from the vortex core and mixing zone to the free flow region, rejoining the bulk flow. On the other hand, particles at the front which are sufficiently distant from the vortex field at most instants may now be entrained due to diffusivity, or even penetrate the vortex core and become permanently trapped.

These particles then lag behind, reducing the number of particles in the leading front. The combined effect thus gives an overall reduction of σ which quantifies longitudinal particle dispersion. The observation is analogous to the relative diffusion of clouds of particles (Fischer *et al.*, 1979). Following the classical analysis of Taylor (1922) for ensemble mean concentration, Fischer *et al.* showed that, provided that the time from release is less than the Lagrangian time scale, an ensemble mean formed by averaging the concentration at points equidistant from the centre of mass of each cloud in the trial is higher than that formed by averaging the concentration at each point in space at identical times. This means that the size of the cloud is smaller and less dispersed along the direction of travel despite the presence of diffusion.

2.4.5 Active mixing

The preceding investigation focuses on passive tracers which are able to follow the physical flow behaviour and be transported with negligible influence on the flow regime regardless of the concentration. The tracers are inert and demonstrate no growth or decay in their course of motion. In practical conditions, however, passive tracers of distinct characteristics may exhibit chemical or biological interactions with the fluid and/or other constituents. In particular, auto-catalytic reactions are those in which at least one of the products is a reactant, and of which the rate equations are fundamentally nonlinear.

The simple auto-catalytic reaction $A + B \longrightarrow 2B$ in a chaotic flow regime was first investigated by Metcalfe & Ottino (1994) for flow in a bounded eccentric cylinder. Their work captured the growth and propagation of patterns in active mixing driven primarily by the highly interwoven nature of the manifold tangle. Toroczkai *et al.* (1998) and Károlyi *et al.* (1999) extended the study to open chaotic flow around a cylinder, and showed that the fractal unstable manifold in the wake of the cylinder acts as a catalyst for the process. A fractal object is highly ramified such that

its surface area (or perimeter in the case of two-dimensional object) is resolution-dependent. As a result, reactions occur only at the fractal boundary and mixing is imperfect. Budyansky *et al.* (2004) studied a simple two-dimensional open flow composed of a fixed point vortex and a background periodic current, and showed that the tracer dynamics is typically chaotic in the mixing region. The boundary of the vortex core acts as a dynamical trap for advected particles resulting in a fractal-like scattering function which depends on the trapping time. Indeed, the mixing problem considered herein is an open flow problem characterised by transient chaos and permanent fractality (Károlyi & Tél, 2007).

The study is now extended to active mixing where the non-escaping vortex core acts as the source of the reacting seed. The effect of the vortex dynamics on the overall mixing mechanism and efficiency will be investigated using the surface reaction theory of Károlyi *et al.* (1999).

2.4.5.1 Numerical implementation of auto-catalytic reaction

Consider the auto-catalytic reaction, $A+B \longrightarrow 2B$ in a wavy channel with an infinite number of vortices, where a single vortex core is selected to carry a finite number of seed particles B which are incapable of escaping. The incoming background flow constitutes the A particles, which will react and be transformed to B particles if they come within a prescribed reaction distance ϵ_0 from the existing B particles in the flow field. These B particles are produced in the mixing zone and are thus capable of being ejected from the vortex and advected downstream, reacting with other A particles they come in contact with.

One way numerically to simulate the above processes is to adopt a uniformly gridded domain with each cell being occupied by either type A or B particle, regardless of the actual number of particles present. If both species are present, then B always survives. At a prescribed reaction rate, the neighbouring cells of a cell occupied with B particles will be converted if they are not already B-type cell (e.g. Toroczkai *et al.*,

1998; Péntek *et al.*, 1999; Liang *et al.*, 2007*a*). After the reaction stage, the particles occupy the positions of their respective cell centres and resume passive advection until the next reaction sets in. The grid size must thus be less than or equal the reaction distance ϵ_0. In the present model, the uniform grid is constructed in the physical ζ-domain, and hence the corresponding grid points in the computational z-domain must first be established via inverse mapping. Both passive and active processes are computed entirely in the z-plane and mapping to the ζ-plane is performed for graphical purposes only.

An initial patch of 400 B-type particles is seeded inside the vortex core. A grid size of $\epsilon_0 = 0.05/\lambda$ is adopted, equivalent to 0.36% of the wall wavelength. The observation window covers five wavelengths, with the reacting vortex core in the first. The vortex motion always commences from its lower middle position (corresponding to the position at $t/T = 0.5$, in Section 2.4.3) for all reaction rates. For reaction rates shorter than the periodicity T of the vortex motion, an integer number of reactions per cycle is considered; for reaction rates longer than T, the reaction rate is taken to be an integer multiple of T. This ensures that the behaviour which is periodic with the period of the vortex motion appears as fixed points, or periodic cycles, on the stroboscopic map taken at the instant of the reaction (Károlyi *et al.*, 1999).

2.4.5.2 Fractal dimensions and reaction theory

Figure 2.26 shows the evolved B particles seeded in the symmetrical wavy channel considered at 2 reactions per cycle. Figure 2.26a shows that within the first half a cycle, species B grows in the vortex core but no particles have yet to escape the vortex field as it grows (refer Section 2.4.3.3). At the end of the first cycle, as the vortex sweeps down the trough at large velocity, a substantial amount of B particles drain along the wall. These particles are advected into the second trough and subsequently entrained by the vortex in the neighbouring trough (Figure 2.26b). The second vortex is eventually infected and acts as another source of the seed particles

(Figure 2.26c). As the process continues, accelerated reaction with the background A particles produces an increasing number of B particles which escape along the unstable manifold. A quasi-equilibrium state is eventually reached after 4 cycles where the number of B particles produced n_B is balanced by the number that have escaped from the observation window (Figure 2.27 inset). However, the vortex in the fifth trough does not operate as a reaction site, being surrounded by B particles. The above reaction rate is relatively low and B particles do not cross the centreline of the channel.

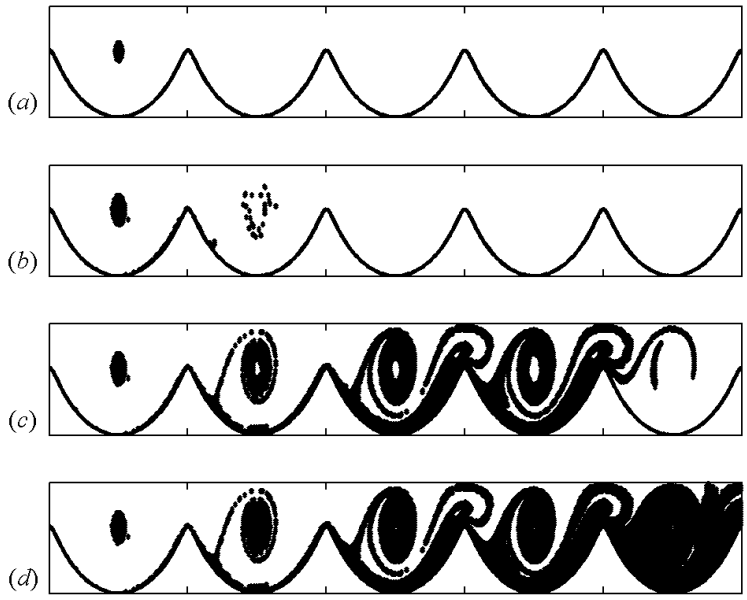

Figure 2.26: Evolved seed patch of reacting B particles in the symmetrical wavy channel at 2 reactions per cycle (η vs ξ, plots showing lower half of the channel only). (a-d) corresponds to $t/T = 0.5, 2.5, 4.5$, and 8.5, respectively, where initial vortex position ($t/T = 0$) is at its nearest to the wall.

The structure observed in Figure 2.26 clearly resembles the unstable manifold shown in Figure 2.21. Amongst others, Károlyi *et al.* (1999) have found that active particles trace out the unstable manifold but with wider coverage due to the advancing reaction process. This means that the reactions occur on the surface of the fattened-up unstable manifold of the chaotic saddle, which has a fractal appearance with filamental structures. Although the chaos is transient in the mixing region, the fractal

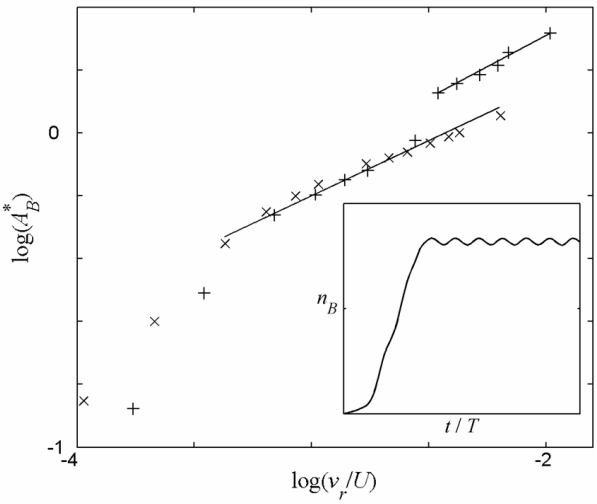

Figure 2.27: Power scaling law of the steady-state reactant front area: + symmetrical channel; × skew-symmetrical channel. Inset showing typical temporal growth of the population of B-particles inside the observation window.

pattern traced out by the reactions is permanent and can be quantified with a fractal dimension D_0 (Péntek *et al.*, 1999). Furthermore, this fractal dimension is the same as that of the unstable manifold in the reaction-free flow.

The continuous reaction equation for an auto-catalytic reaction in an open flow proposed by Károlyi *et al.* (1999) is

$$\dot{A}_B = -kA_B + g_e(t)(2 - D_0)v_r A_B^{-\beta}, \tag{2.28}$$

where A_B is the area covered by the reacting B-particles within the observation window, k is the escape rate of the particles, $g_e(t)$ is a geometrical factor containing information on the unstable manifold, v_r is the reaction front velocity ($= 2\epsilon_0/t$), and t being the lag time between reactions. The positive exponent β is defined as $(D_0 - 1)/(2 - D_0)$, with $1 < D_0 < 2$. The first and second terms on the right hand side of (2.28) describe the escape and the production, respectively, of the B-particles. If the reaction takes place on a simple non-fractal line, i.e. $D_0 = 1$, then $\beta = 0$ and (2.28) reduces to classical surface reaction (Landau & Lifshitz, 1987). In chaotic open flow, the boundary of the unstable manifold is fractal, where $D_0 > 1$. Consequently,

the reaction described by (2.28) is dissipative and possesses an attractor. Solving for the steady solution ($\dot{A}_B = 0$), there is a trivial unstable equilibrium if $A_B^* = 0$ or

$$A_B^* = [g_e v_r (2 - D_0)/k]^{(2-D_0)}. \tag{2.29}$$

Equation (2.29) describes the steady state condition achieved when the newborn and escaping particles are balanced. The fractal dimension D_0 can be easily determined because the slope of the log-log plot of A_B^* vs v_r is $(2 - D_0)$ (Figure 2.27).

Reaction rates ranged from 1/2 to 30 reactions per cycle for both the symmetrical and skew-symmetrical wavy channel (Figure 2.27). The area occupied by the B particles is simply given by $n_B \epsilon_0^2$. Plotting the same data in Figure 2.27 using normal scale (not shown), extrapolation gives zero B particles as the reaction front velocity reduces to zero. There is a linear increase of B particles up to 2 reactions per cycle, beyond which the production rate decreases due to competition from the particle escape rate from the observation window. For a reaction rate $\leq$ one per cycle, the reactions take place at a fixed site, corresponding to the initial position of the vortex at the middle lowest of the vortex trajectory. Should the reaction site be changed, different results are obtained. This corresponds to the zone $v_r/U < 3.5 \times 10^{-4}$ in Figure 2.27. Sensitivity checks confirm that the selection of reaction site has negligible effect on the resulting area occupied for reaction rates ≥ 2 per cycle, which constitutes our region of interest. The fractal dimension D_0 in this region is approximately 1.65, which implies that the reaction rate is slow on the characteristic scale of chaotic advection and verifies the singular enhancement of productivity (Toroczkai *et al.*, 1998; Károlyi *et al.*, 1999). It is interesting to note that for reaction rate ≥ 10 per cycle, the symmetrical channel shows a sudden increase of A_B^* and thus an offset in Figure 2.27. This region of higher reaction rates has a fractal dimension of 1.60 which is slightly different from the intermediate reaction rate. The augmentation of the area covered can be attributed to the entrainment of B particles by the vortex at the

opposite wall immediately after the particles cross the converging part of the channel and are confronted by the swelling separation bubble (Figure 2.28a). The opposite vortex core is eventually infected and as a consequence, more troughs are completely filled with B particles when the quasi-equilibrium state is attained (Figure 2.28b). In the skew-symmetrical channel, despite the fact that B particles regularly visit the opposite side of the channel, they are not entrained. Figure 2.28c shows the B particles intrude into the upstream end of the upper trough when the vortices at the lower wall are at their rightmost positions. At this instant, the upper vortex fields are also located at the rightmost positions near the downstream end of the troughs. As a result, the particles do not encroach into the upper vortex field. At the next instant, the protruding B particles are drawn back by the lower vortices when the vortices at both upper and lower walls sweep down the wall (counter clockwise and clockwise, respectively), and the separation bubble contracts. Similarly, when the lower vortices are at their leftmost positions, the B particles intrude the downstream end of the upper trough (not shown). During the same instant, the upper vortices are also located at their leftmost positions, i.e. the vortex fields are near the upstream end of the troughs, unable to entrain the B particles at the opposite end. Hence, in the absence of the dynamics induced by the converging-diverging flow field, the serpentine-type skew-symmetrical channel maintains a boundary between the A and B particles on the upper and lower walls, respectively, for reaction rates up to 30 per cycle.

It is interesting to note that the fractal dimension obtained above shows grid independence when a coarser cell of size $0.1/\lambda$ is used. Moreover, the simulations are at the limit of weak diffusion, where the reaction range is of the same order as the diffusion distance for $\nu = 0.005$ (Section 2.4.4.2). Tél *et al.* (2000) showed that weak diffusion in such models only renormalizes the effect of reaction velocities. Essentially, chaotic characteristics, which should be treated as averages over sufficiently long

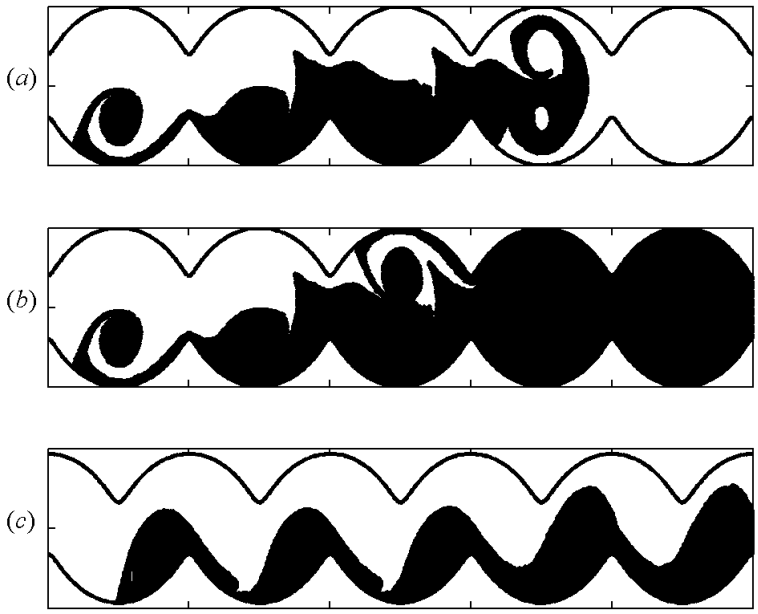

Figure 2.28: Evolved seed patch of reacting B particles at 20 reactions per cycle (η vs ξ) for: symmetrical wavy channel (a) $t/T = 2.5$, (b) $t/T = 4.5$; and (c) skew-symmetrical wavy channel at $t/T = 3.75$. Initial vortex positions ($t/T = 0$) are at their nearest to the wall.

time, can be similarly defined for an ensemble of diffusive particles, owing to the fact that an exact fractal scaling holds without any lower cut-off due to noise in spite of randomness.

For two-dimensional hyperbolic open systems, the fractal dimension can be related to the escape rate k and the Lyapunov exponent λ_n via (Tél *et al.*, 2005)

$$D_0 = 2 - k/\lambda_n. \tag{2.30}$$

For a quantitative characterisation of the escape rates, the ensemble of particles in Figures 2.24 and 2.25 is monitored to determine the fraction n retained within the trough of their origin as a function of time. In both cases, exponential decay is observed and can be fitted with the correlation $n \sim exp(-kt)$, giving $k \sim 0.031$ and 0.030 for the symmetrical and skew-symmetrical channel, respectively. Exponential decay of material from an eddy in a wavy corrugation has been verified experimentally for a range of flow parameters by Wierschem & Aksel (2004). The Lyapunov exponent,

which gives the rate of stretching of nearby particles, is measured by starting a test particle close to that of a reference trajectory with an initial distance of $\delta = 10^{-5}/\lambda$. Whenever the distance of the test particle from the reference trajectory is larger than a threshold value of 10δ, it is shifted back to a distance δ from the reference trajectory along the line which connects them. The number of times n_s this is performed thus provides an estimate of the Lyapunov exponent λ_n along the reference trajectory (Neufeld & Tél, 1998). The spatial distribution of λ_n is highly varied, being positive in the mixing region but vanishing in the regular region within the vortex core (Babiano *et al.*, 1994; Neufeld & Tél, 1998). Using a large number of randomly selected reference trajectories (not taking into consideration those which are permanently trapped by the vortex cores), the largest λ_n for the symmetrical and skew-symmetrical channel are obtained as 0.084 and 0.085, respectively. Using equation (2.30), the fractal dimensions of the symmetrical and skew-symmetrical channel are thus calculated as 1.63 and 1.65, which are in good agreement with the values obtained from Figure 2.27. It may thus be concluded that hyperbolicity plays a crucial role in the dynamics of the present problem outside the stable region, where almost all initial conditions lead to orbits that eventually escape the mixing region at exponential rate. The vortex core, nonetheless, gives rise to non-hyperbolicity and is characterised by space-filling fractality ($D_0 = 2$) (e.g. Lau *et al.*, 1991; Motter *et al.*, 2003; de Moura & Grebogi, 2004).

2.5 Concluding remarks

Open flow in channels where the mixing process is induced primarily by unsteady motion of point vortices located in the trough region of the wavy wall has been considered. Assuming two-dimensional irrotational, incompressible flow, equations of motion for the vortices and the particles were derived. Their instantaneous positions were tracked using the Lagrangian technique and conformally mapped to the physical domain. Perturbation analysis indicates that the frequency of vortex motion is weakly dependent on the wall amplitude but that a characteristic Strouhal number $\omega/UK \sim 0.25$ occurs for a wide range of input parameters. The analytical and numerical vortex paths agree well for small perturbation. It is found that the vortex trajectory is governed mainly by its image, with little effect arising from the presence of neighbouring vortices along the wavy wall or channel.

The particle trajectories and snapshots reveal the stretching and folding processes, and increasing scattering that characterise chaotic motion. Particles seeded within the separation bubble are observed to escape from the trough (hence the vortex), primarily during the first oscillation cycle. A major fraction of the particles retained is made up of those seeded at close proximity to the singular point, a stable region which constitutes a 'core' surrounding and shielding the vortex singularity. Significant mass exchange takes place between particles inside and outside the separation bubble, forming a chaotic-sea-of-mixing region which evolves in size as the vortex moves. This can be attributed to the spiral nature of the invariant manifolds in the perturbed system, which produces infinite self-similar criss-crossing tangles at all scales responsible for the material exchange. The resulting dynamics are in good qualitative agreement with previously reported solutions of the unsteady Navier–Stokes equations for a wavy channel with oscillatory unidirectional flow.

Statistical evaluation of the particle positions shows that the skew-symmetrical wavy channel is more efficient in passive mixing than a symmetrical wavy channel.

Incorporating the effect of diffusion via gridless random walk increases lateral particle dispersion significantly despite a marked reduction in the standard deviation of the longitudinal particle positions.

Using the non-escaping vortex core as a source of reacting particles, auto-catalytic reaction in the wavy channel is studied. The results verify that the unstable manifold acts as an effective catalyst for the process. Fractal enhancement of productivity ($D_0 \approx 1.65$) is identified. The symmetrical wavy channel shows augmentation of area covered by the B particles at high reaction rates due to infection of the vortices at the opposite wall. The fractal dimensions obtained correlate well to the escape rates and the Lyapunov exponents if only the hyperbolic dynamics is considered. Non-hyperbolicity is present but is confined to the stable region within the vortex core.

For the purpose of the present research, the above problem has allowed various analytical tools unique in the study of dynamical systems and chaos to be deployed successfully, when examining chaotic phenomena in a relatively simple flow field. Using the two-layer shallow flow model presented in Chapter 3, the flow field obtained for a shallow water body under external forcing will be used for the purpose of Lagrangian particle tracking and the corresponding results analysed using the tools developed herein. The work reported in this chapter is published in Lee *et al.* (2010*b*).

Chapter 3

Adaptive two-layer shallow water model (A2L-SWM)

3.1 Introduction and literature review

The Navier–Stokes (N–S) equations are assumed to provide a complete description of continuum fluid motion. However, since the equations are inherently nonlinear, analytical solutions are available only for few special cases. Furthermore, direct numerical simulations based on the N–S equations are computationally expensive as they involve treatment of incompressibility, with free surface flows requiring sophisticated algorithms to cope with the nonlinear boundary conditions. For a flow domain where the vertical scale is small compared to the horizontal scale such that the external forcing acting on the free surface and the bed topography can be assumed to apply uniformly throughout the entire water column, relatively simpler equations can be derived from the N–S equations by Reynolds-type time averaging, followed by depth-integration, resulting in the shallow water equations (SWEs). Jirka & Uijttewaal (2004), amongst others, define shallow flows to be largely unidirectional turbulent shear flows driven by a piezometric gradient in a confined layer. The layer confinement leads to a separation of turbulent motions between small scale 3D turbulence, and large scale 2D turbulent motions with some mutual interaction. Owing to their relative simplicity in numerical implementation compared to the full N–S equations,

the SWEs have become a popular choice for representing a range of predominantly horizontal free surface flows such as occur in shallow lakes, wide rivers, the coastal zones, estuaries, other geophysical domains, oceans and the atmosphere.

The past 10 years have seen rapid development in two-layer shallow water models (2L-SWM), aimed at representing near-horizontal flows that have a pronounced two-layer vertical structure with a distinct density difference between the layers. Although there may be no exact separation interface between the layers, the two-layer approximation offers considerable computational advantage in resolving the fluid mechanical behaviour of such flows for practical engineering purposes when compared to numerical solvers based on the full Navier–Stokes equations. Examples of two-layer flow phenomena include fresh water intruding upon denser sea water, mud flow or debris flow beneath water, and circulation in a stratified ocean or lake.

An early attempt to model the two-layer shallow flow problem was reported by Vreugdenhil (1979) who formulated a set of differential shallow water equations in weak-interaction form. Ignoring mixing between the layers, the surface and internal waves were solved using separate grids due to the order of magnitude difference in propagation speed between waves on the free surface and at the density interface. Castro *et al.* (2001) showed that, in general, numerical schemes obtained by independent upwindings of each layer of the two-layer shallow water model are unconditionally unstable. The difficulty arises due to the coupling of momentum between the layers, which involves certain derivatives of the dependent variable. Castro *et al.* (2001) introduced a fully coupled two-layer shallow water model for flow in a straight rectangular channel where the flux and coupling terms are treated together by using a generalized Roe linearization scheme. The scheme was later extended to a straight channel with irregular geometry (Castro *et al.*, 2004, 2007*a*), and implemented in two-dimensions by considering a projected Riemann problem along the normal direction at every intercell (Castro *et al.*, 2006*b*).

Owing to the non-linear coupling between the layers, the system eigenvalues of a two-layer shallow water model have to be evaluated numerically by schemes which utilise characteristic decomposition, such as the Roe-type method. This increases significantly the computational cost of a two-layer shallow water model. In order to avoid the calculation of the system eigenvalues, various strategies have been employed which allow explicit access to the eigenstructure of the modified system, typically using only partial information of the complete wave structure. Examples include operator splitting (Salmon, 2002), Strang splitting (Chen & Peng, 2006; Chen *et al.*, 2007), a relaxation method (Abgrall & Karni, 2009), and a Riemann-problem-solver-free Godunov-type scheme (Kurganov & Petrova, 2009). However, owing to the fact that the internal eigenvalues are usually much smaller than the external ones, it is worth noting that first order numerical schemes that use only the extreme left-going and right-going propagating speeds are in general too diffusive for the simulation of internal waves (Fernández-Nieto *et al.*, 2011).

Another problem associated with the system eigenvalues is that, in the event the system approaches a critical point, at least one of the eigenvalues can become very small, thus causing the system to lose accuracy, with errors that propagate up and downstream. In order to overcome this difficulty, numerical viscosity can be added to the system when close to vanishing internal eigenvalues are detected. Popular choices include Harten regularization (Castro *et al.*, 2001, 2004, 2005, 2007*a*), and the Harten-Hyman entropy fix (Castro *et al.*, 2006*a*; Parés & Castro, 2004). Other researchers have used an explicit viscosity term (Vreugdenhil, 1979; Salmon, 2002). Both Harten regularization (Harten, 1984) and the Harten-Hyman entropy fix (Harten & Hyman, 1983) involve the use of parameters whose values must be tuned empirically on a case by case basis. Chacón-Rebollo *et al.* (2003) introduced an alternative entropy-correction-free solver which is based on the construction of an equivalent parabolic system of partial differential equations (PDEs) from the original hyperbolic PDEs. A

numerical correction term is added so that all smooth steady solutions of the original system are also solutions of the equivalent system. The scheme is well-balanced and satisfies the C-property such that smooth steady solutions are second order accurate. This approach was successfully applied to a two-layer shallow water model by Chacón-Rebollo *et al.* (2004), and extended to a general non-homogeneous hyperbolic system of equations with non-conservative terms by Castro *et al.* (2007*b*).

The idea of the C-property in the context of SWEs was first introduced by Bermúdez & Vázquez-Cendón (1994) for problems where the numerical scheme is required to calculate exactly at grid nodes the stationary solution corresponding to water at rest. For non-homogeneous hyperbolic systems of conservation laws this is of particular importance. Otherwise, large errors in the numerical solution, in particular, to the wave speed, may result in unphysical solutions (Roe, 1986). An extension of the C-property to a more general condition was introduced by Greenberg & Leroux (1996), with the concept of a 'well-balanced' scheme which preserves all equilibria of the system at the grid nodes. The challenge is to balance properly the flux gradient and source terms in the hyperbolic equation system. Numerous approaches have since been reported in the literature and continuously improved (LeVeque, 1998; Vázquez-Cendón, 1999; Zhou *et al.*, 2001; Rogers *et al.*, 2001, 2003; Audusse *et al.*, 2004). In particular, the algebraic approach of Rogers *et al.* (2001, 2003) use a deviatoric form of the shallow water equations that identically balances the set of hyperbolic equations without the need of additional computational effort. This would be appealing for the two-layer shallow water model which already demands higher computational resources due to layer coupling. Unfortunately, the algebraic balancing technique cannot be extended to a two-layer shallow water model in the presence of interface perturbation due to the effect of an additional term associated with the layer coupling which violates the well-balanced property (see Section 3.4). The motivation of the present study is to implement an adaptive grid algorithm that increases the

computational efficiency of a Roe-type two-dimensional shallow water model.

Well-balanced schemes have also been presented for applications involving wetting and drying (Brufau *et al.*, 2002; Begnudelli & Sanders, 2006; Liang & Borthwick, 2009). For a two-layer shallow water model, the wet-dry front treatment needs to consider the disappearance of either or both the layers. Castro *et al.* (2005) used an extended C-property to handle this wet-dry transition. The approach was further improved by Castro *et al.* (2006*c*) who considered a non-linear Riemann problem instead of a linear one.

High order solvers of the two-layer shallow water equations were first reported by Castro *et al.* (2006*a*) for well balanced coupled systems of conservation laws with source terms in one-dimension. This approach, which is based on reconstruction of states, has been subsequently extended to two-dimensions using the original Roe scheme (Castro *et al.*, 2009) and an ADER scheme (Dumbser *et al.*, 2009).

3.2 Governing equations

Consider a hyperbolic system with non-conservative products and source terms. The partial differential equations governing the two-dimensional flow of two superposed immiscible layers of shallow water fluids are written as

$$\mathbf{W}_t + \mathbf{F}_1(\mathbf{W})_x + \mathbf{F}_2(\mathbf{W})_y = \mathbf{B}_1(\mathbf{W})\mathbf{W}_x + \mathbf{B}_2(\mathbf{W})\mathbf{W}_y + \mathbf{S}_1(x,\mathbf{W}) + \mathbf{S}_2(y,\mathbf{W}), \quad (3.1)$$

where the subscripts x, y and t denote partial derivatives with respect to the $x-$direction, $y-$direction, and time. The vector of unknowns, $\mathbf{W}$, the flux function vectors, $\mathbf{F}_1$ and $\mathbf{F}_2$, and the source term vectors which describe the variable bed topography, $\mathbf{S}_1$ and $\mathbf{S}_2$ are defined below:

$$\mathbf{W} = \mathbf{W}(x,y,t) = \begin{bmatrix} W_1(x,y,t) \\ W_2(x,y,t) \end{bmatrix}, \quad W_j = \begin{bmatrix} h_j \\ q_{x,j} \\ q_{y,j} \end{bmatrix}, \quad (3.2)$$

$$\mathbf{F}_1(\mathbf{W}) = \begin{bmatrix} F_{1,1}(W_1) \\ F_{1,2}(W_2) \end{bmatrix}, \quad F_{1,j}(W_j) = \begin{bmatrix} q_{x,j} \\ q_{x,j}^2/h_j + \frac{1}{2}gh_j^2 \\ q_{x,j}q_{y,j}/h_j \end{bmatrix}, \tag{3.3}$$

$$\mathbf{F}_2(\mathbf{W}) = \begin{bmatrix} F_{2,1}(W_1) \\ F_{2,2}(W_2) \end{bmatrix}, \quad F_{2,j}(W_j) = \begin{bmatrix} q_{y,j} \\ q_{x,j}q_{y,j}/h_j \\ q_{y,j}^2/h_j + \frac{1}{2}gh_j^2 \end{bmatrix}, \tag{3.4}$$

$$\mathbf{S}_1(x, \mathbf{W}) = \begin{bmatrix} S_{1,1}(x, W_1) \\ S_{1,2}(x, W_2) \end{bmatrix}, \quad S_{1,j}(x_j, W_j) = \begin{bmatrix} 0 \\ -gh_j b(x,y)_x \\ 0 \end{bmatrix}, \tag{3.5}$$

$$\mathbf{S}_2(y, \mathbf{W}) = \begin{bmatrix} S_{2,1}(y, W_1) \\ S_{2,2}(y, W_2) \end{bmatrix}, \quad S_{2,j}(y_j, W_j) = \begin{bmatrix} 0 \\ 0 \\ -gh_j b(x,y)_y \end{bmatrix}, \tag{3.6}$$

and the matrices $\mathbf{B}_1$ and $\mathbf{B}_2$ are

$$\mathbf{B}_1(\mathbf{W}) = \begin{bmatrix} 0 & B_{1,1}(W_1) \\ B_{1,2}(W_2) & 0 \end{bmatrix}, \quad \mathbf{B}_2(\mathbf{W}) = \begin{bmatrix} 0 & B_{2,1}(W_1) \\ B_{2,2}(W_2) & 0 \end{bmatrix}, \tag{3.7}$$

where

$$B_{1,1}(W_1) = \begin{bmatrix} 0 & 0 & 0 \\ -gh_1 & 0 & 0 \\ 0 & 0 & 0 \end{bmatrix}, \quad B_{1,2}(W_2) = \begin{bmatrix} 0 & 0 & 0 \\ -rgh_2 & 0 & 0 \\ 0 & 0 & 0 \end{bmatrix}, \tag{3.8}$$

and

$$B_{2,1}(W_1) = \begin{bmatrix} 0 & 0 & 0 \\ 0 & 0 & 0 \\ -gh_1 & 0 & 0 \end{bmatrix}, \quad B_{2,2}(W_2) = \begin{bmatrix} 0 & 0 & 0 \\ 0 & 0 & 0 \\ -rgh_2 & 0 & 0 \end{bmatrix}. \tag{3.9}$$

The flow rate components $q_{x,j}(x, y, t)$ and $q_{y,j}(x, y, t)$ and the layer thickness $h_j(x, y, t)$ are the dependent variables, $b(x, y)$ is the bed profile measured from a fixed reference horizontal datum. The subscript j denotes the layers, where index 1 refers to the upper layer and index 2 refers to the lower layer, such that ρ_1 and ρ_2 are the constant densities of the respective layer and $r = \rho_1/\rho_2 < 1$, and g is the gravity acceleration.

The system matrix, to be evaluated at a chosen 'intermediate state', is given by

$$\mathbf{A}(\mathbf{W}) = \begin{bmatrix} A_1(W_1)n_x + A_2(W_1)n_y & -B_{1,1}(W_1)n_x - B_{2,1}(W_1)n_y \\ -B_{1,2}(W_2)n_x - B_{2,2}(W_2)n_y & A_1(W_2)n_x + A_2(W_2)n_y \end{bmatrix}, \tag{3.10}$$

where $\mathbf{n} = (n_x, n_y)$ is the unit vector. Here, $A_1(W_j)$ and $A_2(W_j)$ are Jacobian matrices of each respective layer, and defined as

$$A_1(W_j) = \frac{\partial F_{1,j}}{\partial W_j} = \begin{bmatrix} 0 & 1 & 0 \\ c_j^2 - u_j^2 & 2u_j & 0 \\ -u_j v_j & v_j & u_j \end{bmatrix}, \quad A_2(W_j) = \frac{\partial F_{2,j}}{\partial W_j} = \begin{bmatrix} 0 & 0 & 1 \\ -u_j v_j & v_j & u_j \\ c_j^2 - v_j^2 & 0 & 2v_j \end{bmatrix}, \tag{3.11}$$

where $u_j = q_{x,j}/h_j$, $v_j = q_{y,j}/h_j$, and $c_j^2 = gh_j$.

The system is assumed strictly hyperbolic, i.e. there are 6 distinct eigenvalues in the x- and y-direction, respectively, such that the corresponding eigenvectors are linearly independent. Two of the eigenvalues are given by $\lambda_{1,2} = U_j$ for $j = 1, 2$ where $U_j = u_j n_x + v_j n_y$ is the velocity across the cell face in the respective layer. Another four eigenvalues can be determined from the characteristic equation derived from the matrix (3.10):

$$(\lambda^2 - 2U_1\lambda + U_1^2 - gh_1)(\lambda^2 - 2U_2\lambda + U_2^2 - gh_2) = rg^2 h_1 h_2. \tag{3.12}$$

For $r \ll 1$, the eigenvalues of the system (3.1) approach those of each layer. In particular, when $r = 0$, the eigenvalues exactly correspond to each layer ($U_j \pm \sqrt{gh_j}$) and thus the coupling terms essentially do not affect the nature of the system. Our interest, however, lies in the case when $r \approx 1$, which is commonly encountered in coastal flows and estuaries. In this case, the first order approximation of the eigenvalues can be written as (Schijf & Schonfeld, 1953):

$$\lambda_{3,4} = V_m \pm \sqrt{g(h_1 + h_2)}, \tag{3.13}$$

and

$$\lambda_{5,6} = V_c \pm \sqrt{\frac{g' h_1 h_2}{h_1 + h_2}\left(1 - \frac{(U_2 - U_1)^2}{g'(h_1 + h_2)}\right)}, \tag{3.14}$$

where $g' = g(1 - r)$ is the reduced gravity. The mean velocity V_m and the convective velocity V_c (Castro *et al.*, 2001) are given, respectively, by

$$V_m = \frac{h_1 U_1 + h_2 U_2}{h_1 + h_2}, \quad V_c = \frac{h_1 U_2 + h_2 U_1}{h_1 + h_2}. \tag{3.15}$$

The external eigenvalues $\lambda_{3,4}$ and the internal eigenvalues $\lambda_{5,6}$ are related, respectively, to barotropic and baroclinic components of the flow, noting that the internal eigenvalues have much lower values because $g' \ll 1$ when $r \approx 1$. If the solution has four different real eigenvalues, the flow is stable and the system is hyperbolic. This requires the following approximate condition to be satisfied

$$\frac{(U_2 - U_1)^2}{g'(h_1 + h_2)} < 1. \tag{3.16}$$

Violation of condition (3.16) means that the system loses its hyperbolicity, a situation associated with the appearance of Kelvin-Helmholtz instabilities at the layer interface. In real flow, this corresponds to intense mixing between the layers which dissipates energy and results in an exchange of momentum, a phenomenon which is not compatible with an immiscible-layer model. Numerically, such a disturbance will grow and eventually overwhelm the solution unless a viscous effect is added. Note also that the system is not strictly hyperbolic for the limiting case when $r = 1$, where there are only three real distinct eigenvalues. Note that a two-layer flow of identical densities reduces to a system of three equations which comprise the continuity and momentum equations for a single layer, and a decoupled transport equation for the ratio of the lower layer thickness to the total thickness (Chen *et al.*, 2007).

3.3 Numerical scheme for the 1D and 2D shallow water model

For the ease of presentation, consider the one-dimensional form of the hyperbolic system (3.1):

$$\mathbf{W}_t + \mathbf{F}(\mathbf{W})_x = \mathbf{B}(\mathbf{W})\mathbf{W}_x + \mathbf{S}(x, \mathbf{W}), \tag{3.17}$$

which can be written in quasilinear form:

$$\mathbf{W}_t + \mathbf{A}(\mathbf{W})\mathbf{W}_x = \mathbf{S}(x, \mathbf{W}), \tag{3.18}$$

where

$$\mathbf{A}(\mathbf{W}) = \frac{\partial \mathbf{F}(\mathbf{W})}{\partial \mathbf{W}} - \mathbf{B}(\mathbf{W}). \tag{3.19}$$

Using the original ideas of Chacón-Rebollo *et al.* (2003, 2004) and Castro *et al.* (2007*b*), a standard upwind finite volume discretization of the two-layer shallow water system (3.17) which has the form of a general non-homogeneous non-conservative hyperbolic system can be interpreted as being a second-order centred approximation of an equivalent parabolic system:

$$\mathbf{W}_t + \mathbf{F}(\mathbf{W})_x - \nu \left(|\mathbf{D}(\mathbf{W})|\mathbf{W}_x\right)_x = \mathbf{B}(\mathbf{W})\mathbf{W}_x + \mathbf{S}(x, \mathbf{W}), \tag{3.20}$$

where $\mathbf{D}$ is the upwind matrix known here as the characteristic diffusion of the scheme, and $\nu = \Delta x/2$. Chacón-Rebollo *et al.* (2003) proposed to add a numerical source term $\mathbf{C}(x, \mathbf{W})$ to (3.20),

$$\mathbf{W}_t + \mathbf{F}(\mathbf{W})_x - \nu \left(|\mathbf{D}(\mathbf{W})|\mathbf{W}_x\right)_x = \mathbf{B}(\mathbf{W})\mathbf{W}_x + \mathbf{S}(x, \mathbf{W}) + \mathbf{C}(x, \mathbf{W}), \tag{3.21}$$

such that the centred approximation (in space) of the terms on the right-hand-side in (3.21), will solve (up to second order) all equilibria solutions, which are also the solutions of (3.17), and similarly any higher order approximations.

From (3.17), a smooth stationary solution $\mathbf{W}$ verifies

$$\mathbf{F}(\mathbf{W})_x = \mathbf{B}(\mathbf{W})\mathbf{W}_x + \mathbf{S}(x, \mathbf{W}). \tag{3.22}$$

Hence, if (3.21) approximates (3.17), it is required that the correction term $\mathbf{C}$ exactly balances the diffusion term in (3.20):

$$\mathbf{C}(x, \mathbf{W}) = -\nu \frac{\partial}{\partial x} \left(|\mathbf{D}(\mathbf{W})|\mathbf{W}_x\right). \tag{3.23}$$

Using equation (3.18), and provided that the system matrix $\mathbf{A}$ is non-singular, we have

$$\mathbf{W}_x = \mathbf{A}^{-1}(\mathbf{W})\mathbf{S}(x, \mathbf{W}). \tag{3.24}$$

Therefore, the correction term may be expressed as

$$\mathbf{C}(x,\mathbf{W}) = -\nu\frac{\partial}{\partial x}\left(|\mathbf{D}(\mathbf{W})|\mathbf{A}^{-1}(\mathbf{W})\mathbf{S}(x,\mathbf{W})\right). \tag{3.25}$$

Equation (3.21) can now be written, after rearrangement, as

$$\mathbf{W}_t + \Phi(x,\mathbf{W})_x = \mathbf{B}(\mathbf{W})\mathbf{W}_x + \mathbf{S}(x,\mathbf{W}), \tag{3.26}$$

where $\Phi(x,\mathbf{W})$ is the modified flux given by

$$\Phi(x,\mathbf{W}) = \mathbf{F}(\mathbf{W}) - \nu|\mathbf{D}(\mathbf{W})|\left(\mathbf{W}_x - \mathbf{A}^{-1}(\mathbf{W})\mathbf{S}(x,\mathbf{W})\right). \tag{3.27}$$

Equation (3.26) can be interpreted as providing a viscous approximation to the modified system (3.21). The correction term is essentially a modification to the numerical flux and does not affect the diffusion term. In this thesis, the numerical viscosity approach originally applied in the one-dimensional two-layer shallow water model by Chacón-Rebollo *et al.* (2003, 2004) and Castro *et al.* (2007*b*) is extended to the two-dimensional system described in Section 3.2. The system of equations to solve can thus be written:

$$\mathbf{W}_t + \Phi_1(x,\mathbf{W})_x + \Phi_2(y,\mathbf{W})_y = \mathbf{B}_1(\mathbf{W})\mathbf{W}_x + \mathbf{B}_2(\mathbf{W})\mathbf{W}_y + \mathbf{S}_1(x,\mathbf{W}) + \mathbf{S}_2(y,\mathbf{W}), \tag{3.28}$$

where

$$\Phi_1(x,\mathbf{W}) = \mathbf{F}_1(\mathbf{W}) - \nu|\mathbf{D}_1(\mathbf{W})|\left(\mathbf{W}_x - \mathbf{A}_1^{-1}(\mathbf{W})\mathbf{S}_1(x,\mathbf{W})\right), \tag{3.29}$$

and

$$\Phi_2(y,\mathbf{W}) = \mathbf{F}_2(\mathbf{W}) - \nu|\mathbf{D}_2(\mathbf{W})|\left(\mathbf{W}_y - \mathbf{A}_2^{-1}(\mathbf{W})\mathbf{S}_2(y,\mathbf{W})\right). \tag{3.30}$$

Chacón-Rebollo *et al.* (2003) proposed that the inverse of matrix $\mathbf{A}(\mathbf{W})$ (3.10) be defined differently in the neighbourhood of a critical point as follows:

$$\mathbf{A}^{-1}(\mathbf{W}) = \mathbf{X}(\mathbf{W})\mathbf{\Lambda}^{-1}(\mathbf{W})\mathbf{X}^{-1}(\mathbf{W}), \tag{3.31}$$

where $\mathbf{\Lambda}$ is the diagonal matrix whose coefficients are the system eigenvalues, $\mathbf{X}(\mathbf{W})$ is the corresponding matrix whose columns are the system eigenvectors, and

$$\mathbf{\Lambda}^{-1}(\mathbf{W}) = \mathrm{Diag}(\lambda_\iota^{-1}), \quad \lambda_\iota^{-1} = \begin{cases} 1/\lambda_\iota & \text{if} \quad |\lambda_\iota| > \epsilon \\ 0 & \text{if} \quad |\lambda_\iota| \leq \epsilon \end{cases} . \tag{3.32}$$

Here λ_ι are the system eigenvalues (numbering 4 and 6 in the one- and two-dimensional model, respectively), and ϵ is a small parameter. The redefinition of $\mathbf{A}^{-1}(\mathbf{W})$ ensures that instability caused by the vanishing eigenvalues of the upwind matrix cannot propagate upstream and thus no specific entropy correction is needed near any critical point.

Chacón-Rebollo *et al.* (2004) described the scheme above as being 'asymptotically well-balanced' in the sense that the steady solutions, which need not be known a *priori*, are computed up to second order throughout the domain except those on a set whose measure tends to zero as Δx tends to zero. Specifically, the numerical flux and the numerical diffusion of the scheme are separately balanced by the centred part and the non-centred part of the numerical source term, independent of the discretization parameter (see Section 3.3.1) appearing in each of them. Computationally, the behaviour of the scheme is similar to that of Roe's method. The technique can be applied to any general scheme which can be formulated as an artificial viscosity method.

Castro *et al.* (2007*b*) present several choices for the diffusion matrix $\mathbf{D}(\mathbf{W})$, which is essentially a free parameter. Hence, the scheme readily admits both flux-splitting and flux-difference or Roe methods as particular cases. Chacón-Rebollo *et al.* (2003) describe a hybrid flux-difference–flux-splitting scheme, which allows supercritical conditions to be captured and avoids the propagation of spurious oscillations without excessive diffusion. In the present work, the following definition is chosen:

$$\mathbf{D}(\mathbf{W}) = \mathbf{X}(\mathbf{W})\mathbf{\Lambda}(\mathbf{W})\mathbf{X}^{-1}(\mathbf{W}), \tag{3.33}$$

and

$$|\mathbf{D}(\mathbf{W})| = \mathbf{X}(\mathbf{W})|\mathbf{\Lambda}(\mathbf{W})|\mathbf{X}^{-1}(\mathbf{W}). \tag{3.34}$$

3.3.1 One-parameter discretization of the system

In this section, the general discretization of the two-layer shallow water equations by means of a finite volume scheme is presented. The computational domain is divided into M finite volumes, each comprising a square cell where $\Delta y = \Delta x$. By default, each cell i has four cell faces $\Gamma_k, k = 1, 4$. In this section, a regular grid is assumed. A regular three-point discretization of the system (3.28) yields:

$$\mathbf{W}_i^{n+1} = \mathbf{W}_i^n + \frac{\Delta t}{\Delta x}\left\{[(\Phi_W - \Phi_E) + (\Phi_S - \Phi_N)] + \frac{1}{2}\sum_{k=1}^{4}[\mathbf{B}_{\Gamma_k}\Delta W_{\Gamma_k} + \mathbf{S}_{\Gamma_k}]\right\}, \tag{3.35}$$

where the subscripts N, E, S, W $(\Gamma_1, ..., \Gamma_4)$ indicate approximations at the north, east, south and west faces, and C represents the centre of the cell under consideration. Here, $\mathbf{W}_i^n$ defines an approximation to the average of the solution in the control volume at time $t_n = n\Delta t$, Δt being the time step.

The discretized modified flux Φ is given by

$$\Phi_{\Gamma_k} = \mathbf{F}_{\Gamma_k} - \nu|\mathbf{D}_{\Gamma_k}|\left(\frac{\Delta \mathbf{W}_{\Gamma_k}}{\Delta x} - \mathbf{A}_{\Gamma_k}^{-1}\mathbf{S}_{\Gamma_k}^c\right), \tag{3.36}$$

where $\Delta \mathbf{W}_{\Gamma_k} = \mathbf{W}_R - \mathbf{W}_L$. The subscripts L and R represent the cell-centred values to the left and right of the cell face, respectively, with right being to the north or east side, and where either L or R must be located at the centre of the cell under consideration.

Following Chacón-Rebollo *et al.* (2003), a Godunov-like scheme is used for which the constant values associated with the Riemann problem at the cell interfaces are approximated by

$$\begin{cases} \mathbf{W}_{L+\alpha} &= (1-\alpha)\mathbf{W}_L + \alpha\mathbf{W}_R \\ \mathbf{W}_{R-\alpha} &= (1-\alpha)\mathbf{W}_R + \alpha\mathbf{W}_L \end{cases}, \quad 0 \leq \alpha \leq 0.5, \tag{3.37}$$

The function of the single parameter α is identical to flux limiters used in standard shallow water equations. The lower limit corresponds to a stable but more diffusive scheme, similar to a minmod limiter, whereas the upper limit corresponds to a less diffusive scheme which can become unstable in resolving discontinuities, similar to a superbee limiter. The parameter α has no effect on the smooth regions but becomes important in the transition zones.

The centred approximation of the flux function is thus written as

$$\mathbf{F}_{\Gamma_k} = \frac{1}{2}\left[\mathbf{F}(\mathbf{W}_{L+\alpha}) + \mathbf{F}(\mathbf{W}_{R-\alpha})\right]. \tag{3.38}$$

The matrices $\mathbf{D}_{\Gamma_k}$ (equation 3.33), $\mathbf{A}^{-1}_{\Gamma_k}$ (equation 3.31) and the source term $\mathbf{S}^c_{\Gamma_k}$ associated with the numerical diffusion and the non-centred part of the source term are determined using the intermediate states between the two neighbouring cells. In particular, the Roe's averages used are defined as:

$$u_j = \frac{\sqrt{h_{R,j}}u_{R,j} + \sqrt{h_{L,j}}u_{L,j}}{\sqrt{h_{R,j}} + \sqrt{h_{L,j}}}, \quad v_j = \frac{\sqrt{h_{R,j}}v_{R,j} + \sqrt{h_{L,j}}v_{L,j}}{\sqrt{h_{R,j}} + \sqrt{h_{L,j}}}, \tag{3.39}$$

and

$$c_j = \sqrt{\frac{1}{2}g(h_{R,j} + h_{L,j})}. \tag{3.40}$$

The source term $\mathbf{S}^c_{\Gamma_k}$ in equation (3.36) can then be written as

$$\mathbf{S}^c_{E,W} = \frac{b_R - b_L}{\Delta x}\left[0, -c_1^2, 0, 0, -c_2^2, 0\right]^T. \tag{3.41a}$$

and

$$\mathbf{S}^c_{N,S} = \frac{b_R - b_L}{\Delta y}\left[0, 0, -c_1^2, 0, 0, -c_2^2\right]^T. \tag{3.41b}$$

The components of the discretized coupling terms $\mathbf{B}$ are given by

$$\mathbf{B}_{E,N}(\mathbf{W}) = \alpha\mathbf{B}(\mathbf{W}_{i+\alpha/2}) + (1-\alpha)\mathbf{B}(\mathbf{W}_{i+(1-\alpha)/2}), \tag{3.42a}$$

and

$$\mathbf{B}_{W,S}(\mathbf{W}) = \alpha\mathbf{B}(\mathbf{W}_{i-\alpha/2}) + (1-\alpha)\mathbf{B}(\mathbf{W}_{i-(1-\alpha)/2}). \tag{3.42b}$$

The source terms $\mathbf{S}_{\Gamma_k}$ are

$$\mathbf{S}_N = \frac{(b_{L+\alpha} - b_L)}{\Delta y} \begin{bmatrix} 0 \\ 0 \\ -gh_{1,L+\alpha/2} \\ 0 \\ 0 \\ -gh_{2,L+\alpha/2} \end{bmatrix} + \frac{(b_{R-\alpha} - b_L)}{\Delta y} \begin{bmatrix} 0 \\ 0 \\ -gh_{1,L+(1-\alpha)/2} \\ 0 \\ 0 \\ -gh_{2,L+(1-\alpha)/2} \end{bmatrix}, \tag{3.43a}$$

$$\mathbf{S}_E = \frac{(b_{L+\alpha} - b_L)}{\Delta x} \begin{bmatrix} 0 \\ -gh_{1,L+\alpha/2} \\ 0 \\ 0 \\ -gh_{2,L+\alpha/2} \\ 0 \end{bmatrix} + \frac{(b_{R-\alpha} - b_L)}{\Delta x} \begin{bmatrix} 0 \\ -gh_{1,L+(1-\alpha)/2} \\ 0 \\ 0 \\ -gh_{2,L+(1-\alpha)/2} \\ 0 \end{bmatrix}, \tag{3.43b}$$

$$\mathbf{S}_S = \frac{(b_R - b_{R-\alpha})}{\Delta y} \begin{bmatrix} 0 \\ 0 \\ -gh_{1,R-\alpha/2} \\ 0 \\ 0 \\ -gh_{2,R-\alpha/2} \end{bmatrix} + \frac{(b_R - b_{L+\alpha})}{\Delta y} \begin{bmatrix} 0 \\ 0 \\ -gh_{1,R-(1-\alpha)/2} \\ 0 \\ 0 \\ -gh_{2,R-(1-\alpha)/2} \end{bmatrix}. \tag{3.43c}$$

and

$$\mathbf{S}_W = \frac{(b_R - b_{R-\alpha})}{\Delta x} \begin{bmatrix} 0 \\ -gh_{1,R-\alpha/2} \\ 0 \\ 0 \\ -gh_{2,R-\alpha/2} \\ 0 \end{bmatrix} + \frac{(b_R - b_{L+\alpha})}{\Delta x} \begin{bmatrix} 0 \\ -gh_{1,R-(1-\alpha)/2} \\ 0 \\ 0 \\ -gh_{2,R-(1-\alpha)/2} \\ 0 \end{bmatrix}. \tag{3.43d}$$

Numerical tests (Chacón-Rebollo *et al.*, 2003; Castro *et al.*, 2007*b*) have demonstrated that a choice of $\alpha = 1/8$ gives a satisfactory overall compromise between stability and accuracy, without any need to invoke entropy corrections for the approximate solutions of sonic rarefactions. Nevertheless, $\alpha = 0$ appears to be a better choice for stationary shocks (Castro *et al.*, 2007*b*). Hence, Castro *et al.* (2007*b*) propose the use of an adaptive discretization function $\alpha(x)$ where the value of α used is switched to zero locally, whenever a transition in the sign of the internal eigenvalues

$\lambda_{int}^{\pm}$ is detected at a non-propagating discontinuity:

$$\alpha_{\Gamma_k} = \begin{cases} 1/8 & \text{if } \operatorname{sgn}(\lambda_{int,L}^{\pm}) = \operatorname{sgn}(\lambda_{int,R}^{\pm}) \\ 0 & \text{if } \operatorname{sgn}(\lambda_{int,L}^{\pm} - \lambda_{int,R}^{\pm}) = 1 \end{cases} . \tag{3.44}$$

3.3.2 Wet-dry treatment

The solution of two-layer fluids presents another difficulty associated with the vanishing layer thickness of either layer or both layers, which is commonly referred to as the appearance of wet-dry fronts. Following Castro *et al.* (2005), a numerical scheme for solving system (3.1) satisfies the C-property if, for each cell i, the following equalities hold across any cell interface for any given steady solution:

$$\mathbf{A}_{\Gamma_k}\Delta\mathbf{W}_{\Gamma_k} = \mathbf{F}(\mathbf{W}_R) - \mathbf{F}(\mathbf{W}_L) - \mathbf{B}_{\Gamma_k}\Delta\mathbf{W}_{\Gamma_k}, \tag{3.45a}$$

and

$$\mathbf{A}_{\Gamma_k}\Delta\mathbf{W}_{\Gamma_k} = \mathbf{S}_{\Gamma_k}. \tag{3.45b}$$

For the two-layer shallow water flow, the family of steady-state solutions is given by

$$q_1 = 0, \quad q_2 = 0,$$
$$h_1(x) = \begin{cases} \eta_1 - \eta_2 & \text{if } b(x,y) < \eta_2 \\ \eta_1 - b(x) & \text{if } \eta_2 \le b(x,y) < \eta_1 \\ 0 & \text{if } \eta_1 \le b(x,y) \end{cases}, \quad h_2(x) = \begin{cases} \eta_2 - b(x,y) & \text{if } b(x,y) < \eta_2 \\ 0 & \text{if } \eta_2 \le b(x,y) \end{cases}, \tag{3.46}$$

where η_1 and η_2 are the elevation of the upper and lower layers, respectively, measured from a fixed reference horizontal datum. Using Roe's method as in (3.39), the equality (3.45) is verified. Nonetheless in the presence of a wet-dry front, the equality (3.45) holds at the cell interfaces provided the numerical source terms are redefined as follows

to avoid the emergence of spurious pressure forces:

$$\mathbf{S}_{N,S} = \begin{cases} \begin{bmatrix} 0 \\ 0 \\ -c_1^2(h_{L,1}+h_{L,2}) \\ 0 \\ 0 \\ -c_2^2(rh_{L,1}+h_{L,2}) \end{bmatrix} & \text{if } h_{L,1}+h_{L,2} < \mathrm{d}z, \\ \begin{bmatrix} 0 \\ 0 \\ c_1^2(h_{R,1}+h_{R,2}) \\ 0 \\ 0 \\ c_2^2(rh_{R,1}+h_{R,2}) \end{bmatrix} & \text{if } h_{R,1}+h_{R,2} < -\mathrm{d}z, \\ \begin{bmatrix} 0 \\ 0 \\ -c_1^2\mathrm{d}z \\ 0 \\ 0 \\ -c_2^2(r(\mathrm{d}z-h_{L,2})+h_{L,2}) \end{bmatrix} & \text{if } h_{L,2} < \mathrm{d}z < h_{L,1}+h_{L,2}, \\ \begin{bmatrix} 0 \\ 0 \\ -c_1^2\mathrm{d}z \\ 0 \\ 0 \\ c_2^2(r(-\mathrm{d}z-h_{R,2})+h_{R,2}) \end{bmatrix} & \text{if } h_{R,2} < -\mathrm{d}z < h_{R,1}+h_{R,2}, \\ [0,0,-c_1^2\mathrm{d}z,0,0,-c_2^2\mathrm{d}z]^T & \text{in other cases,} \end{cases} \tag{3.47a}$$

and

$$\mathbf{S}_{E,W} = \begin{cases} \begin{bmatrix} 0 \\ -c_1^2(h_{L,1}+h_{L,2}) \\ 0 \\ 0 \\ -c_2^2(rh_{L,1}+h_{L,2}) \\ 0 \end{bmatrix} & \text{if } h_{L,1}+h_{L,2} < \mathrm{d}z, \\ \begin{bmatrix} 0 \\ c_1^2(h_{R,1}+h_{R,2}) \\ 0 \\ 0 \\ c_2^2(rh_{R,1}+h_{R,2}) \\ 0 \end{bmatrix} & \text{if } h_{R,1}+h_{R,2} < -\mathrm{d}z, \\ \begin{bmatrix} 0 \\ -c_1^2\mathrm{d}z \\ 0 \\ 0 \\ -c_2^2(r(\mathrm{d}z-h_{L,2})+h_{L,2}) \\ 0 \end{bmatrix} & \text{if } h_{L,2} < \mathrm{d}z < h_{L,1}+h_{L,2}, \\ \begin{bmatrix} 0 \\ -c_1^2\mathrm{d}z \\ 0 \\ 0 \\ c_2^2(r(-\mathrm{d}z-h_{R,2})+h_{R,2}) \\ 0 \end{bmatrix} & \text{if } h_{R,2} < -\mathrm{d}z < h_{R,1}+h_{R,2}, \\ [0, -c_1^2\mathrm{d}z, 0, 0, -c_2^2\mathrm{d}z, 0]^T & \text{in other cases,} \end{cases} \tag{3.47b}$$

where $\mathrm{d}z = b_R - b_L$.

For fluids in motion, the source terms are calculated as in (3.47) but with a further modification which treats the front as an internal boundary condition. Suppose at time t_n, I_L is a two-layer cell, and I_R is the corresponding neighbouring cell which is dry or single-layered across the cell interface x_{Γ_k} which is oriented in the x-direction. Here, a wet-dry front is identified and the following adopted:

$$\tilde{\mathbf{W}}_L^n = \begin{cases} \left[(h_1^n)_L, 0, (q_{y,1}^n)_L, (h_2^n)_L, 0, (q_{y,2}^n)_L\right]^T & \text{if } I_R \text{ is a dry cell,} \\ \left[(h_1^n)_L, (q_{x,1}^n)_L, (q_{y,1}^n)_L, (h_2^n)_L, 0, (q_{y,2}^n)_L\right]^T & \text{if } I_R \text{ is a 1-layer cell.} \end{cases} \tag{3.48}$$

The treatment makes sure that the state(s) of the wet cell I_L is(are) modified such that there is no flux across the interface of a wet-dry front. The flux parallel to the

said cell interface remains to be defined following the boundary condition. In practice, $\mathbf{W}_L^{n+1}$ is calculated using the numerical fluxes obtained from $\mathbf{W}_R^n$ and the modified state $\tilde{\mathbf{W}}_L^n$. The approximation given by the treatment is satisfactory provided the mass flow rate in the wet cell is close to zero.

3.3.3 Treatment of loss of hyperbolicity

The hyperbolicity criterion (3.16) is only satisfied provided the velocity difference between the layers $(U_2 - U_1)$ is small. When this is not the case, complex eigenvalues associated with the appearance of Kelvin-Helmholtz instabilities will result. Physically, the destabilizing effect of shear could overcome the stratification of the layers, producing fluid roll-up leading to mixing between the layers. Ideally, a numerical solver is sought that is well defined even if complex eigenvalues appear. Nevertheless, such occurrences are usually localised and can be either avoided or accounted for numerically. Here, the predictor/corrector strategy by Castro *et al.* (2011) is adopted. In the predictor stage, the numerical scheme advance one step in time despite the occurence of complex eigenvalues. Then, a discrete semi-implicit linear friction law is applied in the corrector stage to simulate the exchange of momentum due to mixing processes.

Consider a computation cell i, suppose the approximations at time t^n, $\mathbf{W}_i^n$ are known and the time step is Δt, if complex eigenvalues are detected during time-marching, the numerical scheme is allowed to proceed using the complex eigenvalues in the predictor stage to obtain the approximations at time t^{n+1} as $\mathbf{W}_i^{n+1,-}$. In the absence of complex eigenvalues, $\mathbf{W}_i^{n+1}$ equals $\mathbf{W}_i^{n+1,-}$ by default. Otherwise the corrector stage below is executed to give the state $\mathbf{W}_i^{n+1}$ where:

$$\begin{cases} h_1^{n+1} = h_1^{n+1,-}, \\ h_2^{n+1} = h_2^{n+1,-}, \\ q_{k,1}^{n+1} = q_{k,1}^{n+1,-} - \bar{c_\lambda}\Delta t(u_{k,1}^{n+1} - u_{k,2}^{n+1}), \\ q_{k,2}^{n+1} = q_{k,2}^{n+1,-} - r\bar{c_\lambda}\Delta t(u_{k,1}^{n+1} - u_{k,2}^{n+1}), \end{cases} \tag{3.49}$$

where k is the direction solved and the cell index i has been omitted for clarity. The coefficient $\bar{c_\lambda}$ is given by

$$\bar{c_\lambda} = c_\lambda \frac{h_1^{n+1} h_2^{n+1}}{r h_1^{n+1} + h_2^{n+1}}, \tag{3.50}$$

and c_λ is computed, following the criterion (3.16) so that

$$(u_1^{n+1} - u_2^{n+1})^2 \leq g'(h_1^{n+1} + h_2^{n+1}). \tag{3.51}$$

From the inequality (3.51), the positive root is sought, which yields

$$c_\lambda \geq \frac{1}{\Delta t} \left(\frac{|u_1^{n+1,-} - u_2^{n+1,-}|}{\sqrt{g'(h_1^{n+1} + h_2^{n+1})}} - 1 \right). \tag{3.52}$$

Generally, equality may be chosen in (3.52)to get the value of c_λ.

Further to the above, hyperbolicity may also be lost whenever the internal eigenvalues λ_{int} become the same. In this case, the two eigenvalues are perturbed to give $\lambda_{int} \pm \epsilon$ where ϵ is a small parameter (Castro *et al.*, 2004). Also, for a two-dimensional system, whenever the velocities in both layers along the direction considered are equal, and hence $\lambda_1 = \lambda_2$, these eigenvalues are also perturbed by $\pm\epsilon'$, where $\epsilon' \neq \epsilon$, such that the system always retains 6 real and distinct eigenvalues.

3.3.4 Other source terms

The system of equations governing the two-layer shallow water flow in (3.1) includes only the effect of variable bed in the source term $\mathbf{S}_j$, $j = 1, 2$. For realistic flow, additional terms describing the wind stress, bed friction and interfacial stress may be added to the momentum equations as follows:

$$\begin{cases} (\tau_w - \tau_f)/\rho_1 & \text{in the upper layer} \\ (-\tau_w h_r + \tau_f + \tau_b)/\rho_2 & \text{in the lower layer} \end{cases}. \tag{3.53}$$

Here, τ_w is the wind shear stress, noting that its effect on the lower layer is in the opposite direction to that on the upper layer, and at reduced magnitude in proportion to the ratio of the depth of the lower layer to the total water water depth $h_r =$

$h_2/(h_1+h_2)$. The $x-$ and $y-$components of the interfacial shear stress τ_f and bed shear stress τ_b are given by the functions:

$$\begin{aligned} \tau_{fx} &= \rho_2 C_f u_r \sqrt{u_r^2+v_r^2} \\ \tau_{fy} &= \rho_2 C_f v_r \sqrt{u_r^2+v_r^2} \end{aligned} , \tag{3.54}$$

and

$$\begin{aligned} \tau_{bx} &= -\rho_j C_b u_j \sqrt{u_j^2+v_j^2} \\ \tau_{by} &= -\rho_j C_b v_j \sqrt{u_j^2+v_j^2} \end{aligned} , \tag{3.55),}$$

respectively, where $(u_r, v_r) = (u_1 - u_2, v_1 - v_2)$ is the velocity jump across the layers, C_f is the dimensionless interfacial coefficient, and C_b is the bed friction coefficicent. The expressions in (3.53) are only valid for the two-layer flow condition. Where single-layer flow applies, interfacial shear is non-existent by definition, whereas wind shear and bed friction act simultaneously on the only layer present.

For cases involving wetting and drying, vanishing depth can cause the computed bed shear stress to become unphysically large owing to division by the flow depth to obtain the flow velocity. In order to maintain the stability of the numerical scheme, the bed friction in the present scheme is solved by a splitting method equivalent to solving the following general ordinary differential equations (ODEs) in the momentum equations (Liang & Marche, 2009):

$$\frac{\mathrm{d}q}{\mathrm{d}t} = -\tau_b/\rho_j = S_b, \tag{3.56}$$

where q is the flow variable to be solved in either the $x-$ or $y-$direction, and the subscript j denotes the layer involved. Using a full implicit discretization of the form

$$\frac{q^{n+1}-q^n}{\Delta t} = S_b^{n+1}, \tag{3.57}$$

the right hand side may be expressed using a Taylor series as

$$S_b^{n+1} = S_b^n + (\frac{\partial S_b}{\partial q})^n \Delta q + o(\Delta q^2), \tag{3.58}$$

where $\Delta q = q^{n+1} - q^n$. Substituting (3.58) into (3.57), and ignoring higher-order terms, the following formula is obtained that may be used to update the flow variable q to a new time step:

$$q^{n+1} = q^n + \Delta t(\frac{S_b}{D})^n = q^n + \Delta t F, \tag{3.59}$$

where $D = 1 - \Delta t(\partial S_b/\partial q)^n = 1 + 2\Delta t C_b|q|/h^2$ is the coefficient derived for a full implicit scheme and F is the friction source term including the implicit coefficient. The maximum effect of the friction force is to stop the flow, i.e. $q^{n+1}q^n \geq 0$. Hence a limiting value is derived as:

$$F \begin{cases} \geq -q^n/\Delta t & \text{if} \quad q^n \geq 0 \\ \leq -q^n/\Delta t & \text{if} \quad q^n \leq 0 \end{cases} . \tag{3.60}$$

During simulation, the unknown variable q is updated according to (3.59) at the beginning of each time step, and then used as the initial condition in the numerical solver.

3.4 Algebraic balancing

The one-dimensional single layer shallow water equations may be derived by depth-integrating the Reynolds-averaged Navier-Stokes equations, neglecting the vertical acceleration of water particles, and adopting the hydrostatic approximation. In matrix form, a conservation law of the nonlinear SWEs may be written as:

$$\mathbf{W}_t + \mathbf{F}(\mathbf{W})_x = \mathbf{S}(x, \mathbf{W}), \tag{3.61}$$

where x denotes the horizontal distance, t denotes the time, and the subscript denotes partial derivative. The vectors $\mathbf{W}$, $\mathbf{F}$, and $\mathbf{S}$ represent the conserved variables, fluxes and source terms, respectively. Ignoring Coriolis effects, viscous terms, surface and bed stresses, these vectors are given by:

$$\mathbf{W} = \mathbf{W}(x,t) = \begin{bmatrix} h \\ q \end{bmatrix}, \quad \mathbf{F}(\mathbf{W}) = \begin{bmatrix} q \\ q^2/h + \frac{1}{2}gh^2 \end{bmatrix}, \quad \mathbf{S}(x, \mathbf{W}) = \begin{bmatrix} 0 \\ -ghb_x \end{bmatrix}, \tag{3.62}$$

where $h(x,t)$ is the total water depth, $q(x,t)$ is the flow rate, $b(x)$ is the bed function above the datum, and g is gravity acceleration. Specifically, the flux gradient term is split between a modified flux gradient term and a source term, as follows:

$$gh\frac{\partial \zeta}{\partial x} = \frac{\partial}{\partial x}(\frac{1}{2}gh^2) + gh\frac{\mathrm{d}b}{\mathrm{d}x}, \tag{3.64}$$

where ζ is the elevation of the free surface above still water depth h_s ($h = h_s + \zeta$).

Rogers *et al.* (2001) showed that mathematical balancing of flux gradient and source terms can be implemented by including quiescent still water conditions, hence avoiding the computational effort incurred by the numerical balancing approaches. Rogers *et al.* (2003) report a generalization of the method. The governing hyperbolic system of conservation laws is reformulated in terms of deviations away from an unforced but separately specified equilibrium state. The proposed splitting gives

$$gh\frac{\partial \zeta}{\partial x} = \frac{\partial}{\partial x}(\frac{1}{2}g(\zeta^2 + 2\zeta h_s)) - g\zeta\frac{\mathrm{d}h_s}{\mathrm{d}x}, \tag{3.65}$$

such that the flow is driven only by deviations of the free surface elevations from the still water level. However, both h_s and ζ in the equation set are difficult to define at wet-dry interfaces and dry areas. With applications involving wetting and drying in mind, Liang & Borthwick (2009) proposed an alternative formulation by splitting the free surface gradient term as follows:

$$gh\frac{\partial \zeta}{\partial x} = \frac{\partial}{\partial x}(\frac{1}{2}g(\eta^2 - 2\eta b)) + g\eta\frac{\mathrm{d}b}{\mathrm{d}x}, \tag{3.66}$$

where η is the surface water level above the datum, and the water depth can be evaluated by $h = \eta - b$.

The above mathematical balancing method is now applied to the two-layer shallow water model described in Section 3.2. In the system (3.17), the flux gradient terms have been split between flux gradients and source terms in the conventional way (3.64), i.e.

$$gh_j\frac{\partial \zeta_j}{\partial x} = \frac{\partial}{\partial x}(\frac{1}{2}gh_j^2) + gh_j\frac{\mathrm{d}b}{\mathrm{d}x}, \tag{3.67}$$

where ζ_j is the elevation of the free surface ($j = 1$) or the interface ($j = 2$) above the still water depth of the respective layer. Following the mathematical balancing approach of Rogers *et al.* (2001, 2003), and using the stage-discharge formulation of Liang & Borthwick (2009), the local still water equilibrium can be defined as follows:

$$\mathbf{W}^{\mathrm{eq}} = \begin{bmatrix} h_{s1} \\ 0 \\ h_{s2} \\ 0 \end{bmatrix}, \quad \mathbf{F}^{\mathrm{eq}} = \begin{bmatrix} 0 \\ \frac{1}{2}gh_{s1}^2 \\ 0 \\ \frac{1}{2}gh_{s2}^2 \end{bmatrix}, \quad \mathbf{S}^{\mathrm{eq}} = \begin{bmatrix} 0 \\ -gh_{s1}b_x \\ 0 \\ -gh_{s2}b_x \end{bmatrix}, \tag{3.68}$$

and

$$(\mathbf{B}(\mathbf{W})\mathbf{W}_x)^{\mathrm{eq}} = \begin{bmatrix} 0 \\ -gh_{s1}h_{s2,x} \\ 0 \\ -rgh_{s2}h_{s1,x} \end{bmatrix} = \begin{bmatrix} 0 \\ -g\eta_2 b_x \\ 0 \\ 0 \end{bmatrix}. \tag{3.69}$$

The local still water depth, measured from the free water surface η_1 and the interface η_2, are given by $h_{s1} = -\eta_2$ and $h_{s2} = -b$. Subtracting the vectors of the equilibrium condition (3.68) and (3.69) from the original vectors, and defining the thickness of each layer as $h_1 = \eta_1 - \eta_2$ and $h_2 = \eta_2 - b$, the balanced formulation is obtained as

$$\mathbf{W}'_t + \mathbf{F}'_x = (\mathbf{B}\mathbf{W}_x)' + \mathbf{S}', \tag{3.71}$$

where the modified vectors are given by:

$$\mathbf{W}' = \begin{bmatrix} \eta_1 \\ q_1 \\ \eta_2 \\ q_2 \end{bmatrix}, \quad \mathbf{F}' = \begin{bmatrix} q_1 \\ q_1^2/h_1 + \frac{1}{2}g(\eta_1^2 - 2\eta_1\eta_2) \\ q_2 \\ q_2^2/h_2 + \frac{1}{2}g(\eta_2^2 - 2\eta_2 b) \end{bmatrix} \tag{3.72}$$

$$\mathbf{S}' = \begin{bmatrix} 0 \\ -g\eta_1 b_x \\ 0 \\ -g\eta_2 b_x \end{bmatrix}, \quad (\mathbf{B}\mathbf{W}_x)' = \begin{bmatrix} 0 \\ -g(h_1 h_{2,x} - \eta_2 b_x) \\ 0 \\ -rgh_2 h_{1,x} \end{bmatrix}. \tag{3.73}$$

The formulation is unconditionally well-balanced for still water equilibrium in arbitrary bathymetries, satisfying

$$\mathbf{F}'_x = (\mathbf{B}\mathbf{W}_x)' + \mathbf{S}'. \tag{3.74}$$

However, the well-balanced property is not satisfied in the presence of interface perturbation, which is not obvious from the above analysis. This will be discussed further in Section 4.1.

3.5 Adaptive grid generation system

3.5.1 Literature review

Use of an appropriate computational grid is crucial in successful numerical implementation. Hence grid generation has become an important and stand-alone area of research for numerical computation. For 2D computations, a regular cartesian grid is the simplest to generate and execute but is hampered by various restrictions. It produces jagged boundary fit and can be very expensive when a fine grid is adopted over the entire domain. In order to achieve better representation of the complex domain boundary such as that of a coastal shoreline, boundary-fitted coordinate systems, namely curvilinear grid and conformal mapping procedures may be used. Nonetheless, these techniques require derivation of transformation equations which can become unwieldly with increasing boundary complexity.

The concept of both stretched grids and nested grids are introduced as a way to improve the grid resolution only in certain region of interest within the computational domain. However, these types of grid are typically pre-generated, and so require a prior knowledge of the regions of flow of concern. In physical simulations, the regions of the flow field which are of interest and concern are usually associated with large gradients of the flow variables. These regions move in space and time and hence require on-going localized grid refinement and coarsening if a global fine grid is to be avoided. This underlies the motivation of an adaptive grid which evolves in time in conjunction with a time-dependent solution of the governing flow-field equations.

Finite-volume and finite-element methods do not demand a structured grid or transformations between the computational and physical domain. This has given

rise to the use of the unstructured grid system, a tessellation of the computational domain by simple shapes such as triangles or tetrahedra in an irregular pattern. The grid generation is typically automated, accounting for boundary fitting and can be made adaptable in various contexts. In essence, an adaptive grid generation system should be able to perform grid refinement and coarsening at a fraction of the cost of uniform fine grid implementation, while maintaining sufficient resolution to describe the domain boundary. However, due to its inherent non-uniformity, efficient storage and retrieval of grid information and connectivity is crucial. This can be addressed by using a hierarchical tree structure originally considered in image digitization (Samet, 1984).

In this section, an adaptive quadtree grid for the two-layer shallow water model is presented. The strength of unstructured gridding is combined with the simple Cartesian coordinate system (e.g. Rogers *et al.*, 2001; Liang *et al.*, 2004) to provide an attractive high resolution, yet economical and efficient automated grid generation system.

3.5.2 Adaptive quadtree grid

This section describes the adaptive quadtree grid used for the two-layer shallow water model. Although quadtree grids appear unstructured, they have a tree-like indexing system and can be readily applied in solving discretised partial differential equations written in Cartesian coordinates. The resulting grid generation system is automatic, capable of high local resolution, and computationally efficient.

The quadtree grid generator referred to herein has undergone considerable development since its inception (Yiu *et al.*, 1996) and is presently known as OxQuad. Yiu *et al.* (1996) presented an automatic mesh generation technique which can accommodate local mesh refinement adaptively. The mesh is produced by recursively subdividing the domain into quadrants using a quadtree to store and manipulate the

mesh information. Over the past 15 years or so the data storage structure, grid adaptability, and internal and external boundary fitting have been enhanced. The quadtree technique was successfully implemented for non-linear wave simulation (Greaves *et al.*, 1997), simulation of separated flows (Greaves & Borthwick, 1998), advection of pollutant fronts (Borthwick *et al.*, 2000), wave-current interaction (Rogers *et al.*, 2004), solution of shallow water equations (Borthwick *et al.*, 2001*a*,*b*), and wave runup (Cho *et al.*, 2004). In particular, the dynamically adaptive quadtree grid Godunov-type shallow water equation solver has been rigorously tested by Rogers *et al.* (2001, 2003) and Liang *et al.* (2004).

The OxQuad quadtree grid generation algorithm can be summarised as follows:

1. Input seeding points which describe the locations of internal and external boundaries of the physical flow domain, and positions of initial discontinuities (if known) of the flow variables;

2. Rescale the physical flow domain to fit into the root cell (a unit square) and specify the minimum and maximum level of subdivision;

3. Where there is a seeding point, subdivide the cell into four equal-sized quadrants (children) and check each new child-cell in turn for the presence of seeding points;

4. If two or more seeding points are found inside a cell, step (3) is followed by the current step until no further subdivision is required;

5. Perform regularisation so that all cells achieve a prescribed minimum level of subdivision, and the difference in subdivision levels between adjacent cells (including diagonally touching cells) does not differ by more than one level.

Since the boundaries are described by initial seeding points, the maximum level of subdivision is adopted by default. However, in order to further reduce computational

cost, the minimum level of subdivision may be prescribed for straight boundaries. In this case, the boundary is also subjected to adaptation when the relevant criteria are met. Additional seeding points describing initial discontinuities or other features of interest in the domain can only be specified generally using simple geometrical lines or regions so that maximum subdivision is applied. The maximum subdivision thus produced may be chosen to be adaptable or non-adaptable throughout the simulation. Where the region of interest is not known a *priori* or cannot be described using simple geometries, a universal fine grid configuration may be used at the beginning of simulation and allows the adaptation procedure to subsequently coarsen regions which do not require fine resolution to the minimum level of subdivision.

The above algorithm approaches boundary fitting in a fractal-like manner where a stepped approximation is inherent. The disruptive effect on the flow solution, if any, can be minimized by locally increasing the grid resolution. Alternatively, the grid may be further triangularized (Yiu *et al.*, 1996), or represented by cut-cells (Liang *et al.*, 2007*b*).

Dynamical grid adaptation during numerical simulation is carried out using a set of criteria relating to internal flow features, such as the minimum and maximum root mean square values of the free surface gradients (and/or interface gradients in the present two-layer shallow water model) or depth-averaged velocity component gradients. The cells in the original grid may thus be further subdivided (enriched), and the newly created cells subsequently removed (coarsened) if appropriate. Updated cell identification and neighbour-finding information is stored within the same quadtree grid structure.

The connectivity of the grid generated is stored in a simple hierarchical tree structure. Each cell has a cell number, a parent pointer and four child pointers (if they exist). The root cell (level 0) is numbered 1 with its parent numbered 0 and the four quadrants numbered 2 to 5 (level 1), corresponding to the northwest, northeast,

southwest, and southeast positions, respectively. These four quadrants are given 2-digit reference numbers defined as 11, 21, 12, and 22, respectively, applicable locally at all levels of subdivision, and the sequence adopted in the cell-checking procedure described in step (3). Cell referencing is achieved using a unique identification number which comprises a concatenation of the local reference numbers at each successive level starting from level 1. Since not all cells have the same subdivision level, trailing zeros are added to give cell identification numbers of the same length. For any cell, its level of subdivision is equal to the number of pairs of non-zero digits in its identification number. The root cell has an all-zero cell identification number.

The non-uniform nature of the mesh generated means that hanging nodes are inevitably present when adjacent cells are of different sizes. A hanging node refers to where the vertex of one cell coincides with the middle of an edge of its neighbour. This demands careful treatment during discretization of the partial differential equations in order not to violate the conservation laws. Hanging nodes are minimised by virtue of the regularisation step (5) where the maximum adjacent cell edge length ratio for cells located inside the flow domain is constrained to a factor of two. Despite the presence of different neighbouring mesh sizes, the discretised equations are solved on a uniform grid template, such that whenever values are needed at grid locations where the information is not stored, appropriate interpolation routines must be employed to approximate the required values. In this thesis, linear interpolation is chosen as a compromise between efficiency and accuracy.

A full description of the quadtree grid generator is given by Borthwick *et al.* (2000), Rogers *et al.* (2001, 2003) and Liang *et al.* (2004).

Chapter 4

Validation tests and applications of A2L-SWM

In this chapter, the two-layer shallow water model described in Chapter 3 is verified against a number of 1D and 2D benchmark test cases, and available analytical solutions. Grid convergence tests are performed to evaluate the efficiency of the adaptive quadtree grid generator. Finally, the model is applied to an idealised tidal channel, and a real estuary.

4.1 Smooth steady state solutions

The two-layer shallow water model described by the system of equations (3.17) is verified, for smooth steady state solutions, by the following two Bernoulli-type functions as well as constant mass flow rate in the respective layer:

$$\begin{array}{ll} \frac{1}{2}u_1^2 + g(b + h_1 + h_2) = \text{constant}, & q_1 = \text{constant}, \\ \frac{1}{2}u_2^2 + g(b + h_1) + rgh_2 = \text{constant}, & q_2 = \text{constant}, \end{array} \tag{4.1}$$

where the constants r and g are the density ratio and the gravitational acceleration, respectively, and the variables h_j, u_j and q_j are the water depths, velocities and flow rates, respectively, for the upper (j=1) and lower layer (j=2). These two Bernoulli-type functions are obtained by expanding the momentum equations of system (3.17) using the chain rule, followed by eliminating the depth evolution terms using the corresponding continuity equations. In (Section 3.4), the pre-balanced formulations

(3.71) derived using the algebraic balancing approach of Rogers *et al.* (2001, 2003) appear to satisfy the still water condition (3.74). Nonetheless, the momentum equation of the upper layer has an extra term $-g\eta_2\eta_{2,x}$ prior to division by the layer thickness to give the expression of the form in (4.1). Here, η_j is the free surface (j=1) and interface (j=2) elevations above the horizontal datum, and the subscript x denotes partial derivative. This term is assumed zero in still water condition but is nonvanishing when the interface is not horizontal. This invalidates the algebraically-balanced equations and is confirmed in the numerical test reported in (Section 4.3.3) where unwanted spurious oscillation is detected in the solutions. The above finding has been reported in Lee *et al.* (2010*a*).

4.2 Rigid lid approximation

Armi and Farmer presented a theoretical study of the hydraulics of two flowing layers in a series of papers (Armi, 1986; Farmer & Armi, 1986; Armi & Farmer, 1986). Their theory is based on the Bernoulli equations under the rigid-lid assumption. Using a parameterization of the internal Froude number, the flow characteristics were described for several benchmark problems, including steady 2-layer exchange over a sill, which is described in brief below.

Consider two-way exchange between reservoirs containing fluid of differing densities subjected to hydraulic control by a sill. The composite Froude number G^2 characterizes the nonlinearity of the flow and is expressed in terms of the internal densimetric Froude number $F_j^2, j = 1, 2$:

$$G^2 = F_1^2 + F_2^2 - (1 - r)F_1^2F_2^2, \tag{4.2}$$

where

$$F_j^2 = u_j^2/g'h_j, \tag{4.3}$$

where g' is the reduced gravity. When $G^2 = 1$, the flow is critical and there exists a critical point in the flow domain; when $G^2 < 1$, the flow is subcritical; when $G^2 > 1$, the flow is supercritical.

Defining h_o to be the total water depth at the sill crest, and assuming constant channel breadth, the water depth y_j (measured with reference to the sill crest), layer thickness h_j, and flow rate q_j can be nondimensionalized as follows:

$$y'_j = y_j/h_o, \quad h'_j = h_j/h_o, \quad q'_j = q_j/\sqrt{g'h_o^3}, \tag{4.4}$$

which verifies

$$h'_j = (q'_j/F_j)^{2/3}. \tag{4.5}$$

For cases where $g' \ll g$, the external Froude number is very small and hence the rigid-lid approximation may be adopted:

$$h'_1 + h'_2 + y' = 1, \tag{4.6}$$

Let $q_r = -q_1/q_2$ be the ratio of the flow rates in each layer such that in an exchange flow without barotropic component, then $q_r = 1$, and equation (4.6) can be rearranged to give

$$q_r^{2/3} F_1^{-2/3} + F_2^{-2/3} = q_2'^{-2/3}(1 - y'), \tag{4.7}$$

which gives a family of solutions for different bottom function y'.

Subtracting the Bernoulli equations for each layer, and making use of equations (4.5), (4.6) and (4.7), the solution of a smooth steady flow thus obtained is independent of location:

$$F_2^2 = q_r[2F_1^{-2/3} + F_1^{4/3} - 2\Delta H'' q_1'^{-2/3}]^{3/2}, \tag{4.8}$$

where the dimensionless energy difference between the layers is

$$\Delta H'' = \frac{H_1 - H_2}{g'\rho_2 h_o} + 1, \tag{4.9}$$

H_j being the energy of the respective layer j.

For a given bottom function, the intersection of the solution curves of (4.7) and (4.8) typically admits more than one solution. The physically relevant solution is hence dependent on the boundary conditions imposed. Furthermore, if energy is conserved, the quantity $\Delta H'' {q_1'}^{-2/3}$ is conserved. In the specific case where the flow is critical at the sill crest, there is a unique solution given by $\Delta H'' {q_1'}^{-2/3} = 3/2$, which is identified with the maximal exchange rate $q_2' = 0.208$ (see Farmer & Armi 1986), and reservoir conditions $F_1^2 = 1$ and $F_2^2 = 0$. Since the solution is independent of q_r, it is thus applicable to barotropic flows.

4.3 Numerical tests for 1D 2-layer shallow water model (1D-2LSWM)

In this section, the 1D scheme is tested on a number of numerical experiments. The density ratio r is taken as 0.98, which corresponds to densities of typical stratified coastal water, and $g = 9.81$ m/s^2. Following Castro *et al.* (2005), the CFL-condition is defined as

$$\max\{|\lambda_{i+1/2,k}|; i = 1, M; k = 1, 2j\}\frac{\Delta t}{\Delta x} \leq \gamma, \tag{4.10}$$

where $0 < \gamma \leq 1$. In all the tests reported below, $\gamma = 0.9$ is used.

4.3.1 Still water solution

These tests verify the still water solution for an irregular bed profile. The initial data correspond to steady state at rest, with $q_1 = q_2 = 0$. Figure 4.1 shows that the still water solution is computed exactly for variable bed and stepped bed. Also, the scheme treats the wet-dry transition correctly when the water depth diminishes in the lower layer or both layers.

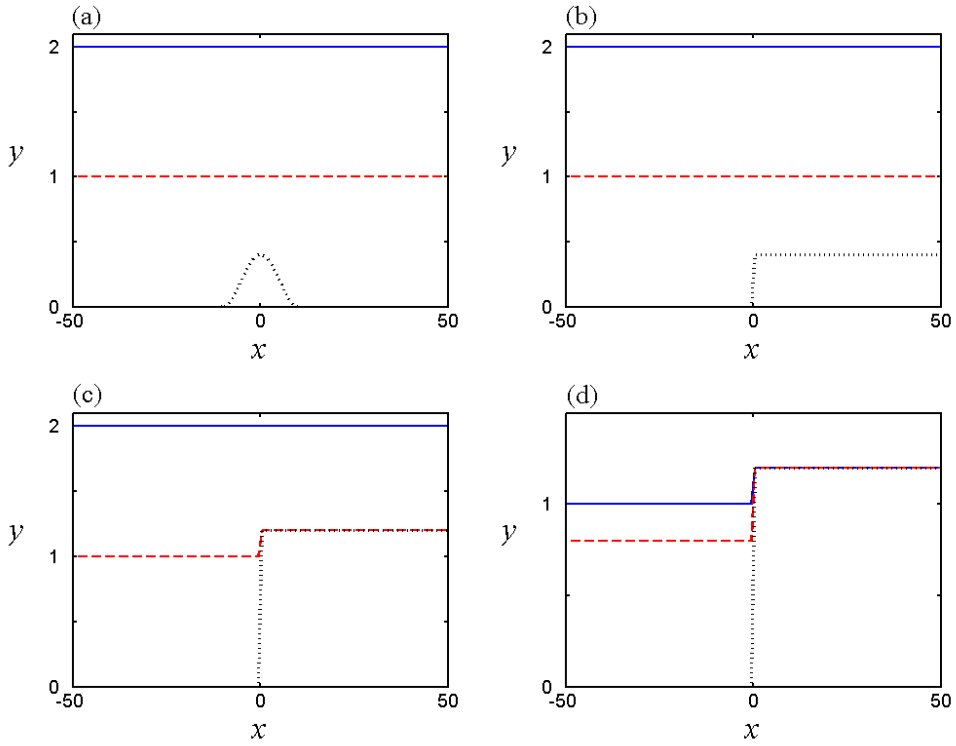

Figure 4.1: Steady state at rest solutions in 1D: (a) uneven bed, (b) stepped bed, (c) drying of lower layer over a stepped bed, and (d) drying of both layers over a stepped bed. Plots showing profiles of surface (solid-line), interface (dashed-line), and bed (dotted-line).

4.3.2 Balancing of discretized equations

In the following numerical test, the scheme (3.26) is verified against the smooth steady state solutions (4.1). Consider a bed profile given by

$$b(x) = 0.5\exp(-x^2), \tag{4.11}$$

where the free water surface $\eta_1 = 2$ is stationary given an exchange flow condition $q_1 = -q_2 = 0.15$. In order to obtain a particular stationary solution, the following conditions are imposed at the interface: $\eta_2(-3) = \eta_2(3) = 1.5$. From these values, the constants in equations (4.1) are computed and thus the solutions at any points are obtained. Using these solutions as the initial conditions, Figure 4.2 shows the numerical scheme remains well balanced throughout. Note that at the boundaries, the interface elevation is slightly lower than the prescribed initial condition. This can be attributed to the reduction of pressure due to acceleration of the flow in the proximity of the hump.

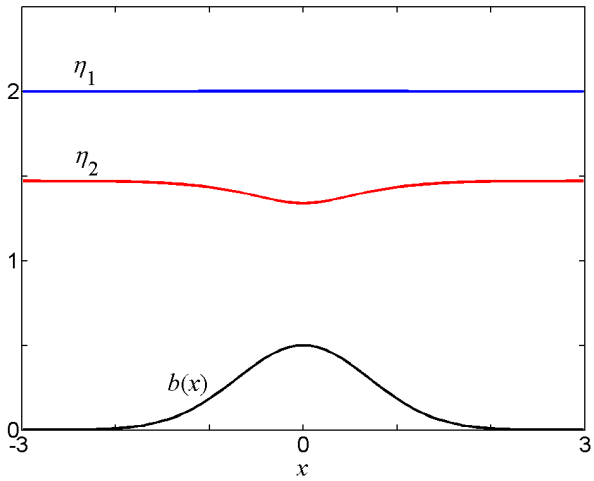

Figure 4.2: Smooth steady state solution in 1D ($t = 500$).

4.3.3 Propagation of interface perturbation

Next, the coupling term in the governing equation is examined using a test problem on propagation of an interface perturbation after Castro *et al.* (2001). The initial condition is given by:

$$h_1(x) = \begin{cases} 0.50 & \text{if} \quad x < 50 \\ 0.55 & \text{if} \quad x > 50 \end{cases}, \quad q_1(x) = \begin{cases} 1.250 & \text{if} \quad x < 50 \\ 1.375 & \text{if} \quad x > 50 \end{cases}, \tag{4.12}$$

$$h_2(x) = \begin{cases} 0.50 & \text{if} \quad x < 50 \\ 0.45 & \text{if} \quad x > 50 \end{cases}, \quad q_2(x) = \begin{cases} 1.250 & \text{if} \quad x < 50 \\ 1.125 & \text{if} \quad x > 50 \end{cases}. \tag{4.13}$$

Figure 4.3 shows the solution where the perturbation has spread out and moved downstream.

Figure 4.4 shows the solution obtained using the algebraically-balanced approach (Section 3.4). The result shows that the scheme produces unwanted spurious oscillations in the presence of an interface perturbation. The oscillations grow subsequently and result in unphysical solutions.

For a larger perturbation, the following initial conditions are adopted:

$$h_1(x) = \begin{cases} 0.20 & \text{if} \quad x < 50 \\ 0.80 & \text{if} \quad x > 50 \end{cases}, \quad h_2(x) = \begin{cases} 0.80 & \text{if} \quad x < 50 \\ 0.20 & \text{if} \quad x > 50 \end{cases}, \tag{4.14}$$

where $q_1 = q_2 = 0$.

Figure 4.5 shows the evolution of the interface perturbation which resembles an internal dam break.

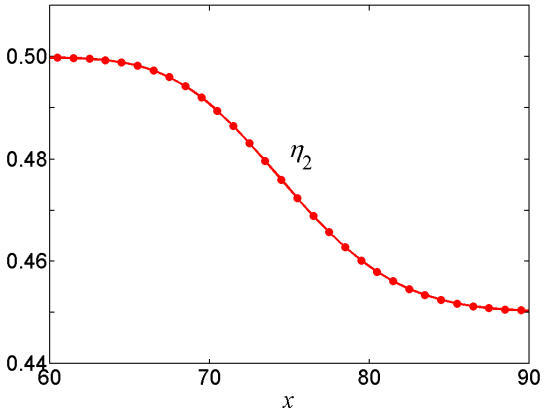

Figure 4.3: Propagation of a small 1D interface perturbation ($t = 10$).

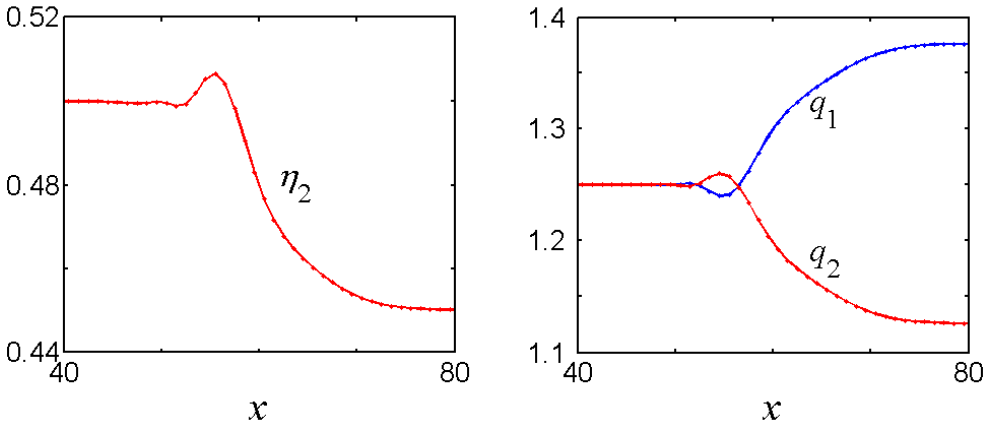

Figure 4.4: Failure of algebraic balancing approach.

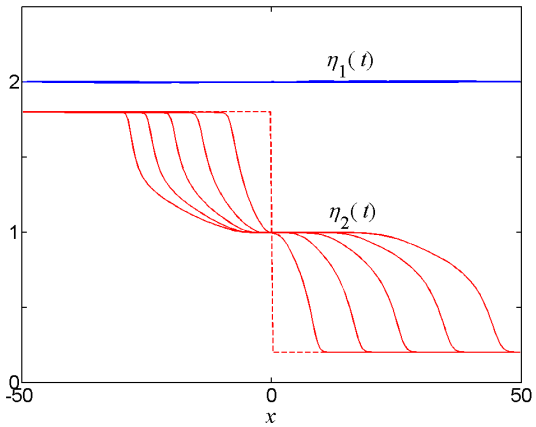

Figure 4.5: Propagation of a large 1D interface perturbation at $\Delta t = 20$ increment (dashed line showing initial interface profile).

4.3.4 Hyperbolicity treatment

The following test (Castro *et al.*, 2011) is performed with an initial condition which is far beyond the hyperbolicity region. Consider a 1D channel with flat bed in the interval [-5,5] with open boundary conditions. The initial condition is

$$h_1(x,0) = \begin{cases} 0.4, & x \in (-0.5, 0.5) \\ 0.5, & \text{otherwise,} \end{cases} \qquad h_2(x,0) = 1 - h_1(x,0),$$

$$u_1(x,0) = 0.2, \quad u_2(x,0) = -0.3.$$

Using $r = 0.99$, Figure 4.6 shows that, when there is no provision for the emergence of complex eigenvalues, the initial perturbation grows in time but remains bounded. Similar unphysical numerical instabilities can be observed for both water depths and velocities. If the corrector step of Castro *et al.* (2011) is performed, there are no spurious oscillations.

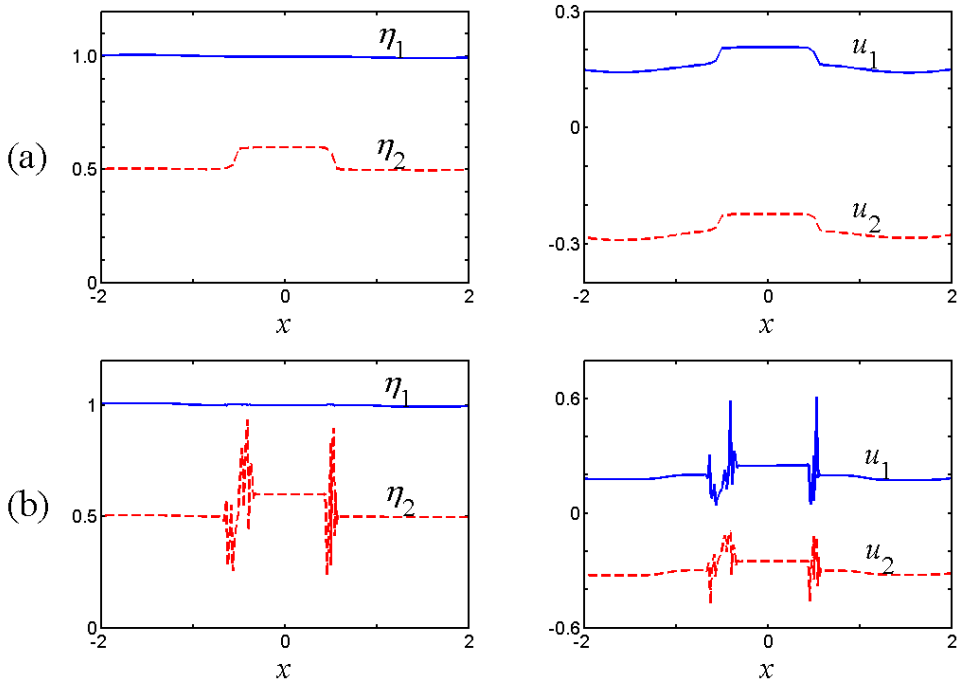

Figure 4.6: Comparison between solutions with (a) and without (b) treatment of complex eigenvalues at $t = 1.0$.

4.3.5 Stationary internal hydraulic jump

The internal hydraulic jump is an interesting feature in a two-layer fluid with a finite density contrast ($\rho_1 \neq \rho_2$). A simple case is considered of horizontal bed and stationary upper layer $q_1 = 0$ and constant discharge in the lower layer ($q_2 = 0.0548$). The depth of the lower layer h_2 before the jump is 0.1250. The theoretical conjugate depth h_2' after the jump is 0.4363, as calculated from the equation

$$\frac{h_2'}{h_2} = \frac{1}{2}(\sqrt{1 + 8Fr_2^2} - 1), \tag{4.17}$$

where $Fr_2 = u_2/\sqrt{g'h_2}$. Figure 4.7 shows the numerical scheme is able to maintain the stability of the discontinuity and excellent agreement with the theoretical solution is obtained. The jump position appears to spread across 2 adjacent cells due to plotting of the discontinuity. The small difference in the interface elevation at the downstream end (towards the right side) of the jump can be attributed to the rigid lid approximation.

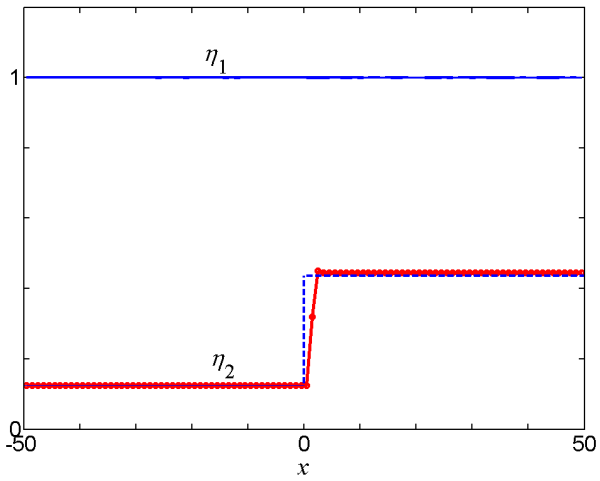

Figure 4.7: A simple stationary 1D internal jump: initial position (-----) and numerical iteration (——) at $t = 500$.

4.3.6 Lock exchange flow

This case considers two infinite reservoirs with fluids of distinct densities connected by a rectangular channel with a hump. The two fluids are separated by a vertical artificial barrier located at $x = 2$ and the bed profile is given by $b(x) = \exp(-x^2)$ where $x \in [-3, 3]$. If the barrier is removed, a lock exchange flow is obtained. The boundary conditions are given by $q_1 = -q_2$ at each channel end. Figure 4.8 shows the time evolution of the interface between the two fluids up to $t = 20$. The test requires accurate treatment of the wetting front of the denser fluid (see Section 3.3.2). Furthermore, as the denser liquid accelerates downstream, the flow approaches a critical condition as one of the system eigenvalues vanishes. Hence, treatment of the complex eigenvalue must also be implemented (see Section 3.3.3).

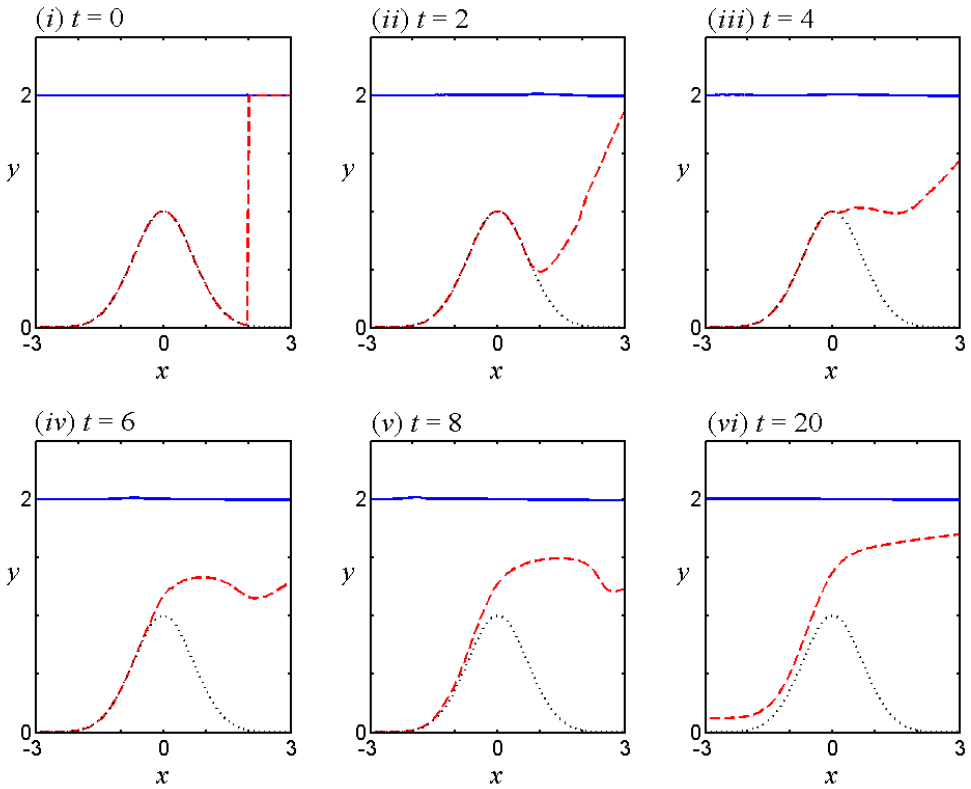

Figure 4.8: Time evolution of a 1D lock exchange flow. Plots showing profiles of surface (solid-line), interface (dashed-line), and bed (dotted-line).

If the numerical scheme is run until steady state is reached, a smooth transcritical

flow is obtained. The denser fluid accelerates smoothly from subcritical to supercritical, reaching criticality at the hump crest. In general, these flow processes are an interaction of purely baroclinic effects due to density differences, and the associated interfacial instabilities, and of additional barotropic components attributed to steady or unsteady external forcing. Negretti *et al.* (2007) studied stratified two-layer exchange flow over a submerged sill experimentally. They showed that baroclinic exchange flow is dominated by the barotropic-forcing-induced instabilities, which are inevitably produced because of the experimental starting conditions. In fact, the combination of baroclinic and unsteady barotropic effects is a common feature of geophysical and environmental flows. Whereas density stratification limits vertical mixing, Negretti *et al.* verified that the superposed unsteady baroptropic component is responsible for the generation of large-scale billows at the interface in the form of surges, and thus promotes vertical transport. Nevertheless, the experiments conducted by Negretti *et al.* are limited to flows with relatively large density differences. Further experimental results by Negretti *et al.* (2008) showed that dense bottom roughness inhibits the generation of large-scale billows, whereas sparse bottom roughness inhibits the collapse mechanism of the billows. In the present model however, the flow is assumed inviscid and to result from a purely inertia-buoyancy balance.

Figure 4.9 compares the rigid-lid solution and the numerical solution at steady state. A minor discrepancy attributed to the rigid-lid approximation (see Section 4.2) can be observed. It is worth noting that the steady state rigid-lid solutions depend on q_i^2 and as such make no distinction between the flow direction, i.e. whether it is an exchange flow ($q_1 = -q_2$) or parallel flow ($q_1 = q_2$), the latter being less prone to shear instability of the interface. Numerical solution of the parallel flow is identical to the exchange flow solution, and is omitted herein.

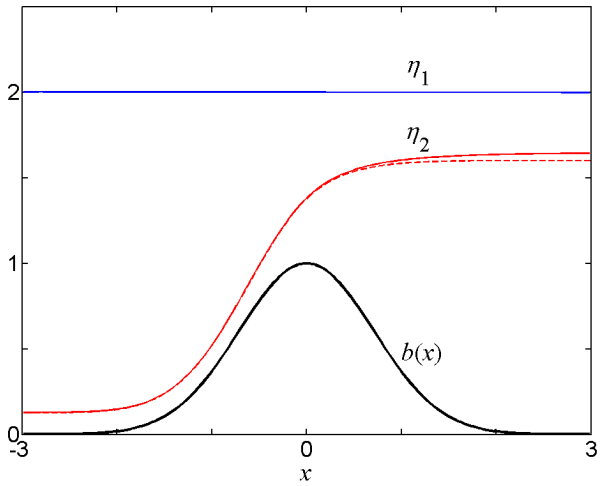

Figure 4.9: Steady-state solutions of a 1D lock exchange flow: rigid lid solution (- - - - -) and numerical iteration (——).

4.3.7 Internal dam break

This test examines an internal dambreak leading to the development of an internal hydraulic jump. The domain and bottom topography are the same as in Section 4.3.6. The initial condition is given by an artificial barrier separating the two fluids of distinct densities at $x = 0$, and the boundary conditions are again described by an exchange flow. At $t = 0$, when the density discontinuity is released, all flows are zero. Figure 4.10 shows how the denser fluid undergoes an internal dam break, accelerating from subcritical to supercritical condition, and subsequently forms a hydraulic jump to dissipate its energy, thus attaining subcritical outflow at the downstream end of the computational domain.

Figure 4.11 compares the rigid-lid solution and the numerical solution at the steady state condition of an internal hydraulic jump. The boundary conditions are given by fixed discharge at the inlet and fixed depth at the outlet. Compared to the exact solution, excellent agreement is obtained except for a minor difference in the jump location due to the rigid-lid approximation, because the small discrepancy in interface height translates into a larger error in velocity and hence the position of the jump.

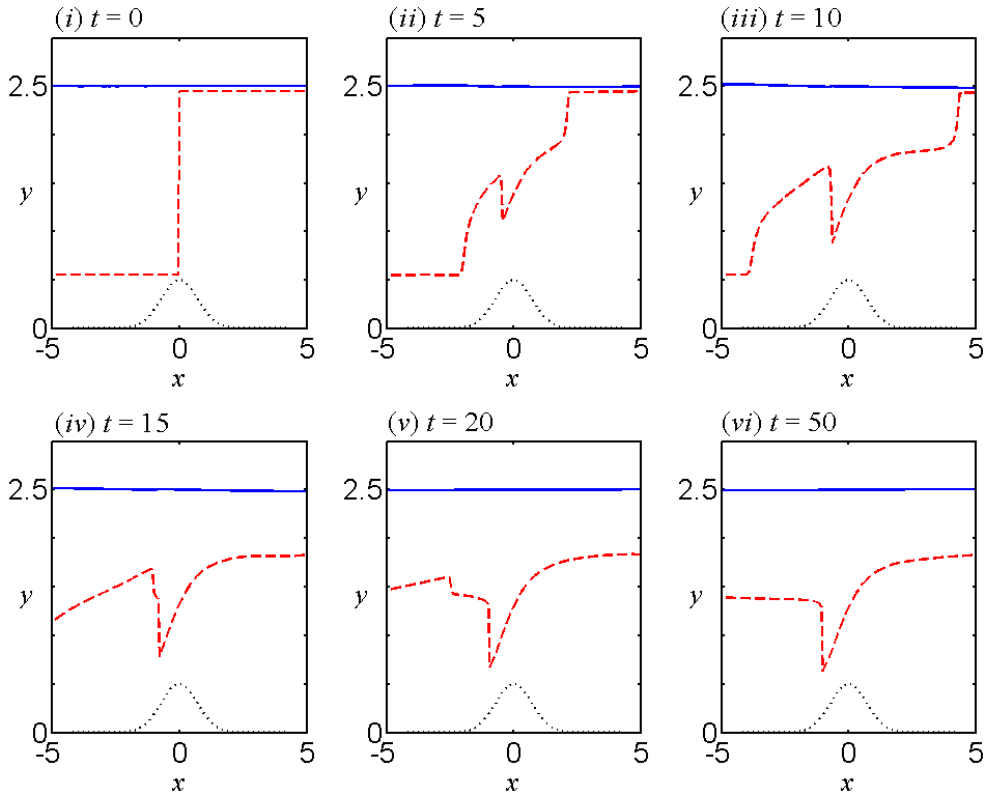

Figure 4.10: Time evolution of a 1D internal dam break. Plots showing profiles of surface (solid-line), interface (dashed-line), and bed (dotted-line).

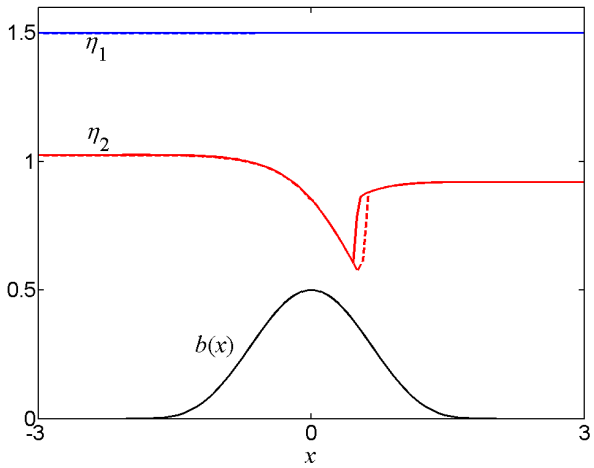

Figure 4.11: Steady state solutions of a 1D internal hydraulic jump: rigid lid solution (- - - - -) and numerical iteration (——).

4.3.8 Shock behind wall

This numerical experiment considers a column of 2-layer liquid moving horizontally towards a vertical wall with constant velocity. The bed elevation is given by:

$$b(x) = \begin{cases} 0, & 0 \leq x < 10 \\ 10, & 10 \leq x \leq 12 \end{cases}, \tag{4.18}$$

the initial conditions are:

$$\begin{cases} h_1(x) = 0.50 & h_2(x) = 0.50 & q_1(x) = 2.0 & q_2(x) = 2.0 & \text{if} & x < 10 \\ h_1(x) = 0 & h_2(x) = 0 & q_1(x) = 0 & q_2(x) = 0 & \text{if} & x \geq 10 \end{cases}, \tag{4.19}$$

and the boundary conditions imposed at $x = 0$ are:

$$\begin{cases} h_1(0,t) = & h_2(0,t) = & 0.5 \\ q_1(0,t) = & q_2(0,t) = & 2.0 \end{cases}. \tag{4.20}$$

Figure 4.12 shows the evolution of the shock developing behind a wall. Due to the relatively large initial velocity close to the wall, the numerical solution exhibits an error at the first iteration, which is rapidly dissipated, leaving behind only small disturbances near the travelling shock. The shock on the lower layer of denser fluid forms later. The numerical scheme fails if the initial velocity becomes too large.

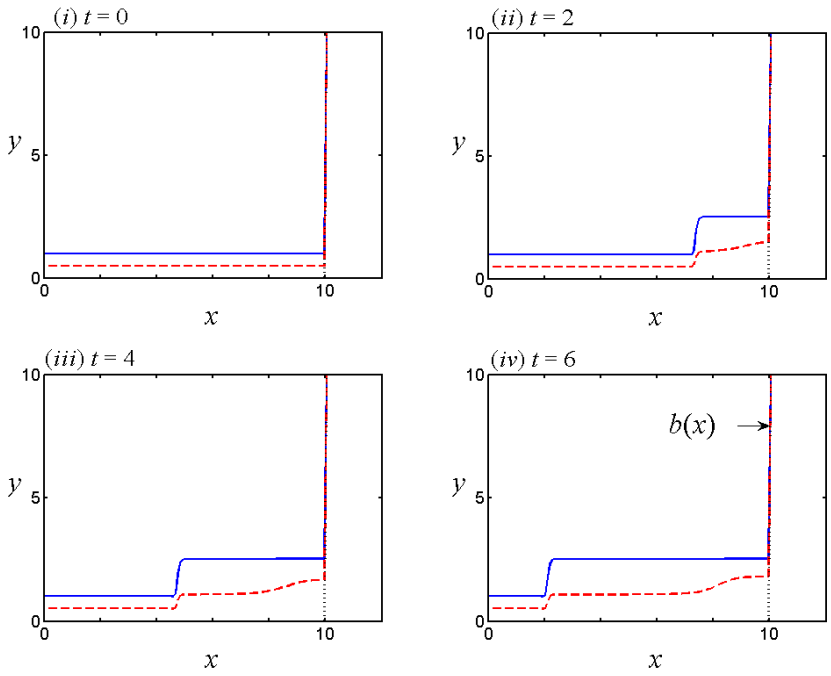

Figure 4.12: Solutions of shock behind wall. Plots showing profiles of surface (solid-line), interface (dashed-line), and bed (dotted-line). Note that the bed forms a vertical wall at $x = 10$ and is otherwise flat ($b(x)$=0, $x \in$(0,10)).

4.4 Numerical tests for 2D 2-layer shallow water model (2D-2LSWM)

In this section, the 2D scheme is tested in a number of numerical experiments. The CFL-condition is defined as

$$\max\{\frac{|\lambda_{i,\Gamma_k,\iota}|}{\Delta x}; i = 1, M; k = 1, 4; \iota = 1, 6\}\Delta t \leq \gamma, \tag{4.21}$$

where i, k and ι are the number of computational cells, the number of faces of each (square) cell, and the number of eigenvalues corresponding to each face. In all the tests reported below, $\gamma = 0.9$ $(0 < \gamma \leq 1)$. Unless otherwise stated, the density ratio $r = 0.98$ corresponding to typical stratified coastal water, and $g = 9.81$ m/s^2.

The various grid configurations used are represented using the notation Ψ_{i-j} where i and j represent the minimum and maximum levels of subdivision, respectively. Hence, where $i = j$ a regular grid has been adopted. The mesh sizes Δx at various levels of cell subdivision in the unit square grid domain $((x, y) \in [0, 1])$ are given by 2^{-n} where n is the level of subdivision. The formal order of accuracy of the numerical scheme is 2. Grid comparison is presented separately in Section 4.5.

4.4.1 Still water solution

These tests verify the still water solution for irregular bed profile. The initial data correspond to steady state at rest, with $q_1 = q_2 = 0$. Figure 4.13 shows that the still water solution is computed exactly for all three cases of variable bed, a bed protrusion above the lower layer, and a bed protrusion above the surface layer.

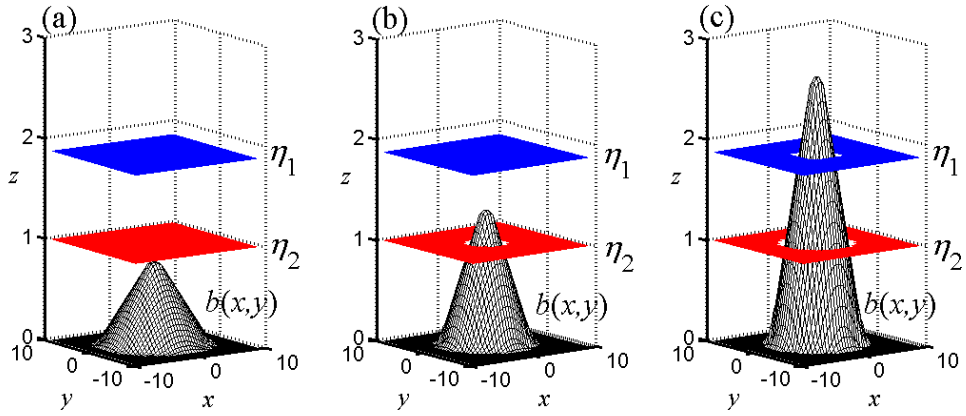

Figure 4.13: Still water conditions in 2D: (a) an uneven bed, (b) a bed protrusion above the lower layer, (c) a bed protrusion above the surface layer.

4.4.2 Balancing of discretized equations

Following Section 4.3.2, the Bernoulli-type functions derived for the 2D case from the system (3.26) can be written in the form:

$$\begin{array}{l} \frac{1}{2}(u_{1,x}^2 - u_{2,x}^2) + g(1-r)h_1 + (v_1 u_{1,y} - v_2 u_{2,y}) = \text{constant}, \quad q_1 = \text{constant}, \\ \frac{1}{2}(v_{1,y}^2 - v_{2,y}^2) + g(1-r)h_1 + (u_1 v_{1,x} - u_2 v_{2,x}) = \text{constant}, \quad q_2 = \text{constant}, \end{array} \tag{4.22}$$

notably the cross-derivative terms in the 2D plane play a role in the balancing issue which poses an immense challenge to the numerical scheme. Here, a smooth steady state solution of a 1D problem (see Section 4.3.2) is sought using the 2D solver to verify that lateral instabilities does not occur.

Consider a bed profile given by

$$b(x) = 0.5\exp(-x^2), \tag{4.23}$$

where the free water surface $\eta_1 = 2$ is stationary given an exchange flow condition $q_1 = -q_2 = 0.15$. In order to obtain a particular stationary solution, the following conditions are imposed on the interface: $\eta_2(-3) = \eta_2(3) = 1.5$. From these values, the constants in equations (4.22) are computed and thus the solutions are obtained throughout the domain. Using these solutions as initial conditions, Figure 4.14 confirms that the numerical scheme remains well balanced throughout.

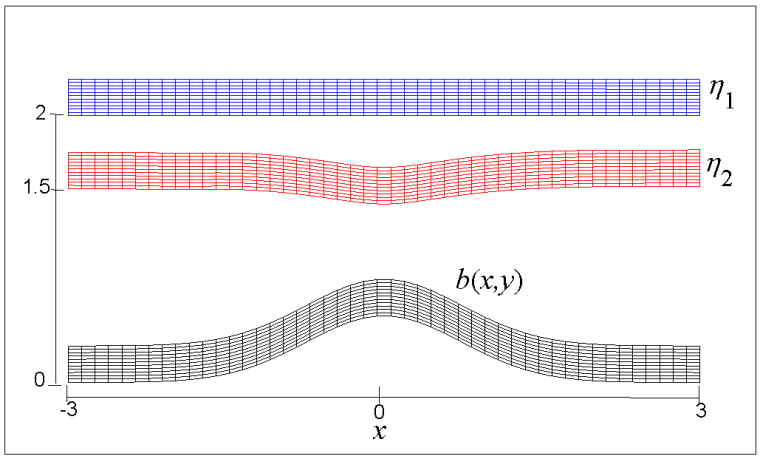

Figure 4.14: Smooth steady state solution in 2D ($t = 500$).

4.4.3 Propagation of interface perturbation over flat bed

This is a benchmark test to examine the coupling term in the two-layer shallow water scheme, originally proposed by Castro *et al.* (2001) for the one-dimensional case, and later adapted for a two-dimensional problem by Kurganov & Petrova (2009). A round-shaped interface perturbation is advected by a uniform flow in both $x-$ and $y-$directions (in the north-east direction) over a flat bed. The initial conditions are given by:

$$(h_1, u_1, v_1, h_2, u_2, v_2) = \begin{cases} (0.50, 2.5, 2.5, 0.50, 2.5, 2.5) & (x+1)^2 + (y+1)^2 \leq 1, \\ (0.45, 2.5, 2.5, 0.55, 2.5, 2.5) & \text{otherwise}, \end{cases} \tag{4.24}$$

in a domain given by $(x, y) \in [-1, 1]$. Transmissive boundary conditions are applied at the domain boundaries. In addition to the domain boundary, seeding points are also applied along the initial discontinuity so that the grids are refined in its vicinity. The simulation is performed until $t = 0.1$. Figure 4.15 shows the free surface and interface at the end of the simulation using grid Ψ_{9-9}.

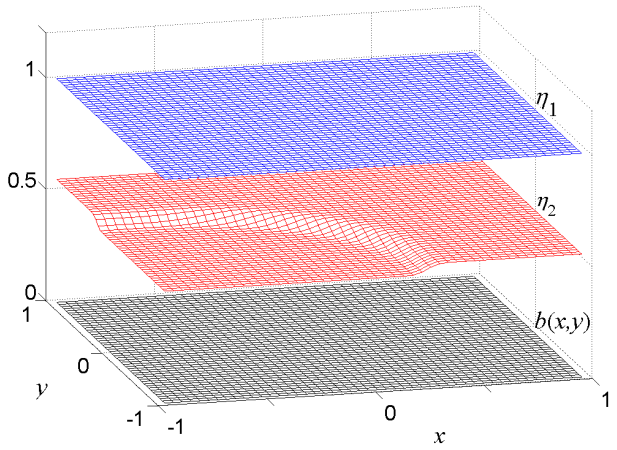

Figure 4.15: Propagation of 2D interface perturbation over flat bed at $t = 0.1$: Ψ_{9-9}.

4.4.4 Propagation of interface perturbation over a hump

The test is adapted from Kurganov & Petrova (2009). The initial conditions are the same as the previous test (4.24). The round-shaped interface perturbation is advected in the north-east direction by a uniform flow of magnitude 2.5 m/s in both directions towards a hump described by

$$b(x, y) = 0.05\exp(-100(x^2 + y^2)). \tag{4.25}$$

The domain is given by $(x, y) \in [-1, 1]$ and the boundary condition is transmissive. Again, a second set of seeding points is applied to the initial discontinuity and the simulation is performed until $t = 0.1$, using grid configuration Ψ_{9-9}. Figure 4.16 shows the free surface and interface at the end of the simulation.

Physically, the flow decelerates immediately upstream, but accelerates immediately downstream in the vicinity of the hump. As the interface perturbation approaches the hump, localised transcritical condition is reached such that a jump occurs just downstream of the hump, whereas a backwater flow develops just upstream of the hump. Both the jump and the backwater on the free surface are more pronounced compared to the interface. Due to the localised point effect of the 2D hump, it can be observed that complicated wave structure develops at both the interface and the free surface. The results are in excellent agreement with those of Kurganov & Petrova (2009).

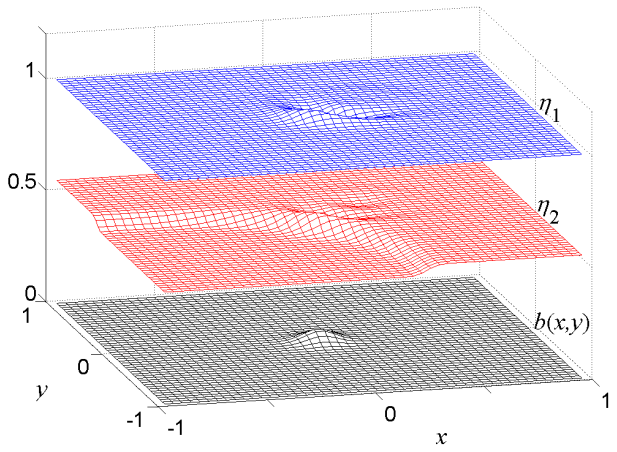

Figure 4.16: Propagation of 2D interface perturbation over a hump at $t = 0.1$: Ψ_{9-9}.

4.4.5 Internal circular dam break

An internal circular dam break with large discontinuity is considered. The initial condition is given by:

$$h_1 = \begin{cases} 1.8 & \text{if} \quad x^2 + y^2 > 4, \\ 0.2 & \text{if} \quad x^2 + y^2 \leq 4, \end{cases} \quad \text{and} \quad h_2 = 2 - h_1, \tag{4.26}$$

where the fluid layers are initially at rest. The domain is given by $(x, y) \in [-5, 5]$ and open boundary conditions are applied. An adaptive quadtree grid Ψ_{6-8} is adopted as a compromise between speed and higher resolution in the region of interest. Figure 4.17 shows the grid evolution in the early stage of the dam break. A set of seeding points is applied along the initial discontinuity as shown at $t = 0$. As the front propagates further, a large proportion of the domain is subdivided to the maximum level of division due to the presence of large free surface and interface gradients. Figure 4.18 shows that as the interface evolves over time, the free surface remains essentially horizontal. The problem is analogous to the circular dam break problem of a single layer flow (e.g. Toro, 2001), where an outward-propagating cicular shock wave and an inward-propagating circular rarefection wave can be observed. At $t = 5$ (Figure 4.18*vi*), the rarefaction wave has reached the centre of the domain, resulting in a localised point of pronounced high gradient. The results are in excellent agreement

with those reported by Castro *et al.* (2009).

In order to examine what happens next, a larger domain of $(x, y) \in [-10, 10]$ is used and the same test repeated. It is observed that the the circular rarefaction wave eventually implodes at the centre of the domain and is reflected, producing a dip in the interface which falls below the original ambient depth of the lower layer. In Figure 4.19, it can be seen that at time $t = 20$, a region with near zero lower layer depth is produced in the centre of the domain.

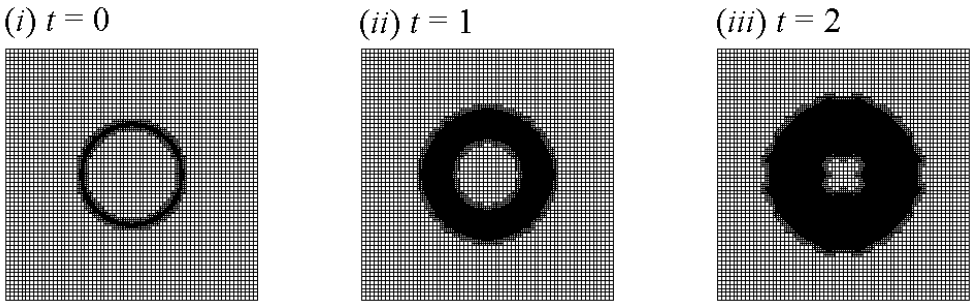

Figure 4.17: Internal circular dam break: Grid evolution using configuration Ψ_{6-8}.

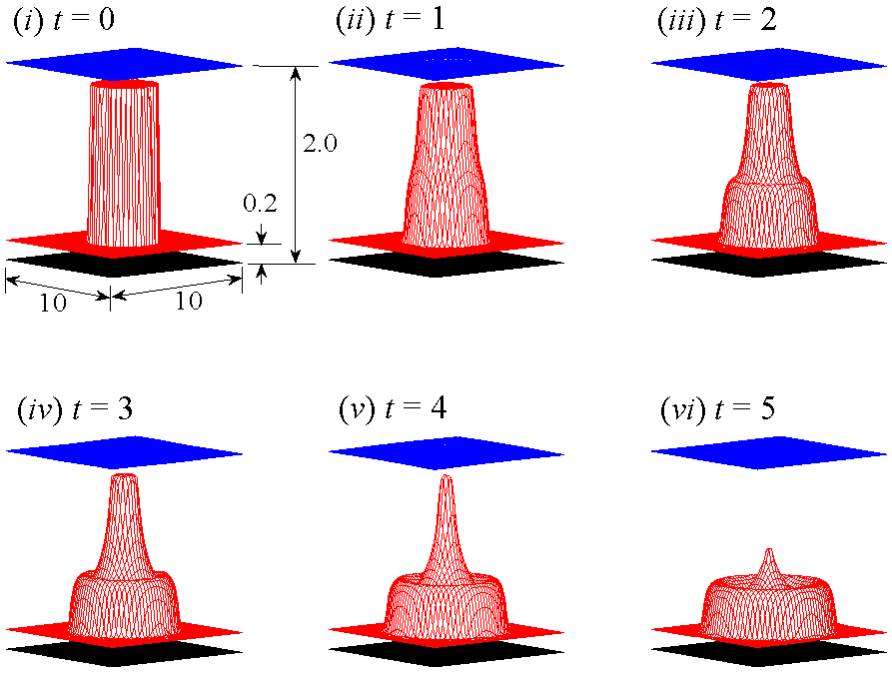

Figure 4.18: Internal circular dam break over a flat bed: Plots showing interface evolution. Note that the free surface remains near horizontal throughout.

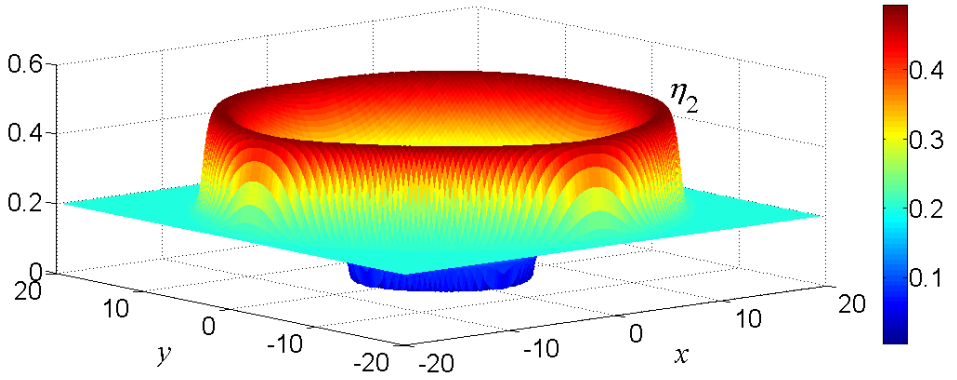

Figure 4.19: Internal circular dam break over a flat bed: Expansion of interface circular rarefaction wave at time $t = 20$.

4.4.6 Partial dam break

In this section, the partial dam break problem studied by Paz *et al.* (2010) is considered (Figure 4.20). The variables and parameters are made dimensionless by using $h_1 = 1$, $r = 0.25$, and $g = 1$. The initial condition is such that the fluids in both layers are at rest and

$$(h_1, h_2) = \begin{cases} (1.0, 1.0) & \text{if} \quad x \leq 0, \\ (0.75, 0.75) & \text{if} \quad x > 0, \end{cases} . \tag{4.27}$$

The domain is given by $(x, y) \in [-10, 10]$ with reflective lateral boundary conditions. A levee is located at $x = 0$ with a symmetrical gap of size 10, which is half the width of the domain. The gap, being also the location of the initial discontinuity, is seeded for cell refinement prior to the beginning of simulation. Adaptive grid Ψ_{6-8} is used.

Figure 4.21 and Figure 4.22 show the sequential development of the partial dam break at the free surface and interface, respectively. The contour plots for the evolution of the free surface and interface are given in Figure 4.23 and Figure 4.24, respectively. Propagation of fluid masses from each layer is evident across the gap and eventually both the free surface and interface approach horizontal (not shown). As the fluid masses propagate across the gap into the downstream end, two vortices are generated in the lee of the levee. Later, the direction of net mass flow is reversed.

Consequently, another two pair of vortices develop at the upstream side of the levee. The vortices on the lee side of the lower layer appear to be more pronounced than those in the upper layer. Moreover, the positions of the vortices in each layer do not exactly coincide. These features are properly captured by the adaptive grid, as shown in Figure 4.25. It is interesting to note that a pair of twin-vortices can be observed developing in the lower layer on the upstream side of the levee (Figure 4.24*vi*).

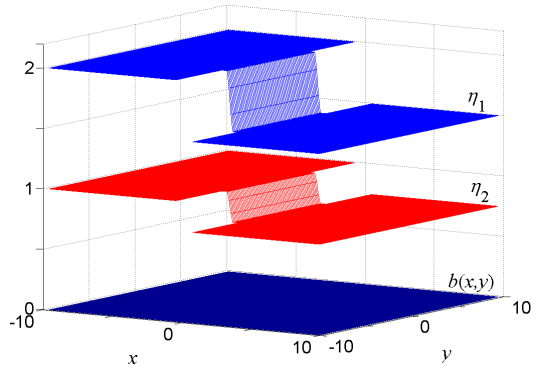

Figure 4.20: Partial dam break over a flat bed: Initial condition. Note that the gap is centred with a width of 10 units; the levees (not shown) have zero thickness.

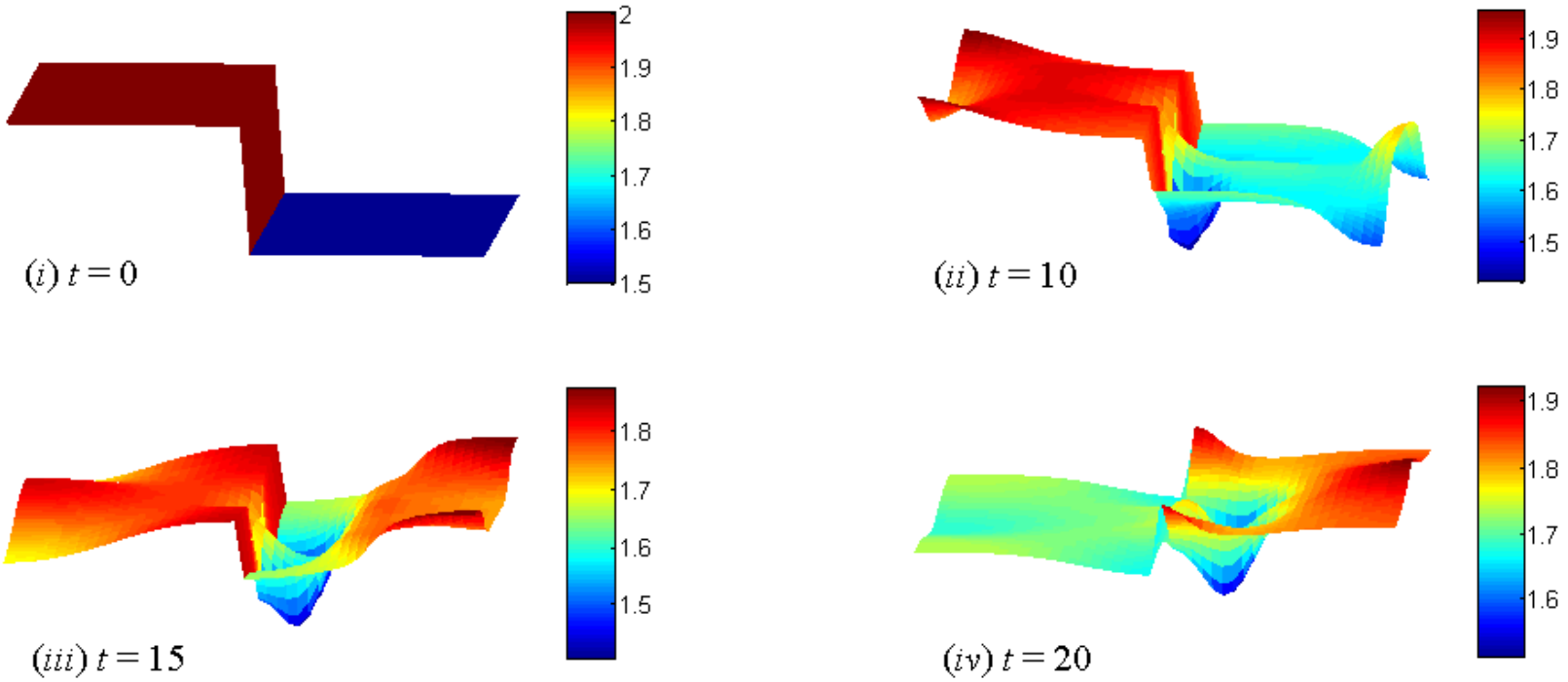

Figure 4.21: Partial dam break over a flat bed: *Free surface* evolution.

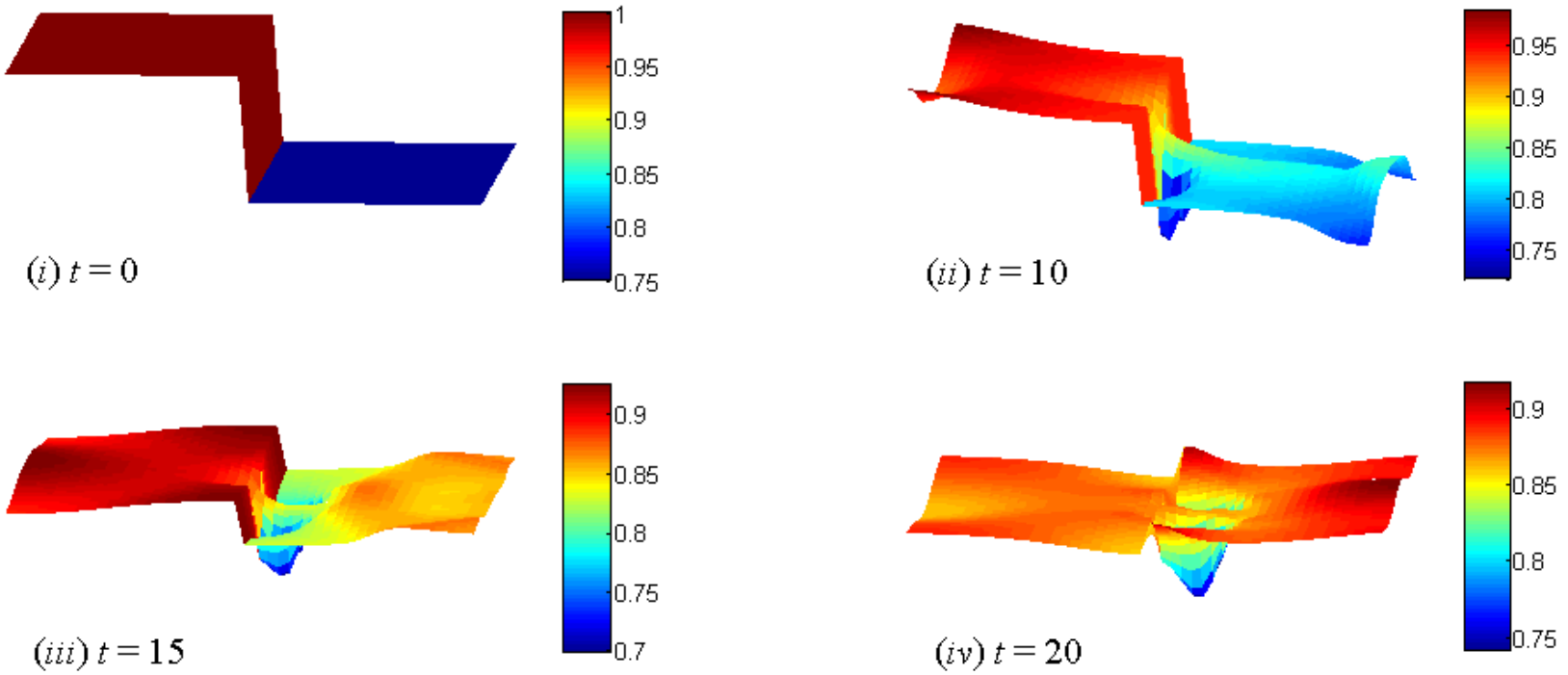

Figure 4.22: Partial dam break over a flat bed: *Interface* evolution.

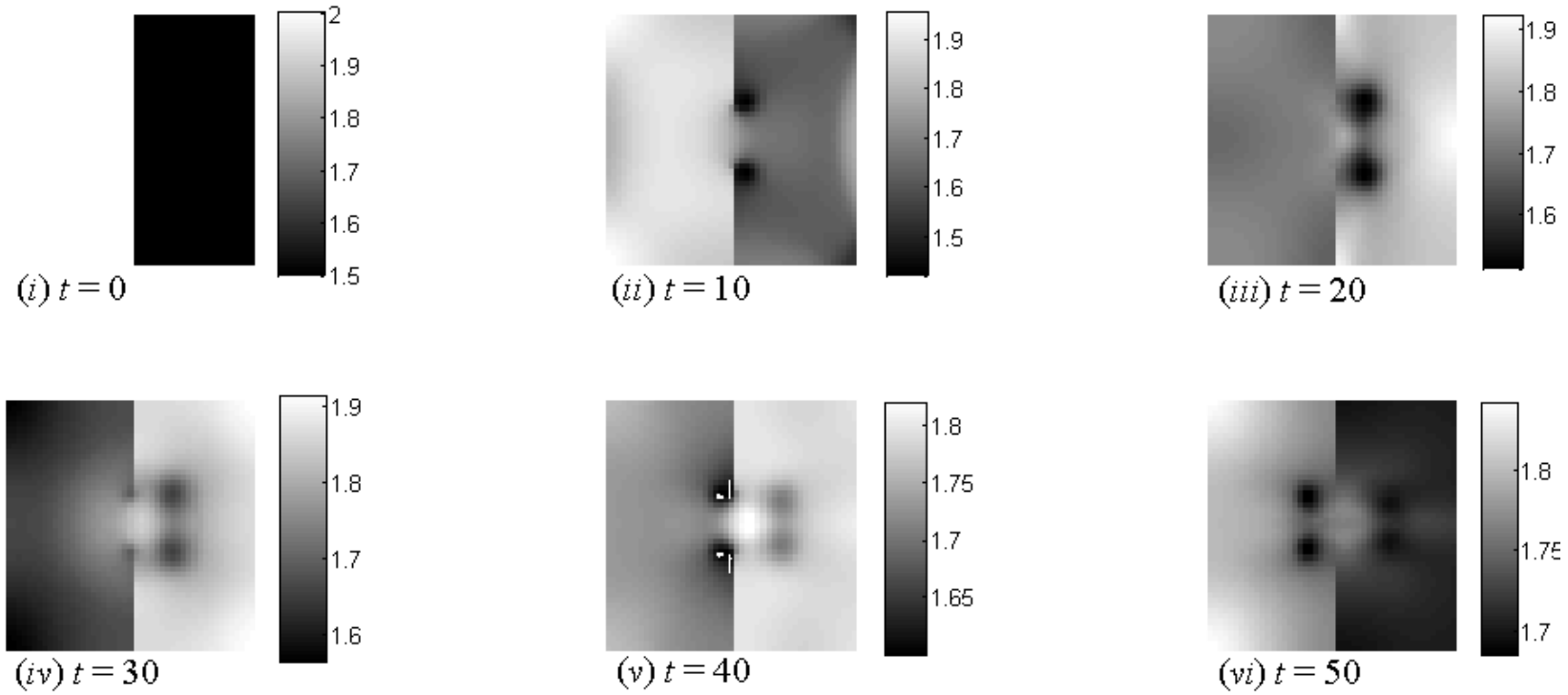

Figure 4.23: Partial dam break over a flat bed: *Free surface* contour.

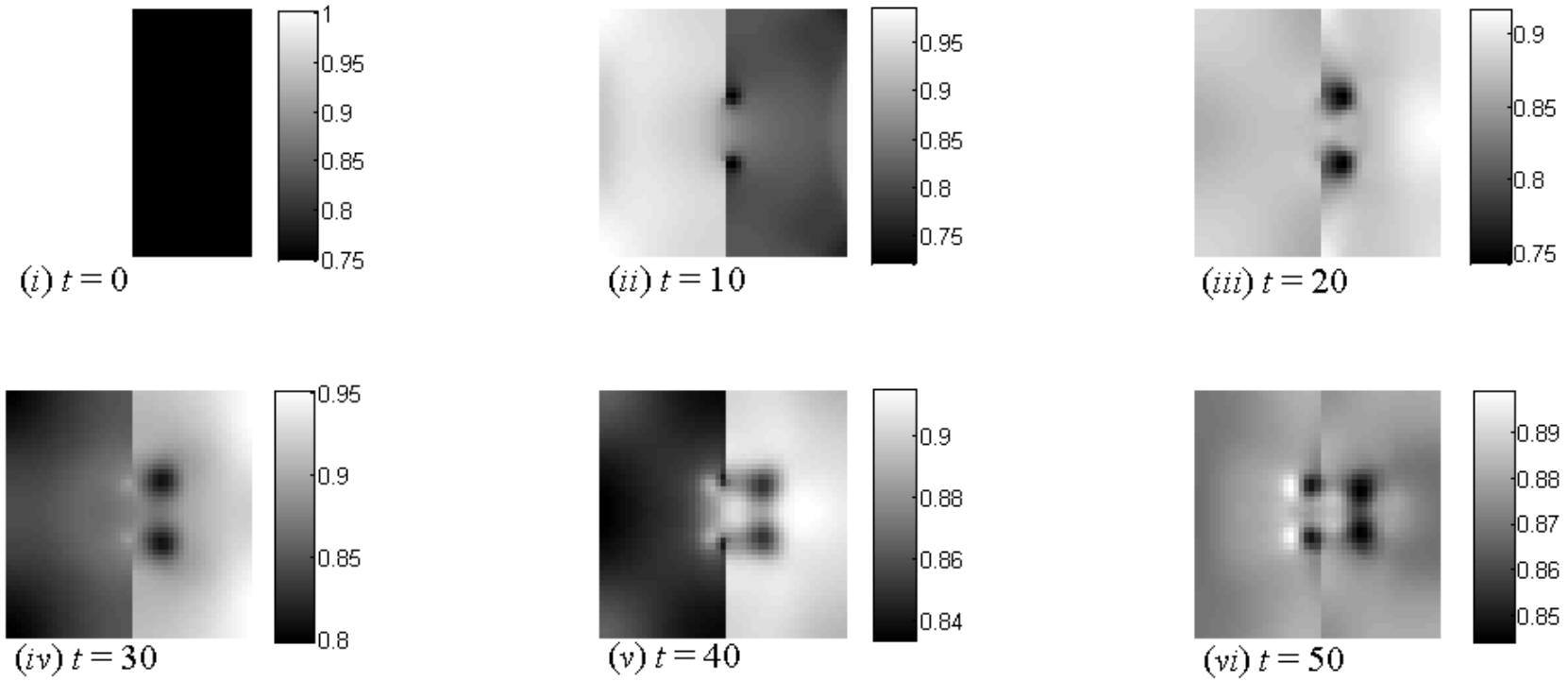

Figure 4.24: Partial dam break over a flat bed: *Interface* contour.

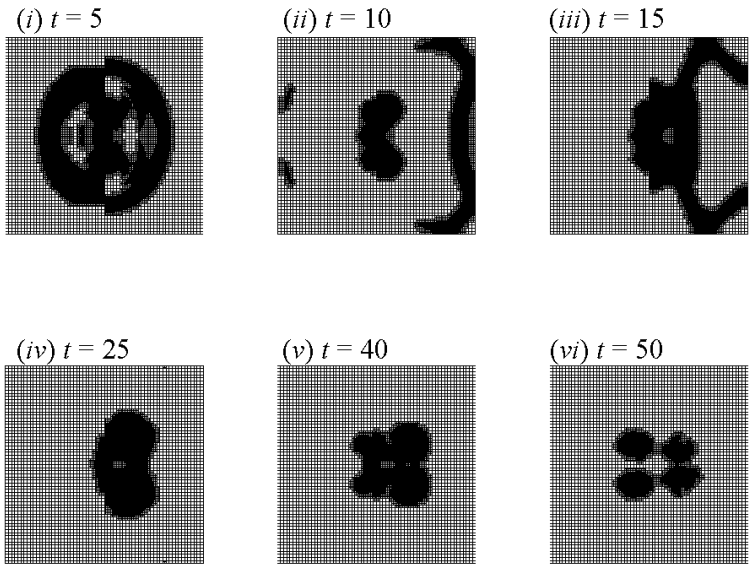

Figure 4.25: Partial dam break: Grid evolution using configuration Ψ_{6-8}.

4.5 Grid convergence tests

This section studies the effect of different grid configurations. For the purpose of comparison, the Grid Convergence Index (GCI) (Roache & Knupp, 1993; Roache, 1994) is evaluated at all grid points:

$$GCI = \frac{3|e|}{r_0^p - 1}, \quad e = 100\frac{\eta^0 - \eta}{\eta^0}, \tag{4.28}$$

where e is the percentage relative error, η^0 and η are the elevations of the surface or interface from a fixed datum, computed using the finer and the coarser grid, respectively. Generally, the GCI values computed using the surface and interface elevations have the same order of accuracy as those obtained using the velocity fields. Hence only the former are presented in the discussions that follow. The grid refinement ratio r_0 is given by $\Delta x/\Delta x^0$, and the formal order of accuracy of the numerical scheme p is 2. Asymptotic range is considered to be achieved when $GCI_{23} = r_0^p GCI_{12}$, where GCI_{12} compares the finer grid to the intermediate grid, and GCI_{23} compares the intermediate grid to the coarser grid (Roache, 1994).

Grid adaptation is performed based on the maximum R.M.S of the surface and

interface gradients:

$$\Phi = \max(\Phi_1, \Phi_2), \quad \Phi_{1,2} = \sqrt{(\frac{\partial \eta_{1,2}}{\partial x})^2 + (\frac{\partial \eta_{1,2}}{\partial y})^2}, \tag{4.29}$$

where grid refinement and coarsening are performed when Φ exceeds 0.05 and falls below 0.02 (i.e. 5% and 2% gradient), respectively. Rogers *et al.* (2004) showed that there is minimal gain by not adapting every time step. Hence, the calculation of Φ and adaptation are performed at every time step.

4.5.1 Propagation of interface perturbation over flat bed

Consider the propagation of interface perturbation over flat bed as in Section 4.4.3. Figure 4.26 illustrates the GCI contours of the free surface and interface when different grid configurations are adopted. Overall, the results indicate that the computations converge to the asymptotic value, with slightly higher differences at the interface but still well within the acceptable range. Some differences due to small oscillations can be observed in Figure 4.26*ii*, but disappear at finer resolutions (Figure 4.26*i*). In general, solutions of the free surface are unlikely to contain marked features of interest for two-layer problems with level initial free surface condition. Note that the staircase features at the edges are a consequence of adaptation at the boundaries. Examining Figure 4.26*iii* and Figure 4.26*iv*, it is worth noting that grid convergence of the Ψ_{5-9} configuration compared to Ψ_{9-9}, is marginally poorer than the Ψ_{6-8} configuration compared to Ψ_{8-8}. This suggests that with larger difference between the minimum and maximum level of subdivisions, the result may be partially affected by the region of poorer resolution. Figure 4.27 plots the adapted grid of both configurations at $t = 0.1$.

Figure 4.28 compares the computational efficiency of the various grid configurations. It is evident from the figure that the CPU time increases linearly when the level of subdivision of the regular grids is increased. For the adaptive grid configurations, the normalized CPU time is plotted against the maximum number of cells at

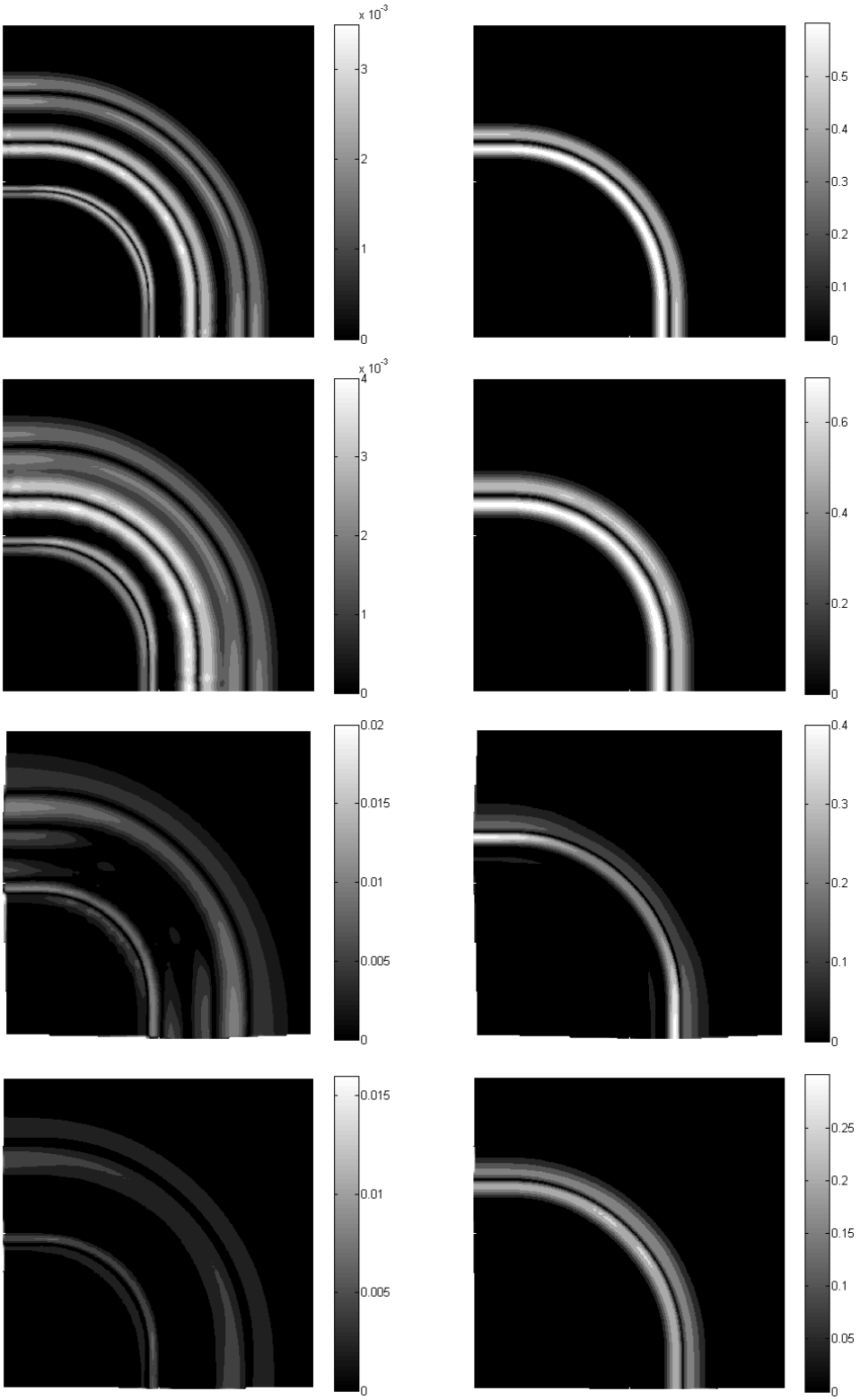

Figure 4.26: Propagation of 2D interface perturbation over a flat bed: *GCI* contours at the free surface (left) and interface (right), comparing grid configurations (from top to bottom) (*i*) Ψ_{9-9} and Ψ_{8-8}, (*ii*) Ψ_{8-8} and Ψ_{7-7}, (*iii*) Ψ_{9-9} and Ψ_{5-9}, and (*iv*) Ψ_{8-8} and Ψ_{6-8}.

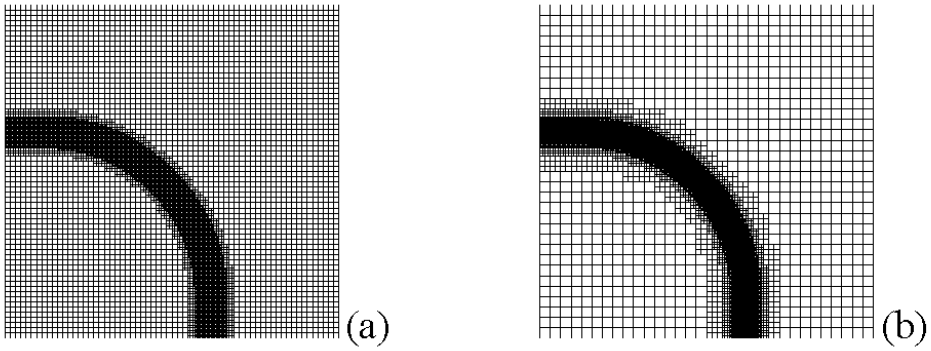

Figure 4.27: Propagation of 2D interface perturbation over a flat bed: Adapted quadtree grid for (a) Ψ_{6-8} and (b) Ψ_{5-9} at $t = 0.1$.

the end of the simulations. Note that the time used for adaptation varies throughout the simulations. For the adaptive grids Ψ_{6-8} and Ψ_{5-9}, the maximum times used for the purpose of adaptation at any time interval are 0.0119 and 0.0318, respectively, normalized by the respective total time of simulation. Longer time is needed for Ψ_{5-9} compared to Ψ_{6-8} because refinement in the region of large gradient creates more cells than the reduction offered by lower resolution in the rest of the domain. The negligible adaptation cost and the accuracy of the results obtained suggest that the adaptive quadtree grid is an attractive choice for the present scheme.

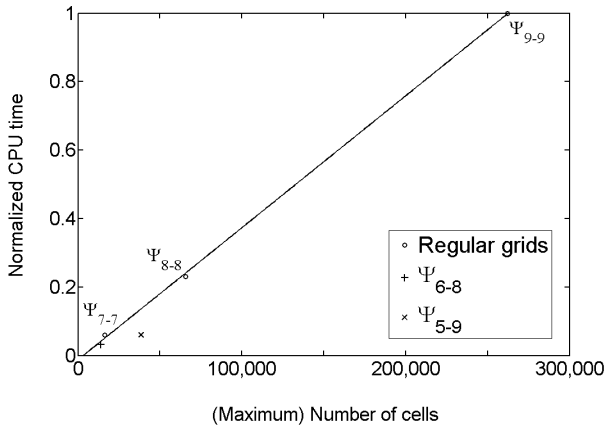

Figure 4.28: Propagation of 2D interface perturbation over a flat bed: Normalized CPU times for the different grid configurations.

4.5.2 Propagation of interface perturbation over a hump

Next, consider the propagation of interface perturbation over a hump as in Section 4.4.4. As noted previously, a complicated wave structure develops at both the interface and the free surface when the interface perturbation approaches the hump. Consequently, additional grid adaptation is performed in the vicinity of the hump (Figure 4.29), resulting in higher numbers of cells for both Ψ_{6-8} and Ψ_{5-9} configurations and hence, slightly longer computation times, whereas the numbers of cells and computation times for the regular grids remain the same as for the flat bed case. The normalized adaptive times per time step for Ψ_{6-8} and Ψ_{5-9} are 0.0148 and 0.0328, respectively, which are slightly higher values than obtained from the flat bed case (Figure 4.30).

Using the solutions obtained from grid configuration Ψ_{9-9} as a basis for comparison, Figure 4.31 shows that the scheme exceeds second order accuracy when using regular grid configurations (e.g. Ψ_{7-7}). On the coarser grid Ψ_{5-5}, the numerical results predict an L1-error that is smaller than expected and the solution fails to converge. At higher resolution of Ψ_{8-8}, the order of accuracy reduces to just above one (≈ 1.3) probably because the round-off error becomes dominant with smaller grid size. In addition, higher resolution in the refinement results in a globally smaller time step which increases the computational time taken considerably. Hence, the choice of the minimum level of grid refinement is governed by accuracy whereas the choice of the maximum level of subdivision both accuracy and computational time. The Ψ_{6-8} and Ψ_{5-9} configurations have similar L1-errors. In comparison with the Ψ_{6-6} configuration, it seems that Ψ_{6-8} produces a relatively higher order of accuracy (≈ 2) compared to Ψ_{5-9} (≈ 1.3). Figure 4.32 shows the correlation between the L1-error and the normalized CPU time for the different grid configurations. The adaptive configuration Ψ_{6-8} is more cost efficient compared to Ψ_{5-9} whilst the L1-errors are in the same order and just slightly higher than the regular grid Ψ_{8-8} which takes

considerably longer CPU time. Hence it is concluded that the adaptive grid Ψ_{6-8} is the more attractive choice compared to Ψ_{5-9} considering the compromise between accuracy and the cost of computation.

Figure 4.33 presents the GCI contours of the free surface and interface when different grid configurations are adopted. Here, the results are inferior overall to those of the flat bed case (Section 4.4.3), but maintain the trend where better convergence is observed at the surface. The GCI values, though higher in the vicinity of the hump, are still well within the acceptable range except for the case comparing the regular grid Ψ_{9-9} and the adaptive grid Ψ_{5-9}, where $GCI > 4.0$ near the interface. Comparing the regular grid Ψ_{8-8} and the adaptive grid Ψ_{6-8} shows better convergence (as also found for the flat bed case).

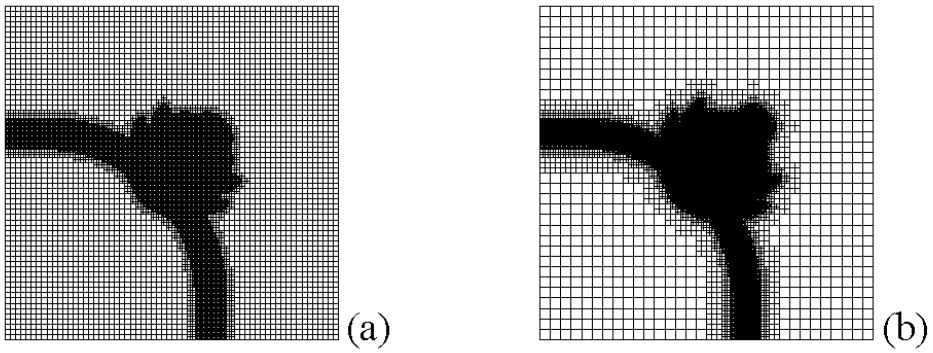

Figure 4.29: Propagation of 2D interface perturbation over a hump: Adapted quadtree grids for (a) Ψ_{6-8} and (b) Ψ_{5-9} at $t = 0.1$.

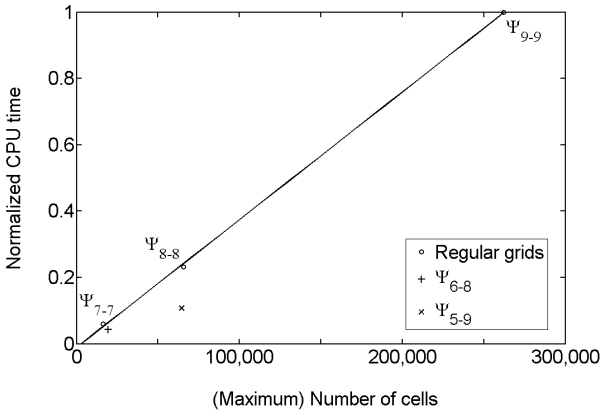

Figure 4.30: Propagation of 2D interface perturbation over a hump: Normalized CPU times for the different grid configurations.

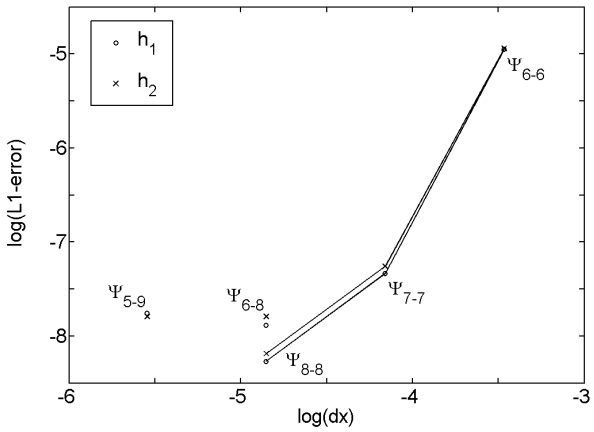

Figure 4.31: Propagation of 2D interface perturbation over a hump: Error analysis.

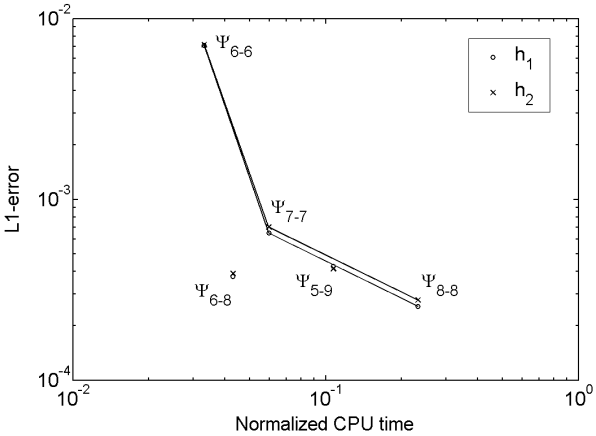

Figure 4.32: Propagation of 2D interface perturbation over a hump: Correlation between L1-error and normalized CPU time.

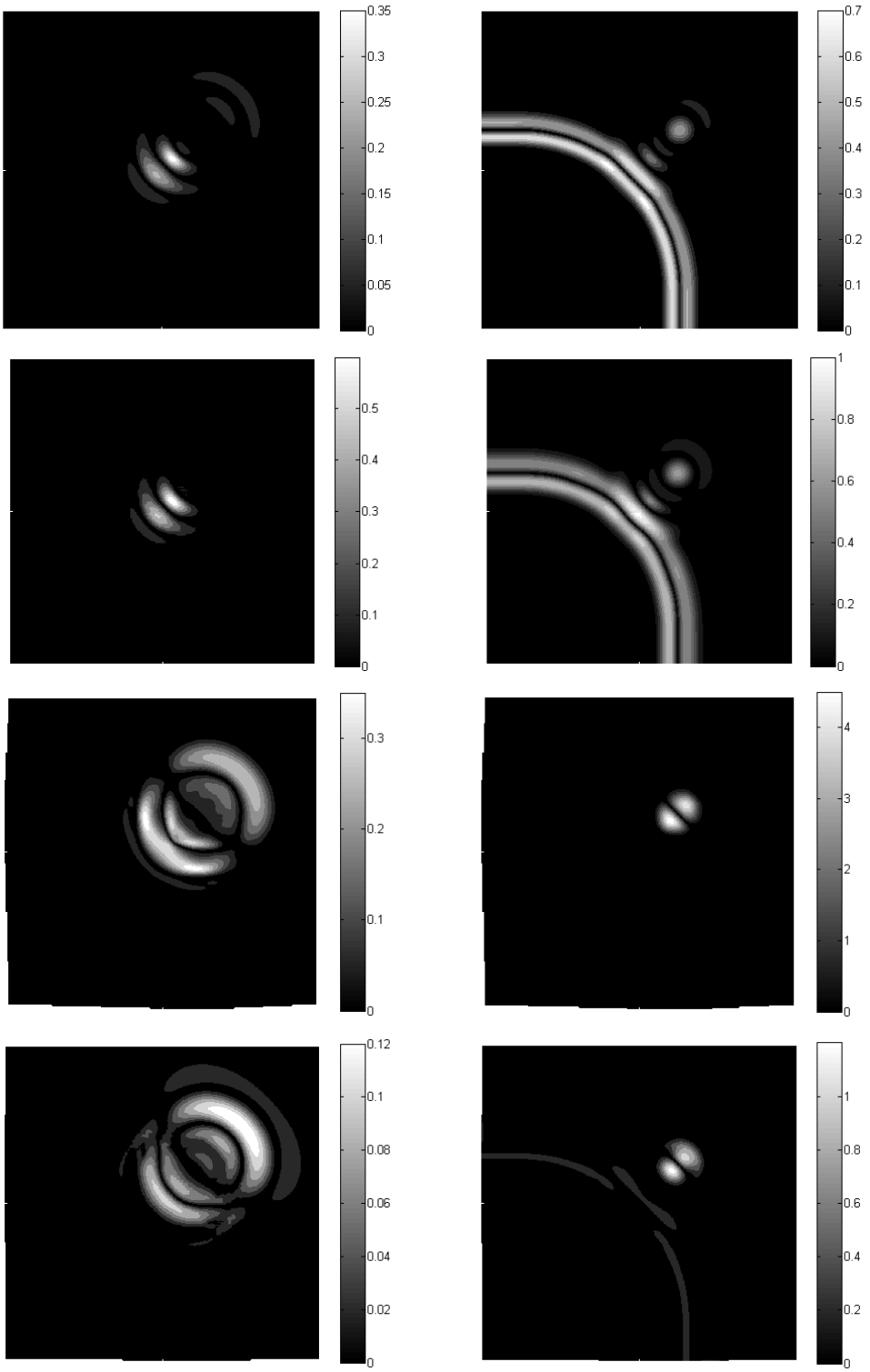

Figure 4.33: Propagation of 2D interface perturbation over a hump: GCI contours at the free surface (left) and interface (right), comparing grid configurations (from top to bottom) (*i*) Ψ_{9-9} and Ψ_{8-8}, (*ii*) Ψ_{8-8} and Ψ_{7-7}, (*iii*) Ψ_{9-9} and Ψ_{5-9}, and (*iv*) Ψ_{8-8} and Ψ_{6-8}.

4.5.3 Tidal channel with a hump and a constriction

In this section, the model is used to simulate a simple tidal flow in a channel characterised by a hump and a constriction. The aim is to examine the dynamics of tidal effects on the behaviour of the two-layer flow. The problem is inspired by the works of Castro *et al.* (2004) and Castro *et al.* (2007*a*) where tidal and exchange flows in the Straits of Gibraltar were studied using a two-layer one-dimensional model with a width function.

Consider a narrow channel (Figure 4.34) of length $x \in [-10, 10]$, with a sill placed at $x = 0$ and a contraction at $x = 1$. The bed function $b(x)$ and width function $\sigma(x)$ are given by:

$$b(x) = \begin{cases} 1.2\exp(-x^2) & \text{if } x \in [-4, 4] \\ 0.5\exp(-(x+10)^2) & \text{if } x \leq -8 \\ 0 & \text{otherwise} \end{cases}, \tag{4.30}$$

and

$$\sigma(x) = \begin{cases} 2.5 + 1.5(1 - \exp(-a^2(x-1)^2)) & \text{if } x \in [-1, 2] \\ 3.7 & \text{otherwise} \end{cases}, \tag{4.31}$$

respectively, the latter of which is adapted from Castro *et al.* (2004), where

$$a = \begin{cases} 0.637 & \text{if } -1 \leq x \leq 1 \\ 1.273 & \text{if } 1 < x \leq 2 \end{cases}. \tag{4.32}$$

Consider two fluids with constant densities of ratio $r = 0.98$, the lock exchange experiment is conducted using the initial conditions:

$$(h_1, h_2) = \begin{cases} (1.5, 0.5) & \text{if } x \leq 0 \\ (0.2, 1.8) & \text{if } x > 0 \end{cases}, \tag{4.33}$$

and water at rest. Physically, this is akin to having a vertical barrier located at $x = 0$ which is instantaneously removed at $t = 0$. The effect of bottom friction τ_b and interfacial friction τ_f are included into the model as additional source terms in the form of:

$$\begin{cases} \tau_{bx} = -\rho_j C_b u_j \sqrt{u_j^2 + v_j^2}, \\ \tau_{by} = -\rho_j C_b v_j \sqrt{u_j^2 + v_j^2}, \end{cases} \quad j = 1, 2, \tag{4.34}$$

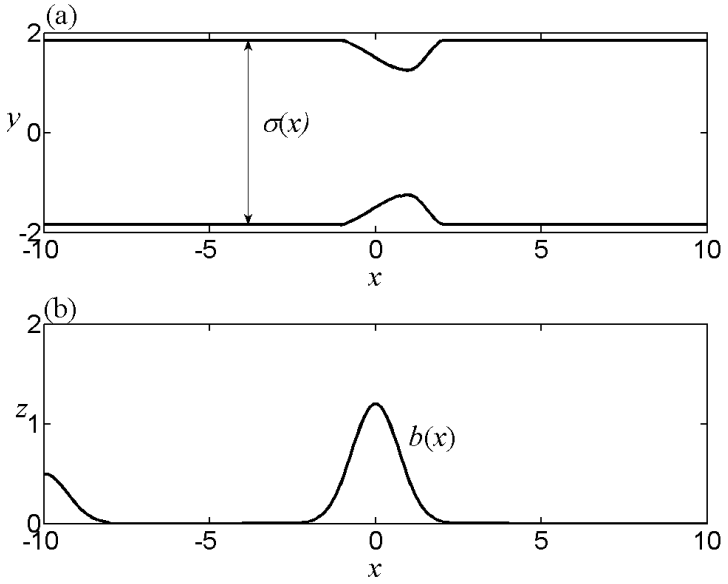

Figure 4.34: A narrow channel with a hump and a constriction: (a) plan view of channel width profile, and (b) side view of channel bed profile.

and

$$\begin{cases} \tau_{fx} = -\rho_2 C_f u_r \sqrt{u_r^2 + v_r^2}, \\ \tau_{fy} = -\rho_2 C_f v_r \sqrt{u_r^2 + v_r^2}, \end{cases} \tag{4.35}$$

where $(u_r, v_r) = (u_1 - u_2, v_1 - v_2)$. Following Murillo *et al.* (2009), these additional source terms are treated in the same manner as the bed topography in order to maintain overall well-balanced property for steady state with non-zero velocity. The dimensionless bottom friction coefficient C_b and interface friction coefficient C_f are arbitrarily taken as 5×10^{-3} and 5×10^{-4}, respectively.

The model is integrated until steady state is reached using exchange flow boundary conditions, i.e. $Q_1 = -Q_2$. Figure 4.35 shows the evolution of the interface and the grid adaptation during the initial stage of simulation. The surface profile remains near horizontal throughout and hence is omitted for clarity. The plots show, that after the initial transient, the interface at both upstream and downstream boundaries approaches horizontal and the coarser grid is adopted. Finer resolution is maintained at the vicinity of the constriction and the hump where there is considerable interface gradient. Figure 4.36 shows the GCI comparing the steady state solutions of grid

configurations Ψ_{8-8} and Ψ_{6-8}. Here, the GCI values of the free surface and interface are very small except a narrow band of the latter which approaches 2.5 at the jump location. The L1-errors based on simulated velocities are 0.0043 and 0.0023 for the upper and lower layer, respectively; the L1-errors based on simulated depths are 0.0039 for both layers.

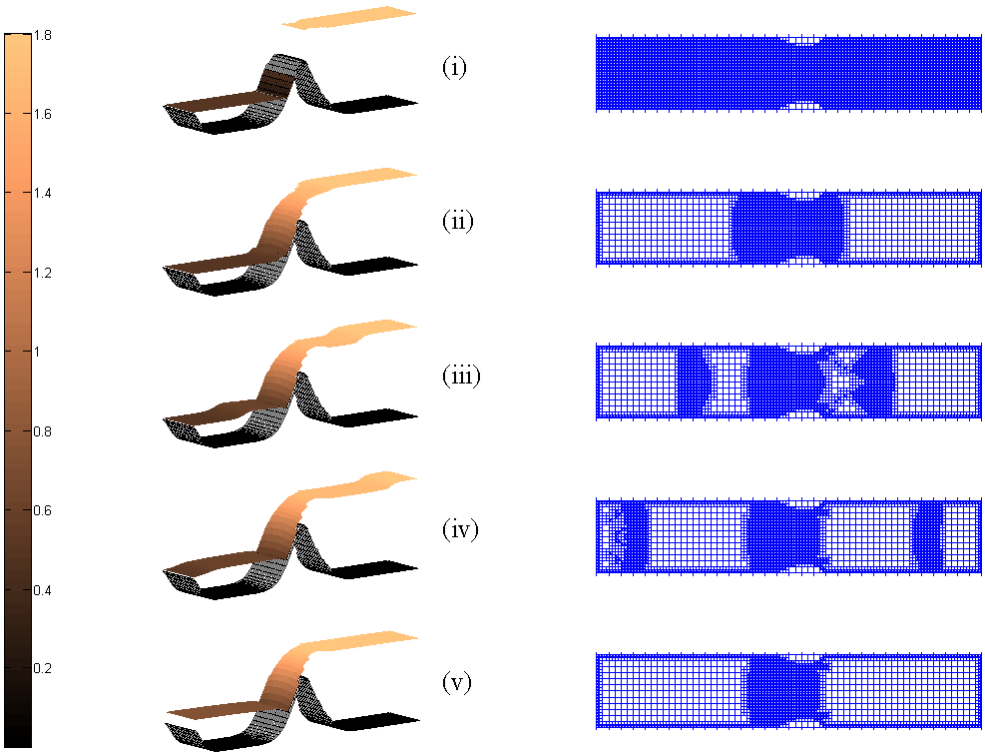

Figure 4.35: 2D lock exchange in a narrow channel with a hump and a constriction: Plots showing evolution of interface elevation with reference to the bed (left), and grid adaptation (right) at times $t = 0, 5, 10, 15, 30$ (*i*-*v*).

Figure 4.36: 2D lock exchange steady state solution: GCI contours comparing grid configurations Ψ_{8-8} and Ψ_{6-8} at: (a) free surface, and (b) interface.

Using the above steady state solutions as the initial condition, tidal forcing is applied at the downstream open boundary while maintaining an exchange flow boundary condition at the upstream end. This initial condition describes an inflow of the denser fluid and an outflow of the less dense fluid at the downstream boundary, and the opposite at the upstream boundary. Physically, the downstream boundary represents connection to an open sea which acts as a reservoir of denser fluid, while the upstream represents consistent supply of riverine inflow. In the discussions that follow, the region between the humps is referred to as the basin.

The downstream tidal boundary condition associated with the variation of total water depth is given as a function of time by

$$h_1(x_B, t) + h_2(x_B, t) = \overline{h}_B - A\sin(\frac{2\pi t}{T}), \tag{4.36}$$

where the subscript B denotes specified values at the boundary. Here, $\overline{h}_B = 2$ is the total water depth, $A = 0.01$ is the surface elevation amplitude, T is the period of the tidal wave. The dimensionless tidal time is defined as $T\sqrt{g\overline{L}_v}/L_h$, where L_v and L_h are the vertical and horizontal scales, respectively, and $g = 9.81$ m/s^2 is the gravitational acceleration. Consider varied horizontal and vertical scales of 1:1000 and 1:10, respectively, the problem thus represents a 20 km long channel with minimum and maximum widths of 2.5 km and 3.7 km, respectively. The quiescent water depth is 20 m and the tidal range is 2 m. At the middle of the channel, the hump rises up to a height of 12 m above the horizontal bed. For the S_2 tide ($T = 12$ hour), the equivalent tidal period in the model is thus 136.6 s. At the boundaries, the depth and velocities of both layers are determined using Riemann invariants specified according to the internal Froude number Fr_j^2 of the respective layer, which is defined as

$$Fr_j^2 = U_j^2/(g'h_j), \quad j = 1, 2, \tag{4.37}$$

and the composite Froude number is given by

$$G^2 = Fr_1^2 + Fr_2^2 - (1 - r)Fr_1^2Fr_2^2. \tag{4.38}$$

Figure 4.37 shows the free surface and interface during the S_2 tidal cycle. At $t/T = 0.5$ when the downstream elevations are rising, strong currents flow into the basin in both the layers as observed from the plot of velocity vectors (not shown), and the flow approaches critical (Figure 4.38a) condition. At $t/T = 1.0$ when the downstream elevations are reducing, the current is reversed with net flow out of the basin. As shown in Figure 4.38b, the flow reaches supercritical condition resulting in a weak internal jump. Figure 4.39 shows the GCI comparing the solutions at $t/T = 1.0$ of grid configurations Ψ_{8-8} and Ψ_{6-8}. Here, the GCI values for both the free surface and interface are generally small but approach a maximum of up to 3.0 at the jump location. The L1-errors based on simulated velocities are 0.0038 and 0.0036 for the upper and lower layers, respectively; the L1-errors based on simulated depths are 0.0044 and 0.0043 for these layers.

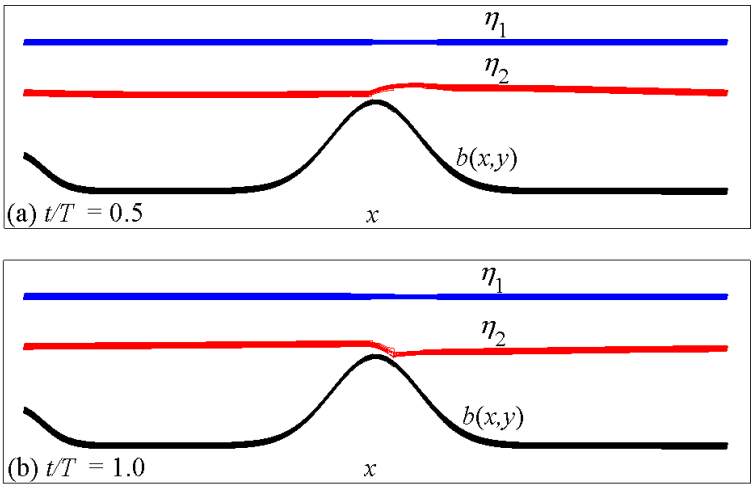

Figure 4.37: Tidal channel: Simulated free surface and interface in an S_2 tidal cycle using grid configuration Ψ_{6-8}.

The results above demonstrate the robustness of the present model in solving a two-dimensional tidal-exchange flow. Despite a relatively simplified representation of an actual tidal channel, the model is able to capture most of the physics of the tidal flows. The solutions obtained are highly dependent on the geometry of the domain, the scaling of the tidal period, as well as the bed friction and interfacial friction

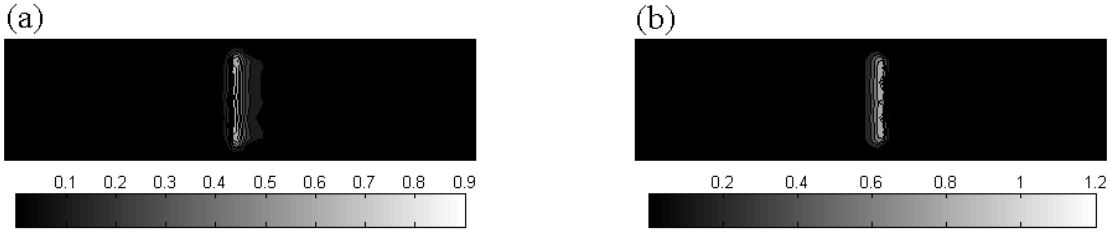

Figure 4.38: Tidal channel: Composite Froude number G^2 at (a) $t/T = 0.5$, and (b) $t/T = 1.0$.

Figure 4.39: Tidal-exchange flow: GCI contours comparing grid configurations Ψ_{8-8} and Ψ_{6-8} at $t/T = 1.0$: (a) free surface, and (b) interface.

coefficients. For the purpose of a full-scale study, a realistic geometry and tidal signal should be employed (e.g. Castro *et al.*, 2004, 2007*a*).

4.6 Application: Tidal-driven 2-layer flow in Tampa Bay, Florida

Tampa Bay (Figure 4.40), located to the west of central Florida in United States of America (USA), is the largest of the Florida estuaries. It comprises four subregions, namely Old Tampa Bay, Hillsborough Bay, and the Middle and Lower Tampa Bay. It is heavily used for shipping and recreation, as well as municipal fresh water consumption, sanitation requirements, and power generation. In addition, it is the home of four aquatic reserves for several species of marine life on both the state and federal list of endangered species (Weisberg & Zheng, 2006). With such heavy and diverse usage, the importance of ecological health of the estuary cannot be over-emphasized.

By classification, Tampa Bay constitutes a drowned river bed estuary with a mean depth ranging from 4 m at mean lowest low water up to 15 m along the dredged

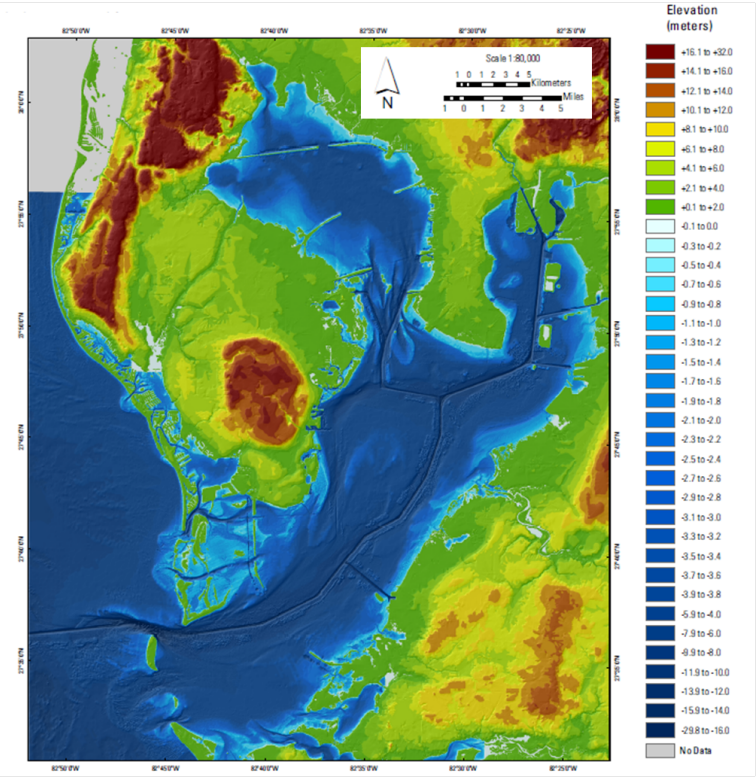

Figure 4.40: Tampa Bay topobathymetric data.
Source: U.S. Geological Survey Open-File Report 2007-1051 (revised), 2007.
`http://pubs.usgs.gov/of/2007/1051/`

navigational channel. The surface area of the estuary is approximately 1000 km^2, and that of the surrounding watershed (Figure 4.41) is approximately 4600 km^2. Hydrodynamic advection in the bay is governed primarily by tidal flow from the adjoining Gulf of Mexico, and to a lesser degree by river inflow and wind. Tidal flow, which accounts for up to 95% of the current energy, largely determines the transport of chemical tracers, nutrients, organic and inorganic micropollutants. Mean annual fresh water discharge is about 63 m^3/s. Despite being weaker by an order of magnitude compared to the tidal current, density-driven circulation remains an important mode of circulation (Weisberg & Zheng, 2006; Meyers & Luther, 2008).

The model domain, geographical features, and inflow locations are shown in Figure 4.42, and the bathymetry data is approximated from Figure 4.40. The bay length is about 50 km with a maximum width of approximately 15 km at the midsection.

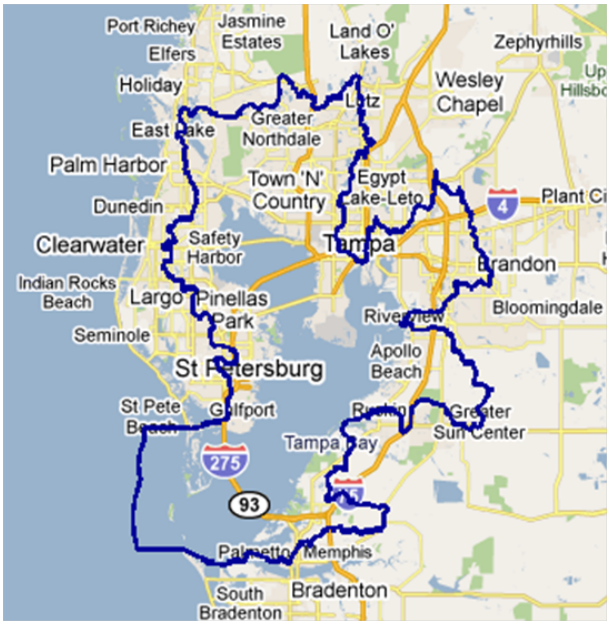

Figure 4.41: Tampa Bay watershed.
Source: Florida's Water homepage, `http://www.protectingourwater.org/`.

For the purpose of the present study, 13 river inflow locations are used, including Hillsborough (23.8%), Manatee (15.9%), Alafia (20.6%), Little Manatee (9.5%), with the balance contributed by the rest of the locations in proportion to their respective catchment size. Low fresh water inflow equivalent to 1.2×10^6 m^3/day (Meyers & Luther, 2008) is considered such that the initial thickness of the upper layer may be assumed constant at 2 m depth arbitrarily. The densities of the upper and lower layers are taken to be 1020.65 kgm^{-3} and 1025 kgm^{-3}, respectively, i.e. density ratio $r = 0.99$. A diurnal tide of 24-hour period with tidal range of 1 m at the tidal boundary at the southwest of the domain is used in the simulation (see Figure 4.42).

An initial grid configuration Φ_{9-9} is used, which is coarsened to Φ_{6-9} immediately after the first time step (see Figure 4.43 for a typical example). Maximum and minimum horizontal grid resolutions are thus 97.66 m and 781.25 m, respectively. Maximum grid refinement is applied at the mouth of Hillsborough River, which represents the main inflow location and thus localized high velocity gradient. This highest resolution is also used for the strait between Old Tampa Bay and Middle Tampa

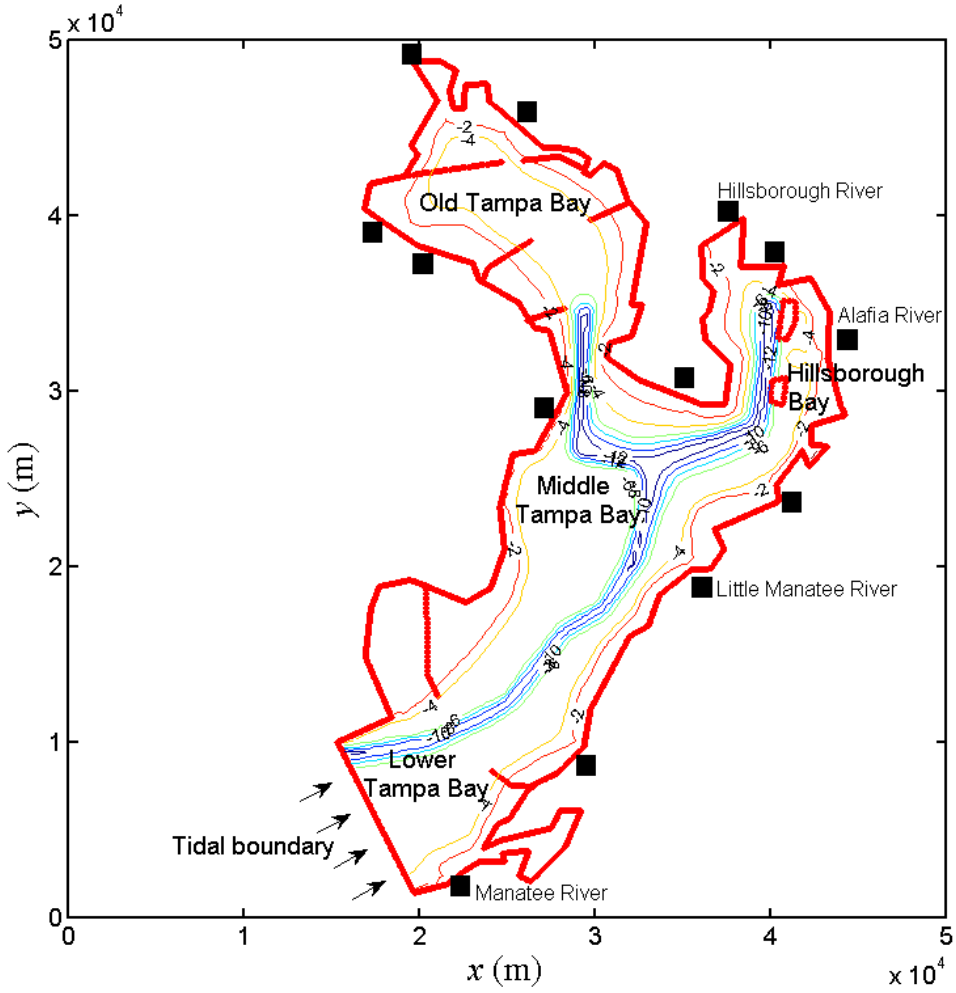

Figure 4.42: Tampa Bay computational domain showing tidal boundary, river inlets (■), and discretized bathymetry.

Bay, as well as at the wet-dry interface of the lower layer to circumvent interpolation at the transition between single and dual-layer flow. The bed Manning's roughness coefficient is taken as $n = 0.025$ s.m$^{-1/3}$ (Shi *et al.*, 2003), and the interfacial stress coefficient approximated at 0.03.

Figure 4.44 shows the depth-averaged streamlines during flood and ebb tide in the bay. Figure 4.45 and Figure 4.46 show the simulated flow field in the upper and lower layer, respectively, in Tampa Bay over a typical 24-h cycle for low fresh water inflow condition. The results verify that the circulation is tidal-dominant. For the grid scale chosen, no distinct recirculation zone is identified despite the presence of

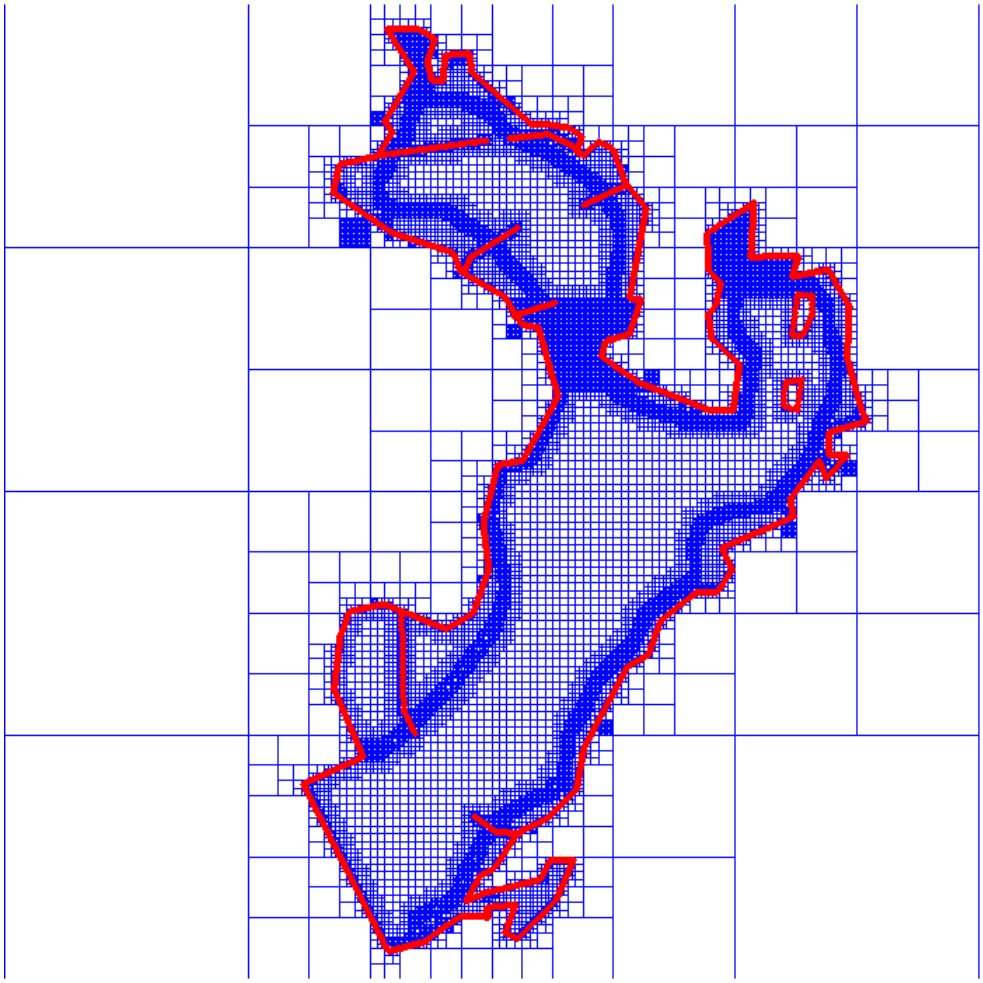

Figure 4.43: Tampa Bay computational grid layout using configuration Φ_{6-9}. Plot showing maximum subdivision used in specific area (e.g. in the vicinity of Hillsborough inlet, and the narrow strait between Old Tampa bay and Middle Tampa Bay), and at the transition from two-layer to single layer, typically near the domain boundary.

island structures and groynes in the domain. Flow features observed in the two layers are identical, largely due to the dominating effect of tidal flushing. The average velocity in the surface layer is 2.9 cm/s which is comparable to those reported by Weisberg & Zheng (2006). It is worth noting that the velocity in the denser layer below is smaller by up to two orders of magnitude than that of the surface layer for the present low inflow case considered. Hence, tidal energy is essentially concentrated in the upper layer whereas little flow takes place in the layer beneath as shall be shown in Section 5.5. The relatively low flow velocity implies there is little or no vertical

convection between the layers, and so the two-layer immiscible model is a reasonable approximation for the problem.

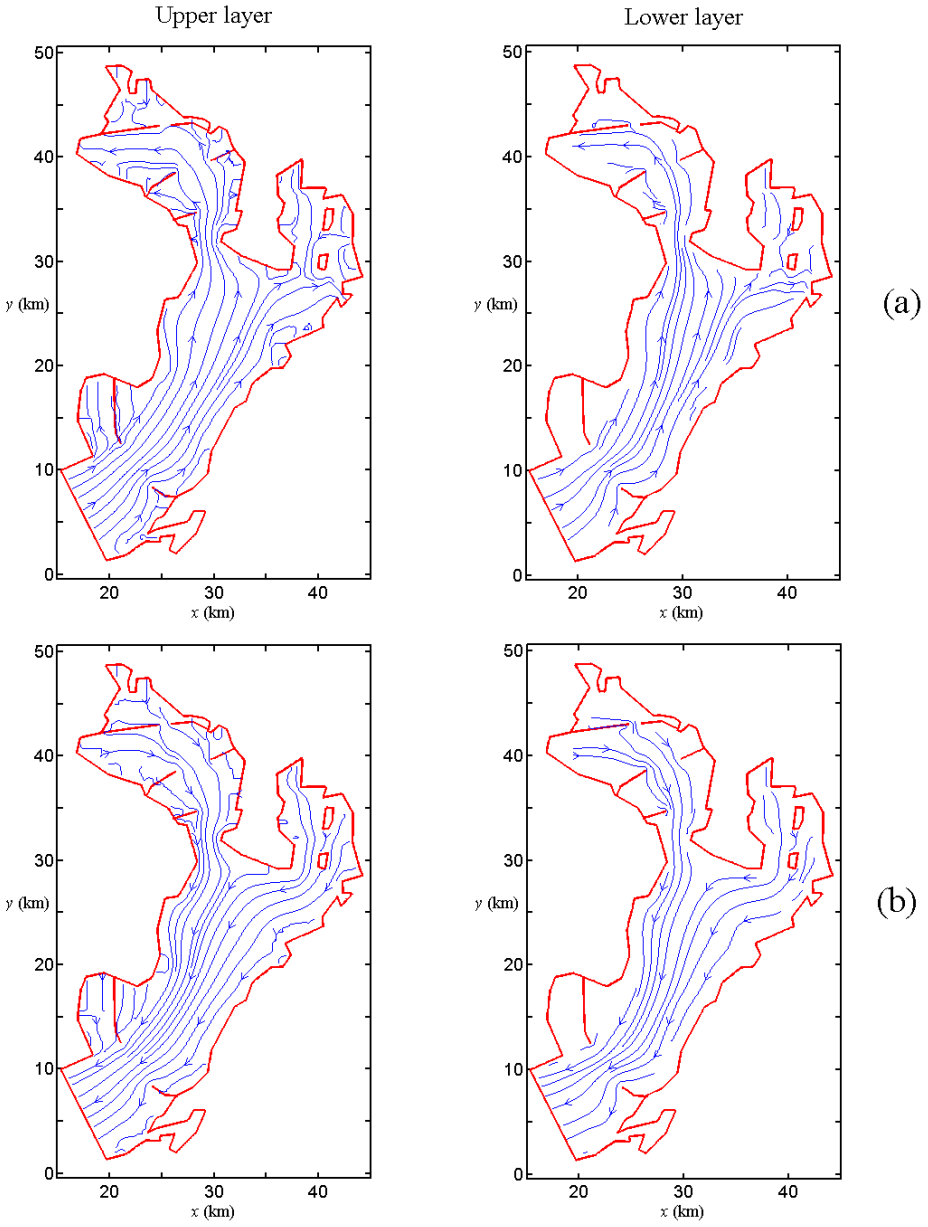

Figure 4.44: Tampa Bay: Depth-averaged streamlines during (a) flood tide, and (b) ebb tide.

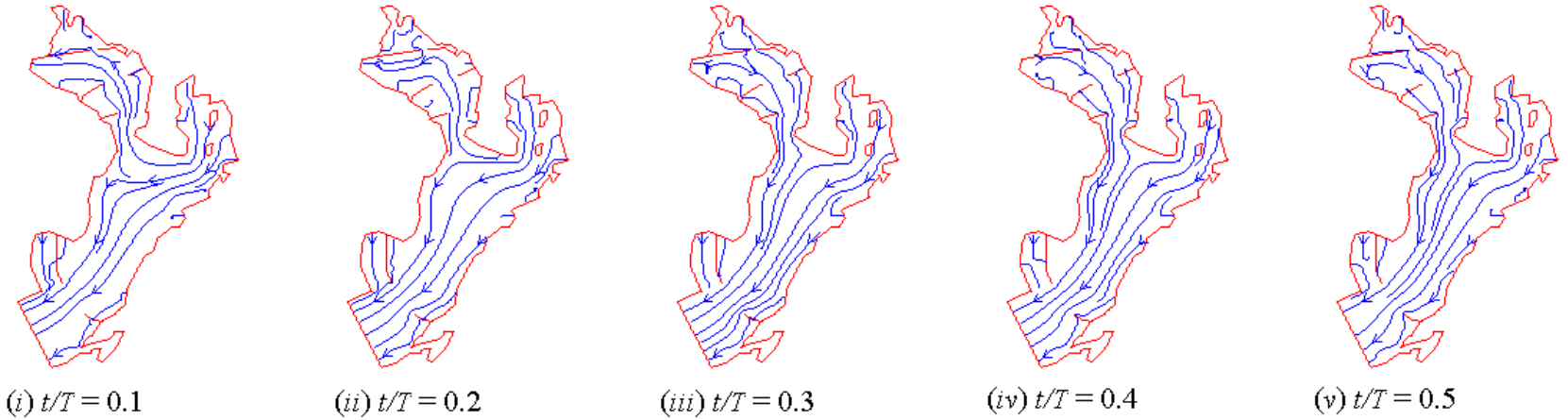

(*i*) $t/T = 0.1$ (*ii*) $t/T = 0.2$ (*iii*) $t/T = 0.3$ (*iv*) $t/T = 0.4$ (*v*) $t/T = 0.5$

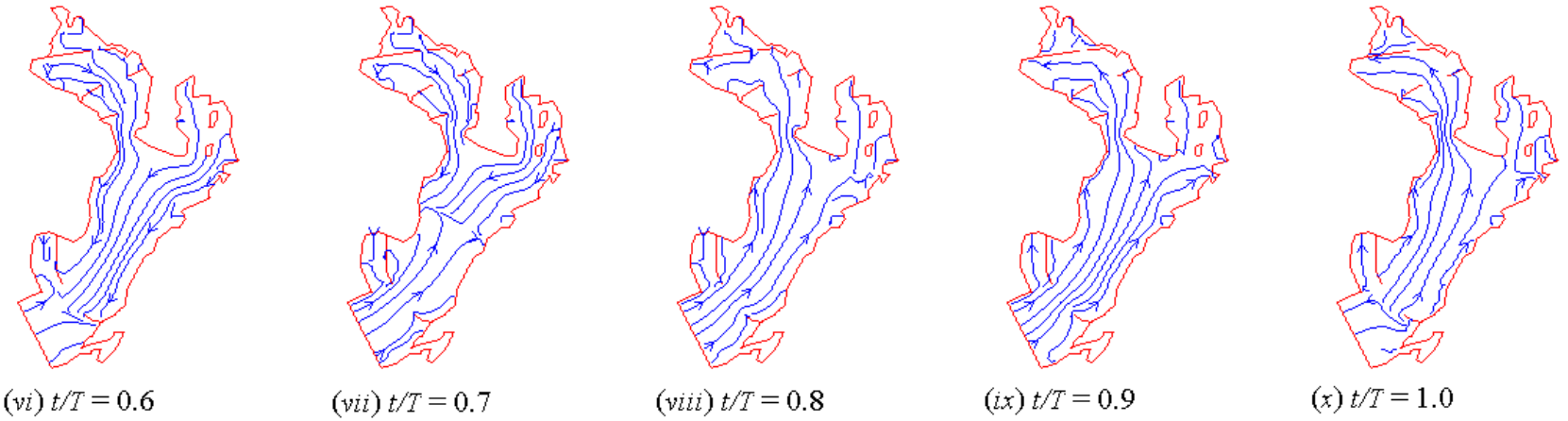

(*vi*) $t/T = 0.6$ (*vii*) $t/T = 0.7$ (*viii*) $t/T = 0.8$ (*ix*) $t/T = 0.9$ (*x*) $t/T = 1.0$

Figure 4.45: Tampa Bay: Depth-averaged streamlines in the upper layer over a 24-h cycle.

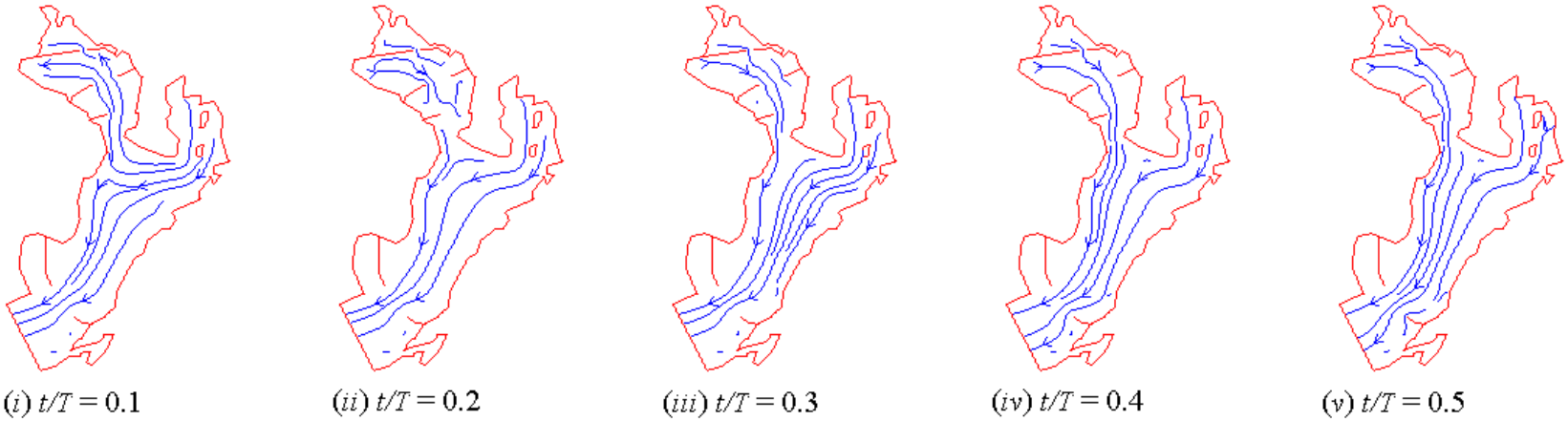

(*i*) $t/T = 0.1$ (*ii*) $t/T = 0.2$ (*iii*) $t/T = 0.3$ (*iv*) $t/T = 0.4$ (*v*) $t/T = 0.5$

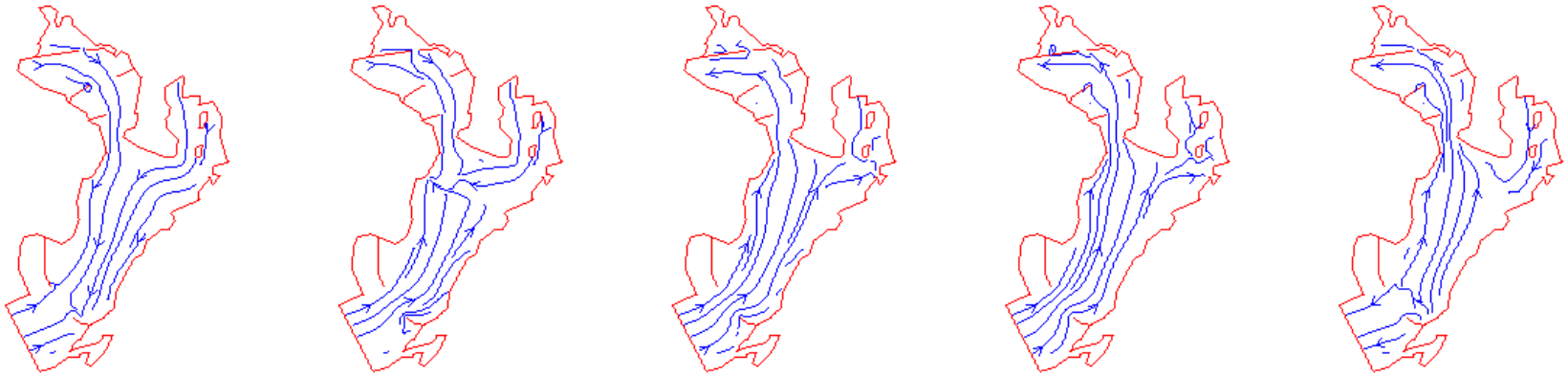

(*vi*) $t/T = 0.6$ (*vii*) $t/T = 0.7$ (*viii*) $t/T = 0.8$ (*ix*) $t/T = 0.9$ (*x*) $t/T = 1.0$

Figure 4.46: Tampa Bay: Depth-averaged streamlines in the lower layer over a 24-h cycle.

4.7 Concluding remarks

The entropy-correction-free solver for a two-layer shallow flow has been verified in one- and two-dimensions. Results obtained are in excellent agreement with available analytical solutions and predictions by alternative numerical models in the published literature. For the implementation of dynamically adaptive quadtree grid generation system, grid convergence has been evaluated by means of the Grid Convergence Index (GCI) of Roache & Knupp (1993) and Roache (1994). The results obtained are in excellent agreement with those produced on regular grids, and it may be concluded that the use of adaptive quadtree grids offers considerable computational advantages for Roe-type two-layer shallow water models. The numerical model can be used for the simulation of two-layer flow in a domain with complicated boundaries and realistic bathymetry at a fraction of the cost incurred by a scheme applied on a regular grid. The scheme has been applied to the simulation of tidal-driven flow in an idealised tidal channel, and Tampa Bay, Florida. Part of the work reported in the current and the preceding chapters has been published in Lee *et al.* (2011).

Chapter 5

Chaotic mixing in shallow water bodies

5.1 Introduction and literature review

Shallow flow mixing processes are important for the water quality of lakes, reservoirs, coastal waters and the ocean. Mixing takes place via two main processes, namely diffusion and advection. Usually, large-scale spreading is attributed primarily to advection, with hardly any effect from diffusion.

Shallow water flows often involve horizontal circulation zones confined within the surface layer. Such gyres are typically driven by wind stress acting on the surface of the water bodies. The resulting flow is largely dependent on the bathymetry, hence the term topographic gyres. For uniformly distributed wind shear, depth-averaged velocities are directed with the wind in the shallow region, and against the wind in the deep region (Csanady, 1975).

Kranenburg (1992) studied chaotic particle motions in a shallow water lake model of two-dimensional, depth-averaged flow subjected to alternating wind action, considering an idealized analytical velocity field. Liang *et al.* (2005) solved the problem using a quadtree-based Godunov-type shallow water equation (SWE) solver to address the complicated bed topographies and flow patterns, assuming a sinusoidal wind field. Liang *et al.* also considered the effect of different bed configurations (2006*a*)

and non-circular basin (2006*b*). In general, the results confirm that the particle motions change from regular to chaotic as the dimensionless storm duration increases. Recently, Pattantyús-Ábrahám *et al.* (2008) applied the tools of dynamical systems to determine the mixing properties of a square-shaped shallow lake model subjected to irregularly distributed wind forcing due to the development of an external boundary layer immediately above the free surface typical in a large spatial domain. The presence of an internal hyperbolic point is identified and coherent structures such as manifolds are found to act as Lagrangian barriers that hinder local material transfer in the transverse direction, while providing avenues of streamwise transport. Pattantyús-Ábrahám *et al.* also showed that turbulent diffusion has little effect on the distribution of finite-size Lyapunov exponents.

For lakes with a layered stucture, such as a cold layer beneath a warm layer, or salt water beneath fresh water, an internal seiche may take over the role of the free surface, though with relatively larger motion compared to an ordinary surface seiche. There are two primary modes of motion: the barotropic mode which is essentially identical to the motion of a homogeneous fluid, and the baroclinic mode arising from the density difference in the vertical water column. A two-layer model is sufficient to capture the dynamics of the motion since the contribution of the higher baroclinic modes are typically negligible (Csanady, 1975). Since the barotropic motion is more directly affected by the depth variations ('feel' the bottom more), particles in the upper and lower layers are likely to experience different fates in a wind-dominant lake circulation.

Estuaries are highly dynamic environments, characterised by tidal flows, wind-induced turbulence, seasonal and diurnal surface variation, and riverine inputs. Due to the transient nature of flows into and out of the water body, the size of an estuary is also highly variable, translating to cyclic wetting and drying along the shore. The flow field is predominantly tidal-driven, with localised recirculation attributed to the

coastline geometry, and net outflow towards the sea. Consequently, particles in estuaries are typically subjected to hydrodynamic oscillations as they travel seawards, while undergoing stirring and mixing induced by localised effects. At the surface, the flow is further driven by wind shear and bed friction is only applicable in the absence of the lower layer near the shore. On the contrary, the lower subsurface layer is relatively shielded from the wind effect but directly experiences bed roughness. In brief, the fate of mixing particles are likely to be highly varied in the two layers.

In a review of horizontal dispersion by tidal and residual currents, Zimmerman (1986) showed that a highly irregular Eulerian velocity field is typically induced in a tidal inland sea, resulting in Lagrangian chaos as opposed to shear dispersion in the open tidal shelf sea. An analytical study of chaotic stirring by Beerens *et al.* (1994) showed that the difference between the occurrence of global chaos in a realistic tidal model and local chaos in the kinematical model is likely to be caused by over simplification of the velocity field. Analytical expressions for the mixing coefficients are in good agreement with numerical results and can explain the non-monotonic dependence of mixing processes on the topographic wavenumber.

This chapter consider a two-layer density-stratified shallow water regime, where the hydrodynamics can be adequately described by the two-layer shallow flow model in the form of (3.1). Using the second-order Roe-type finite volume scheme (3.28), the flow field is obtained by solving the system of governing equations on dynamically adaptive quadtree grids (described in Section 3.5.2). Particle advection is then simulated by Lagrangian tracking. Chaotic mixing in wind-induced circulation is considered for 2-layer circular basin (Section 5.3) and square basin (Section 5.4). In Section 5.5, particle mixing in Tampa Bay is studied.

5.2 Lagrangian particle tracking

In a two-dimensional Cartesian coordinate system, the advection equation is expressed as

$$\frac{\mathrm{d}x}{\mathrm{d}t} = u(x, y, t), \quad \frac{\mathrm{d}y}{\mathrm{d}t} = v(x, y, t), \tag{5.1a, b}$$

where (x, y) is the position of a given particle at time t; and u and v denote the Eulerian velocity components in the $x-$ and $y-$directions of the flow at the same spatial and temporal point as the particle. Equations (5.1) are integrable for steady and incompressible flow, which is associated with regular advection. On the other hand, for unsteady flow associated with chaotic advection, the equations may be non-integrable.

In order to obtain the Lagrangian particle paths, time-integration of equations (5.1) is performed using a Runge-Kutta Cash-Karp algorithm (Press *et al.*, 1992) with the Eulerian velocity field provided by the two-layer shallow water solver.

5.3 Wind-induced chaotic advection in a 2-layer shallow circular basin

Consider Kranenburg's circular shallow basin (Kranenburg, 1992) for which the still water depth h_s as a function of the radial distance r from the basin's centre is given by:

$$h_s = H\left(\frac{1}{2} + \sqrt{\frac{1}{2}(1 - \frac{r}{R_0})}\right), \tag{5.2}$$

where the basin characteristic length R_0 and weighted mean water depth H are 120 m and 0.5 m, respectively (Figure 5.1), and the upper layer has a uniform thickness equivalent to one-fifth the maximum depth at the centre of the basin. The densities of each layer are given by (ρ_1,ρ_2)=(1000,1020) (i.e. density ratio $r = 0.98$), and $g = 9.81$ m/s^2. Quadtree grid configuration Φ_{6-8} is used, giving grid layout as shown in Figure 5.2.

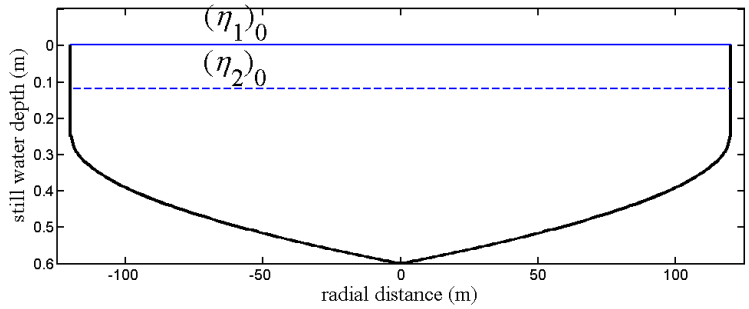

Figure 5.1: Kranenburg's geometry: Basin cross section, showing initial profiles of the free surface $(\eta_1)_0$ and the interface $(\eta_2)_0$, where upper layer thickness is equivalent to 1/5 of the maximum depth.

In the problem, the flow field is a weak system governed by a single parameter related to the storm duration t_s. The dimensionless storm duration parameter (Kranenburg, 1992) is defined as

$$\Gamma = \frac{\ln Z}{8\kappa} \frac{u_* t_s}{R_0}, \tag{5.3}$$

where $Z = H/z_0$, $z_0 = 2.8$ mm is the roughness height of the bed, $u_* = \sqrt{\tau_w/\rho_1}$ is the friction velocity at the free surface, t_s is the storm duration, and $\kappa = 0.4$ is the von Kármán constant. For all cases considered, constant wind shear stress $\tau_w = 2.0 \times 10^{-3}$ Nm^{-2} is applied uniformly throughout the entire domain but its direction changes abruptly at half-period intervals $T/2$ between the north-east and north-west directions alternately. The Eulerian velocity field is assumed to adapt instantaneously to the wind conditions. Hence, the streamlines of the flows (Figure 5.3) switch abruptly as the wind direction changes, but otherwise remain unchanged throughout each storm event which lasts half a period.

According to Csanady (1975), a two-layer model adequately describes a stratified lake. The model essentially suppresses any higher baroclinic modes which are unimportant with regard to the observed motions. The effects of bottom and interface friction are also negligible relative to the wind forcing and pressure gradient (Csanady, 1975). However, for the purpose of the present study, these energy dissipations are

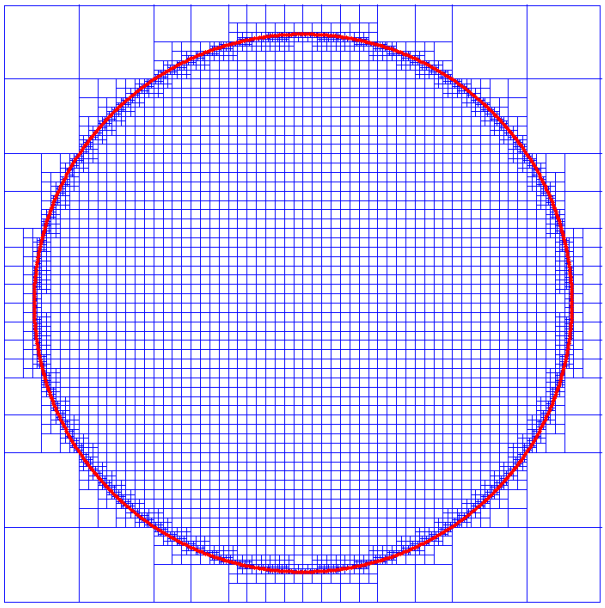

Figure 5.2: Kranenburg's geometry: Quadtree grid configuration: Φ_{6-8}.

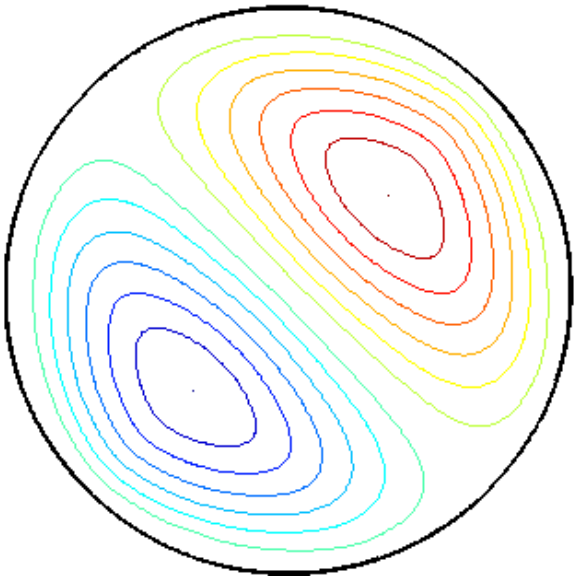

Figure 5.3: Kranenburg's geometry: Steady state streamlines due to north-westerly wind.

included following Liang *et al.* (2006*a*). The bed stress is evaluated empirically from equations (4.34) in which the bed roughness coefficient C_b is estimated using

$$C_b = \left(\frac{\kappa}{1 + \ln(z_0/h_j)} \right)^2, \tag{5.4}$$

where h_j is the instantaneous depth of the layer in contact with the bed, and the depth-averaged eddy viscosity is given by

$$\epsilon = \frac{1}{6} \kappa u_* h_j. \tag{5.5}$$

The interfacial stress is evaluated using equations (4.35) where the interface friction coefficient C_f is taken as 0.03 arbitrarily. Equivalent wind stress on the lower layer is given by $-\tau_w h_2/(h_1 + h_2)$, and the effect of the Earth's rotation is ignored.

Using a no-slip boundary condition, and time step $\Delta t = 0.1$, the simulations are run until steady state for the various storm duration t_s. Both the upper and lower layers span across the entire domain and share the same boundary which is essentially vertical at the basin perimeter. The streamlines of both layers are similar, with the pairs of topographic gyres in both layers separated by a dividing streamline located diametrically across the basin and aligned with the wind direction. Along this main axis which runs through the deeper water, the velocities in the upper layer are directed against the wind, whereas those in the lower layer are in the same direction as the wind. As these upwind and downwind flows of the upper and lower layers, respectively, reach the far end of the basin, they turn around along the shallow area near the basin perimeter, creating a rapid jet of flow along the shore in the opposite direction – similar to that observed in a single layer model (Kranenburg, 1992; Liang *et al.*, 2005, 2006*a*). The result is essentially an internal set-up/ set-down, which is common in a stratified lake. The interface separating the layers sinks at the downwind section and rises at the upwind section. The balanced internal forces cause the free surface to remain near horizontal with negligible surface gradient. At density ratio

close to unity, e.g. $r = 0.99$, the lower layer is observed to outcrop the surface of the upper layer. The effect of this is not considered in the present study.

Figure 5.4 shows the Poincaré sections for tracer particles released at intervals along the x-axis in both layers. These plots are generated by plotting the intersections of particle trajectories with the time plane at the end of each period for different dimensionless storm durations $\Gamma = 0.14, 0.42, 0.70$. The particles are tracked for up to 100 cycles.

For $\Gamma = 0.14$, the basin is clearly divided into two regions by the dividing streamline along the north-south axis. Large islands of regular particle motions can be observed either side of the main axis. Further away from the centres of these islands, the regularity of particle motions degenerates near the main axis and the basin boundary. As Γ increases, the period-one islands diminish in size but remain. The regions away from the islands become increasing chaotic and generally lose their distinctive features. The observations hold for both layers, though regularity in the lower layer persists better, due to the fact that the layer is shielded and is subjected indirectly to reduced shear from the wind forcing. The results are in close agreement with those of the single layer models of Kranenburg (1992) and Liang *et al.* (2005, 2006*a*).

Chaotic mixing is characterized by stretching and folding, and can best be visualized by deploying a line of particles in the domain. For this purpose, 10,000 particles are initially positioned in the interval [-$2R_0/3$,$2R_0/3$] along the x-axis in each layer. For $\Gamma = 0.28$ (Figure 5.5), near symmetrical patterns are observed in both layers at times $t = 50T$ and $t = 100T$. Particles in the vicinity of the regular islands form two whorl-type structures under the influence of the period-one points. Tendrils appear near the perimeter of the basin and can be associated with the unstable manifolds of the hyperbolic periodic points. As the line of particles evolve, complicated fractal structures becomes increasingly visible and the basin is gradually filled with pseudo-stochastic particle tracks. Again, the lower layer lags behind in its time-development

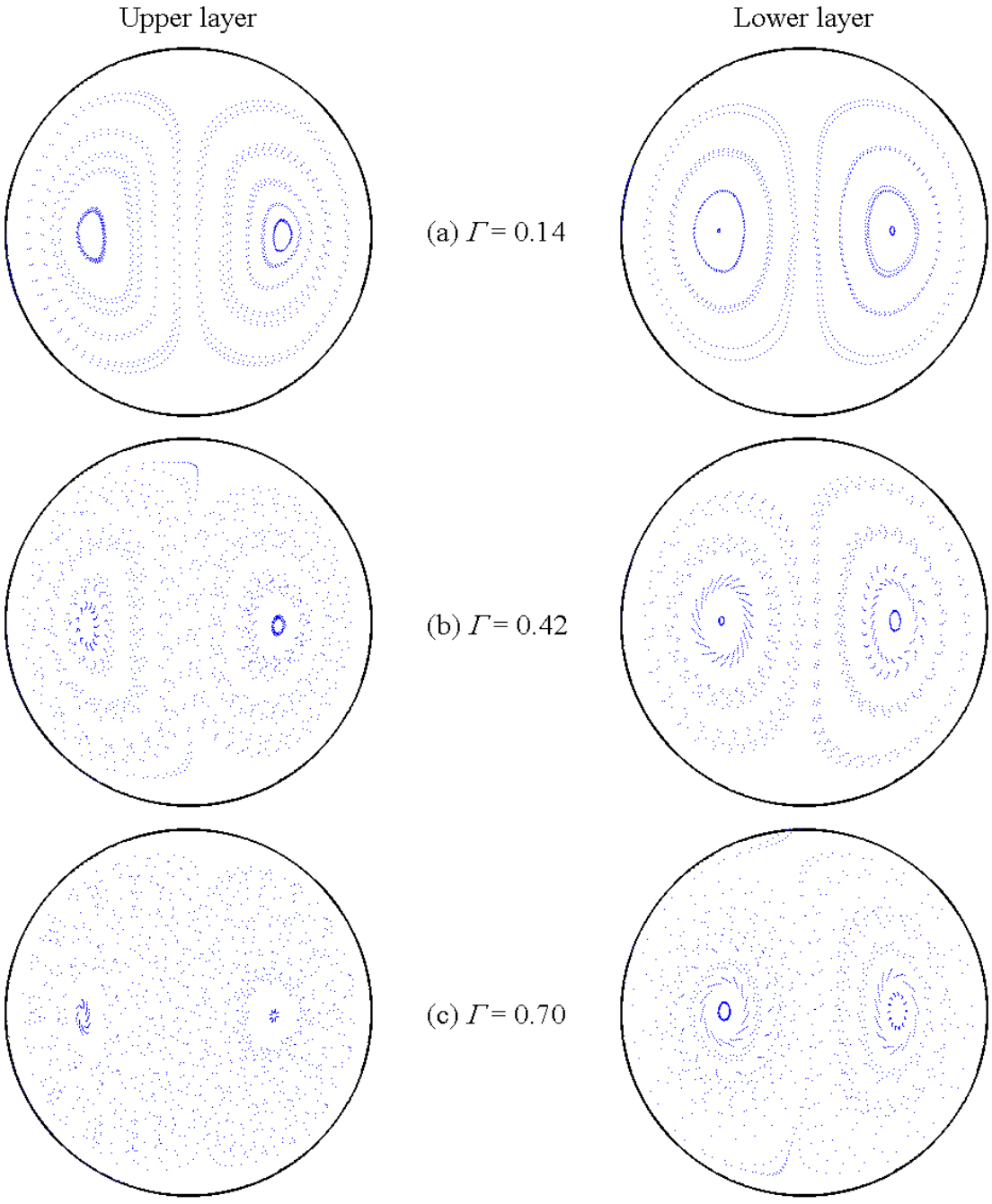

Figure 5.4: Kranenburg's geometry: Poincaré sections for different dimensionless storm durations with wind periodically blowing from ±45°N.

due to the reduced effect of the wind forcing compared to the top layer. At a higher value of $\Gamma = 0.84$ (Figure 5.6), particles near the boundary and the main dividing axis are scattered rapidly. The whorl structures in the elliptical zones exhibit much irregular stretching and folding and continue to occupy a significant extent of area in the lower layer even at $t = 100T$, but are heavily encroached by the scattered particles in the upper layer. Hence, good mixing, which is characterised by exponential stretching, is restricted (even at high storm duration) in the lower layer, particularly the elliptical regions either side of the main axis aligned with the direction of the wind. Although the wind field is switched between north-westerly and north-easterly periodically, symmetry of the particles distribution in the basin is lost in higher storm duration of Γ=0.84 (Figure 5.6) compared to Γ=0.28 (Figure 5.5) due to the longer duration of the initial storm direction.

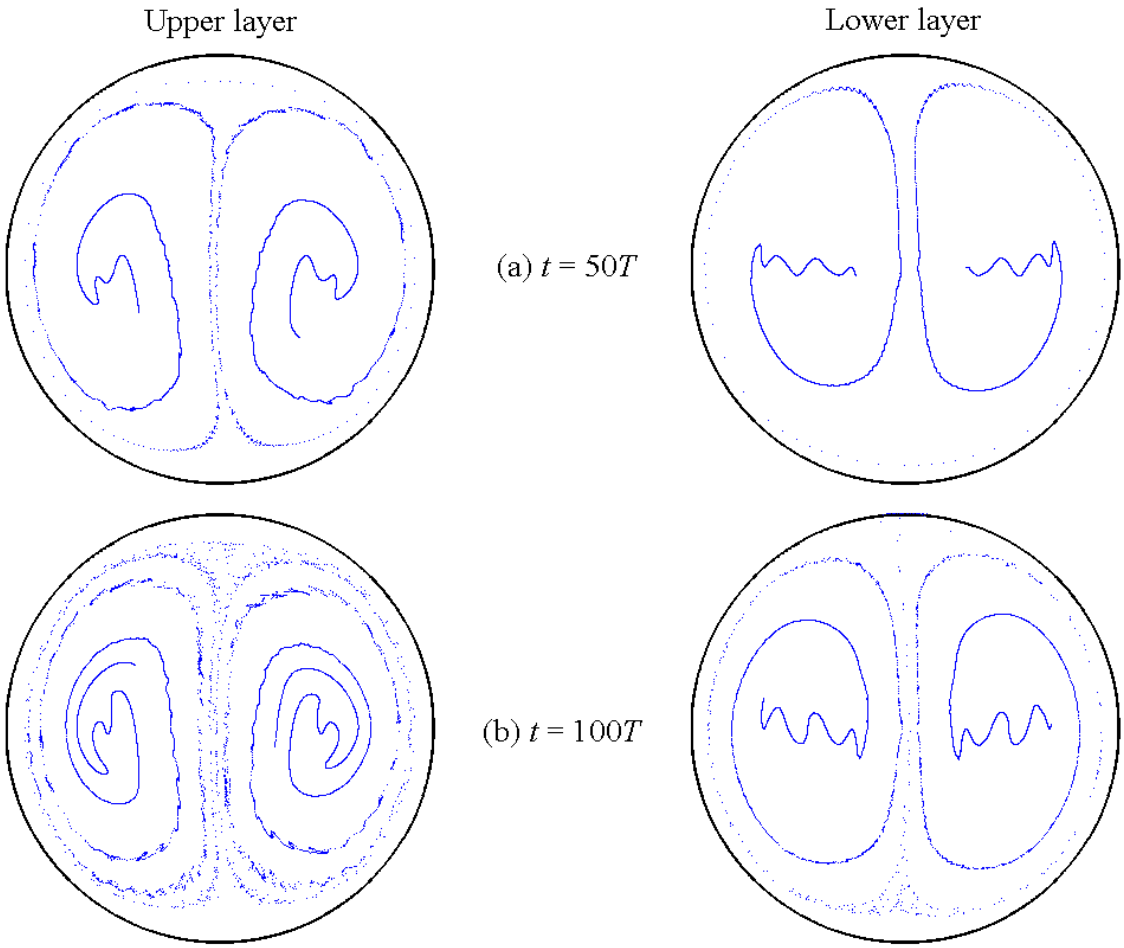

Figure 5.5: Kranenburg's geometry: Advection of a line of particles for Γ=0.28.

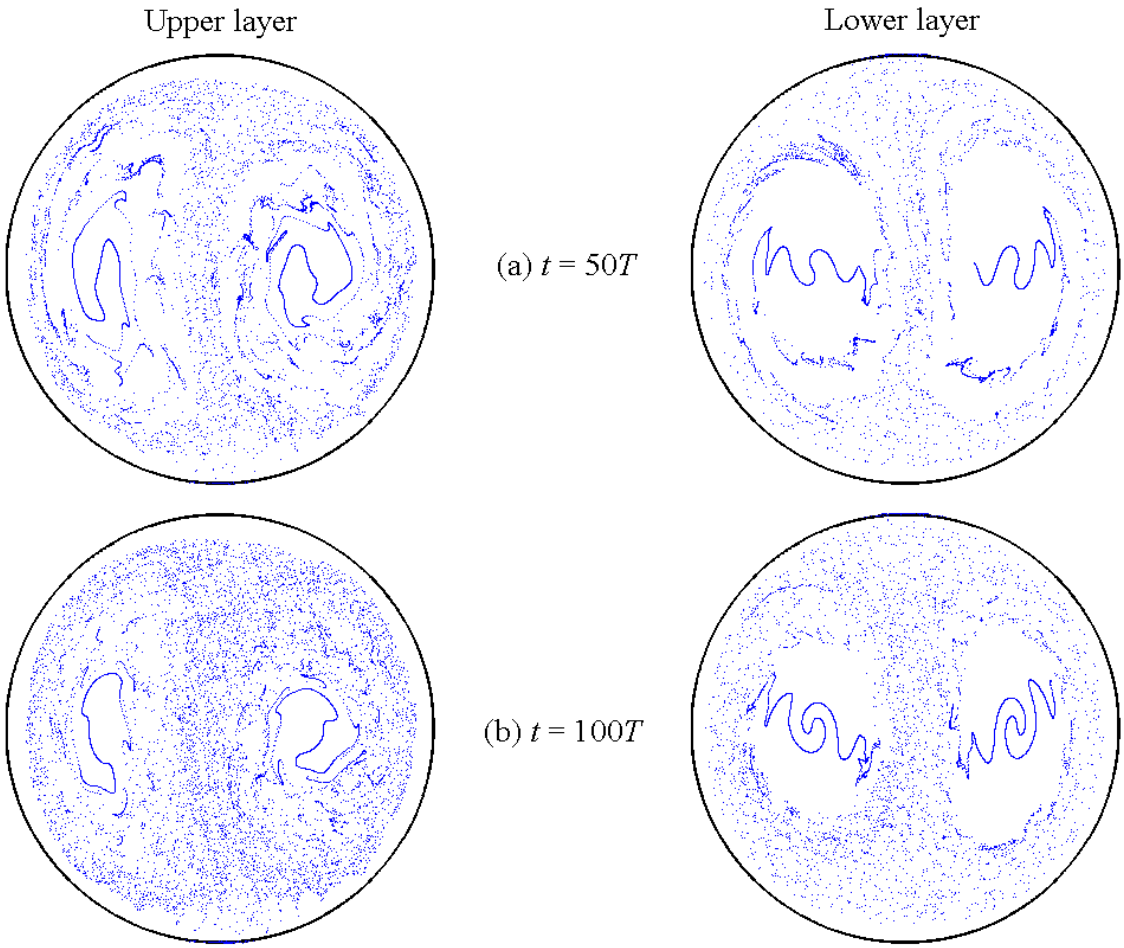

Figure 5.6: Kranenburg's geometry: Advection of a line of particles for Γ=0.84.

5.4 Wind-induced chaotic advection in a 2-layer shallow square basin

In this section, an inverted pyramidal square basin of size 2 km $\times$ 2 km is considered (Pattantyús-Ábrahám *et al.*, 2008). A density ratio $r = 0.99$ is adopted where the upper layer is fresh water with an initial depth of 1.0 m at the centre of the basin. Maximum overall depth at the centre of the basin is 2.5 m. Using a linear depth transition, two bed configurations are considered: one in which the total depth at the alongshore boundary is 2.0 m (BED_A), and another in which the total depth at the alongshore boundary is 0.5 m (BED_B) (Figure 5.7). BED_A results in a 2-layer

flow where both layers share the same vertical wall boundary, whereas in $\mathrm{BED_B}$, the lower layer has a reduced flow domain and its boundary undergoes wetting and drying along the inclined bed. Grid configuration Φ_{6-8} is used, and fine grid is maintained along the wetting and drying front of the lower layer.

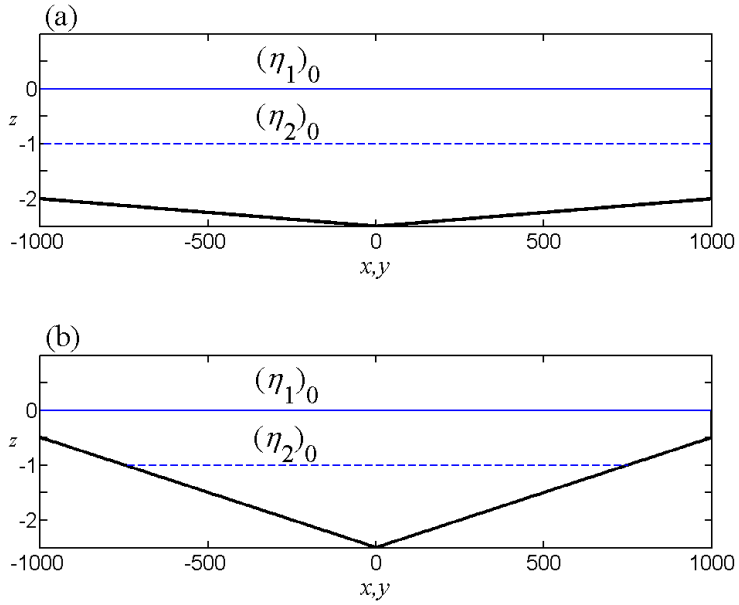

Figure 5.7: Inverted pyramidal square basin: (a) $\mathrm{BED_A}$, with alongshore depth of 2.0 m, and (b) $\mathrm{BED_B}$, with alongshore depth of 0.5 m. The maximum depth of both bed profiles is 2.5 m at the center of the basin. The plots illustrate the initial profiles of the free surface $(\eta_1)_0$ and the interface $(\eta_2)_0$.

A constant wind shear stress of $\tau_w = 1.3 \times 10^{-3}$ $\mathrm{Nm^{-2}}$ is applied uniformly over the free surface. No-slip boundary conditions are applied at the wall. Simulation of the flow field is carried out until steady state is achieved. For the purpose of particle advection, the flow field is switched back and forth periodically to represent an abruptly alternating wind field from the north-westerly and north-easterly directions. Here, the flow field is assumed to adapt instantaneously to the sudden change of wind direction, and otherwise, remains unchanged throughout the storm event. The dimensionless storm duration parameter of Kranenburg (1992) (5.3) is adapted by taking R_0 to be the equivalent hydraulic radius of the square basin, and the bed roughness height $z_0 = 1$ cm. The weighted mean water depth H is 2.1688 m and

1.8376 m for BED_A and BED_B, respectively. Bed friction, interfacial friction and viscosity terms are treated similarly as in Section 5.3.

Figure 5.8 shows the wind-induced streamline patterns obtained for the BED_A and BED_B cases. For BED_A where both layers share the same vertical boundary and thus have the same flow area, simple opposing recirculation is observed in both layers. Along the diagonal parallel to the direction of the wind, the flow in the upper layer is directed against the wind, whereas the flow in the lower layer is in the same direction as the wind. The pair of topographic gyres is symmetrical about this diagonal with strong jets along the shore. The features result in an internal displacement, with the interface between the layers set-up in the upwind part of the basin, and set-down in the downwind part of the basin.

For BED_B, transition of the 2-layer flow to single layer flow along the shore creates highly complicated flow features in both layers, though the symmetry about the main axis parallel to the wind direction is maintained. In the lower layer, there is clearly a dominant pair of topographic gyres which occupies a large portion of the surface area of the lower layer, rotating in the same direction as that in BED_A. In addition, there are two smaller pairs of gyres which rotate in the opposite direction to that of the dominant pair of gyres, one located in the north-west corner, and another, of which the shape is slightly elongated, located to the east and the south along the shore. Between the dominant pair of gyres and the small pair of gyres located at the north-west corner, a hyperbolic point can be identified where, at any instant of time, there is a contracting curve running towards it from either side of the main axis, and a diverging curve running away from it in two opposite directions along the main axis. In the upper layer, the main axis is observed to be straddled by four pairs of gyres. Contrary to BED_A, the flow is primarily in the same direction as that of the wind in the upwind part, but against the wind in the downwind part. As a result of these flow features, a hyperbolic point appears to exist on the main axis where

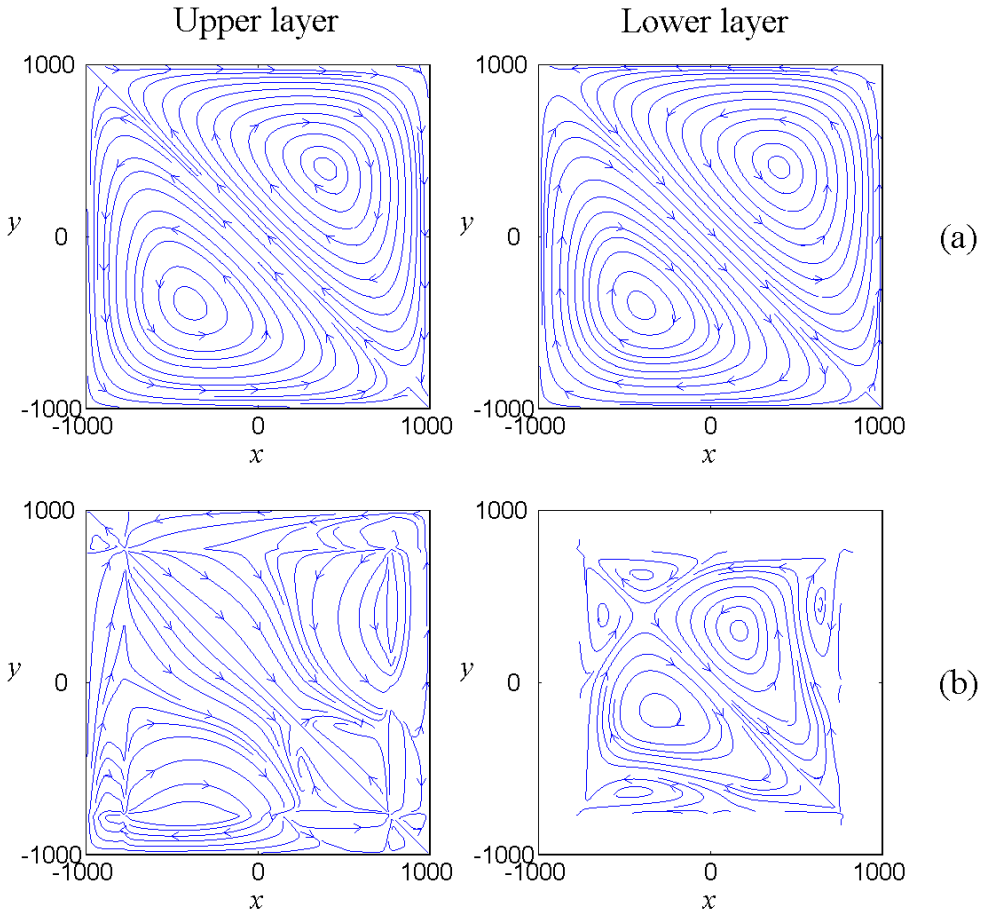

Figure 5.8: Shallow water square basin: Steady state streamlines due to north-westerly wind for (a) BED_A, and (b) BED_B.

the opposing flows meet. However, the streamlines are clearly not smooth along the boundary of the transition between the single-layer region along the shore and the two-layer region in the middle of the basin. Physically, this can be attributed to the fact that the magnitude of resistance experienced by the upper layer is discontinuous as it traverses between the two regions. The alongshore friction is significantly larger than the interfacial stress in the two-layer zone. Furthermore, the jet-like flow in the lower layer along its boundary inevitably affects the flow in the upper layer. In the north-west corner of the upper layer, localized recirculation confined to the single layer zone can be identified. The recirculation in the south-east region of the upper layer, on the other hand, is less well defined, with evidence of the strong influence of the

phenomenon of single-layer–to–two-layer transition. Further work on the numerical treatment is still in progress to resolve this issue satisfactorily. Nonetheless, the present results suggest that the flow features in the upper layer differ significantly in the presence of a single layer shore.

The presence of internal hyperbolic points in both the upper and lower layer under uniform wind shear for $\mathrm{BED_B}$ suggests that complex intersection of stretching and contracting manifolds occurs in both layers despite the relative low wind wind forcing applied. The resulting dynamics is expected to be chaotic (Pattantyús-Ábrahám *et al.*, 2008), and differ significantly from that for $\mathrm{BED_A}$ as shall be shown next.

Figure 5.9 and Figure 5.10 show the Poincaré sections for different dimensionless storm durations for $\mathrm{BED_A}$ and $\mathrm{BED_B}$, where 10 particles are released in both layers along the x-axis at equal intervals within [-$2R_0/3$,$2R_0/3$], and tracked for up to 100 cycles. Owing to the low wind shear, regular advection is observed for all the 3 storm durations for $\mathrm{BED_A}$. Meanwhile for $\mathrm{BED_B}$, increasing chaotic behaviour can be observed in the lower layer as the storm duration increases. Particles in the upper layer, on the other hand, are scattered with no distinctive features evident especially for low values of storm duration. For the higher storm duration, such as Γ=0.70, the relative longer storm duration at the initial stage force most of the particles into the single layer region at the corners. The motion of these particles are then subjected only to the small pair of gyres at the corner, and appear to assume the same periodicity as that of the storm duration.

The prevalent chaotic behaviour in $\mathrm{BED_B}$ can be attributed to the presence of an alternating hyperbolic point in each layer as the wind field switches direction abruptly each half cycle. The striking difference in particle advection between cases $\mathrm{BED_A}$ and $\mathrm{BED_B}$ suggests that simulations using a single layer approach to stratified two-layer shallow water flow may result in an unrealistic and inaccurate representation of the actual particle motion.

It is further noted that the wind forcings considered herein for the inverted-pyramidal basin and Kranenburg's basin (Section 5.3) are relatively small. The equivalent physical conditions are likened to a gentle breeze, which avoided the occurrence of large set-up/ set-down and eliminated the likelihood of surface outcropping. Care should thus be taken in generalization of the results to the strong wind regime. Spigel & Imberger (1980) presented a detailed analysis of processes relevant to wind mixing in lakes, and proposed a general classification with respect to the thermocline deepening behaviour at the interface between the upper and lower layers, depending on the relative sizes of the parameters describing the wind strength, basin size and stratification. In Stocker & Imberger (2003*a*), the dynamics of the tilted interface of a stratified circular rotating basin was studied with the focus solely on particle trajectories on the surface layer. Using Lagrangian GPS drifter experiments carried out in the surface layer of stratified Lake Kinneret in Israel, Stocker & Imberger (2003*b*) quantified the dominant horizontal dispersion mechanisms when wind is the primary external forcing. It is shown that internal waves are responsible for cloud dispersion over short time scales, in the order of a day. Over intermediate time scales, shear dispersion is found to be important due to the large horizontal velocity gradients. Stocker & Imberger noted that pseudo-chaotic advection, like horizontal shear dispersion, is the key to the large-scale circulation in the lake and that vertical shear dispersion appears to be negligible for typical surface layer conditions.

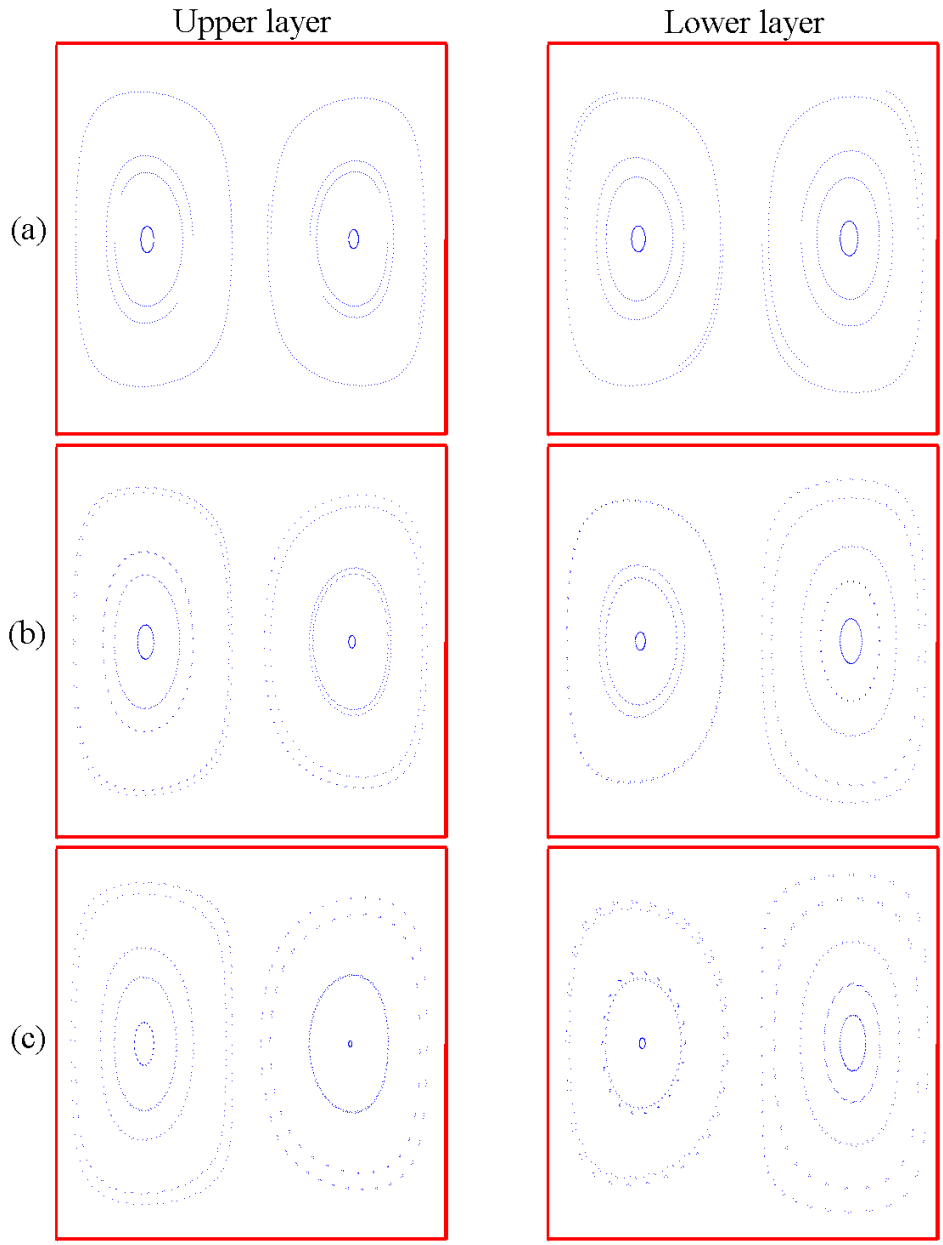

Figure 5.9: Shallow water square basin: Poincaré sections for different dimensionless storm durations in $\mathrm{BED_A}$, with wind periodically blowing from $\pm 45°$N. From top to bottom: (a-c) $\Gamma = 0.14, 0.42, 0.70$.

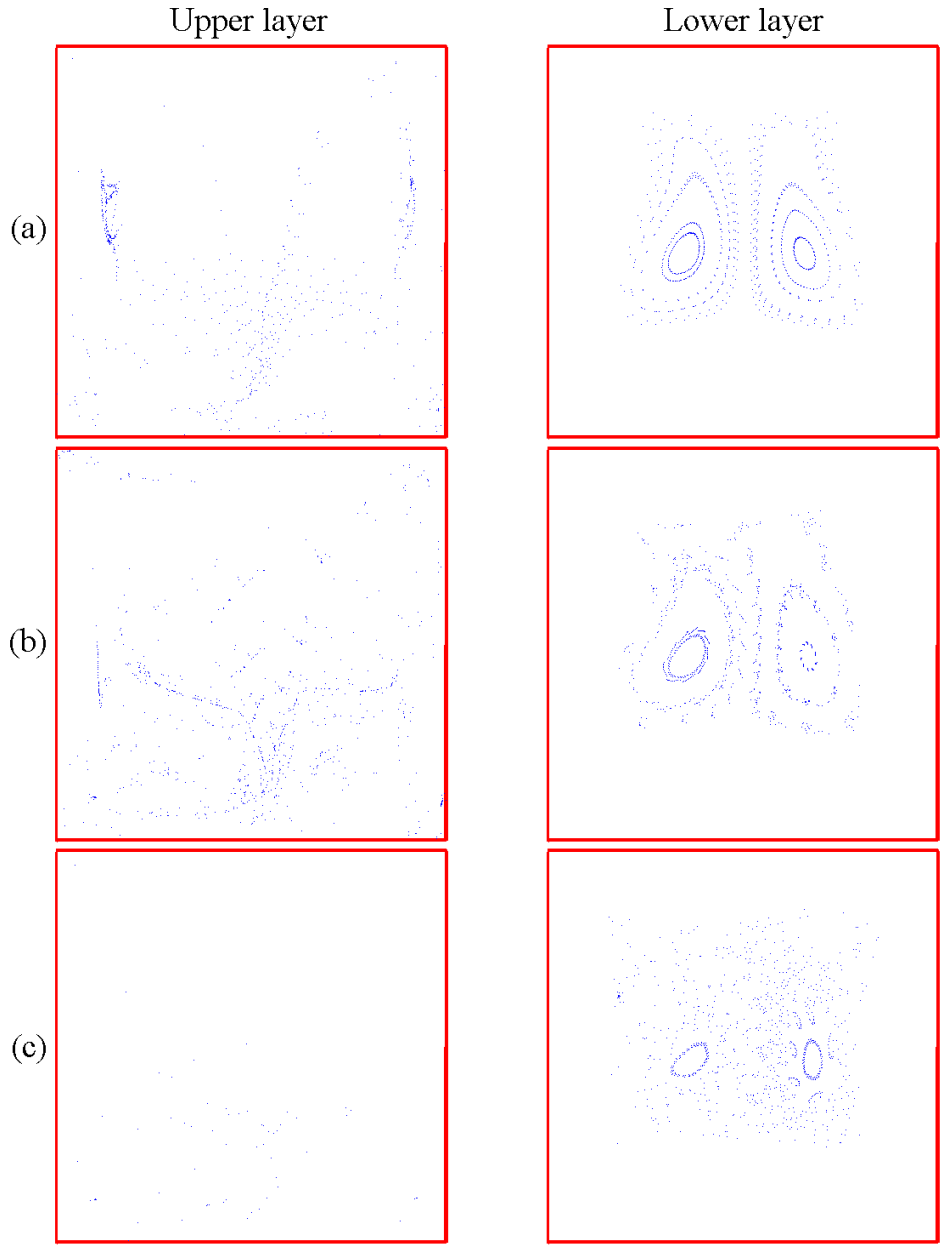

Figure 5.10: Shallow water square basin: Poincaré sections for different dimensionless storm durations in $\mathrm{BED_B}$, with wind periodically blowing from $\pm 45°$N. From top to bottom: (a-c) $\Gamma = 0.14, 0.42, 0.70$.

5.5 Tampa Bay, Florida: A study of mixing in a 2-layer tidal driven flow

In this section, the tidal-driven flow obtained in Section 4.6 is used to examine particle advection and mixing in Tampa Bay, Florida. A simple diurnal tide is considered and the low riverine inflow condition chosen so that particles deployed do not get flushed out of the domain too soon. Wind forcing has been omitted.

Firstly, a single particle is deployed at the same initial position in both layers at selected locations, and the particles tracked for up to 25 cycles. Figure 5.11 shows the trajectories of the particles in both the upper and lower layers for 4 different initial positions (a) to (d). In all cases considered, although particles in the upper layer are advected a substantial distance after 25 cycles, advection in the lower layer is almost negligible. This is due to the fact that the velocities in the lower layer are smaller by two orders of magnitude. There is, however, a clear net drift out of the bay in both layers. Considering the particles in the upper layer, the results show that particles in the shallow Old Tampa Bay have relatively low velocities and are just about to exit into the Middle Tampa Bay after 25 cycles (Figure 5.11a(i)). Once a particle reaches the mouth of Old Tampa Bay, it moves at a faster rate alongshore in the deeper trench to the west of the shallow central rise region in Middle Tampa Bay (Figure 5.11b(i)). A particle seeded in Hillsborough Bay (Figure 5.11c(i)), on the other hand, advects relatively rapidly along the main axis of Tampa Bay, which is to the east of the central rise in the Middle Tampa Bay region where the deep navigational channel is located (see Figure 4.42). This advection route can be attributed to the relatively large river inflow from Alafia River, which accounts for one-fifth the river inflow in Tampa Bay. A particle seeded near the upstream end of the Lower Tampa Bay is flushed out of the basin relatively quickly (Figure 5.11d(i)), and hence this region is not of interest in the subsequent study.

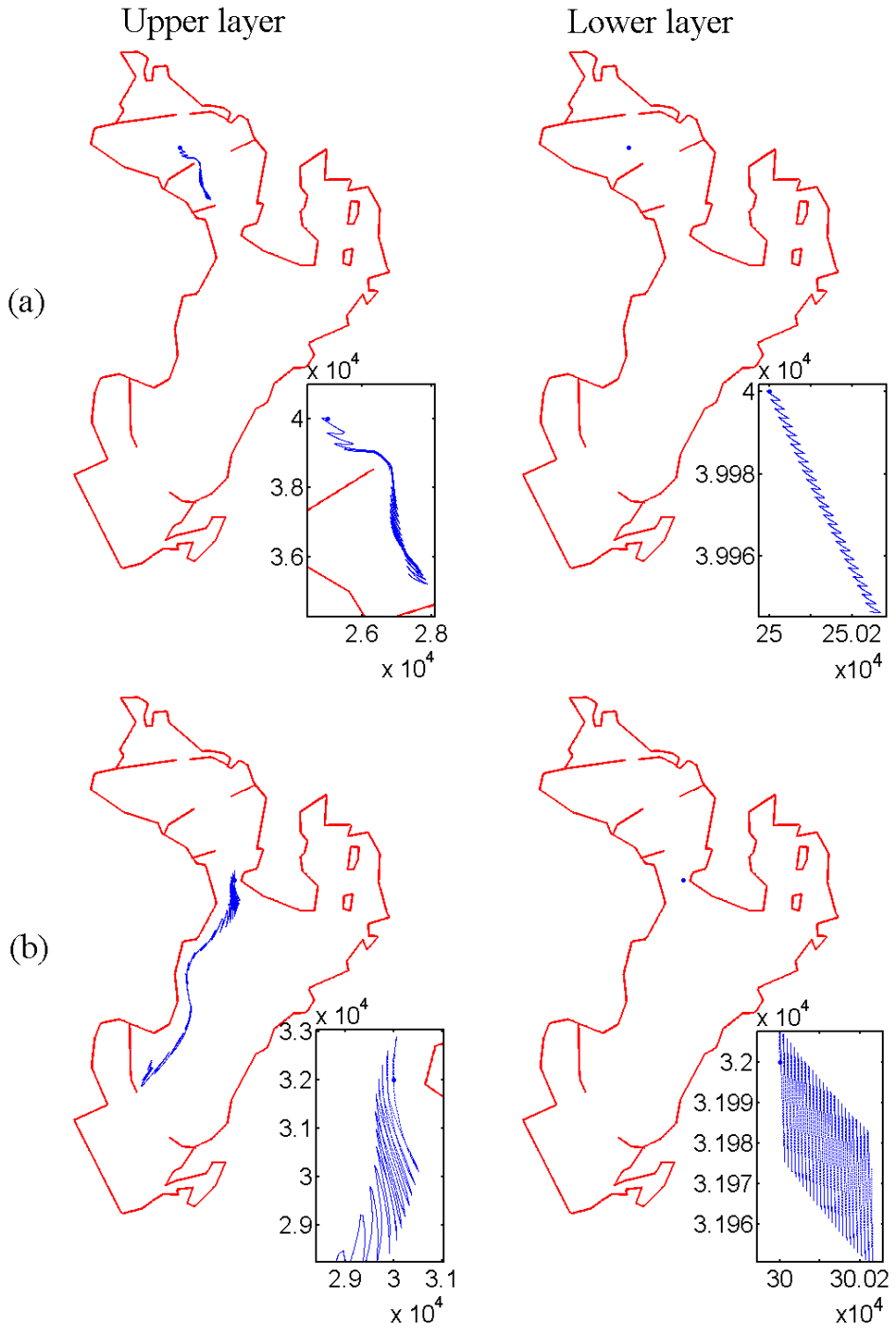

Figure 5.11: Tampa Bay: Trajectories of a single particle for a period of 25 cycles. Particle initial positions (marked •) are: (a) (2.5×10^4, 4.0×10^4), and (b) (3.0×10^4, 3.2×10^4). Insets show details of the respective trajectories. (Figure continues next page.)

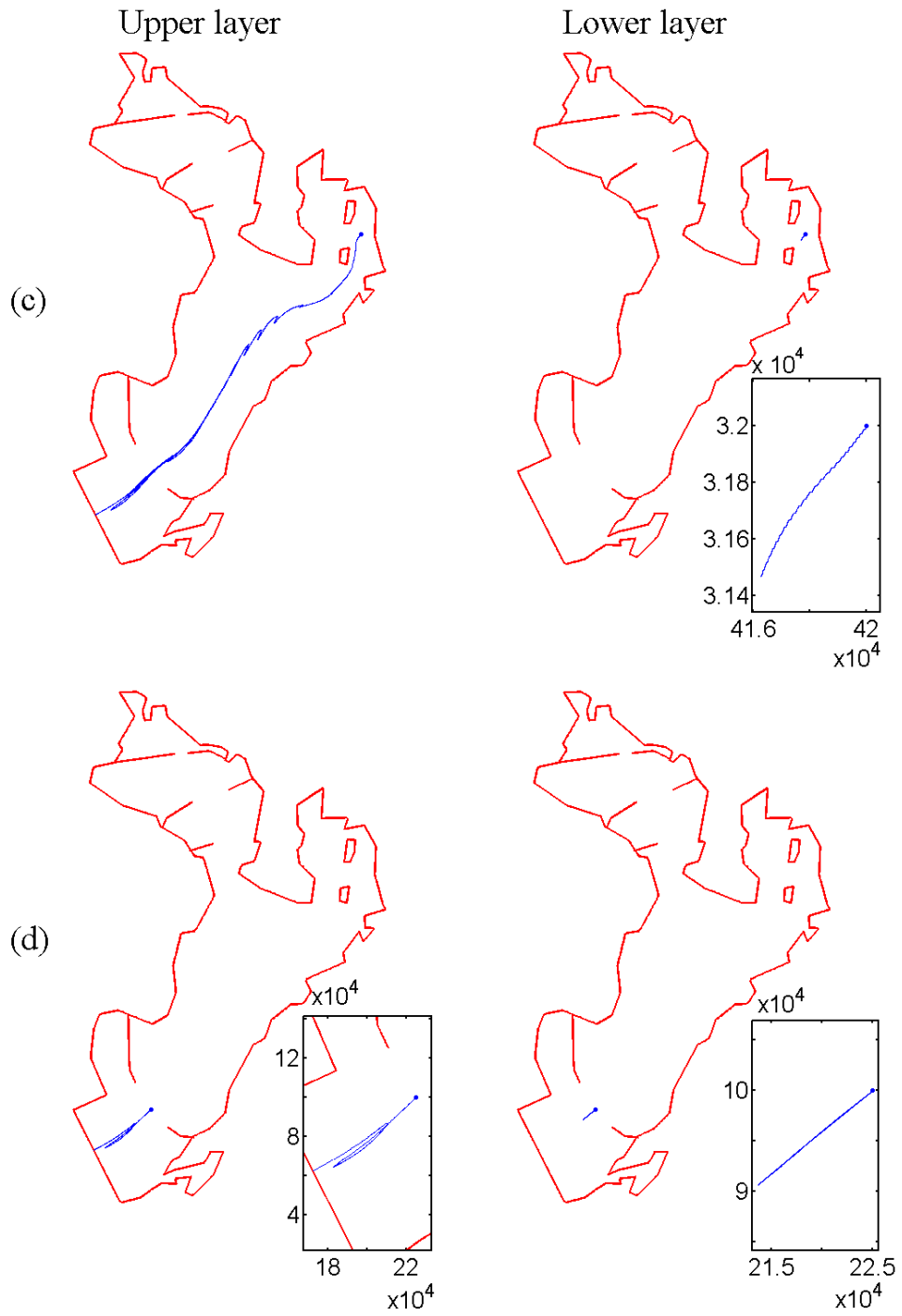

Figure 5.11: Tampa Bay: Trajectories of a single for a period of 25 cycles. Particle initial positions (marked •) are: (c) (4.2×10^4, 3.2×10^4), and (d) (2.25×10^4, 1.0×10^4). Insets show details of the respective trajectories. (Figure continues from previous page.)

Next, a square patch of 10,000 particles is deployed in each layer at different initial locations. Figure 5.12a(i) shows that by 100 cycles, the square patch from the Old Tampa Bay region is greatly stretched along the eastern shore of Middle Tampa Bay but a considerable quantity of particles still remain at the mouth of Old Tampa Bay. Evidently, the narrow strait connecting the Old and Middle Tampa Bay acts like an hourglass neck and releases particles from the Old Tampa Bay in a constrained manner. This is likely to result from the flood tide which forces some of the escaping particles back into the Old Tampa Bay before they are entrained into the alongshore coastal jet in the Middle Tampa Bay. This is supported by the observations made in Figure 5.11b(i) where the trajectory of the single particle near the mouth of Old Tampa Bay undergoes cyclic to-and-fro motions before it is finally washed out of the strait region. Figure 5.12a(i) also shows that the particles become increasingly scattered as they approach the Lower Tampa Bay, and spread out in the shallow lagoon in the vicinity of the groyne. The results show that 65.2% of particles still remain in the Old Tampa Bay after 100 cycles, and this reduces gradually to 48.9% at the end of 200 cycles, suggesting that the strait is an efficient barrier to the outflow of tracers. Furthermore, the particles that escape Old Tampa Bay are mostly scattered in the shallow lagoon near the Lower Tampa Bay, and only 11.3% exit the domain by the end of 200 cycles.

Two square patches of particles are deployed in Hillsborough Bay. The patch near the mouth of River Alafia (Figure 5.12b(i)) (PATCH_{B1}) is significantly stretched but not scattered as it is advected towards the Lower Tampa Bay. The other patch is located initially in the relatively shielded region to the west of the northern island in Hillsborough Bay (see Figure 5.12c(i)) (PATCH_{B2}). This initial location is away from the direct river influxes especially that from the Hillsborough River, which accounts for almost a quarter of the river inflow in Tampa Bay. Interestingly, while PATCH_{B2} is advected at almost the same rate as PATCH_{B1}, it clearly experiences much less

stretching. The two square patches of particles in the Hillsborough Bay, PATCH_{B1} and PATCH_{B2} exit the computational domain within 18.4 cycles and 16.3 cycles, respectively. In the former case, the longer duration taken is due to the stretching of the particle patch. It is also worth noting that close to 7% of the particles in PATCH_{B1} are washed ashore on the southern island in the Hillsborough Bay and are not further entrained into the flow field.

In summary, the energy of the two-layer stratified Tampa Bay under low river inflow condition is concentrated in the upper surface layer and can be attributed almost entirely to tidal forcing, with a net drift out of the bay. Particle advection and mixing in the denser fluid below is extremely poor with excessively long residence time, with important implications for water quality in the lower layer. Particles in the surface layer, on the other hand, experience rather different rates of advection and mixing dependent on their location. The phenomenon can be attributed to the fact that the surface layer typically experiences a relatively stronger ebb flow compared to the flood flow over a tidal cycle due to the effect of river input. The opposite is true for the lower or subsurface layer. Hence, the difference between streamwise particle advection in the upper and lower layers is likely to increase for large riverine inflow. Old Tampa Bay has a relatively long residence time due to the narrow outlet, whereas Hillsborough Bay has a relatively short residence time due to the large fluxes of inflow from the tributaries. The Middle Tampa Bay is where particles are typically stretched and washed out. Particles which are not scattered into the slow-flowing shallow lagoon adjacent to the Lower Tampa Bay are typically flushed out of the domain rapidly.

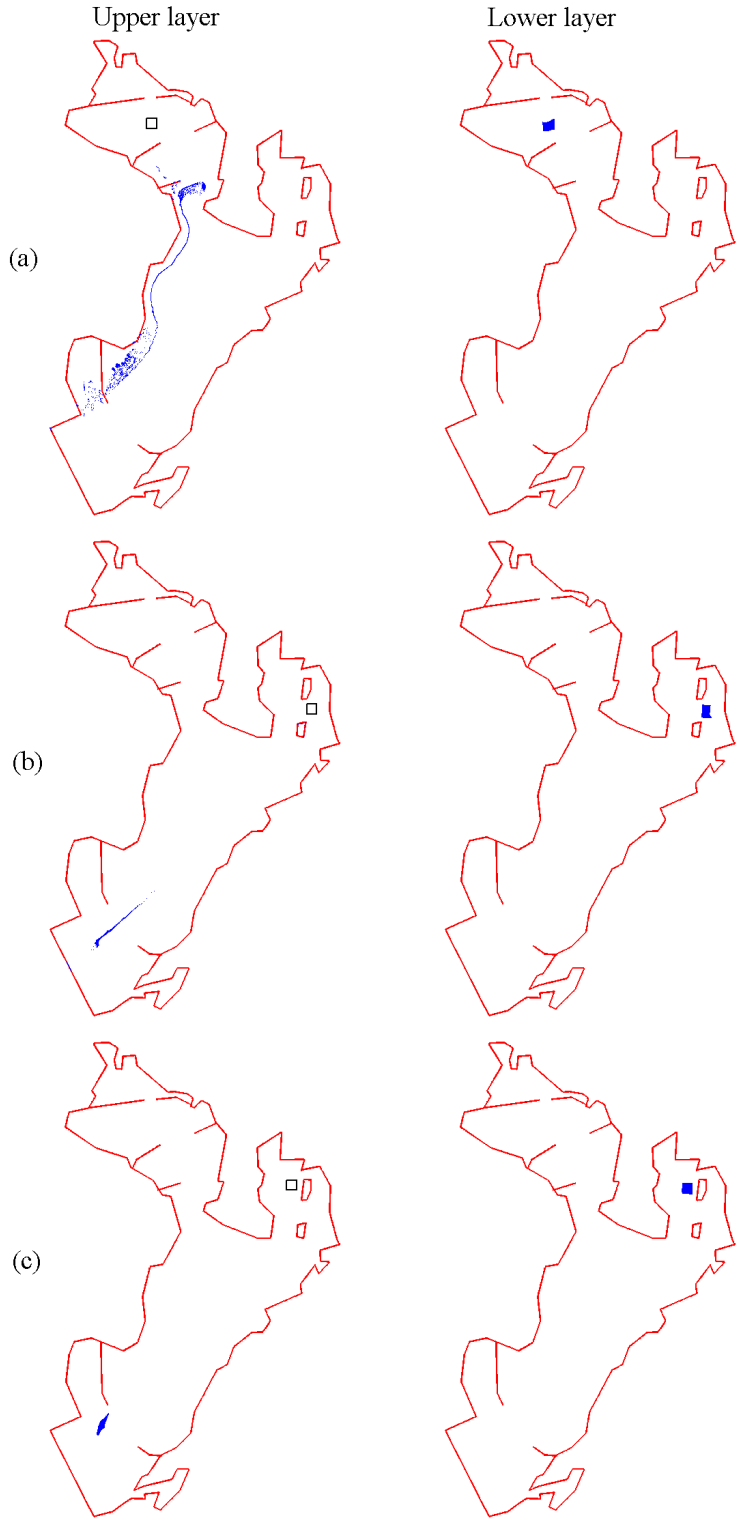

Figure 5.12: Tampa Bay: Advection of a square patch of 10,000 particles. Plots showing particle positions after 100 cycles (a), and 15 cycles (b,c). Initial particle positions (marked □ on the upper layer) is centred at: (a) (2.55×10^4, 4.05×10^4), (b) (4.15×10^4, 3.2×10^4), and (c) (3.95×10^4, 3.45×10^4).

Chapter 6

Conclusions and Recommendations

6.1 Conclusions

Lagrangian chaos can be observed even in a relatively simple deterministic flow field. Consequently, the paths of particles, including those which are initially close together, can significantly diverge and are thus difficult to predict. Furthermore, trajectories in Lagrangian chaos can show coherent areas (islands) from which particles do not escape, and fractal-like filamental structures. The resulting patchiness is in considerable contrast to the smooth variations of a Gaussian distribution and is critical to water quality of aquatic and marine environments. In the present thesis, chaotic mixing processes in wavy-type channels and two-layer shallow water flow have been studied using analytical tools developed in the field of nonlinear dynamics.

For wavy-type channels, mixing induced by the unsteady motion of trapped vortices located in the trough region of the wavy wall has been considered. The equations of motion for the vortices and the particles were derived assuming two-dimensional irrotational, inviscid and incompressible flow. Using Lagrangian tracking, the instantaneous positions of the vortices and particles were determined in a mapped plane and conformally mapped to the physical domain. A characteristic Strouhal number ~ 0.25 is found to hold for the vortex motion over a wide range of input parameters. The results show that each vortex trajectory is governed mainly by its image, and the numerical vortex paths agree well with the analytical ones for small perturbation.

As particles travel along the wavy channels, significant stretching and folding, and increasing scattering is observed. There exists a stable region which constitutes a 'core' surrounding and shielding each vortex singularity. Outside this region, mass exchange takes place between the interior and exterior of each separation bubble, creating a chaotic-sea-of-mixing region which evolves in size as the vortex moves. Analysis of the perturbed system shows that the spiral nature of the invariant manifolds produces infinite self-similar criss-crossing tangles at all scales, which is responsible for material exchange between the eddy in the furrow and the overlying steady flow. The observed dynamics agree well qualitatively with solutions of the unsteady Navier–Stokes equations for oscillatory unidirectional flow in a wavy channel (Sobey, 1980, 1982). Statistical evaluation shows that the skew-symmetrical wavy channel is more efficient in passive mixing than a symmetrical wavy channel. Diffusion increases lateral particle dispersion significantly at the expense of longitudinal particle dispersion. Using the non-escaping vortex core as a source of reacting particles, active mixing in the wavy channel has been studied. The unstable manifold is shown to be an effective catalyst for the reactive process. The fractal dimensions obtained correlate well to the escape rates and the Lyapunov exponents, provided the hyperbolic dynamics is solely considered.

A density-stratified two-layer flow regime is commonly observed in large lakes, reservoirs, and estuaries. Ignoring vertical mixing, chaotic stirring may occur, leading to Lagrangian chaos to different degrees in the layers due to the varying flow field. In the present thesis, an entropy-correction free Roe-type two-layer shallow water solver has been developed for a hyperbolic system with non-conservative products and source terms. The flow is assumed to comprise two superposed immiscible layers of shallow liquid. The scheme is well-balanced and satisfies the C-property such that smooth steady solutions are second order accurate (Chacón-Rebollo *et al.*, 2003, 2004; Castro *et al.*, 2007*b*). Numerical treatment of the wet-dry fronts of both layers, and the loss

of hyperbolicity associated with Kelvin-Helmholtz instabilities are incorporated in the numerical scheme. The solver has been tested rigorously on a number of 1D and 2D benchmark test cases, including still water solutions, well-balanced smooth steady state solutions, the propagation of small and large interface perturbations (over a flat bed and a hump), correct treatment in the non-hyperbolic region of the flow, a stationary internal jump, lock exchange flow, shock behind wall, 1D internal dam break, 2D internal circular dam break, 2D partial dam break, and a tidal channel with a hump and constriction. For 2D implementation, a dynamically adaptive quadtree grid generation system is deployed. It is shown, using grid convergence tests, that the adaptive grid system produces results in excellent agreement with those on regular grids at a fraction of the cost of the latter. This thesis also shows that the algebraic balancing of Rogers *et al.* (2003, 2004) cannot be extended directly to a two-layer shallow water flow due to the lack of simultaneous referencing for the still water position of both the two layers.

The dynamics of the two-layer shallow water flow without vertical mixing relies heavily on momentum and energy exchanges between the layers. Generally, only the lower layer 'feels' the bed, whereas the free surface is predominantly undisturbed. The model is applied successfully to an idealised two-layer tidal channel, and a two-layer model of Tampa Bay, Florida, which is tidal-driven with low river inflow. It is also used to simulate wind-induced circulation in circular and square basins. In the cases of flow in inverted pyramidal basins, it is found that the flow features in the upper layer differs significantly in the presence of single layer shore zone. This can be attributed to the jet-like flow along the boundary of the lower layer along the shore, as well as the discontinuous jump in resistance across the transition between the single-layer and two-layer region. Additional numerical treatment is required to address this issue satisfactorily.

Lagrangian particle tracking in wind-induced recirculation in shallow water basins

wherein the two layers share the same vertical boundary wall shows that chaotic behaviour in the lower layer is less pronounced than that of the upper layer due to the reduced wind-forcing. In the case where the lower layer undergoes wetting and drying along the shore such that there exists a single-layer shore region, the flow features in both layers become more complicated. As a consequence, chaotic behaviour is enhanced.

For Tampa Bay, the simulation results show that particle advection and mixing in the lower layer is extremely poor, whereas that of the surface layer is highly dependent on the release location in the bay. This verifies that the flow in Tampa Bay is predominantly tidal driven, and riverine inflow, though relatively small in comparison, plays a significant part in the much larger seaward surface drift. The simulation also shows that geographical features can play a significant role in the fate of particles. For example, the narrow strait between the Old Tampa Bay and Middle Tampa Bay acts as a constriction that delays the release of particles from the Old Tampa Bay region. The flood tides tend to force particles into the shallow lagoon instead of flushing them out into the open sea.

6.2 Recommendations

6.2.1 On the oscillatory point-vortex model

1. In the present study, simulated vortex motion is driven by specifying its perturbation from the equilibrium position in the uniform flow field. As an alternative, an external time-periodic oscillatory flow or a pulsatile-type flow component on top of the steady mean flow may be used to drive the vortex motion.

2. The wavy wall paramaters may be modified to investigate the effect of wall wavelength and amplitude on the overall mixing efficiencies. The approach can be easily adapted to other geometries such as a sawtooth-type channel by using appropriate conformal mapping. A preliminary study not reported in this thesis shows interesting mixing behaviour in a sawtooth-type channel due to the presence of sharp corners.

3. Another problem of interest would be to construct a long channel with a regular profile interspersed by joints described with a different mapping function. In this case, the vortex dynamics and mixing efficiencies could be compared with those reported in the present thesis.

4. Using a suitable mapping function, the present model could be used to describe a river with a series of groynes, or a coastline with a series of breakwaters and dominated by longshore current. The model is valid for the above cases provided the water depth variation and free surface dynamics are negligible, or if the structures concerned are fully submerged. Potential applications are to determine the optimum spacing and length of these (proposed) structures to achieve the best mixing result for tracers, or alternately, to achieve desirable sediment trapping.

6.2.2 On the two-layer shallow water solver

1. The present solver can be further improved to handle the case of a lower layer out-cropping on the free surface. This will allow simulation of the development and evolution of a salt wedge in the estuary, as well as a wind-induced internal seiche in a lake with a thin upper layer and/or density ratio approaching unity.

2. The Coriolis forcing should be included, especially in the simulation of large lakes and coastal basins, to account for the Earth's rotation; frequency dispersion should be added as a source term in order that the model can simulate correctly phenomena such as internal waves and solitons, which require a local balance between frequency and amplitude dispersion.

3. Owing to the difference in wave speed in the two layers, the two-layer model requires a much smaller time step compared to the single layer model. Hence, it is desirable to parallelize the computation for better time performance.

4. Solution of the two-layer shallow water model requires the viscosity matrix $\mathbf{D}$ (3.33). This involves substantial computational cost to evaluate the system eigenvalues, as well as to invert the matrix $\mathbf{X}$ of which the columns are the right eigenvectors of the correponding system eigenvalues. Recently, Fernández-Nieto *et al.* (2011) introduced the idea of using a parabolic viscosity matrix given in terms of the system matrix $\mathbf{A}$ which is readily available. Fernández-Nieto *et al.* show that it is sufficient to use the first-order approximations of the system eigenvalues to obtain a linearly L^{∞}-stable scheme with accuracy approaching that of the Roe scheme considered in this thesis. A similar approach to circumvent the numerical solution of the system eigenstructures could significantly reduce the computational time.

5. Flow behaviour in the upper layer where the single layer on a sloping bed abuts against the two-layer region presents a physical and numerical challenge. The flow features in the lower layer coupled with the discontinuity in the resistance experienced by the upper layer results in jagged features in the flow along this boundary. Additional examination of both the local physics and the numerical treatment is needed to resolve this issue especially for cases which requires steady state solutions.

6.2.3 On the adaptive grid generation system

1. The adverse effect of stepped approximation to boundary-fitting in the current grid system is alleviated by increasing the grid resolution. Fine grid cells have also been adopted in this thesis to resolve the wet-dry front of the lower layer in the present two-layer model. For better approximation, grid cells near the boundary may be triangularized (Yiu *et al.*, 1996), or represented using cut-cells (Liang *et al.*, 2007*b*). This additional treatment is relatively straight forward for the boundary but present a further challenge when applied to smooth out the wet-dry front of the lower layer where the adaptations will need to alternate between square and triangular or cut-cell grid cells.

2. In the present thesis, the idea of coarsening from a universally-fine initial grid is adopted in lieu of grid refinement from a coarse initial grid in order to retain as much critical information as possible especially the location of the wet-dry front of the lower layer which is not known a *priori*. Presently, the minimum and maximum level of grid cell subdivisions is user-prescribed. However, it may be attractive to only need to prescribe the maximum subdivision, i.e. the finest initial grid, and design the algorithm to coarsen to the appropriate grid level according to certain flow variables. The obvious advantage is achieving

computational efficiency and accuracy without prior knowledge of the minimum permissible grid.

3. The adaptive grid has the advantage of allocating computational resources on the region where fine resolution is required. Although the additional interpolation routine incurs only minimal computational cost, it could be a source of rounding errors. In particular, if the minimum and maximum levels of subdivision differ greatly, the large amount of interpolation computations in the grid transition zone may cause error to accumulate. A possible alternative would be to widen the region between cells of different levels using appropriate flags to create these buffer zones.

6.2.4 On the study of chaotic mixing in a two-layer shallow water flow

1. In the present thesis, horizontal chaotic mixing in a two-layer shallow water flow is carried out solely for passive tracers. A possible problem of interest is to examine the advection of active particles in an open flow around an obstacle, such as a cylinder (e.g. Toroczkai *et al.*, 1998; Liang *et al.*, 2007*a*) or an island. Uniform flow, tidal flow or exchange flow conditions may be examined.

2. Although the present immiscible model do not allow for vertical mixing between the layers, computation of the hyperbolicity criterion (3.16) provides information with regard to the appearance of Kelvin-Helmholtz instabilities in the flow. This can potentially be used to identify grid cells where tracers in either layer may acquire the necessary energy to mix into the other layer. Hence, a simple model problem would be to seed particles in either layer and identify the entrainment into the other layer, as well as the eventual fate of the particles.

3. The model can be extended to consider sediment transport, and water quality parameters.

Bibliography

Abgrall, R. & Karni, S. 2009 Two-layer shallow water system: A relaxation approach. *SIAM J. Sci. Comput.* **31** (3), 1603–1627.

Abraham, Edward R. & Bowen, Melissa M. 2002 Chaotic stirring by a mesoscale surface-ocean flow. *Chaos* **12** (2), 373–381.

Amon, C. H., Guzmán, A. M. & Morel, B. 1996 Lagrangian chaos, Eulerian chaos, and mixing enhancement in converging-diverging channel flows. *Phys. Fluids* **8** (5), 1192.

Aref, H. 1984 Stirring by chaotic advection. *J. Fluid Mech.* **143**, 1–21.

Aref, Hassan 2002 The development of chaotic advection. *Phys. Fluids* **14** (4), 1315–1325.

Armi, L. 1986 Hydraulics of two flowing layers with different densities. *J. Fluid Mech.* **163**, 27–58.

Armi, L. & Farmer, D. M. 1986 Maximal two-layer exchange through a contraction with barotropic net flow. *J. Fluid Mech.* **164**, 27–51.

Audusse, E., Bouchut, F., Bristeau, M. O., Klein, R. & Perthame, B. 2004 A fast and stable well-balanced scheme with hydrostatic reconstruction for shallow water flows. *SIAM J. Sci. Comput.* **25** (6), 2050–2065.

Babiano, A., Boffetta, G., Provenzale, A. & Vulpiani, A. 1994 Chaotic advection in point vortex models and two-dimensional turbulence. *Phys. Fluids* **6** (7), 2465–2474.

Bagtzoglou, Amvrossios C. & Novikov, Andrei 2007 Chaotic behaviour and pollutant dispersion characteristics in engineered tidal embayments: A numerical investigation. *J. Am. Water Res. Assoc.* **43** (1), 207–219.

Beerens, S. P., Ridderinkhof, H. & Zimmerman, J. T. F. 1994 An analytical study of chaotic stirring in tidal areas. *Chaos, Solitons Fractals* **4** (6), 1011–1029.

Begnudelli, L. & Sanders, B. F. 2006 Unstructured grid finite-volume algorithm for shallow-water flow and scalar transport with wetting and drying. *J. Hydraul. Eng.* **132** (4), 371–384.

Bermúdez, A. & Vázquez-Cendón, M. E. 1994 Upwind methods for hyperbolic conservation laws with source terms. *Comput. Fluids* **23** (8), 1049–1071.

Biemond, J. J. B., Moura, A. P. S. De, Károlyi, G., Grebogi, C. & Nijmeijer, H. 2008 Onset of chaotic advection in open flows. *Phys. Rev. E - Stat., Nonlinear, Soft Matter Phys.* **78** (1).

Boffetta, G., Celani, A. & Franzese, P. 1996 Trapping of passive tracers in a point vortex system. *J. Phys. A: Math. Gen.* **29** (14), 3749–3759.

Borthwick, A. G. L. & Barber, R. W. 1992 Numerical simulation of jet-forced flow in a circular reservoir using discrete and random vortex methods. *Int. J. Numer. Meth. Fluids* **14** (12), 1453–1472.

Borthwick, A. G. L., León, S. Cruz & Józsa, J. 2001*a* Adaptive quadtree model of shallow-flow hydrodynamics. *J. Hydraul. Res.* **39** (4), 413–424.

Borthwick, A. G. L., León, S. Cruz & Józsa, J. 2001*b* The shallow flow equations solved on adaptive quadtree grids. *Int. J. Numer. Meth. Fluids* **37** (6), 691–719.

Borthwick, A. G. L., Marchant, R. D. & Copeland, G. J. M. 2000 Adaptive hierarchical grid model of water-borne pollutant dispersion. *Adv. Water Res.* **23** (8), 849–865.

Brufau, P., Vázquez-Cendón, M. E. & García-Navarro, P. 2002 A numerical model for the flooding and drying of irregular domains. *Int. J. Numer. Meth. Fluids* **39** (3), 247–275.

Budyansky, M., Uleysky, M. & Prants, S. 2004 Hamiltonian fractals and chaotic scattering of passive particles by a topographical vortex and an alternating current. *Phys. D: Nonlinear Phenom.* **195** (3-4), 369–378.

Budyansky, M. V., Uleysky, M. Yu & Prants, S. V. 2007*a* Lagrangian coherent structures, transport and chaotic mixing in simple kinematic ocean models. *Comm. Nonlinear Sci. Numer. Simul.* **12**, 31–44.

Budyansky, M. V., Uleysky, M. Y. & Prants, S. V. 2007*b* Lagrangian coherent structures, transport and chaotic mixing in simple kinematic ocean models. *Commun. Nonlinear Sci. Numer. Simul.* **12** (1), 31–44.

Cadwell, L. H. 1994 Singing corrugated pipes revisited. *Am. J. Phys.* **62** (3), 224–227.

Cannell, P. & Williams, J. E. Ffowcs 1973 Radiation from line vortex filaments exhausting from a two-dimensional semi-infinite duct. *J. Fluid Mech.* **58** (1), 65–80.

Castro, M. J., Fernández-Nieto, E. D., Ferreiro, A. M., García-Rodríguez, J. A. & Parés, C. 2009 High order extensions of Roe schemes

for two-dimensional nonconservative hyperbolic systems. *J. Sci. Comput.* **39** (1), 67–114.

Castro, M. J., Fernández-Nieto, E. D., González-Vida, J. M. & Parés, C. 2011 Numerical treatment of the loss of hyperbolicity of the two-layer shallow-water system. *J. Sci. Comput.* **48**, 16–40.

Castro, M. J., Ferreiro, A. M. Ferreiro, García-Rodríguez, J. A., González-Vida, J. M., Macías, J., Parés, C. & Vázquez-Cendón, M. E. 2005 The numerical treatment of wet/dry fronts in shallow flows: Application to one-layer and two-layer systems. *Math. Comput. Modell.* **42** (3-4), 419–439.

Castro, M. J., Gallardo, J. M. & Parés, C. 2006*a* High order finite volume schemes based on reconstruction of states for solving hyperbolic systems with nonconservative products. Applications to shallow-water systems. *Math. Comput.* **75** (255), 1103–1134.

Castro, M. J., García-Rodríguez, J. A., González-Vida, J. M., Macías, J. & Parés, C. 2007*a* Improved FVM for two-layer shallow-water models: Application to the Strait of Gibraltar. *Adv. Eng. Software* **38** (6), 386–398.

Castro, M. J., García-Rodríguez, J. A., González-Vida, J. M., Macías, J., Parés, C. & Vázquez-Cendón, M. E. 2004 Numerical simulation of two-layer shallow water flows through channels with irregular geometry. *J. Comput. Phys.* **195** (1), 202–235.

Castro, M. J., García-Rodríguez, J. A., González-Vida, J. M. & Parés, C. 2006*b* A parallel 2D finite volume scheme for solving systems of balance laws with nonconservative products: Application to shallow flows. *Comput. Meth. Appl. Mech. Eng.* **195** (19-22), 2788–2815.

Castro, M. J., González-Vida, J. M. & Parés, C. 2006*c* Numerical treatment of wet/dry fronts in shallow flows with a modified Roe scheme. *Math. Models Methods Appl. Sci.* **16** (6), 897–931.

Castro, M. J., Macías, J. & Parés, C. 2001 A Q-scheme for a class of systems of coupled conservation laws with source term. Application to a two-layer 1D shallow water system. *Math. Modell. Numer. Anal.* **35** (1), 107–127.

Castro, M. J., Rebollo, T. C., Fernández-Nieto, E. D. & Parés, C. 2007*b* On well-balanced finite volume methods for nonconservative nonhomogeneous hyperbolic systems. *SIAM J. Sci. Comput.* **29** (3), 1093–1126.

Chacón-Rebollo, T., Delgado, A. D. & Fernández-Nieto, E. D. 2003 An entropy-correction free solver for non-homogeneous shallow water equations. *Math. Modell. Numer. Anal.* **37** (5), 755–772.

Chacón-Rebollo, T., Delgado, A. D. & Fernández-Nieto, E. D. 2004 Well-balanced finite volume schemes: Some stability and convergence results. *Monografías del Seminario Matemático García de Galdeano* **31**, 101–110.

Chen, S. C. & Peng, S. H. 2006 Two-dimensional numerical model of two-layer shallow water equations for confluence simulation. *Adv. Water Res.* **29** (11), 1608–1617.

Chen, S. C., Peng, S. H. & Capart, H. 2007 Two-layer shallow water computation of mud flow intrusions into quiescent water. *J. Hydraul. Res.* **45** (1), 13–25.

Cho, Y. S, Park, K. Y & Lin, T. H 2004 Run-up heights of nearshore tsunamis based on quadtree grid system. *Ocean Eng.* **31** (8-9), 1093–1109.

Chorin, Alexandre Joel 1973 Numerical study of slightly viscous flow. *J. Fluid Mech.* **57**, 785–796.

Coulliette, C., Lekien, F., Paduan, J. D., Haller, G. & Marsden, J. E. 2007 Optimal pollution mitigation in Monterey Bay based on coastal radar data and nonlinear dynamics. *Environ. Sci. Technolo.* **41**, 6565–6572.

Crawford, F. S. 1974 Singing corrugated pipes. *Am. J. Phys.* **42** (4), 278–288.

Csanady, G. T. 1975 Hydrodynamics of large lakes. *Ann. Rev. Fluid Mech.* **7**, 357–386.

Csanady, G. T. 2001 *Drag generation mechanisms*, pp. 124–141. Cambridge: Cambridge University Press.

de Moura, A. P. S. & Grebogi, C. 2004 Reactions in flows with nonhyperbolic dynamics. *Phys. Rev. E - Stat., Nonlinear, Soft Matter Phys.* **70** (3 2), 036216–1–036216–9.

Dumbser, M., Castro, M., Parés, C. & Toro, E. F. 2009 ADER schemes on unstructured meshes for nonconservative hyperbolic systems: Applications to geophysical flows. *Comput. Fluids* **38** (9), 1731–1748.

Farmer, D. M. & Armi, L. 1986 Maximal two-layer exchange over a sill and through the combination of a sill and contraction with barotropic flow. *J. Fluid Mech.* **164**, 53–76.

Fernández-Nieto, E. D., Castro-Díaz, M. J. & Parés, C. 2011 On an intermediate field capturing Riemann solver based on a parabolic viscosity matrix for the two-layer shallow water system. *J. Sci. Comput.* **48**, 117–140.

Fischer, H. B., List, E. J., Koh, R. C. Y., Imberger, J. & Brooks, N. H. 1979 *Mixing in inland and coastal waters*. Academic Press, New York.

Greaves, D. M. & Borthwick, A. G. L. 1998 On the use of adaptive hierarchical meshes for numerical simulation of separated flows. *Int. J. Numer. Meth. Fluids* **26** (3), 303–322.

Greaves, D. M., Borthwick, A. G. L., Wu, G. X. & Taylor, R. Eatock 1997 A moving boundary finite element method for fully nonlinear wave simulations. *J. Ship Res.* **41** (3), 181–194.

Greenberg, J. M. & Leroux, A. Y. 1996 A well-balanced scheme for the numerical processing of source terms in hyperbolic equations. *SIAM J. Numer. Anal.* **33** (1), 1–16.

Guzmán, A. M. & Amon, C. H. 1994 Transition to chaos in converging-diverging channel flows: Ruelle-Takens-Newhouse scenario. *Phys. Fluids* **6** (6), 1994–2002.

Guzmán, A. M. & Amon, C. H. 1996 Dynamical flow characterization of transitional and chaotic regimes in converging-diverging channels. *J. Fluid Mech.* **321**, 25–57.

Harten, A. 1984 On a class of high resolution total-variation-stable finite-difference schemes. *SIAM J. Numer. Anal.* **21** (1), 1–23.

Harten, A. & Hyman, J. M. 1983 Self adjusting grid methods for one-dimensional hyperbolic conservation laws. *J. Comput. Phys.* **50** (2), 235–269.

Jirka, G. H. & Uijttewaal, W. S. J. 2004 Shallow flows: a definition. In *Shallow flows* (ed. G. H. Jirka & W. S. J. Uijttewaal). Taylor & Francis, London.

Károlyi, G., Péntek, A., Toroczkai, Z., Tél, T. & Grebogi, C. 1999 Chemical or biological activity in open chaotic flows. *Phys. Rev. E - Stat. Phys. Plasmas Fluids Relat.* **59** (5), 5468.

Károlyi, G. & Tél, T. 2007 Effective dimensions and chemical reactions in fluid flows. *Phys. Rev. E - Stat., Nonlinear, Soft Matter Phys.* **76** (4), 046315.

Klein, P. 1990 Transition to chaos in unstable baroclinic systems: A review. *Fluid Dyn. Res.* **5** (4), 235–254.

Koshel, K. V. & Prants, S. V. 2006 Chaotic advection in the ocean. *Phys.-Uspekhi* **49** (11), 1151–1178.

Kozlov, V. F. & Koshel, K. V. 1999 Barotropic model of chaotic advection in background flows. *Izvestiya - Atmos. Ocean Phys.* **35** (1), 123–130.

Kozlov, V. F. & Koshel, K. V. 2001 Some features of chaos development in an oscillatory barotropic flow over an axisymmetric submerged obstacle. *Atmos. Ocean Phys.* **37** (3), 351–361.

Kozlov, V. F., Koshel, K. V. & Stepanov, D. V. 2005 Influence of the boundary on chaotic advection in the simplest model of a topographic vortex. *Izvestiya - Atmos. Ocean Phys.* **41** (2), 217–227.

Kranenburg, C. 1992 Wind-driven chaotic advection in a shallow model lake. *J. Hydraul. Res.* **30** (1), 29–46.

Kurganov, A. & Petrova, G. 2009 Central-upwind schemes for two-layer shallow water equations. *SIAM J. Sci. Comput.* **31** (3), 1742–1773.

Lacorata, G., Aurell, E. & Vulpiani, A. 2001 Drifter dispersion in the Adriatic Sea: Lagrangian data and chaotic model. *Annales Geophysicae* **19**, 121–129.

Lamb, H. 1953 *Hydrodynamics*, 6th edn. Cambridge: Cambridge University Press.

Landau, L. D. & Lifshitz, E. M. 1987 *Fluid Mechanics*, 2nd edn. Oxford: Pergamon.

Lau, Y. T, Finn, J. M. & Ott, E. 1991 Fractal dimension in nonhyperbolic chaotic scattering. *Phys. Rev. Lett.* **66** (8), 978–981.

Lee, W. K., Borthwick, A. G. L. & Taylor, P. H. 2010*a* On mathematical balancing of a two-layer shallow flow model. IAHR Eur. Div. Congress, 1st., Edinburgh: IAHR.

Lee, W. K., Borthwick, A. G. L. & Taylor, P. H. 2011 A fast adaptive quadtree scheme for a two-layer shallow water model. *J. Comput. Phys.* **230**, 4848–4870.

Lee, W. K., Taylor, P. H., Borthwick, A. G. L. & Chuenkhum, S. 2010*b* Vortex-induced chaotic mixing in wavy channels. *J. Fluid Mech.* **654**, 501–538.

Lekien, F., Coulliette, C., Mariano, A. J., Ryan, E. H., Shay, L. K., Haller, G. & Marsden, J. 2005 Pollution release tied to invariant manifolds: A case study for the coast of Florida. *Phys. D: Nonlinear Phenom.* **210** (1-2), 1–20.

LeVeque, R. J. 1998 Balancing source terms and flux gradients in high-resolution Godunov methods: The quasi-steady wave-propagation algorithm. *J. Comput. Phys.* **146** (1), 346–365.

Liang, Q. & Borthwick, A. G. L. 2009 Adaptive quadtree simulation of shallow flows with wet-dry fronts over complex topography. *Comput. Fluids* **38** (2), 221–234.

Liang, Q., Borthwick, A. G. L. & Stelling, G. 2004 Simulation of dam- and dyke-break hydrodynamics on dynamically adaptive quadtree grids. *Int. J. Numer. Meth. Fluids* **46** (2), 127–162.

Liang, Q., Borthwick, A. G. L. & Taylor, P. H. 2005 Chaotic mixing in a basin due to a sinusoidal wind field. *Int. J. Numer. Meth. Fluids* **47** (8-9), 871–877.

Liang, Q., Borthwick, A. G. L. & Taylor, P. H. 2006*a* Wind-induced chaotic advection in shallow flow geometries. Part I: Circular basins. *J. Hydraul. Res.* **44** (2), 170–179.

Liang, Q., Borthwick, A. G. L. & Taylor, P. H. 2006*b* Wind-induced chaotic advection in shallow flow geometries. Part II: Non-circular basins. *J. Hydraul. Res.* **44** (2), 180–188.

Liang, Q. & Marche, F. 2009 Numerical resolution of well-balanced shallow water equations with complex source terms. *Adv. Water Res.* **32** (6), 873–884.

Liang, Q., Taylor, P. H. & Borthwick, A. G. L. 2007*a* Particle mixing and reactive front motion in unsteady open shallow flow - Modelled using singular value decomposition. *Comput. Fluids* **36** (2), 248–258.

Liang, Q., Zang, J., Borthwick, A. G. L. & Taylor, P. H. 2007*b* Shallow flow simulation on dynamically adaptive cut cell quadtree grids. *Int. J. Numer. Meth. Fluids* **53** (12), 1777–1799.

Metcalfe, Guy & Ottino, J. M. 1994 Autocatalytic processes in mixing flows. *Phys. Rev. Lett.* **72** (18), 2875.

Meyers, S. D. & Luther, M. E. 2008 A numerical simulation of residual circulation in Tampa Bay. Part II: Lagrangian residence time. *Estuaries Coasts* **31** (5), 815–827.

Milne-Thomson, L. M. 1968 *Theoretical hydrodynamics*, 5th edn. London: Macmillan Press Ltd, revised.

Motter, A. E., Lai, Y. C. & Grebogi, C. 2003 Reactive dynamics of inertial particles in nonhyperbolic chaotic flows. *Phys. Rev. E - Stat., Nonlinear, Soft Matter Phys.* **68** (5 2), 563071–563075.

Mundt, M. D. & Hart, J. E. 1994 Secondary instability, EOF reduction, and the transition to baroclinic chaos. *Phys. D: Nonlinear Phenom.* **78** (1-2), 65–92.

Mundt, M. D., Hart, J. E. & Ohlsen, D. R. 1995 Symmetry, sidewalls, and the transition to chaos in baroclinic systems. *J. Fluid Mech.* **300**, 311–338.

Murillo, J., García-Navarro, P. & Burguete, J. 2009 Time step restrictions for well-balanced shallow water solutions in non-zero velocity steady states. *Int. J. Numer. Meth. Fluids* **60** (12), 1351–1377.

Nayfeh, A. H. 1985 *Problems in perturbation*. New York: John Wiley & Sons.

Negretti, M. E., Zhu, D. Z. & Jirka, G. H. 2007 Barotropically induced interfacial waves in two-layer exchange flows over a sill. *J. Fluid Mech.* **592**, 135–154.

Negretti, M. E., Zhu, D. Z. & Jirka, G. H. 2008 The effect of bottom roughness in two-layer flows down a slope. *Dyn. Atmos. Oceans* **45**, 46–68.

Neufeld, Z. & Tél, T. 1997 The vortex dynamics analogue of the restricted three-body problem: Advection in the field of three identical point vortices. *J. Phys. A: Math. Gen.* **30** (6), 2263–2280.

Neufeld, Z. & Tél, T. 1998 Advection in chaotically time-dependent open flows. *Phys. Rev. E - Stat. Phys. Plasmas Fluids Relat.* **57** (3 SUPPL. A), 2832–2842.

Nishimura, T. & Matsune, S. 1996 Mass transfer enhancement in a sinusoidal wavy channel for pulsatile flow. *Heat Mass Transfer* **32** (1-2), 65–72.

Novikov, A. & Bagtzoglou, A. C. 2006 Hydrodynamic model of the Lower Hudson River estuarine system and its application for water quality management. *Water Res. Manage.* **20** (2), 257–276.

Orre, S., Gjevik, B. & LaCasce, J. H. 2006 Characterizing chaotic dispersion in a coastal tidal model. *Cont. Shelf Res.* **26** (12-13), 1360–1374.

Osborne, A. R., Kirwan, A. D. Jr, Provenzale, A. & Bergamasco, L. 1986 A search for chaotic behaviour in large and mesoscale motions in the Pacific Ocean. *Physica D* **23**, 75–83.

Ottino, J. M. 1989 *The kinematics of mixing: Stretching, chaos and transport*. Cambridge: Cambridge University Press.

Parés, C. & Castro, M. J. 2004 On the well-balance property of Roe's method for nonconservative hyperbolic systems. Applications to shallow-water systems. *Math. Modell. Numer. Anal.* **38** (5), 821–852.

Pattantyús-Ábrahám, M., Tél, T., Krámer, T. & Józsa, J. 2008 Mixing properties of a shallow basin due to wind-induced chaotic flow. *Adv. Water Res.* **31** (3), 525–534.

Paz, R. R., Storti, M. A. & Garelli, L. 2010 Local absorbent boundary condition for nonlinear hyperbolic problems with unknown Riemann invariants. *Elsevier Science* **40** (1), 52–67.

Péntek, A., Károlyi, G., Scheuring, I., Tél, T., Toroczkai, Z., Kadtke, J. & Grebogi, C. 1999 Fractality, chaos, and reactions in imperfectly mixed open hydrodynamical flows. *Phys. A: Stat. Mech. Appl.* **274** (1), 120–131.

Press, W. H., Teukolsky, S.A., Vetterling, W. T. & Flannery, B. P. 1992 *Numerical Recipes in* F*ortran 77: The art of scientific computing.*. Cambridge: Cambridge University Press.

Ralph, M. E. 1986 Oscillatory flows in wavy-walled tubes. *J. Fluid Mech.* **168**, 515–540.

Read, P. L., Collins, M., Früh, W. G, Lewis, S. R. & Lovegrove, A. F. 1998 Wave interactions and baroclinic chaos: A paradigm for long timescale variability in planetary atmospheres. *Chaos, Solitons Fractals* **9** (1-2), 231–249.

Ridderinkhof, H. & Loder, J. W. 1994 Lagrangian characterization of circulation over submarine banks with application to the outer Gulf of Maine. *J. Phys. Oceanogr.* **24** (6), 1184–1200.

Roache, P. J. 1994 Perspective: A method for uniform reporting of grid refinement studies. *J. Fluids Eng., Trans. ASME* **116** (3), 405–413.

Roache, Patrick J. & Knupp, Patrick M. 1993 Completed Richardson extrapolation. *Comm. Numer. Meth. Eng.* **9** (5), 365–374.

Roberts, E. P. L. & Mackley, M. R. 1996 The development of asymmetry and period doubling for oscillatory flow in baffled channels. *J. Fluid Mech.* **328**, 19–48.

Roe, P. L. 1986 Characteristic-based schemes for the Euler equations. *Ann. Rev. Fluid Mech.* **18**, 337–365.

Rogers, B. D., Borthwick, A. G. L. & Taylor, P. H. 2003 Mathematical balancing of flux gradient and source terms prior to using Roe's approximate Riemann solver. *J. Comput. Phys.* **192** (2), 422–451.

Rogers, B. D., Borthwick, A. G. L. & Taylor, P. H. 2004 Godunov-type adaptive grid model of wave-current interaction at cuspate beaches. *Int. J. Numer. Meth. Fluids* **46** (6), 569–606.

Rogers, B. D., Fujihara, M. & Borthwick, A. G. L. 2001 Adaptive Q-tree Godunov-type scheme for shallow water equations. *Int. J. Numer. Meth. Fluids* **35** (3), 247–280.

Rom-Kedar, V., Leonard, A. & Wiggins, S. 1990 Analytical study of transport, mixing and chaos in an unsteady vortical flow. *J. Fluid Mech.* **214**, 347–394.

Rom-Kedar, V. & Wiggins, S. 1990 Transport in two-dimensional maps. *Arch. Ration. Mech. Anal.* **109** (3), 239–298.

Routh, E. J. 1881 Some applications of conjugate functions. *Proc. London Math. Soc.* **s1-12**, 73–89.

Salmon, R. 2002 Numerical solution of the two-layer shallow water equations with bottom topography. *J. Marine Res.* **60** (4), 605–638.

Samet, Hanan 1984 Hierarchical data structures for image processing. In *Proceedings of the International Conference on Systems, Man, and Cybernetics*, pp. 1072–1075.

Schijf, J. B. & Schonfeld, J. C. 1953 Theoretical considerations on the motion of salt and fresh water. In *Proc. of the Minn. Int. Hydraulics Conv.*, pp. 321–333. Joint meeting IAHR and Hyd. Div. ASCE.

Shi, Z., Meyers, S. & Luther, M.E. 2003 Modeling of wind wave-induced bottom currents and fine sand transport in Tampa Bay, Florida, USA. Int. Conf. Estuaries & Coasts, Hangzhou, China.

Silverman, M. P. & Cushman, G. M. 1989 Voice of the dragon: the rotating corrugated resonator. *Eu. J. Phys.* **10**, 298–304.

Sobey, I. J. 1980 On flow through furrowed channels. Part 1 Calculated flow patterns. *J. Fluid Mech.* **96** (1), 1–26.

Sobey, I. J. 1982 Oscillatory flows at intermediate Strouhal number in asymmetric channels. *J. Fluid Mech.* **125**, 359–373.

Sobey, I. J. 1985 Dispersion caused by separation during oscillatory flow through a furrowed channel. *Chem. Eng. Sci.* **40** (11), 2129–2134.

Spigel, R. H. & Imberger, J. 1980 The classification of mixed-layer dynamics in lakes of small to medium size. *J. Phys. Oceanogr.* **10**, 1104–1121.

Stephanoff, K. D., Sobey, I. J. & Bellhouse, B. J. 1980 On flow through furrowed channels. Part 2. Observed flow patterns. *J. Fluid Mech.* **96** (1), 27–32.

Stirling, J. R. 2000 Transport and bifurcation in a non-area-preserving two-dimensional map with applications to the discharge of pollution in an estuarine flow. *Phys. D* **144**, 169–193.

Stirling, J. R. 2003 Chaotic advection, transport and patchiness in clouds of pollution in an estuarine flow. *Discrete Cont. Dyn. Syst. - Series B* **3** (2), 263–284.

Stocker, R. & Imberger, J. 2003*a* Energy partitioning and horizontal dispersion in a stratified rotating lake. *J. Phys. Oceanogr.* **33**, 512–529.

Stocker, R. & Imberger, J. 2003*b* Horizontal transport and dispersion in the surface layer of a medium-sized lake. *Limnol. Oceanogr.* **48** (3), 971–982.

Taylor, G. I. 1922 Diffusion by continuous movements. *Proc. London Math. Soc.* **20** (1), 196–212.

Taylor, P. H. 1981 Flow excited motion of some unusual surfaces. PhD thesis, Cambridge University Press.

Tél, T. & Gruiz, M. 2006 *Chaotic dynamics: An introduction based on classical mechanics*. Cambridge: Cambridge University Press.

Tél, T., Károlyi, G., Péntek, A., Scheuring, I., Toroczkai, Z., Grebogi, C. & Kadtke, J. 2000 Chaotic advection, diffusion, and reactions in open flows. *Chaos* **10** (1), 89–98.

Tél, T., de Moura, A., Grebogi, C. & Károlyi, G. 2005 Chemical and biological activity in open flows: A dynamical system approach. *Phys. Rep.* **413** (2-3), 91–196.

Toro, E. F. 2001 *Shock-capturing methods for free-surface shallow flows*. Chichester: Wiley.

Toroczkai, Z., Károlyi, G., Péntek, A., Tél, T. & Grebogi, C. 1998 Advection of active particles in open chaotic flows. *Phys. Rev. Lett.* **80** (3), 500–3.

Vázquez-Cendón, M. E. 1999 Improved treatment of source terms in upwind schemes for the shallow water equations in channels with irregular geometry. *J. Comput. Phys.* **148** (2), 497–526.

von Hardenberg, J., Fraedrich, K., Lunkeit, F. & Provenzale, A. 2000 Transient chaotic mixing during a baroclinic life cycle. *Chaos* **10** (1), 122–134.

Vreugdenhil, C. B. 1979 Two-layer shallow-water flow in two dimensions, a numerical study. *J. Comput. Phys.* **33** (2), 169–184.

Walker, J. 2007 *The flying circus of physics*. John Wiley & Sons.

Waseda, T. & Mitsudera, H. 2002 Chaotic advection of the shallow Kuroshio coastal waters. *J Oceanogr.* **58** (5), 627–638.

Weisberg, R. H. & Zheng, L. 2006 Circulation of Tampa Bay driven by buoyancy, tides, and winds, as simulated using a finite volume coastal ocean model. *J. Geophys. Res. C: Oceans* **111** (1).

Wierschem, A. & Aksel, N. 2004 Influence of inertia on eddies created in films creeping over strongly undulated substrates. *Phys. Fluids* **16** (12), 4566–4574.

Wierschem, A., Scholle, M. & Aksel, N. 2003 Vortices in film flow over strongly undulated bottom profiles at low Reynolds numbers. *Phys. Fluids* **15** (2), 426–435.

Wilson, M. C. T., Summers, J. L., Kapur, N. & Gaskell, P. H. 2006 Stirring and transport enhancement in a continuously modulated free-surface flow. *J. Fluid Mech.* **565**, 319–351.

Yiu, K. F. C., Greaves, D. M., Cruz, S., Saalehi, A. & Borthwick, A. G. L. 1996 Quadtree grid generation: Information handling, boundary fitting and CFD applications. *Comput. Fluids* **25** (8), 759–769.

Zhou, J. G., Causon, D. M., Mingham, C. G. & Ingram, D. M. 2001 The surface gradient method for the treatment of source terms in the shallow-water equations. *J. Comput. Phys.* **168** (1), 1–25.

Zimmerman, J. T. F. 1986 The tidal whirlpool: A review of horizontal dispersion by tidal and residual currents. *Neth. J. Sea Res.* **20** (2-3), 133–154.